Sorption thermal energy storage for sustainable heating and cooling

by

Mina Rouhani

M.Sc., Amirkabir University of Technology, 2008

B.Sc., K.N.T. University of Technology, 2006

Thesis Submitted in Partial Fulfillment of the
Requirements for the Degree of
Doctor of Philosophy

in the
School of Mechatronic Systems Engineering
Faculty of Applied Science

SIMON FRASER UNIVERSITY

Summer 2019

Approval

Name:	**Mina Rouhani**
Degree:	**Doctor of Philosophy**
Title:	**Sorption thermal energy storage for sustainable heating and cooling**
Examining Committee:	**Chair:** Helen Bailey Lecturer
	Majid Bahrami Senior Supervisor Professor
	Gary Leach Supervisor Associate Professor
	Byron Gates Supervisor Associate Professor
	Woo Soo Kim Internal Examiner Associate Professor
	Angelo Freni External Examiner Senior Researcher Institute of the Chemistry of OrganoMetallic Compounds (CNR- ICCOM) Italian National Council of Research (CNR)
Date Defended/Approved:	July 12, 2019

Abstract

Heating and cooling of residential buildings account for 15% of the total energy use in Canada and produce 11% of the total GHG emissions, due to reliance on fossil fuels. Renewable thermal energy and usage of low-grade waste heat offer solutions for decarbonization of heating and cooling. Inherent intermittent nature of such energy resources makes integration of thermal energy storage (TES) systems inevitable. High energy storage density, low heat loss, and using non-toxic and non-polluting refrigerants make sorption TES (S-TES) more appealing and effective for heat/cold storage, compared to other thermal storage methods.

This PhD research is set out to assess the performance of low-grade heat-driven S-TES systems for space heating and cooling. As such, the focus of this study is on the thermal and sorption characterization of the sorber bed, mathematical S-TES system modeling, and experimental testing of an S-TES prototype. An analytical model is developed for prediction of thermal conductivity and thermal resistance of packed bed sorbers. Thermal conductivity of packed bed sorber of AQSOA FAM-Z02 with different numbers of layers is measured by heat flow meter for the first time. The model, which is validated by the experimental data, provides a comprehensive platform for the design of packed bed S-TES to (i) predict thermal conductivity and thermal contact resistance of packed bed under the target operating condition and (ii) optimize the packed bed by finding the optimum particle size and arrangement. Small-scale characterizations and screening of sorbent candidates are performed by thermogravimetric analysis/differential scanning calorimetry. Moreover, comprehensive experimental studies are carried out on a custom-built lab-scale S-TES in our lab to study storage performance under various conditions, namely, i) coated vs loose grain sorbent configurations, ii) various heat storage durations, iii) adding high conductive additives in the sorbent material, iv) different operating temperatures, and v) different discharge-to-charge time ratios. A comprehensive transient resistance-capacitance lumped-parameter model is developed to assess the performance of a closed S-TES system. The model is proved to be accurate in comparison with the experimental data and offers a reliable platform for the design and optimization of an S-TES system.

Keywords: thermal energy storage; sorption thermal energy storage; thermochemical energy storage; renewables; thermal conductivity; thermal resistance; sorption kinetics

Acknowledgements

I would like to deeply thank the many great people who have helped me throughout the course of my doctoral study at Simon Fraser University. First and foremost, I wish to express my sincere gratitude to my senior supervisor, Dr. Majid Bahrami, for his continuous support, guidance, encouragement, and constructive critiques throughout my PhD studies. I have been fortunate to present my work at various conferences, workshops, and seminars and to connect with other researchers in the field.

I am very thankful to my supervisory committee members, Dr. Byron Gates and Dr. Gary Leach, for their time and valuable feedback throughout my PhD proposal and defense. I am also grateful to Dr. Angelo Freni and Dr. Woo Soo Kim for their time reading this thesis and comments. I extend many thanks to my colleagues and alumni at Laboratory for Alternative Energy Conversion at Simon Fraser University for their valuable time, support, and contributions. I would especially like to thank Dr. Wendell Huttema and Dr. Claire McCague for their support and the insightful discussions of the sorption technologies.

I would like to acknowledge the Canadian Queen Elizabeth II Diamond Jubilee Scholarship Program, not only for giving me the honor of the Queen Elizabeth Advanced Scholar but also for the collaboration opportunity with CanmetENERGY-Ottawa, Natural Resources Canada. I would particularly like to thank Dr. Reda Djebbar for being my mentor and constant support when I worked at CanmetENERGY-Ottawa under his supervision as a visiting researcher. I gratefully acknowledge the financial support received from Natural Sciences and Engineering Research Council of Canada (NSERC) through the Automotive Partnership Canada Grant No. APCPJ 401826-10.

Table of Contents

List of Tables

List of Figures

Nomenclature

A	(cm^2)	Surface area of the packed bed
ACS		Adsorption cooling system
a_L	(mm)	Radius of microcontact
ATES		Adsorption thermal energy storage
α_T		Thermal accommodation coefficient
β		Volume fraction
COP		Coefficient of performance
c_{HEX}	($J\ kg^{-1}\ K^{-1}$)	Heat exchanger specific heat capacity
c_p	($J\ kg^{-1}\ K^{-1}$)	Specific heat capacity at constant pressure
$\mathrm{C_{st}}$	($\$\ MJ^{-1}$ or $\$\ kW^{-1}$)	Cost of storage system
$\mathrm{C_m}$	($\$\ kg^{-1}$)	Material cost per material mass
d	(mm)	Adsorbent particle diameter
D	($m^2\ s^{-1}$)	Mass diffusivity
δ	(mm)	Displacement
Δm	(kg)	Mass changes
ε		Adsorbent particle porosity
E	(G Pa)	Young's modulus
ESD	($GJ\ m^{-3}$ / $MJ\ kg^{-1}$)	Energy storage density
$\eta_{\mathrm{th,st}}$		Thermal efficiency of storage system
F	(N)	Contact force
FCC		Face center cubic arrangement
h_{fg}	($J\ kg^{-1}$)	Enthalpy of evaporation
HEX		Heat exchanger
HTF		Heat transfer fluid
k_{ads}	(s^{-1})	adsorption rate
k	($W\ m^{-1}\ K^{-1}$)	Thermal conductivity
k_{tot}	($W\ m^{-1}\ K^{-1}$)	Total thermal conductivity of the packed bed adsorber (effects of TCR is included.)
$k_{\mathrm{eff,bed}}$	($W\ m^{-1}\ K^{-1}$)	Effective (medium) thermal conductivity of the packed bed adsorber (effects of TCR is not included.)
k_{init}	(s^{-1})	Initial sorption rate coefficient
L_{bed}	(mm)	Length (thickness) of the packed bed
LDF		Linear driving force equation
LMTD		log mean temperature difference
L_{w}	($kJ\ kg^{-1}$)	Latent heat of water
m	(kg)	Mass
$\dot{m}$	($kg\ s^{-1}$)	Mass flow rate
m		Number of adsorbent particles in each adsorbent layer
MSP	($W\ kg^{-1}$)	Maximum attainable specific power
n		Number of layers of adsorbent particles
r	(mm)	Adsorbent particle radius
ν		Poisson's ratio
ω	($kg_w\ kg_{ads}^{-1}$)	Water uptake
ω_0	($kg_w\ kg_{ads}^{-1}$)	Initial water uptake
ω_∞	($kg_w\ kg_{ads}^{-1}$)	Maximum water uptake

PCM		Phase change material
P	(Pa)	Gas pressure
P_0	(Pa)	Saturation pressure at adsorbent temperature
P_{contact}	(Pa)	Contact pressure at the contact of adsorbent particle and the metal surface
$\dot{Q}$	(W)	Heat flow
$\dot{Q}_{\mathrm{C,macro}}$	(W)	Macro-contact heat flow
$\dot{Q}_{\mathrm{c,micro}}$	(W)	Micro-contact heat flow
$\dot{Q}_{\mathrm{g,micro}}$	(W)	Micro-gap heat flow
$\dot{Q}_{\mathrm{G,macro}}$	(W)	Macro-gap heat flow
Q_{stored}	(J)	Stored energy
Q_{total}	(J)	Total heat transfer
R	(K m^2 W^{-1})	Thermal resistance
ρ	(kg m^{-3})	Density
S	(m^2)	Heat transfer surface area
SC		Simple cubic arrangement
SCP	(W kg$_{\mathrm{dry,ads}}^{-1}$)	Specific cooling power
SE	(MJ kg^{-1})	Specific energy, same as the gravimetric ESD
SP	(W kg$_{\mathrm{dry,ads}}^{-1}$)	Specific power
$\mathrm{S-TES}$		Sorption thermal energy storage
ψ		Packed bed solid fraction
t	(s)	Time
T	(K)	Temperature
τ	(s)	Characteristic time
TCR	(K m^2 W^{-1})	Thermal contact resistance
TCS		Temperature control system
t_{cycle}	(s)	Cycle time
TCES		Thermochemical energy storage
TCM		Thermochemical material
TES		Thermal energy storage
TGA		Thermogravimetric analysis
U	(W m^{-2} K^{-1})	Overall heat transfer coefficient
V	(m^{-3})	Volume
VCP	(W m^{-3})	Volumetric cooling power

Subscripts

0	Initial condition
$\mathrm{adsorbate}$	Adsorbate
$\mathrm{adsorbent}$	Adsorbent material
as	Aluminum sheet
$\mathrm{b\ cell}$	Boundary unit cell
bed	Sorber bed
cell	Unit cell
cf	Cooling fluid
ch	Charge process (desorption)
$\mathrm{chilled}$	Chilled water
closed	Closed
cond	Condenser

$contact$	At the contact of adsorbent particles and the HEX metal surface
$coolant$	Coolant water
dch	Discharge process (adsorption)
ECU	Evaporator/condenser unit
eff	Effective
eq	Equilibrium
$evap$	Evaporator
g	Adsorbate gas
hf	Heating fluid
∞	Equilibrium condition
i	Inlet
$input$	Input
mat	Material
lw	Liquid water
o	Outlet
$open$	Open
p	Adsorbent particle
s	Solid particle (adsorbent skeleton)
sys	System
t	Through the time
tot	Total
w	Water
wet	Wet adsorbent particle

Executive Summary

Over 60% of residential and 50% of commercial building energy usage are devoted to heating and cooling. Currently, around 75% of this energy is generated by fossil fuels, meaning heating and cooling have a significant share of greenhouse gas emissions. Renewable thermal energy and usage of low-grade waste heat offer solutions for decarbonization of heating and cooling. Inherent intermittent nature of such energy resources makes integration of thermal energy storage (TES) systems inevitable. TES is a promising alternative to conventional heating and cooling methods, which plays a key role in synchronizing energy demand and supply. Among heat storage methods, sorption TES (S-TES) has recently attracted immense attention for its relatively high energy storage density (ESD), up to 3 $GJ \cdot m^{-3}$ at the material level, with minimal sensible heat loss. Considering the high ESD of the sorption materials, developing S-TES is aligned with the Net Zero Energy (NZE) housing goal, i.e. the buildings that produce at least as much energy as they consume on an annual basis, which is being pursued by the government of Canada.

S-TES uses low-grade energies to take advantage of sorption/desorption of a sorbate (e.g., water) on the surface of moisture-retentive sorbents (e.g., silica gel), or in the bulk of the sorbents (e.g., $CaCl_2$ in silica gel-$CaCl_2$), through an exothermic/endothermic reaction, which leads to discharging/charging of sorption energy. Most of the sorbent materials are non-toxic, non-flammable, thermally stable, and environmentally friendly with low global warming and low ozone depletion potential. Sorption-based technologies have proven to be promising for cooling, heating, and thermal energy storage. However, system complexity, high vacuum operation, poor heat and mass transfer within sorber beds, and low thermodynamic efficiency remain barriers to wide-scale adoption of this storage technology. Accordingly, an in-depth understanding of the S-TES performance is set as the main focus of this PhD research and is achieved through (i) characterization of the sorbent material, (ii) performing thermodynamic system analysis, and (iii) conducting a comprehensive experimental study on the performance of the S-TES.

Objectives

The objectives of this research are sorbent material characterization, sorbent candidate screening, and development of an S-TES demonstration system for sustainable low-grade heating and cooling applications. This, in turn, requires an in-depth understanding of the mechanisms of heat and mass transfer in the sorber bed and storage performance analysis of S-TES with various working pairs by comprehensive theoretical and experimental studies.

Methodology

In this PhD research, a systematic approach is adopted to understand different processes in an S-TES system and to address the following key research questions:

(i) How to measure and model the effective thermal conductivity (ETC) of a loose-grain packed bed sorber?
(ii) What are the effects of particle size, sorbent thermal conductivity, and sorbate pressure on the ETC?
(iii) What is the role of thermal contact resistance on the total thermal conductivity of a packed bed sorber and the performance of such systems?
(iv) What is the performance of thermochemical energy storage system compared to the adsorbent storage systems?
(v) What is the effect of storage duration on storage performance?
(vi) What is the effect of sorbent configuration (coated vs loose grain) on the performance of sorber bed?

To this end, and as shown in Figure 1, this program entails the following milestones:

- Characterization of thermal and sorption properties, including thermal conductivity, water uptake capacity, and sorption rate of the sorbent material candidates for thermal storage applications;
- Development of mechanistic thermodynamic models to predict thermal storage performance of S-TES under various operating conditions and with different working pairs; and
- Design and experimental study of an S-TES cycle for residential application.

Contributions

A summary of the contributions of this research is listed below:

Sorbent material properties

- Effective thermal conductivity (ETC) of a loose-grain packed bed sorber is measured [1], [2], for the first time. The ETC of a packed bed AQSOA FAM-Z02 is measured using a heat flow meter (HFM) for various numbers of layers of adsorbent under mean temperatures ranging from 10 to 80 °C. Thermal contact resistance (TCR) at the interface between the particles and heat exchanger surface is deconvoluted from the total packed bed resistance and its relative importance to the total resistance of the bed is studied.

- ETC of a packed bed adsorber is modeled [3]–[5] analytically, based on a unit-cell approach, to predict the ETC of the packed bed sorbers as a function of number of adsorbent layers, adsorbent type, particle size, bed porosity, water uptake, temperature, contact pressure, particle surface roughness, particle arrangement, and gas pressure. This model also predicts the thermal contact resistance qualitatively.

- A full-scale in-situ water uptake rate measurement setup of a coated AQSOA FAM-Z02 S-TES is built [6]. Kinematics of water sorption of a full-scale coated AQSOA FAM-Z02 thermal energy storage are experimentally studied through an in-situ temperature and mass measurement. Effects of cycle time and evaporator temperature on the uptake rate are also studied.

- A sorbent material screening is performed under typical operating conditions for heat storage systems. Studied sorbent candidates include AQSOA FAM-Z02, silica gel-$CaCl_2$, and vermiculite-$CaCl_2$ using simultaneous thermal analysis—thermogravimetric analysis/differential scanning calorimetry (TGA/DSC).

Storage system modeling and experimental study

- Theoretical and experimental investigations on the performance of an AQSOA FAM-Z02 energy storage system are performed for both packed and coated

sorbent configurations [7], [8]. A thermodynamic lumped model is developed to study the effect of various operating conditions on the ESD of an AQSOA FAM-Z02 in a lab-scale closed energy storage setup. An experimental study is conducted to assess the performance of the AQSOA FAM-Z02 storage for both coated and loose grain configurations.

- Experimental investigation on the performance of a silica gel-$CaCl_2$ thermal storage system is performed [9]. Effects of storage period on the performance of the storage system are studied. Moreover, the effect of high conductive additives on storage performance is investigated by adding graphite flakes to a silica gel-$CaCl_2$ composite.

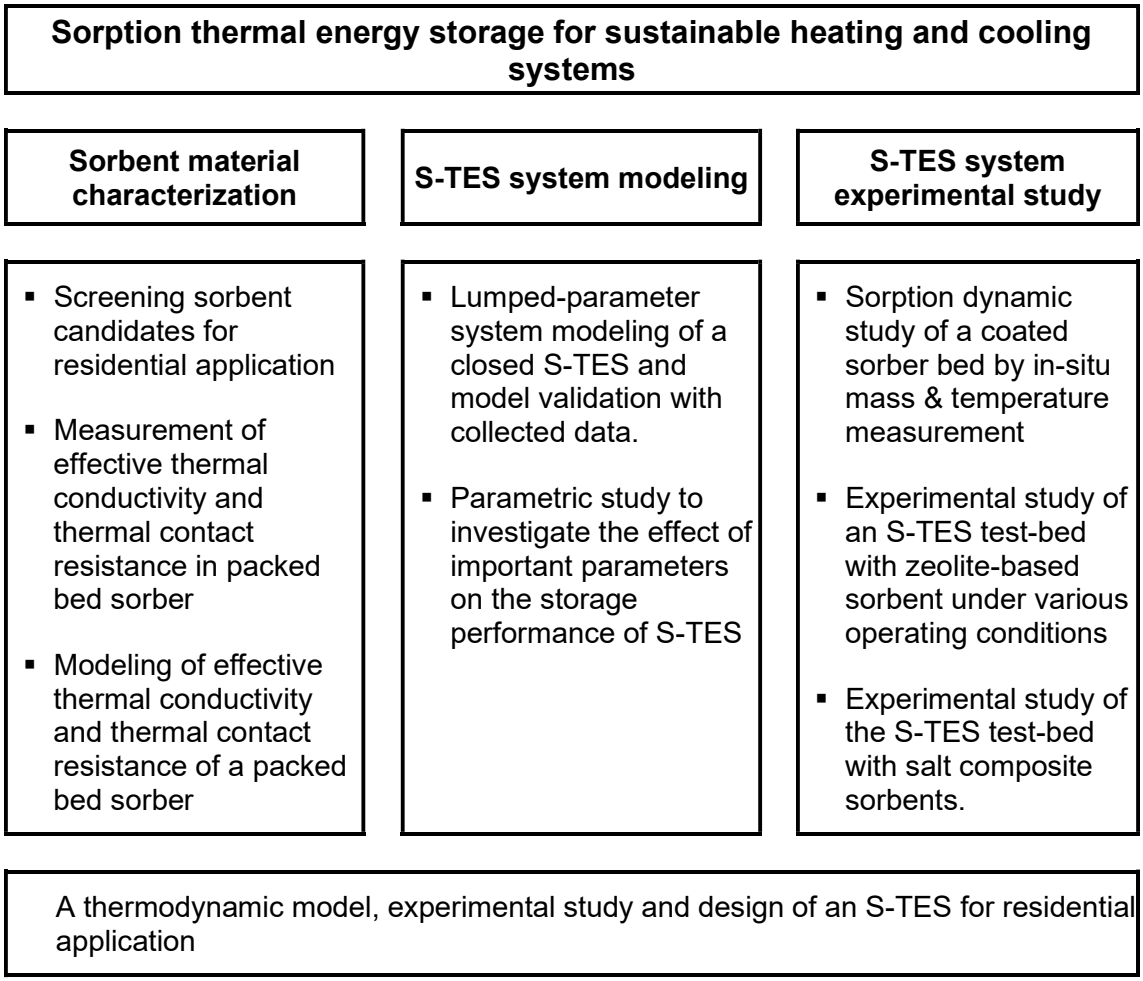

Figure 1. Research roadmap and components of the PhD program.

Chapter 1.

Introduction

With significant growth in population, energy demand, and industrial activities, the global primary energy consumption has been more than doubled in the last 40 years [10]. About 32% (115 EJ) of the global energy demand is associated with the building sector (24% for residential and 8% for commercial) [11]. As shown in Figure 2a, heating and cooling account for 58%, i.e. space heating, 32%, water heating, 24%, and cooling, 2%, of the global yearly energy demand in the building sector. Among energy carriers in the building sector, about 60% are non-renewable resources, Figure 2b, which are responsible for 30% of the global CO_2 emissions [11].

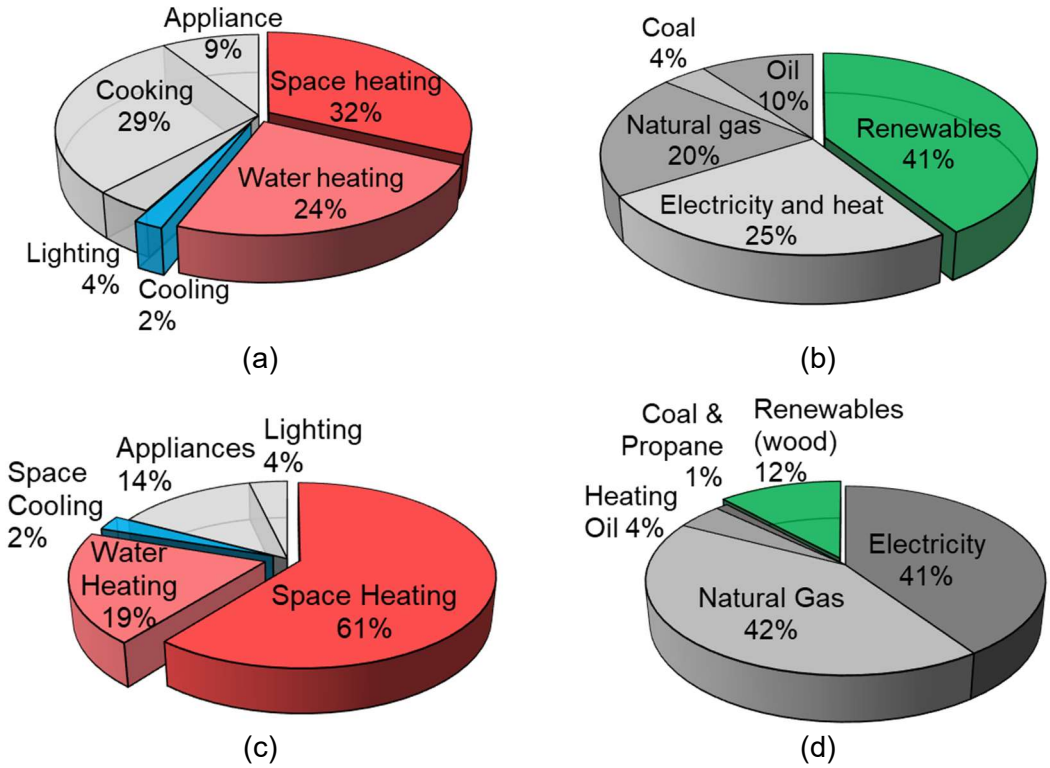

Figure 2. (a) Global energy consumption, (b) energy carriers of the building sector in 2010 [11], and (c) energy consumption and (d) energy carriers of the building sector in Canada in 2016.

In Canada, about 83% of residential and 64% of commercial building energy usage are devoted to heating and cooling with more than 90% share of heating. Currently, more

than 80% of this energy is generated using fossil fuels, meaning heating and cooling have a significant share of greenhouse gas emissions in residential buildings (13%) and commercial buildings (9%).

Hence, the heating and cooling of the building sector is a major contributor to the climate change and air pollution. Concerns over the increasing energy consumption and increasing CO_2 emissions have resulted in numerous studies to develop efficient clean sustainable heating and cooling technologies. Renewable thermal energy and usage of low-grade waste heat, with temperatures below 100 °C, offer solutions for decarbonization of heating and cooling in the building sector. Figure 3 shows the energy transition of Canada to renewable sources over the last two decades [12], [13].

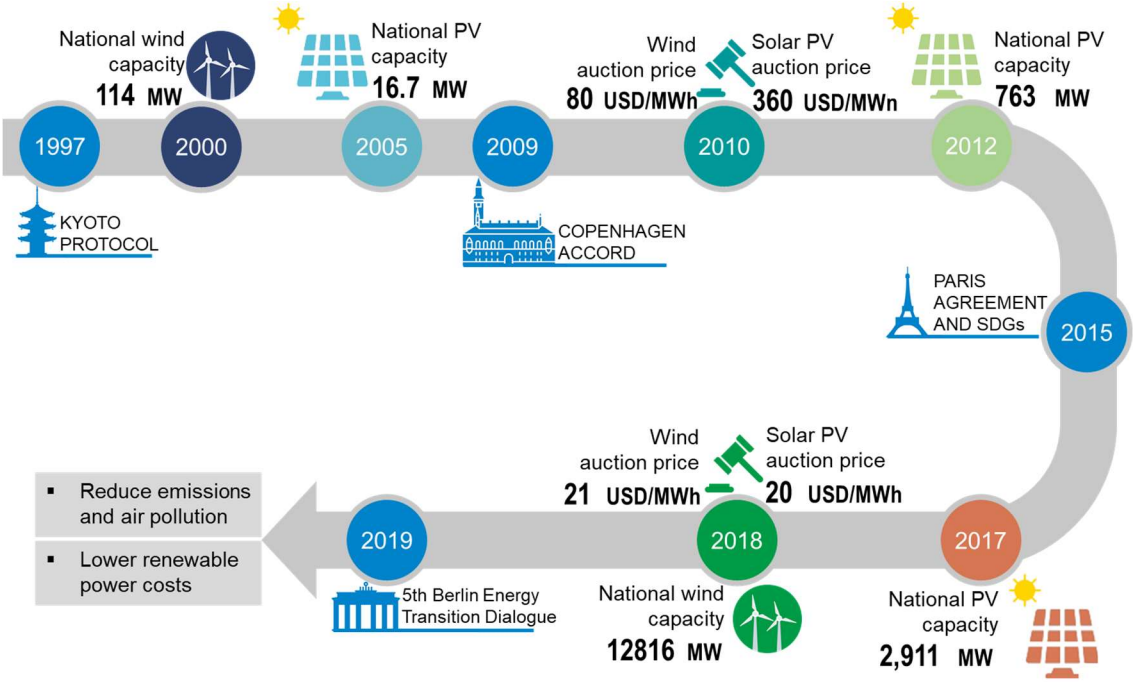

Figure 3. Canada's energy transition pathway to renewable sources ([12], adopted from Ref. [13]).

However, the intermittent nature of these energy sources necessitates integrating thermal energy storage unit with the main heating/cooling system to utilize these sustainable heat sources effectively. Thermal energy storage (TES) is an essential energy conservation technology for efficient heating, cooling and moisture control applications. Heat and cold can be stored in a storage compartment to be used later, controlled by the temperature and power which are demanded by the user. During the charging process, thermal energy is received by TES system to be stored in the storage chamber during the

storage period. Thereafter, the stored energy is released contingent on the thermal energy demand. Hereby, TES mitigates the mismatch between the energy supply and demand.

1.1. Thermal energy storage methods

There are three common types of TES: (i) sensible TES; (ii) latent TES using phase change materials (PCM); and (iii) thermochemical energy storage (TCES), including the sorption TES (S-TES) and chemical reactions. Specific sensible energy is stored by changes in the temperature and is proportional to the specific heat and temperature difference, as shown in Figure 4a. Sensible energy is stored in various materials such as water, air, brick, and concrete, and the storage material is selected based on its specific heat and operating temperature. The sensible TES systems are mature and proven technologies for large-scale heating and cooling applications, although they are bulky and suffer from high heat loss to the ambient.

Latent TES uses the phase transition of a material, usually solidification-melting, to charge/discharge thermal energy at a constant temperature (melting temperature), as shown in Figure 4b. After solidification is completed, further heat transfer results in storage of sensible energy. PCM selection is mainly based on their phase change enthalpy and melting temperature. Despite higher storage capacity of PCM compared to the sensible TES, issues such as phase separation, subcooling, low thermal conductivity, corrosion, and lack of long-term stability limit their applications [14], [15]. Moreover, latent TES suffers from inflexible heat source temperature, meaning that a certain melting temperature should be provided and cannot be partially charged/discharged by heat source/sink at temperatures far from the melting temperatures.

In TCES, energy can be stored through an endothermic reaction and released in a reverse exothermic process. TCES refers to the sorption process and chemical reactions [16]. Chemical reaction storage systems are mostly used at high temperatures (above 400 °C) and their enthalpy of the reaction is typically high (80–180 kJ mol^{-1}) [14]. For low-grade heat application, S-TES systems offer higher storage capacity – an order of magnitude on the material-scale – compared to the sensible and latent TES systems, as shown in Figure 4c.

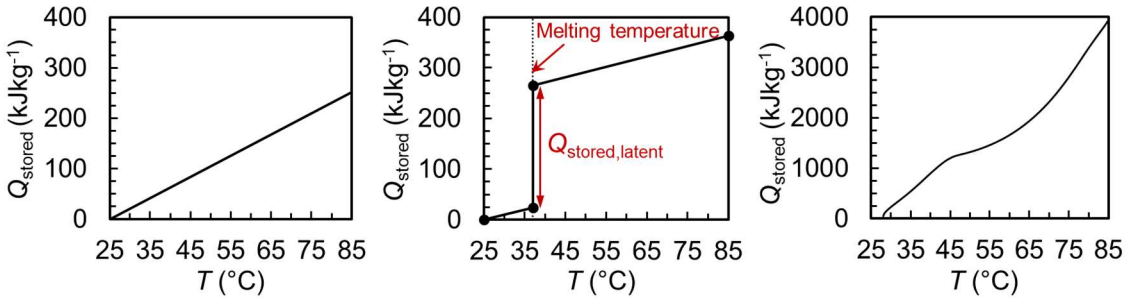

$Q_{\text{stored,sens}} = c_p \Delta T$ (a)

$Q_{\text{stored,latent}} = \Delta h_{\text{fg}}$ (b)

$Q_{\text{stored,sorp}} = \Delta h_{\text{sorp}}$ (c)

Figure 4. Stored specific heat versus temperature and the related thermodynamic equation for (a) sensible TES (water at reference temperature of 25 °C), (b) latent TES (n-Eicosane $C_{20}H_{42}$ with melting temperature of 37 °C, phase change enthalpy of 241 kJkg^{-1}, and specific heat of 2.01-2.04 kJ kg^{-1} K^{-1} [14]), and (c) thermochemical energy storage (sorbent material of Na_2S-H_2O with heating rate of 1 Kmin^{-1} from 25 °C to 85 °C).

1.2. Thermal energy storage performance indicators

A successful TES system should have the following key features: (i) high energy storage per volume, (ii) low thermal losses during the storage period, (iii) high heat transfer rate between the heat transfer fluid (HTF) and the storage material to enable desirable and fast charge/discharge thermal power, (iv) reasonable total cost, (v) reversibility of the storage cycle, (vi) negligible corrosion and degradation, (vii) contribution to reduction of GHG emissions, and (vii) easy control [14]. Accordingly, the following indicators are used for the performance assessment of TES:

- **Energy storage density (ESD, GJm^{-3}):** stored energy per volume of the storage system, which shows the storage capacity as well as the compactness of a TES system. ESD is also reported per volume of the sorbent material, storage bed, or the whole storage system that includes the auxiliary components such as heat exchanger(s), chamber, etc., as shown in Eq. (1).

$$\text{ESD} = \frac{Q_{\text{dch}}}{V_{\text{mat/bed/sys}}} \quad (1)$$

- **Specific energy (SE, kJkg^{-1}):** stored energy per mass of the storage system (or the storage material), which shows the storage capacity as well as the weight of the TES system. As shown in Eq. (2), SE is also presented per mass of the sorbent material, storage bed, or the whole storage system.

$$\mathrm{SE} = \frac{Q_{\mathrm{dch}}}{m_{\mathrm{mat/bed/sys}}} \tag{2}$$

SE and ESD are often used interchangeably in the literature. For making a precise comparison between different storage systems, the diversity in the SE and ESD definition should be taken into consideration. Figure 5 shows the ESD of the above-mentioned storage technologies. Latent TES provides higher ESD (≈ 0.3-0.5 GJm^{-3}), compared to the sensible TES systems (≈ 0.0072-0.2 GJm^{-3}), at an almost constant temperature. Chemical reaction storage systems require high-temperature heat sources (above 400 °C) [14]. S-TES systems offer higher ESD (≈ 0.5-3 GJm^{-3}) compared to the sensible and latent TES systems. Table 1 also provides a comparison of various TES technologies in terms of SE and ESD.

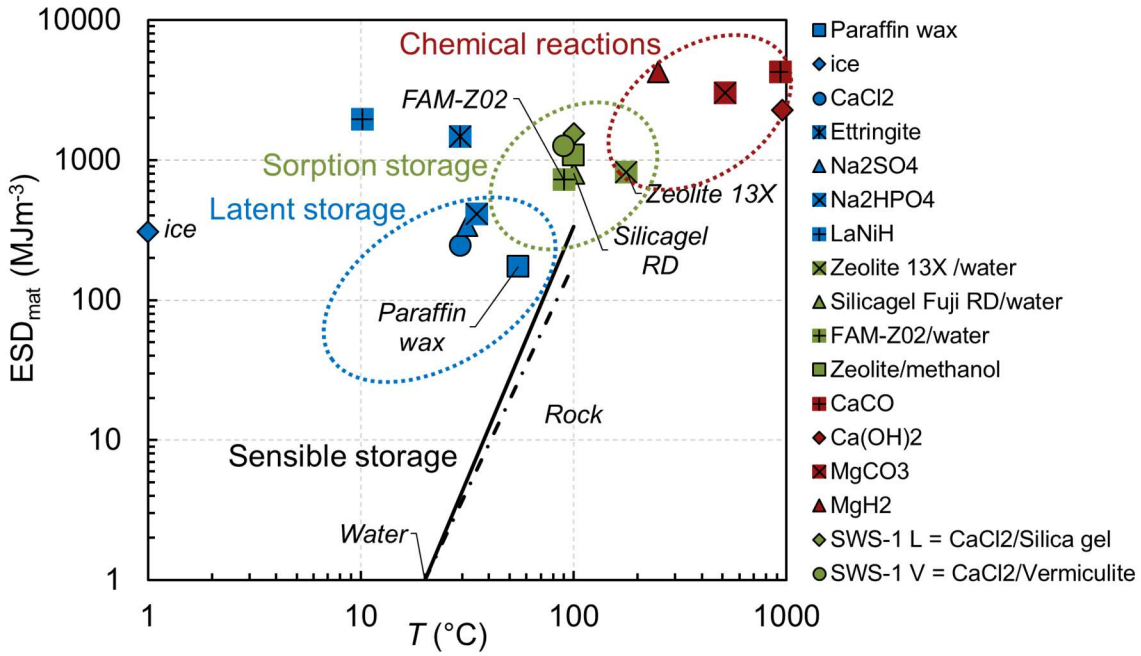

Figure 5. Energy storage density of various thermal energy storage materials (adopted from Refs. [17], [18]).

Table 1. Comparison of different storage technologies for sustainable heating applications [14], [19]–[24]

	Material	Density (kgm^{-3})	c_p ($Jkg^{-1}K^{-1}$)	Phase change enthalpy ($kJkg^{-1}$)	Sorption enthalpy ($kJkg^{-1}$)	SE ($MJkg^{-1}$)	ESD (GJm^{-3})
Sensible (0.0072-0.2 GJm^{-3})	Brick	1800	837	-	-	0.017 (ΔT=20°C)	0.0302 (ΔT=20°C)
	Water	988	4182	-	-	0.084 (ΔT=20°C)	0.084 (ΔT=20°C)
Latent (0.3-0.5 GJm^{-3})	Paraffin C22-C45	795 (liquid,70°C) 920 (solid,20°C)	2400	189	-	0.189	0.174 (58-60 °C)
	S19 (salt hydrates)	1520	1900	160	-	0.160	0.243
Thermochemical including sorption (0.5-3 GJm^{-3})	Silica gel Fuji RD	730	921	-	2400	0.96 (uptake = 0.4 $kgkg^{-1}$)	0.77
	AQSOA FAM-Z02	600-700	822-942	-	3250	1.07 (uptake = 0.33 $kgkg^{-1}$)	0.55 (90°C)
	$MgSO_4$ / $7H_2O$	1670	-	-	-	-	2.3-2.8 (122°C)

- **Averaged specific discharge/charge power ($SP_{ch/dch}$, Wkg^{-1}):** the average discharge/charge rate per mass of the storage material, which shows how fast a storage system can charge/discharge the thermal energy.

$$\mathrm{SP}_{\mathrm{dch/ch}} = \frac{Q_{\mathrm{dch/ch}}}{\left(t_{\mathrm{dch/ch}}\ m\right)} \tag{3}$$

- **Maximum specific power ($MSP_{ch/dch}$, Wkg^{-1}):** the maximum attainable power, based on the minimum possible discharge time, and the storage system mass (or storage material mass) [25].

- **Storage thermal efficiency (η_{th}):** the delivered thermal energy in the discharging process to the input heat during the charging process, which shows the heat loss in the storage system.

$$\eta_{\mathrm{th}} = \frac{Q_{\mathrm{dch}}}{Q_{\mathrm{ch}}} \tag{4}$$

The efficiency of the system is also defined by the overall energy efficiency (η), i.e., the ratio of the discharged thermal energy to the total energy consumed for charging

and discharging of the system, which shows all inefficiencies and losses in the storage system [26].

- **Cost (C_{st}, \$MJ^{-1} or \$kW^{-1}):** the capital and operation costs of the storage system per storage capacity (\$MJ^{-1}) or power (\$kW^{-1}) [26]. In the storage material screening process, the cost of material per material-based storage capacity should be minimized.

In addition to the above-mentioned performance indices, the operation strategy and the integration into the main heating/cooling system have significant effects on the thermal- and cost-effectiveness of the storage system.

1.3. Classification of sorption storage systems

S-TES systems can be divided in four categories, as shown in Figure 6: (i) liquid absorption, (ii) solid adsorption, (iii) sorption reaction, and (iv) composite materials, salts in porous matrix [28].

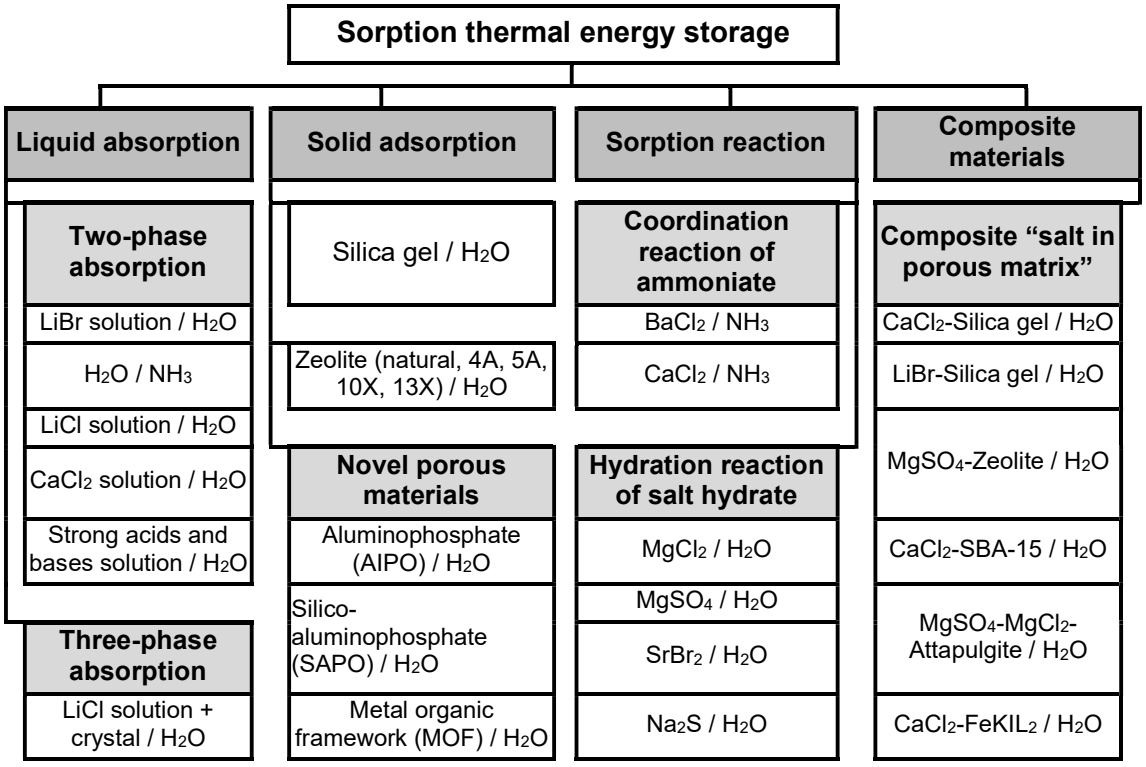

Figure 6. Classification of the sorption thermal energy storage systems (from ref. [29])

Absorption is the transfer of a substance (absorbate) to the bulk of another substance (absorbent), where the absorbent phase is enriched with the absorbate phase

and sorption does not happen only on the surface (see Figure 7a). On the other hand, adsorption in the adsorption TES (ATES) systems occurs on the surface of a substance (see Figure 7b), where the adsorbate molecules attach to the surface of the adsorbent through the van der Waals forces [30], [31]. Liquid absorption is referred to the two-phase absorption process, although a three-phase absorption has also been proposed, where a salt crystal (such as lithium chloride crystals [32]) is also used to increase ESD [32].

Sorption chemical reactions are divided into coordination reaction of ammoniate with ammonia and hydration reaction of salt hydrate with water [29]. In contrast to the liquid absorption and solid adsorption, the chemical reaction is monovariant, so the equilibrium uptake is defined by only one independent property (pressure or temperature) and the working temperature is easily controlled and adjusted by changing the pressure [33]. In the sorption chemical reaction hysteresis may exist [29]. Sorption reaction systems provide high ESD and cover different ranges of the heat source temperatures depending on the slat type [28].

The composite salt porous matrix consists of a porous matrix (e.g. silica gel, zeolite and expanded vermiculite) and an inorganic salt (e.g. LiCl, $CaCl_2$ and $MgSO_4$). The porous matrix is supposed to provide enough surface area for the sorption process and large pore volume for holding the liquid solution, as well as thermal and mechanical stability [34].

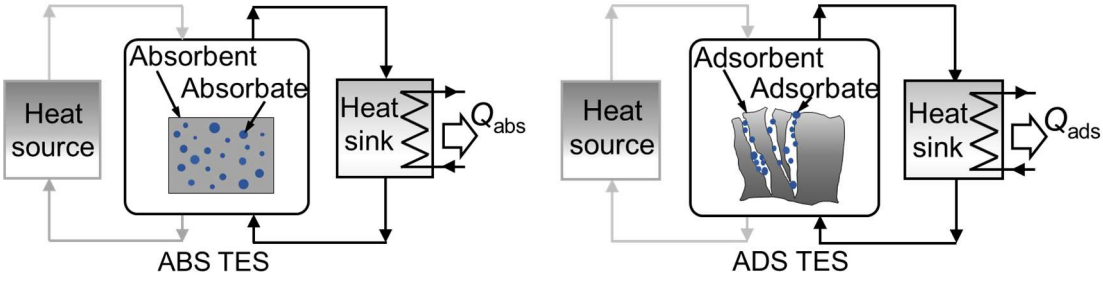

(a) (b)

Figure 7. (a) Absorption storage vs (b) adsorption storage systems.

1.4. Open and closed S-TES systems

From the perspective of operating pressure, two types of sorption systems are defined: open (Figure 8a) and closed (Figure 8b) systems. In open S-TES, an air stream carries the sorbate and heat in/out of the sorber bed. During the charging process, dry hot air enters the sorber bed, water vapor is desorbed from the sorbent and cooler humid air

leaves the bed. In the discharging process, wet cool air enters the sorber bed, water vapor is adsorbed by the sorbent materials and dry hot air leaves the bed. Open S-TES systems operate at ambient pressure.

Closed sorption systems are used to provide thermal compression of the refrigerant, as alternatives to the mechanical compression in conventional vapor compression systems. In such systems, the pressure difference between the sorber bed and evaporator (condenser) is the driving force for vapor transport. As shown in Figure 8b, a heat exchanger is used to transfer heat to/from the sorbent material during desorption/sorption process and consequently, the sorbate is released to/taken from the condenser/evaporator. The ideal thermodynamic cycle of a closed solid-sorption TES system consists of 4 processes (Figure 8b): 1) preheating of the sorber bed; 2) desorption process in the sorber bed and condensation in the condenser during the charging process; 3) precooling of the sorber bed; and 4) adsorption process in the sorber bed and evaporation in the evaporator during the discharging process. During the adsorption process (discharging), if the cold produced by the evaporator is used, the TES is called “cold storage”, while it is a “heat storage” if the heat produced by the sorber bed is utilized.

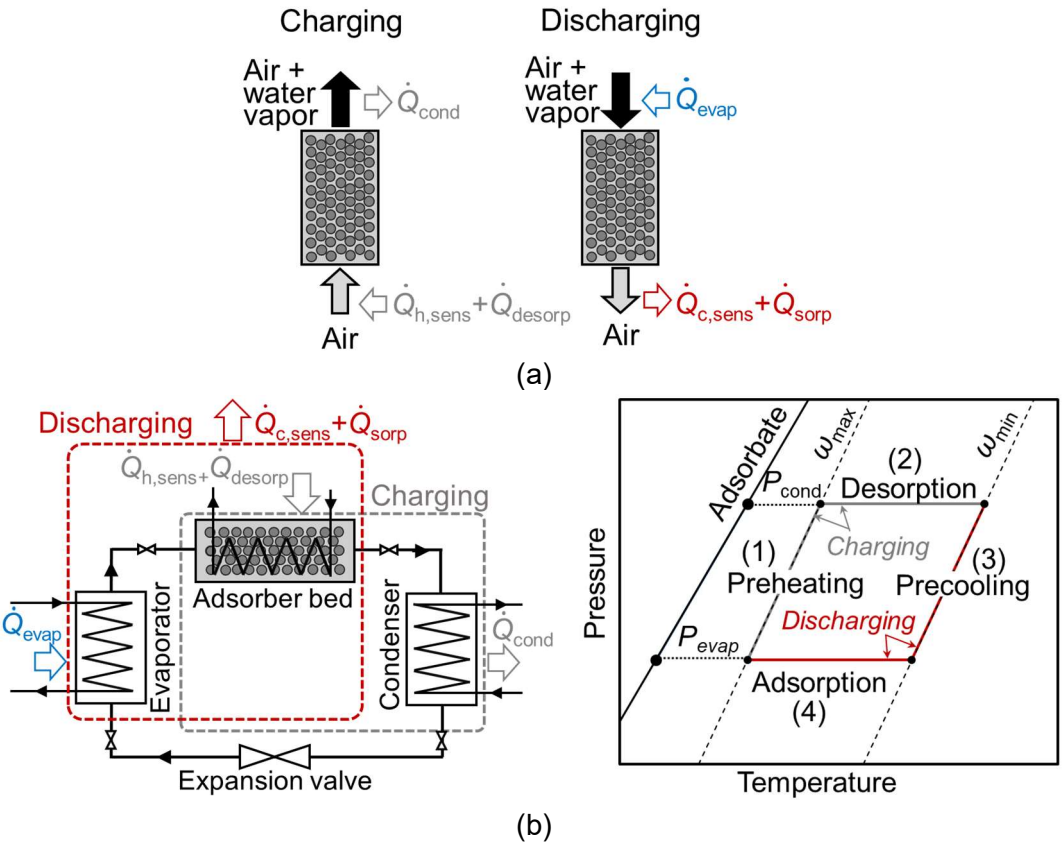

Figure 8. (a) Schematic of an open S-TES [35] and (b) schematic and the ideal thermodynamic cycle of a closed S-TES system.

Table 2 presents the main features of closed and open S-TES. Open S-TES systems are simpler, without a need for evaporator and condenser, although they require: i) fans, to drive the airflow through the sorber bed, and ii) humidifiers, when the water content of air is not adequate [36]. The system-based ESD of a closed sorption system is lower than that of an open sorption system because the adsorptive fluid is a part of the storage system in the closed system and also has to be stored [14]. Moreover, closed sorption systems are chemical heat pumps, which offer both heating and cooling in the discharging process and upgrade the waste heat to a higher temperature for residential and industrial applications.

Table 2. Closed and open S-TES features (from refs. [36], [37]).

Sorption storage type	-	+
Closed systems (vacuum condition)	▪ Advanced heat exchanger technologies are required. ▪ In the case of heat storage, evaporation heat should be provided. ▪ Lower system-based ESD, since the sorbate needs to be stored as well. ▪ Low pressure (vacuuming and leakage issues); need to be evacuated occasionally, due to the formation of incondensable gases. ▪ Generally, heat transfer is the limiting factor, compared to mass transfer.	▪ Capable of reaching higher and lower output temperatures compared to an open system. ▪ Can be used for both cooling (evaporator) and heating (sorber bed) ▪ No mass transfer with ambient ▪ Variety of sorbate can be used.
Open systems (atmospheric condition)	▪ An air fan is needed. ▪ Temperature lift in the sorption process is limited by the bed thermal mass. ▪ Humid air is not usually available (up to 80% RH is needed); thus, high power humidifier is required in most cases [37]. ▪ The sorbent may not take up the water vapor, at the same water vapor pressure and under the atmospheric conditions [37]. ▪ Small particles of sorbent materials may flow out of the sorber bed [37]. ▪ Limited to water as sorbate. ▪ Generally, mass transfer is the limiting factor, compared to the heat transfer.	▪ Atmospheric pressure ▪ Simple design ▪ A good and controllable heat transfer through forced air circulation ▪ Simpler and cheaper construction and maintenance ▪ No heat exchanger is needed.

1.5. Adsorption and absorption TES systems

The principle of closed adsorption TES is shown in Figure 9a. During the charging process, adsorbate is released from the adsorbent by heating the adsorber bed and flows to the condenser. Adsorber bed is isolated during the storage period, meaning the bed remains charged. During the discharging process, adsorbate vapor generated in the

evaporator is adsorbed by the adsorbent material and heat of adsorption is released for the heat storage. Cold produced by the evaporator is used for the cold storage application.

Figure 9b shows the absorption closed TES. During the charging process, heat is supplied to the weak (low-concentration) solution in the generator. The adsorbate vapor is separated from the weak solution, making a strong solution, and flows to the condenser where it condenses. In the storage period, the strong solution is isolated from the absorbate and there is no heat loss in this period. During the discharging process, the strong solution absorbs vapor from the evaporator and heat of absorption is released by changing the strong solution to a weak solution [18].

Major differences between the absorption and adsorption systems are the sorbent, sorption cycle time [38], and the ESD. Sorbent in the absorption system should be a pumpable fluid to provide efficient heat transfer and shorter sorption cycle time but a movable part is added to the sorption system [39]. Nevertheless, as shown in Figure 5, ESD in the absorption and chemical processes is typically higher than that of the adsorption process. Liquid absorption systems are usually not suitable for applications that involve vibrations, such as mobile applications [26]. Moreover, solution corrosion in the absorption systems is a challenging issue, which should be considered for the absorber bed design. Moreover, in absorption TES, when the absorbate is thoroughly desorbed from the solution, further desorption results in the formation of solid crystals, which should be considered during the operation [40], while adsorption TES do not require an intense selection of maximum desorption duration. A more detailed comparison between the absorption and adsorption processes can be found in Table 3.

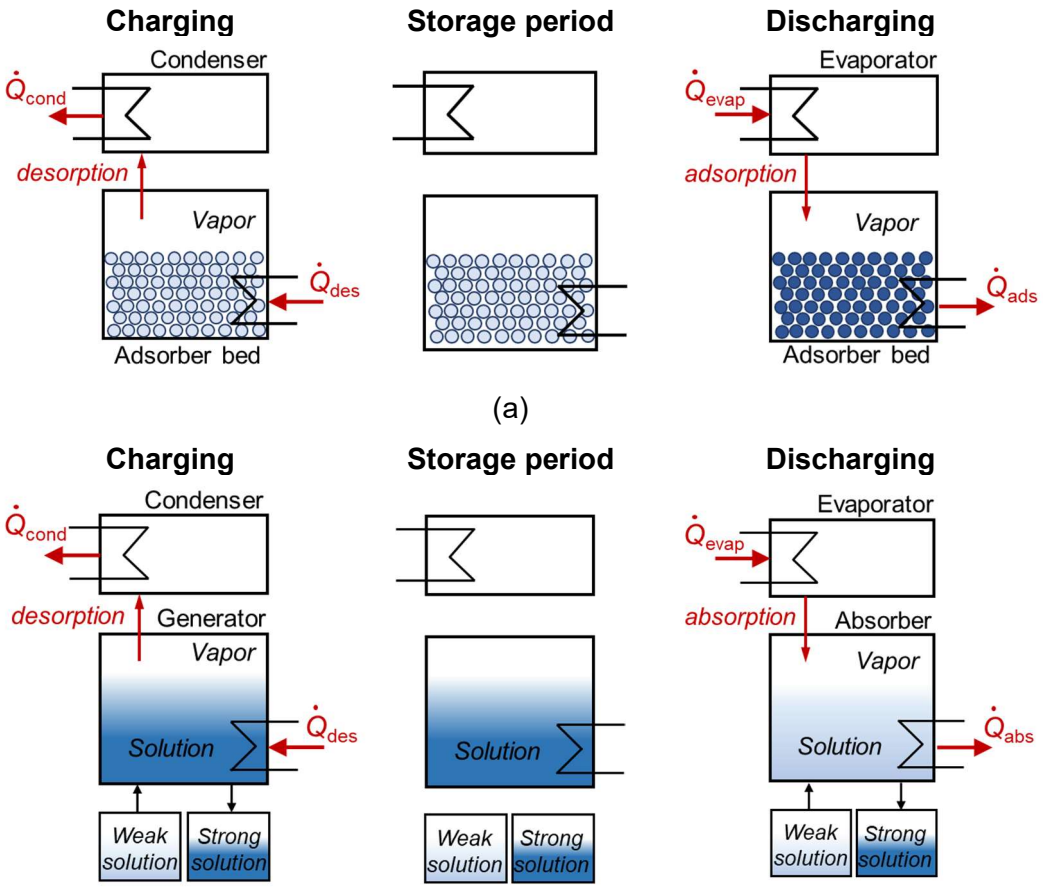

Figure 9. Principle of closed (a) adsorption and (b) absorption TES systems during charging, storage period, and discharging.

Table 3. Comparison between the absorption and adsorption systems [41].

Sorption storage type	-	+
Absorption	▪ Not applicable for applications include vibrations, such as mobile applications [41] ▪ The issue with the solution crystallization [41] ▪ Need for the solution pump and rectification equipment [41] ▪ Corrosive solutions	▪ More efficient systems compared to adsorption systems [41] ▪ Higher uptake rates and heat storage capacity
Adsorption	▪ Large volume systems ▪ Generally, lower energy storage density	▪ Wide choice of adsorbents for temperatures between 50 to 400 °C [41] ▪ Generally, driven by lower temperature heat sources [41]

Chapter 2.

Literature review on S-TES

Recently, many studies on the TES system for renewable heating and cooling have been devoted to the S-TES to take advantage of its high energy storage capacity and low heat loss. However, most of the studies are on the small-scale basis measurement, and only a few studies are available on full-scale systems. This chapter provides a review of the available studies on the S-TES and highlights the need for further research.

2.1. Adsorption TES systems

2.1.1. Small-scale performance investigation of ATES systems

Many studies on ATES were conducted by small-scale measurements in laboratory set-ups, which represents the theoretical performance of the full-scale ATES systems [37], [42]. Jänchen and Stach [43] used thermogravimetric analysis (TGA) and differential scanning calorimetric (DSC) method to study less than 600 mg of zeolite SAPO-34 and silica gel at 20 °C and relative vapor pressure of 0.3 and the theoretical ESD of 0.468 MJ kg^{-1} for SAPO-34 and 0.443 MJ kg^{-1} for silica gel were achieved. Barreneche et al. [44] reported theoretical ESD of 0.2 MJ kg^{-1} (0.18 GJ m^{-3}) for Zeolite 5A (Sigma Aldrich), using a Mettler Toledo TGA/DSC device under 20 ml min^{-1} N_2 and 10 K min^{-1} heating rate from 50 to 400 °C. Frazzica and Freni [45] conducted a thermodynamic analysis to investigate some candidate working pairs for heat storage in buildings and showed that AQSOA FAM-Z02 delivered a promising material-based ESD; for desorption, condensation, adsorption, and evaporation temperatures of 100, 30, 30, 10 °C, higher seasonal heat ESD of 0.401 GJ m^{-3} (not including condensation heat) was achieved compared to silica gel Siogel (0.292 GJ m^{-3}) and Zeolite 13X (0.132 GJ m^{-3}).

2.1.2. Full-scale experimental study of ATES systems

Lu et al. [46] investigated the application of cold sorption storage for air conditioning of the driver's cab of an internal combustion locomotive with running time of about 2 h between Shanghai and Hangzhou, and an intermission of several hours

between two runs. The desorption process lasted for 30 min at 350 °C and the condenser temperature was 60 °C [46]. The average cooling power of about 4.1 kW was reported for 140 kg of zeolite 13X. The cooling capacity was obtained as 19.7 MJ, i.e. ESD_{cold}=141 kJ kg^{-1}, when the bed temperature reached its maximum temperature of 125 °C [46], [47].

An open ATES with working pair of Zeolite 13X/water was installed in a school building in Munich, Germany since 1997 [35]. During night, 7,000 kg of Zeolite 13X was charged by the steam line of the district heating system, at temperature of 130-180 ˚C, and during the peak power demand in daytime, air at temperature of 25 °C passed through the zeolite bed to provide heating to the school building with ESD of 0.446 GJ m^{-3} (0.92% of the theoretical value). The evaporation energy was supplied by low-temperature return flow of the district heating system [35]. Cooling of a jazz club in this building was also done by air dehumidification (latent cooling) and a temperature of 25.5 °C was successfully maintained during the concerts in the Jazz club only with desiccant cooling and ventilation. This cold storage provided an ESD of 0.360 GJ m^{-3} and maximum cooling power of 50 kW [35].

Over the past 20 years, several international projects have been conducted to find more efficient renewable heating and cooling systems. HYDES (High Energy Density Sorption Heat Storage for Solar Space Heating) was one of the first European Union storage projects, from 1998 to 2001. A seasonal silica gel S-TES was developed for a single-family house heating, which provided ESD of 0.43 GJ m^{-3}, while the theoretical material-based ESD was 0.54 GJ m^{-3} [36], [48]–[50]. In winter, low-temperature heat from the solar collectors was used as the evaporation heat supplier for the evaporator [51]. The main outcome of the HYDES project was to include the evaporator/condenser inside the sorber chamber to reduce the travel distance of the sorbate vapor and increase the cross-sectional area of the vapor passage [48], [49].

Based on the results of HYDES, in MODESTORE (Modular High Energy Density Sorption Heat Storage) project, the evaporator/condenser unit and the sorber bed were placed in a single chamber. However, MODESTORE only provided material-based ESD of 0.18 GJ m^{-3}, which is 30% less than the sensible heat of a water tank working between temperatures of 25 and 85 °C, and system-based ESD of 0.118 GJ m^{-3} [18], [39]. It was concluded that the working pair of silica gel/water was not suitable for the seasonal storage

because it did not provide enough temperature lift over the water uptake of about 13% [18].

In the Monosorp project (IWT, Germany), an open S-TES was developed, using extruded zeolite honeycomb structures [52]. Honeycomb structure was used to improve the adsorption kinetics and reduce the pressure drop along the storage bed [18]. In summer, the excess solar heat heated the ambient air in a heat exchanger and this hot air stream dried the zeolite storage by flowing through the storage bed. In the discharge period, the wet indoor air was blown through the storage medium and due to the adsorption, hot air left the storage. The hot dry air was transferred to the inlet air stream of the room, in the ventilation heat exchanger [18]. A maximum temperature lift of 22 °C and a material-based ESD of 0.468 GJm^{-3} were achieved if only the adsorption heat was delivered. However, if both sensible heat and adsorption heat were delivered during the discharging process, the material-based ESD of 0.576 GJm^{-3} could be provided. In conclusion, high regeneration temperature (180 °C) of zeolite 4A led to high sensible heat in the charging process (desorption), which could not be stored in the case of long storage period [52].

In 2006, SPF (the institute for Solartechnik Prüfung Forschung) investigated a seasonal closed ATES, using 7 kg of zeolite 13X [40]. System-based ESD of 0.208 GJ m^{-3} was obtained for desorption temperature of 180 °C. A zeolite 13X ATES was also studied by Schreiber et al. [53] to investigate the feasibility of integration of the ATES system into a brewery batch process with cogeneration energy supply, where high-temperature waste heat was available for the regeneration process. In the 6 hours operating cycle, the zeolite 13X closed ATES stored the exhaust gas heat at temperature up to 250 °C for 5 hours and at the last 1 hour, when a large amount of heat at the temperature of 120 °C was needed, the stored heat was discharged [53].

Li et. al [54], [55] studied a closed FAM-Z01-coated ATES system for both heat storage and cold storage applications. For desorption temperature of 70 °C and adsorption, condensation and evaporation temperatures of 30 °C, ESD and energy efficiency were 805 kJ kg^{-1} (i.e. 0.483-0.564 GJ m^{-3} for $\rho_{FAM\text{-}Z01}$=600-700 kg m^{-3} [20]) and 96% for the heat storage, while ESD and energy efficiency were 400 MJ kg^{-1} (i.e. 0.240-0.280 GJ m^{-3} for $\rho_{FAM\text{-}Z01}$=600-700 kg m^{-3} [20]) and 46.6% for the cold storage. They suggested the addition of adsorbent grains between the coated fins, forming a denser

adsorbent arrangement, to increase the volumetric storage capacity of the storage system, and use of radiation-shielding materials to reduce the heat loss [55].

Narayanan et al. [56] developed a NaX zeolite-water closed ATES for air conditioning of an electric vehicle. The desorption process was carried out at temperature of 300 °C in a charge station when the electric vehicle was parked. The material-based ESD and SP of 1.30 MJ kg^{-1} (0.714 GJ m^{-3}) and 180 W kg^{-1} for heating were achieved, while 0.938 MJ kg^{-1} (0.516 GJ m^{-3}) and 130 W kg^{-1} were obtained for cooling. The system-based ESD was 0.512 and 0.37 GJ m^{-3} for heating and cooling, respectively [57]. Palomba et al. [58] experimentally studied a full-scale sorption storage system with 4.3 kg FAM-Z02 grains (1-2 mm) filled in an aluminium fin-flat tube heat exchanger and seasonal $ESD_{heat,mat}$ of 0.515 MJ kg^{-1} (0.335 GJ m^{-3} for $\rho_{FAM\text{-}Z02} \approx 650$ kg m^{-3} [20]) and $ESD_{cold,mat}$ of 0.242 MJ kg^{-1} (0.157 GJ m^{-3}) were achieved for desorption, condensation, adsorption, and evaporation temperatures of 90, 35, 35, and 10 °C.

In addition to the space heating and cooling of the residential buildings and mobile applications, S-TES was used in some felicitous applications. Hauer and Fischer [59] presented the idea of using an open S-TES system within a dishwasher system, where humid air is available for the discharging process, to decrease the energy consumption for heating process in the washing and drying steps. Heating during drying step was produced by a packed zeolite 13X, which had been charged during the washing process. They showed that the energy consumption was reduced from 3.82 MJ to 2.88 MJ per cycle, compared to a conventional dishwasher, meaning 24% energy saving [59]. Self-chilling beverage keg is another example for closed ATES system, which has been commercialized by Cool-Systems Bev. GmbH (www.coolsystems.de) [51], [60]. In this S-TES, as soon as the valve between the zeolite vessel and the evaporator, which is at the lower external part of the keg, is opened, water in the evaporator will evaporate and heat of evaporation will be extracted from the beverage and keep it cold.

2.2. Thermochemical energy storage systems

2.2.1. Small-scale performance investigation of thermochemical energy storage systems

Composite sorbents (salt in a porous matrix) are among the promising sorbents for sorption TES systems. Grekova et al. [61] studied LiCl/vermiculite and achieved a theoretical ESD_{mat} of 0.81 GJ m^{-3} for seasonal storage and 0.63-0.91 GJ m^{-3} for cyclic operation at the charging temperature of 75–85 °C, considering the composite density of 350 kg m^{-3}. Yu et al. [62] developed a composite of LiCl (30 wt%) with silica gel and reported theoretical ESD_{mat} of 0.39 GJ m^{-3} for cold storage and 0.59 GJ m^{-3} for heat storage for a charging temperature of 80 °C. Brancato et al. [63] developed a new composite sorbent of LiCl inside multi-wall carbon nanotubes (LiCl/MWCNT/PVA) with low charging temperature of 75 °C. The highest ESD of 1.6 MJ kg^{-1} achieved by TGA/DSC method for daily heat storage. Considering the composite density of 300 kg m^{-3} [63], the volumetric ESD_{mat} was 0.48 GJ m^{-3}.

High desorption temperature brings larger binding energy and higher storage capacity, although some solid sorbents, such as salt-hydrates, take advantage of the absorption process to provide high energy storage density while requiring a low-temperature heat source for charging process [36]. Using salt-hydrate sorbents with higher sorption capacities in TCES significantly increases the ESD. Sögütoglu et al. [64] studied some salt-hydrate sorbent materials by a TGA/DSC device and introduced K_2CO_3 as the most suitable sorbent for residential heat storage. They reported the theoretical ESD_{mat} of 1.28 GJ m^{-3} for open systems and 0.95 GJm^{-3} for a closed system and discharge power of 283–675 kW m^{-3} for K_2CO_3. They showed that in spite of higher energy storage density of $MgCl_2$ and Na_2S, only K_2CO_3 demonstrated chemical stability in the cyclic operation [64].

Salt-hydrate of $SrBr_2$ was used in ESSI project and theoretical ESD_{mat} of 1.548-1.656 GJ m^{-3} and specific powers between 1.93 and 2.88 W kg_{salt}^{-1} were achieved [65]. Donkers et al. [66] studied 563 salt-hydrate sorbents for seasonal storage for domestic hot water and space heating; Na_2S showed the highest ESD_{mat} of 2.79 GJ m^{-3} for an open system and 1.58 GJ m^{-3} for a closed system under hydration temperature of 66 °C (suitable for domestic hot water), dehydration temperature of 82 °C, evaporation pressure of 12 mbar and condensation pressure of 20 mbar [66]. The salt hydrate of Na_2S-H_2O was also used

in SWEAT/ECN project and the theoretical ESD_{mat} was 2.81 GJ m^{-3} [36]. Although, due to the corrosiveness and risk of outgassing of H_2S, the salt-hydrate of N_2S was not suggested as a suitable candidate for the residential application [66]. In spite of the promising results from the researches on sorption storage systems, it is in an early stage of development.

2.2.2. Full-scale experimental study of thermochemical energy storage systems

A composite sorbent of $CaCl_2$ and silica gel was developed for low-grade open S-TES and a fin-plate HEX was used as the sorber bed, which contained 40 kg of the sorbent [67]. An ESD_{mat} of 0.95 MJ kg^{-1} (0.766 GJ m^{-3}) and sorber bed ESD_{bed} of 0.396 GJ m^{-3} were achieved. The thermal efficiency for the regeneration temperature of 90 °C was 0.78 [67].

SWEAT (Salt Water Energy Accumulation and Transformation) project, which was conducted in the energy research centre of the Netherlands (ECN), was focused on the development of a modular solid-sorption system for residential and industrial cooling applications [68] and Na_2S-H_2O with regeneration temperature of 83 °C, was used in this project. Due to the significant corrosiveness of Na_2S, the material used for the storage module, including heat exchanger and chambers, should be: i) inert to the chemical reactions of the salt or have a defect-free corrosion-protection layer, ii) suitable for maintaining a vacuum condition, and iii) with very low out-gassing rates [68]. In the SWEAT project, stainless steel was selected as the material for chambers and the evaporator and condenser coils. A corrosion-protective coating was applied to the sorber bed copper spiro-tube heat exchanger (HEX) [68].

The maximum charging power was 1.2 kW and the cooling power at evaporation temperature of 20 °C was 1.5 kW, while at the practical evaporation temperatures of 10 to 15 °C was 0.5 to 0.7 kW [68]. The heat storage ESD_{heat} was 2.81 GJ m^{-3} and the cold storage ESD_{cold} was 1.84 GJ m^{-3} [36]. They concluded that the night-time charging was favorable because of the lower condenser temperature, which caused more temperature difference between the condenser and the sorber bed and more charging power [68].

A thermo-chemical accumulator (TCA), using LiCl-water as the absorbent working pair, was built and commercialized by the ClimateWell company in 2007 [69]. The operation is described briefly here; During the charging process, when the solution

reached the saturation point, further desorption could result in the formation of solid crystals, which fell under the gravity and were transferred to the storage vessel to prevent to go into the pump. During the discharging process, the solution was pumped over the reactor heat exchanger and absorbed the refrigerant vapor [69], [70]. ESD_{mat} was reported as 0.911 GJ m^{-3} and the system-based ESD_{sys} was 0.306 GJ m^{-3} (for short-term heat storage) [40]. In spite of the high capacity of LiCl, it was not recommended for the seasonal application because of its high price (3,600 €m^{-3}) [39]. This commercialized system was not developed for only storage purpose. Instead, the storage chamber was integrated with an absorption heat pump for continuous operation.

2.3. Summary of literature review

2.3.1. Sorber bed heat exchanger and sorbent to metal mass ratio

To increase the heat and mass transfer inside the sorber bed, heat exchangers (HEX) with extended surfaces are commonly used. The HEX design and its compactness play a key role in the overall storage performance of an S-TES system. Figure 10 shows different types of sorber beds used in the S-TES systems. Fin-tube HEXs have been widely used for the sorber beds with wavy fins [71] and triangular louvered fin-flat tube [72]. Fopah-Lele et al. [73] used honeycomb structure heat exchanger for $SrBr_2$-H_2O S-TES to prevent agglomeration of salt particles and heat distribution within the bed through the aluminum walls of honeycomb cells. Tubular HEX including copper-wire-fin tubular HEX (Spiro-tube, manufactured by Spirotech BV, Helmond) [36], [68] and series of extruded aluminum tubes [74], [75] were used for sorber beds. Sorbent material, Na_2S-H_2O was fixed in the wire structure of the Spiro-tube sorber bed and copper wires transported the heat into the sorbent material [68]. Due to the corrosiveness of Na_2S-H_2O, the corrosion protection coating was applied to the external surface of this HEX. Lanzerath et al. [75] used a series of extruded aluminum tubes with both outer fin, to hold zeolite 13X and increase heat transfer within the sorbent, and inner fin structure, to enhance the convective heat transfer of the inner water circuit, as shown in Figure 10h. Plate HEX was also used for a sorber bed of an $SrBr_2$-expanded natural graphite S-TES [76]. In spite of compactness of plate HEX, the potential for leakage between the streams, the narrow spacing between plates that makes packing of sorbent materials difficult, and high pressure drop are the challenges against the plate HEX sorber beds.

To evaluate the types of sorber beds, the specification and performance of the S-TES systems, reported in the literature are summarized in Table 4 in terms of working pairs, sorber bed HEX, storage capacity, ESD, specific power, and sorber bed to adsorbent mass ratio. The highest ESD_{bed}, based on the sorber bed volume, was 0.611 GJ m^{-3} for 8 mm LiCl/ expanded graphite with a compact copper coil-tray HEX [77]. A thermophysical battery with stackable fin-tube HEX for climate control of electric vehicles provided an ESD_{bed} of 0.597 GJ m^{-3} [57].

The highest ESD_{mat}, based on the sorbent material mass, were achieved by Na_2S-H_2O with Spiro-tube HEX (3.833 MJ kg^{-1}) and LiCl/ expanded graphite (EG) with compact copper coil-tray HEX (3.143 MJ kg^{-1}) [68], [77]. Due to the differences in the operating conditions, sorbent materials, sorbent configurations, vapor supplier units, and definition of performance indicators, one can conclude that the experimental studies available in the literature are not conclusive about a unique heat exchanger type for the sorber bed which provides the best storage performances.

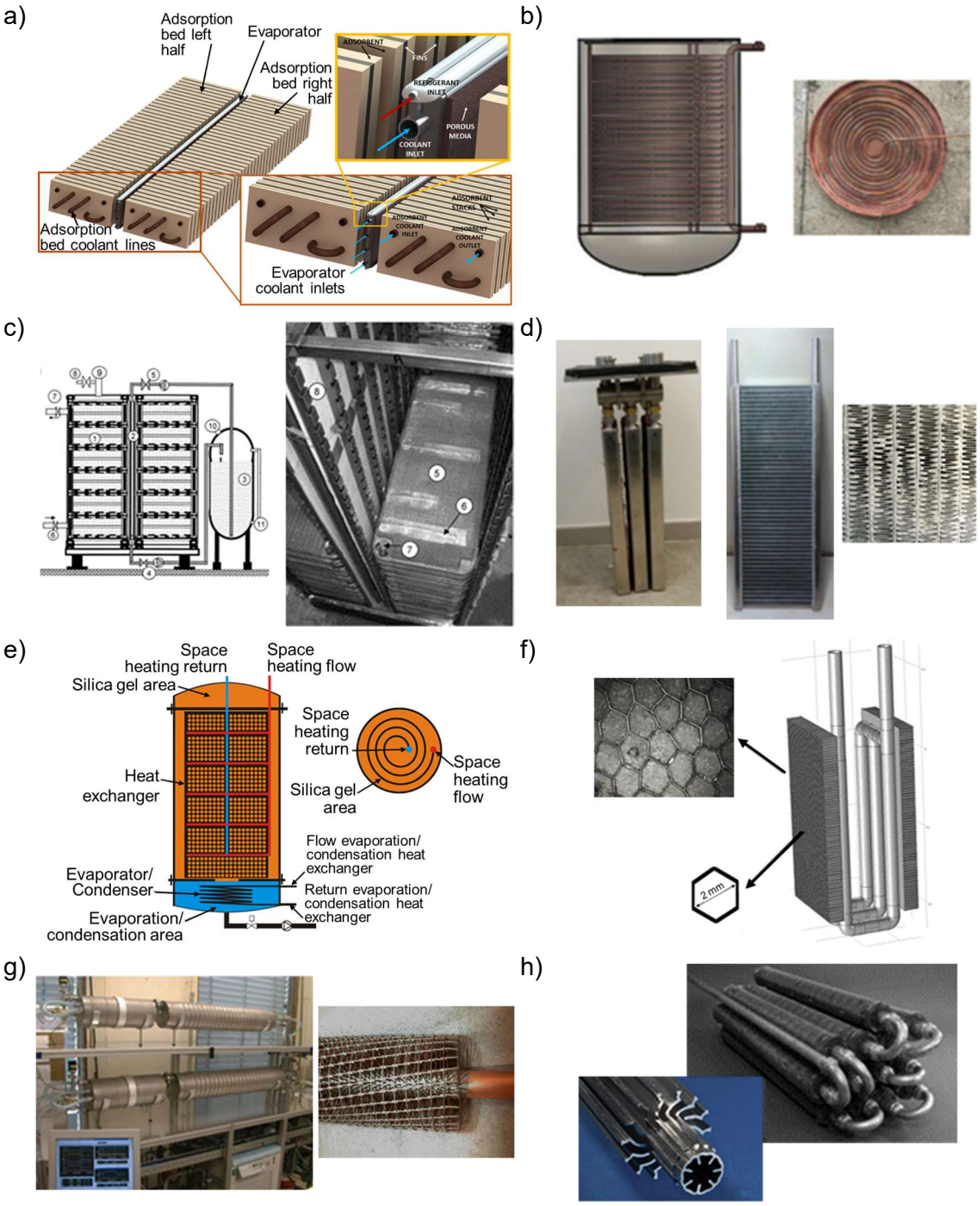

Figure 10. Heat exchanger types used as the sorber bed in S-TES. (a) plain fin-tube HEX with stackable design [57], (b) compact copper coil-tray HEX [78], (c) plate HEX in a stacking modular arrangement [76], (d) triangular louvered fin-flat tube HEX [50], (e) spiral plate HEX [79], (f) honeycomb-tube HEX [73], (g) Spiro-tube HEX (copper-wire-fin tubular HEX) [36], [68], (h) extruded aluminum tubes in series [74], [75].

Table 4. Experimental studies on S-TES systems for heat storage in the literature.
* C / O: Closed/ Open, CO/ STS/ S: Cyclic operation/ Short-term storage/ Seasonal

Ref.	Type of storage		Operating conditions		Sorbent	m_{ads}	Sorber bed type	V_{bed}	Bed heat transfer area	m_{bed}	m_{bed}/m_{ads}	Ch / Dch time	SP	Q_{dch}	η_{th}	ESD	
	C /O	CO /STS /S														Mat	Bed
			T	°C		kg		m^3	m^2	kg		min	Wkg^{-1}	MJ		$MJkg^{-1}$ GJm^{-3}	GJm^{-3}
[80]	C	CO	Ch: Dch: Cond: Evap:	70 30 30 30	FAM-Z01 Coated 0.25 mm thk.	2.8	Fin-tube (12 parallel four-pass)	0.016	16.7	~ 7.8	~ 2.78	Ch: 18 Dch: 42 eff:12	Ch: - Dch: 319.4	2.25	0.96	0.805 ($MJkg^{-1}$) 0.523 (GJm^{-3})	0.140
[58]	C	CO	Ch: Dch: Cond: Evap:	90 35 15 10	FAM-Z02 Grains 1-2 mm	4.3	Flat-tube and fins	0.107 (case)	1.75	-	-	Ch: 35 Dch: 40	Ch: - Dch: 151.2	3.96	1.5	1.008 (with Q_{cond}) ($MJkg^{-1}$) 0.6552 (GJm^{-3})	0.432
[81]	C	CO	Ch: Dch: Cond: Evap:	250 70 40 40	Zeolite 13X Grains 1.4 mm	10	Tubes and steel lamellae	0.022	-	20.6	2.06	Ch: - Dch: -	Ch: 90-170 Dch: 70-350	10.77	0.85	1.077 ($MJkg^{-1}$) 0.690 (GJm^{-3})	0.490
[82]	C	STS (5 h)	Ch: Dch: Cond: Evap:	150 40 40 40	Zeolite 13X (WE-G 592) Grains	13.2	Fin-tube HEX	0.034 (vessel)	-	32.8	2.48	Ch: 90 Dch: 540	Ch: - Dch: 1.79	11.23	0.67 1.09 (with Qcond)	0.851 ($MJkg^{-1}$) 0.638 (GJm^{-3})	0.330
[35], [51]	O	CO	Ch: Dch: Cond: Evap:	130-180 25-30 - -	Zeolite 13X	7000	3 connected cylinders in a horizontal line	-	-	-	-	Ch: Dch: 840	Ch: - Dch: 13.57	-	0.92	- 0.446 (GJm^{-3})	-
[77]	C	CO	Ch: Dch: Cond: Evap:	85 40 18 18	LiCl/ expanded graphite (EG) Consolidated 8 mm	11.57	Compact copper coil-tray HEX	0.0595	3.14	56	4.84	Ch: 50 Dch: 64.5	Ch: Dch: 631.8	36.9	0.94	3.1428 ($MJkg^{-1}$) 1.603 (GJm^{-3})	0.611
[67]	O	-	Ch: Dch: Cond: Evap:	90 15 - -	Slica gel/ $CaCl_2$ (40%wt) Pelleted using binders and additives	40	Plate-fin HEX * hot plates by electric power in charging	0.096	-	-	-	Ch: 720 Dch: 300	Ch: 28.19 Dch: 52.78	38.0	0.78	0.950 ($MJkg^{-1}$) 0.766 (GJm^{-3})	0.396
[76]	C	-	Ch: Dch: Cond: Evap:	80 35 - 12	$SrBr_2 \cdot H_2O$/ 6-8% expanded natural graphite (ENG) Consolidated 12 mm thk.	171.3 15.6 (ENG) 186.9	Plate HEX	0.979	-	-	-	Ch: Dch:	Ch: - Dch: -	216	-	1.156 ($MJkg^{-1}$) -	≈ 0.324
[57]	C	CO	Ch: Dch: Cond: Evap:	300 40 40 15	Zeolite NaX Consolidated stack adsorbent 2 mm thk.	4.992 with cu-foam: 9.465	Fin-tube HEX with stackable arrangement	0.0109	-	7.001	1.4	Ch: 120 Dch: 120	Ch: Dch: 180.3	6.48		1.298 ($MJkg^{-1}$) 0.714 (GJm^{-3})	0.597
[68] [36] [14]	C	CO	Ch: Dch: Cond: Evap:	83 35 - -	Na_2S-H_2O cellulose-Na_2S composite material	3	6 Spiro-tube HEX	-	-	-	-	Ch: 240 Dch: 240	Ch: 307.9 Dch: 266.2	11.5	0.865	3.833 ($MJkg^{-1}$) -	-

2.3.2. Material-level ESD and sorber bed ESD

Figure 11 shows the comparison between the material-based ESD (ESD_{mat}) and the sorber bed ESD (ESD_{bed}) for heat and cold storage extracted from the literature. The variety of sorbent material in Figure 11 makes a wide range of ESD (0.260-1.603 GJ m^{-3}). Although the lower ESD_{bed} compared to ESD_{mat} is inevitable, a huge difference between these two values reveals the bulkiness and inefficiency of the storage beds. Among the reported studies in Figure 11, the thermophysical battery for the climate control of the electric vehicles [57] showed better performance ($ESD_{bed}/ESD_{mat} \approx 84\%$).

Figure 12 also shows the difference between the maximum sorbent potential ESD (ESD_{max}), ESD_{mat} and ESD_{sys}. The ESD_{sys} is even much lower than the ESD_{mat} since the whole design and compactness of the S-TES play an important role in the ESD_{sys}. This value has not been reported for most of the studies since their systems were not optimized in all aspects. Therefore, there is still immense room for improvement of the sorber bed heat exchanger design, enhancing the thermal conductivity of sorbent, selection of sorbent configuration, and its size, to guarantee the high storage performance and particularly fast sorption dynamic.

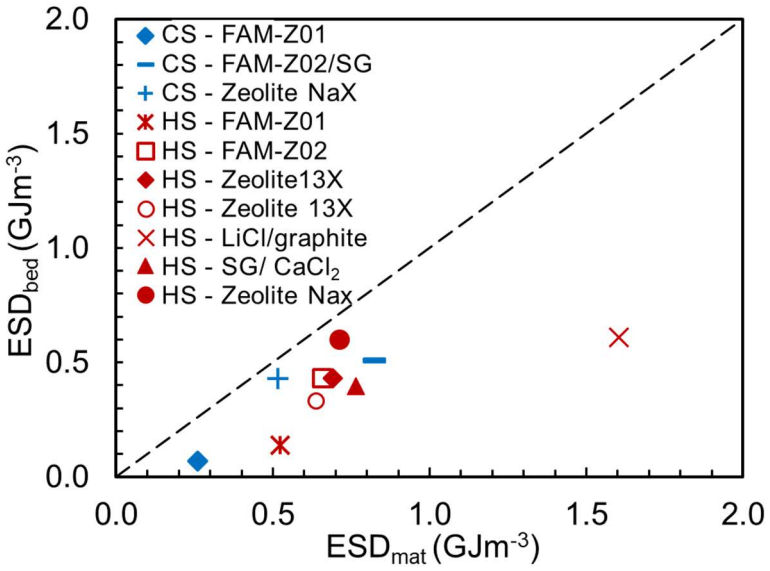

Figure 11. Sorber bed ESD (ESD_{bed}) versus material ESD (ESD_{mat}) for heat storage (HS) and cold storage (CS) in the literature. Sorbent materials used for cold storage were ♦ FAM-Z01 [54], – FAM-Z02/silica gel [72], + zeolite NaX [57], and for heat storage were ✱ FAM-Z01 [80], □ FAM-Z02 [58], ♦ zeolite 13X [81], ○ zeolite 13X [82], × LiCl/graphite [77], ▲ silica gel/$CaCl_2$ [67], and ● zeolite NaX [57].

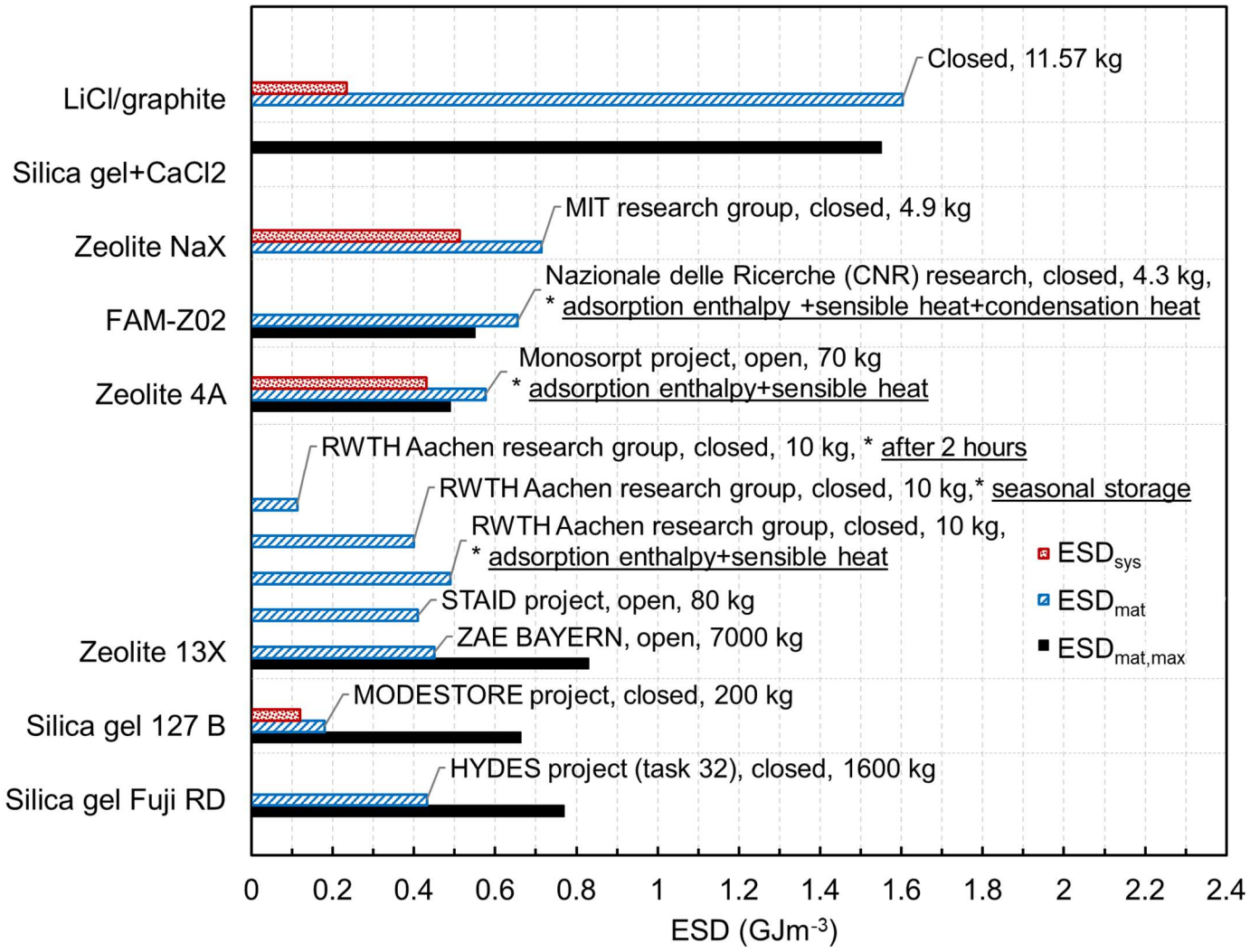

Figure 12. Relevant activities on the development of S-TES: comparison of maximum sorbent ESD ($ESD_{mat,max}$), material-level ESD (ESD_{mat}), and system-based ESD (ESD_{sys}).

Chapter 3.

Screening sorbent material candidates

In this chapter, the storage capacity, charge/discharge power, and sorption rate of some sorbent material candidates for residential heating application are presented. The screening process was carried out during my internship at CanmetENERGY, Natural Resources Canada, in Ottawa.[1]

3.1. Suitable sorbent material properties for TES application

To develop an efficient S-TES system, the first step is the selection of a proper sorption working pair for each application. Suitability of a sorption working pair is assessed based on the following criteria and properties:

I. High material-based ESD (ESD_{mat}), to assure high theoretical storage capacity; high ESD_{mat} requires high water uptake, the heat of sorption, and density of the sorbent material.

II. Usable temperature lift in the discharging process, over a larger range of water content [79], which also depends on the operating conditions and application.

III. Low charging (desorption) temperature;

IV. High specific charging/discharging power, which is a function of the uptake rate (sorption kinetics), thermal conductivity, and thermal diffusivity of the sorbent material. A high-performance sorption working pair requires both high uptake equilibria and kinetics [83]. An S-TES with high equilibrium uptake capacity but slow kinetics cannot provide fast energy discharge, while a fast-discharge TES system with small sorption capacity material leads to a low ESD since much more sorbent is needed to deliver a certain amount of energy. To this end, an experimental and theoretical study on the effective thermal conductivity of the S-

[1] The results of this chapter were presented in: (i) 5th Experts meeting of the Joint IEA Technology Collaboration Programs on Solar Heating and Cooling (SHC) Task 58 and Energy Conservation through Energy Storage (ECES) Annex 33 on Compact Thermal Energy Storage R&D, May 1-3 2019, and (ii) International Sustainable Energy Conference (ISEC 2018), October 3-5 2018.

TES packed bed is presented in Chapter 4 and an experimental study on the dynamics of a coated S-TES is presented in Chapter 5.

V. Higher fraction of binding energy from the total heat of sorption compared to the latent energy [40]. For seasonal application, where the sensible heat of the sorber bed is lost, higher binding energy ensures higher ESD [79].

VI. Cycle-ability and stability under the operating conditions; full reversibility of the sorption/desorption process over a large number of cycles is essential for a reliable S-TES system.

VII. Non-corrosiveness of sorbent materials; salt corrosion is an issue with the absorption TES systems, which limits the heat exchanger material options.

VIII. Environmental harmlessness of the working pair.

IX. Low cost; low sorption material cost eases the market penetration of S-TES systems.

3.2. Sorbent materials

Sorption working pairs consist of a sorbate fluid, such as water, ethanol, ammonia and methanol, and sorbent materials which can be categorized as (i) mesoporous silicates, (ii) classical zeolites; (iii) (silico)aluminophosphates, (iv) porous coordination polymers (PCPs), (v) porous carbons, (vi) composite sorbents, (vii) salt hydrates, and (vii) liquid sorbents. In this section, the relevant solid sorbents are briefly reviewed.

3.2.1. Mesoporous silicates

Silica (SiO_2) is a chemically inactive non-polar material in nature, but when it has a silanol functional group, the surface becomes polar and hydrophilic [84]. This sorbent is widely used for water removal in a number of industries such as clothing, pharmaceutical, electronics, computers, paper, and home appliances. A-type silica gel with pores size of 2-3 nm and internal surface areas of about 650 m^2g^{-1} is suitable for ordinary drying, while B-type silica gel with a larger pore size of about 7 nm and internal surface areas of 450 $m^2\,g^{-1}$ is more suitable for applications with a relative humidity of higher than 50% [84].

The specific surface area depends on the preparation conditions, and for silica gel this area can be between 250 to 900 m^2g^{-1} [83], as shown in Table 5.

3.2.2. Classical zeolites

Microporous zeolite consists of a negatively charged aluminosilicate host framework which is balanced by the counterions [85]. The water uptake characteristics of the classical zeolite can be tailored by the Si/Al ratio [86]. Lower Si/Al ratio increases the hydrophilicity of the zeolite such as in type A zeolite [87]. Classical zeolite is more advantageous for gas drying applications rather than sorption closed systems, due to their high desorption temperature [85]. Figure 13 shows the thermal evolution of silica gel versus zeolite13X in an open ATES during sorption by saturated air at the temperature of 25 °C, after desorption at 130 °C [88]. As shown in Figure 13, zeolite remains at its highest outlet temperature until the adsorption is over, while silica gel has a descending outlet temperature just after reaching the maximum outlet temperature. Moreover, the adsorption rate is higher for zeolite compared to silica gel since the adsorption duration for zeolite is half of that of the silica gel [88]. In classical zeolite, temperature lift can exceed 50-70 °C [87].

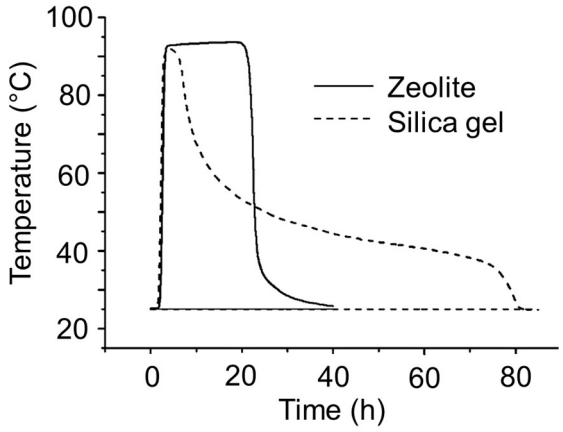

Figure 13. Thermal breakthrough curves for zeolite and silica gel from ref. [88].

3.2.3. (Silico)aluminophosphates

High charging temperature of zeolite sorbents made researchers develop new classes of zeolite-like microporous sorbents, namely aluminophosphates (AlPOs) and silico-aluminophosphates (SAPOs), which require low-grade heat sources, i.e. below 100

°C, with comparable ESD to that of the zeolite. Silicon or metal cations introduced inside the AlPO structure are advantageous for heat storage application due to the introduction of structural defects, which improves surface interactions of polar water molecules, and creation of new hydroxyl groups on the material surface [36], [89]. AlPOs are the first generation of framework oxide molecular sieves synthesized without silica [90]. CHA-type structure SAPOs are better candidates for storage application due to the strong interactions between Si-centers and water molecules [91].

Among the classes of AlPOs and SAPOs, AlPO-18 and SAPO-34 are regarded as the most attractive candidates for storage application under most favorable operating conditions, meaning a low charging temperature and discharging at water vapor pressure similar to the saturation water vapor pressure at ambient temperature [36]. AQSOA FAM-Z02 (commercial SAPO-34), which was developed by Mitsubishi Plastics Incorporation [20], shows desirable performance for adsorption heat pump (AHP) and desiccant air conditioning system driven by heat sources below 90 °C [71], [92], [93].

3.2.4. Porous coordination polymers (PCPs)

PCPs are a new family of super-molecular sorbents, which are also called metal-organic frameworks (MOFs). Unlike zeolites, MOFs are not purely inorganic, but inorganic-organic materials based on metal ions or metal ion clusters, which are linked by organic ligands forming a 3-dimensional coordinated network [41], [85], [94], [95]. High surface area, crystalline open structures, tunable pore size, and functionality are the properties, which make MOFs attractive sorbent candidates [85].

Gordeeva et al. [96] introduced a promising MOF for storage application, NH_2-MIL-125, which is a framework with a basic unit of $Ti_8O_8(OH)_4$-$(O_2CC_6H_5$-CO_2-$NH_2)_6$ and a bipyramid structure with six cyclic octamers $Ti_8O_{20}(OH)_4$ at the corner connected by eight NH_2-BDC linkers. They reported the theoretical ESD of 1.1 MJ kg^{-1} at low charging temperature of 75-80 °C [96]. However, due to the low density of NH_2-MIL-125 (300-450 kg m^{-3} [17], [97], [98]), the theoretical volumetric ESD was 0.330-0.495 GJ m^{-3} for heat storage. Low temperature lift was reported as one of the key drawbacks of MOFs, as a result of a relatively weak affinity to water [61].

3.2.5. Porous carbons

Activated carbon (AC) is a microporous carbonaceous sorbent with high porosity and small, low-volume pores, which increases the surface area [14]. It is produced when a char is gasified by oxidizing agents or a carbonaceous material is impregnated with a dehydrating agent and then subjected to carbonization. Carbons can be used with most refrigerants, except for water. ACs have been highly utilized for solar ice making purposes with methanol [99]. The evaporation latent heat of methanol is about half that of water, meaning low ESD of cold storage, although it offers the possibility of subzero evaporation temperature. Activated carbon fiber (ACF) is a fiber form of activated carbons with a small diameter of the microporous fibers that allows rapid sorption process [85].

3.2.6. Composite sorbents

Composites, salt in porous matrix (CSPM), are among promising sorbents. The active sorbent is the confined salt, while the matrix acts as a media that disperses the salt and provides efficient heat and mass transfer in the CSPM [85]. The composite of Silica gel and $CaCl_2$ was introduced for the heat storage application for the first time and the ESD of up to 2 MJ kg^{-1} was reported [100].

Low charging temperature, large storage capacity, and the possibility of modification of sorption properties based on the specific storage application by variation of the salt and matrix nature are the main benefits of CSPMs [17]. On the other hand, a relatively low temperature lift is the disadvantage of CSPMs, which can be improved by applying salts with higher affinity to water at the cost of an increase in the charging temperature [17].

3.2.7. Salt hydrates

Among thermochemical sorbents, hygroscopic salt hydrates offer high theoretical ESD, low desorption temperature, and suitable discharge temperature for space heating and domestic hot water [101]. The general reversible reaction of a salt hydrate is shown in Eq. (5). One of the issues that may happen in the salt hydrate storage systems is deliquescence, which results in the saturated salt solution rather than a salt hydrate, as shown in Eq. (6). Deliquescence happens when RH is higher than a certain limit,

deliquescence RH (DRH), which depends on the salt properties and temperature [41]. Forming of liquid film on the surface of salt crystal prevents the hydration reaction and causes corrosion issues due to the dripping of solution to the metal components [41]. LiCl and LiBr are not the proper salt hydrates for storage applications due to their low DRH (11.3% for LiCl and 6.2% for LiBr) at 30 °C, meaning that the solid salt hydrate could easily be changed to solution in most situations [41].

$$\mathrm{Salt(s)} + \mathrm{H_2O(g)} \leftrightarrow \mathrm{Salt\ hydrate(s)} + \mathrm{heat} \qquad \text{for RH} < \text{DRH} \qquad (5)$$

$$\mathrm{Salt(s)} + \mathrm{H_2O(g)} \leftrightarrow \mathrm{Salt\ hydrate(l)} + \mathrm{heat} \qquad \text{for RH} \geq \text{DRH} \qquad (6)$$

Table 5. Thermo-physical properties of selected sorbent materials.

		Mesoporous silicates	Classical zeolite	SAPO	AlPO	MOFs	Composite	Activated carbon
		RD silica gel	Zeolite 13X	SAPO-34	AlPO-18	NH2-MIL-125	SWS-1L	ACM-34.5
Chemical formula and composition		SiO_2(99.7%) Fe_2O_3(0.008%) Al_2O_3(0.025%) CaO(0.01%) Na_2O(0.05%) [102]	Na_2O Al_2O_3 $3SiO_2$ $6H_2O$ [103]	$Al_{0.56}$ $Si_{0.02}$ $P_{0.42}$ O_2 [104]	$Al_{0.25}$ $P_{0.25}$ O_2 [105]		Silica gel KSK+ 33.7 wt.% $CaCl_2$ [41]	
Particle density (ρ)	g cm^{-3}	1.158 [102] 0.72 [106]	0.730 [107]	0.6-0.7 [20]		0.3 [17], [97] 0.45 [98]	0.817 [108] 1 [23]	
Porosity	-	0.5-0.65 [83]	0.395					
Pore volume	cm^3 g^{-1}	0.4 [102] 0.44 [106]		0.27 [109]	0.53 [89]	0.57 [110]	0.6 [23]	0.69 [111]
Specific surface area	m^2 g^{-1}	720 [102] 780 [106]		590 [104]		1310 [110]	230 [23]	1200 [111]
Pore size	nm	0.8-7.5 [102] 2.24 [106]		0.38 [112]	0.38 [105]		7.5 [41] 15 [23]	2.3 [111]
Specific heat capacity	$Jkg^{-1}K^{-1}$	921 [102]	1080 [107]	0.822-0.942 [20]			800-900 [23]	
Optimal desorption temperature	°C			90		100-110		

Table 6 provides a comparison between the maximum uptake and ESD of some common sorbent materials of the above-mentioned sorbent categories from ref. [17]. Aristov [113] highlighted the importance of finding the optimal sorbent for any sorption heat transformation systems, and categorized the selection process into:

i. screening of the known sorbent candidates, and

ii. tailoring of novel sorbents suitable for the targeted application.

Table 6. specifications of different adsorbent with water as the adsorbate for heat storage application (from ref. [17])

Adsorbent group	Adsorbent	ω_{max}	Δh_{sorp}	ESD_{mat}	
		kg kg_{ads}^{-1}	MJ kg_{H2O}^{-1}	MJ kg_{ads}^{-1}	GJ m^{-3}
Mesoporous silicates	Silica gel Fuji RD	0.4	2.40	0.96	0.77
Classical zeolite	Zeolite 13X	0.34	3.8	1.29	0.83
	Zeolite 4A	0.22	3.05	0.67	0.49
CSPM	SWS-1 L ($CaCl_2$/silica gel)	0.65	2.65	1.72	1.55
	SWS-9 V ($LiNO_3$/Vermiculite)	1.80	2.30	4.15	1.16
	SWS-1 V ($CaCl_2$/Vermiculite)	1.80	2.35	4.2	1.25
	SIM-3b ($MgSO_4$/Vermiculite)	1.94	-	0.41	0.14
	($MgSO_4$ + $MgCl_2$)/Attapulgite	-	-	1.59	-
SAPO	AQSOA-Z02	0.33	3.25	1.07	0.55
AlPO	AlPO-Tric	0.31	3.17	0.98	-
MOF	MIL-101	1.40	1.83	2.57	-
	MIL-125NH_2	0.47	2.85	1.33	0.39
	MOF-841	0.48	3.05	1.47	-

3.3. Screening of sorbent candidates for the low-temperature S-TES

Among the above-mentioned sorbent categories, the following sorbents are selected for further investigations for the residential heating application:

1. AQSOA FAM-Z02
2. Silica gel + $CaCl_2$
3. Vermiculite + $CaCl_2$
4. Na_2S-H_2O

This screening process was conducted at CanMET Energy, Natural Resources Canada, in Ottawa during an internship. Characterization of sorbent materials has been mainly performed by simultaneous thermo-gravimetric analysis (TGA) and differential scanning calorimetry (DSC), TGA/DSC [24], [44], [114]. A simultaneous thermal analyzer (STA 449 *F3 Jupiter*, NETZSCH) device was used to examine the thermophysical properties of the sorbent materials at CanMET Energy.

3.3.1. Sample preparation

Among the sorbent candidates, FAM-Z02, vermiculte+$CaCl_2$, and Na_2S-H_2O were commercial sorbents and silica gel+$CaCl_2$ was developed in our lab [115]. Concentrated $CaCl_2$ salt solutions were dried in an oven (Fisher Scientific). Chromatography-grade commercial silica gels (Silicycle Inc., Quebec, Canada) with four distinct pore size distributions and 0.2–0.5 mm irregular-shaped grains were wetted with ethanol, and then an aqueous $CaCl_2$ solution was added to the silica. The mixtures were dried for 24 h in a fume hood. The damp material was baked at 200 °C until judged dry by consistent successive weight measurements [115]. The original states of the sorbent candidates are shown in Figure 14. Afterwards, the sorbents were crushed to form powdery samples, before the measurements. Alumina (Al_2O_3) crucible was used to hold 10 mg of the powdery sorbent materials.

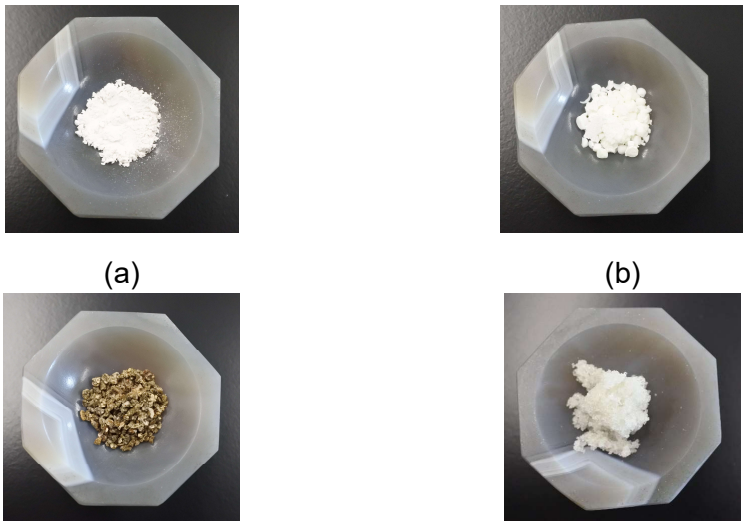

(a) (b)

(c) (d)

Figure 14. Sorbent samples: (a) AQSOA FAM-Z02, (b) silica gel+$CaCl_2$, (b) vermiculite+$CaCl_2$, and (d) Na_2S-H_2O.

3.3.2. Experimental test procedure

The measurements were performed in dry nitrogen at desorption temperature of 80 °C, sorption temperature of 25 °C, and water vapour pressure of 12 mbar (i.e., equivalent to 10°C) for three cycles. The heating rate during the desorption was set to 1 K min^{-1}, while the coolingr rate, after the desorption and before the sorption, was set to 5 K min^{-1}. Figure 15a shows the temperature and water vapour pressure for each cycle in

the following steps: (i) 0-30 min, at 25 °C (only for the first cycle), (ii) 30-85 min, from 25 °C to 80 °C with 1 K min^{-1} heating rate, (iii) 85-115 min, at 80 °C, (iv) 115-126 min, from 80 °C to 25 °C with 5 K min^{-1} cooling rate, (v) 126-141 min, at 25 °C, (vi) 141-381 min, at 25 °C and relative humidity (RH) 38% (P_v=12 mbar), and (vii) 381-386 min, at 25 °C and RH 0%. The low heating rate of 1 $Kmin^{-1}$ was selected for all sorbents because the high heating rate may lead to the melting of the salt and irreversibility of the process for Na_2S-H_2O [24]. This heating rate is low for other materials, such as FAM-Z02, which do not show any stability issues at higher heating rates. For instance, in the experiment conducted on FAM-Z02 in Chapter 5, the initial (first 2 min) heating rate was 13 K min^{-1}, and afterwards, the heating rate became 2 K min^{-1}.

Figure 15b shows the mass change percentage and specific heat flow of one layer of 2-mm FAM-Z02 particles during sorption. The repeatable trend was achieved, and the third cycle is studied for the performance assessment. The water uptake was 0.19 kg kg_{ads}^{-1} and the sorption heat was 3001 kJ kg_{H2O}^{-1} for one layer of FAM-Z02.

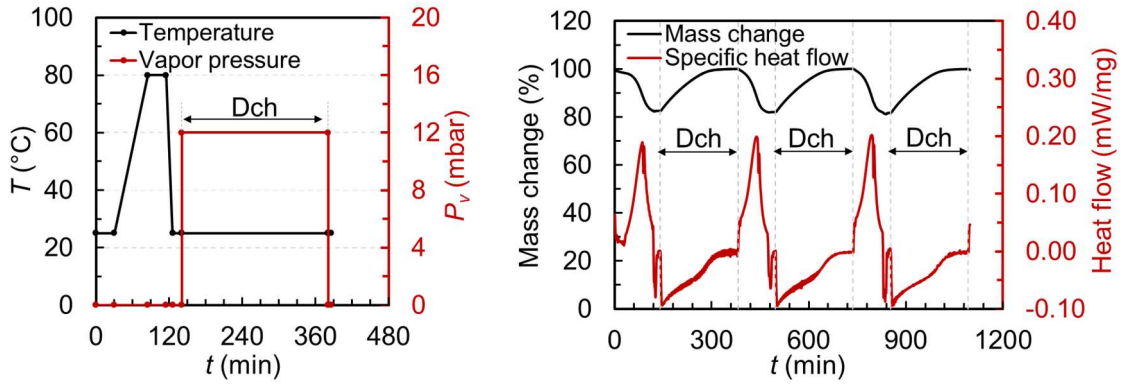

(a) (b)

Figure 15. (a) Operating conditions including temperature and vapor pressure during the desorption and sorption for each cycle, similar to the experimental procedure in ref. [24] and (b) mass change percentage and specific heat flow during the three cycles for 40.60 mg AQSOA FAM-Z02 2 mm particles in one layer.

3.3.3. Sorption rate of sorbent candidates

To study the sorption rate of sorbent candidates, the dimensionless water uptakes are compared, as shown in Figure 16a. For the above-mentioned operating conditions, FAM-Z02 show the fastest sorption rate and Na_2S-H_2O has the second fastest rate. The characteristic time (τ_{sorp}) is obtained from Eq. (7), where ω, ω_0, and ω_∞ are the water uptake, initial water uptake, and maximum water uptake.

$$(\omega - \omega_0)/(\omega_\infty - \omega_0) = 1 - \exp(-t/\tau_{\text{sorp}}) \quad (7)$$

As shown in Figure 16b, τ_{sorp} is the lowest (1411 s) for FAM-Z02, and follows by 1897 s for Na_2S-H_2O, 4386 s for vermiculite+$CaCl_2$, and 5173 s for silica gel+$CaCl_2$. Discharge rate, $1/\tau_{\text{sorp}}$, is 7×10^{-4} s^{-1} for FAM-Z02. Figure 16c shows the initial sorption rate of the sorbent candidates, which is based on the slope of the linear dimensionless uptake in the first 15 min. FAM-Z02 has the highest initial sorption rate of 3.95×10^{-4} s^{-1}.

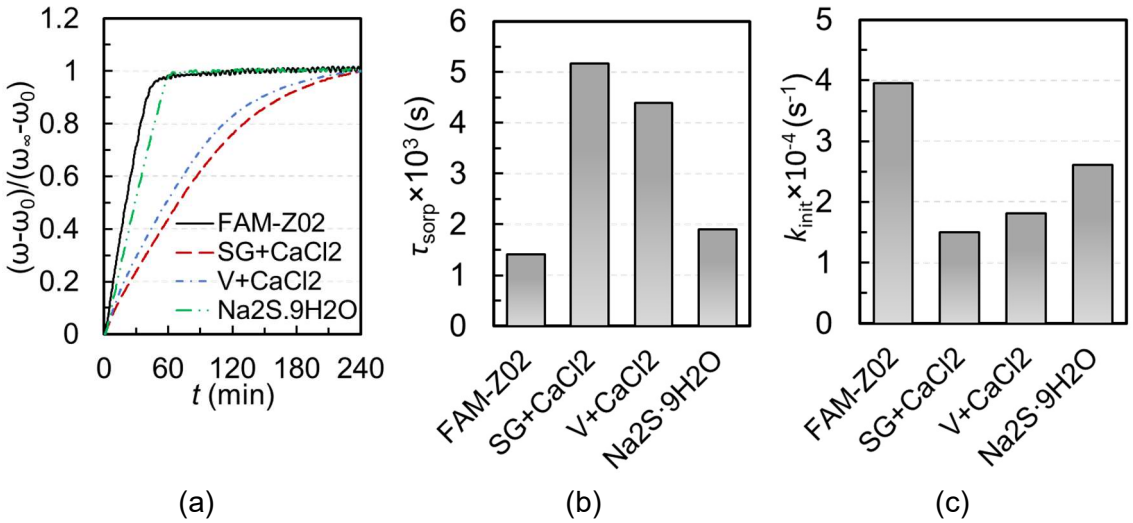

Figure 16. Sorption characteristics: (a) dimensionless water uptake (ω/ω_∞), (b) sorption characteristic time (τ_{sorp}), obtained from Eq. (7), $(\omega - \omega_0)/(\omega_\infty - \omega_0) = 1 - \exp(-t/\tau_{\text{sorp}})$, and (c) initial sorption rate (k_{init}) for the first 15 min of sorption, obtained from equation $k_{\text{init}} = d((\omega - \omega_0)/(\omega_\infty - \omega_0))/dt$, for the sorbent candidates of FAM-Z02, silica gel+$CaCl_2$ (SG+$CaCl_2$), vermiculite+$CaCl_2$ (V+$CaCl_2$), and Na_2S-H_2O.

3.3.4. Charging and discharging power of sorbent candidates

Instantaneous specific power (SP_{inst}) during each cycle is shown in Figure 17. Similar to the sorption rate, maximum discharge SP_{inst} is the highest for Na_2S-H_2O (1.061 kW $kg_{dry,ads}^{-1}$), as listed in Table 7. FAM-Z02 has the second highest maximum discharge SP_{inst} of 0.431 kW $kg_{dry,ads}^{-1}$. Likewise, the maximum charge SP_{inst} is the highest for Na_2S-H_2O (1.876 kW $kg_{dry,ads}^{-1}$). Composite of vermiculite+$CaCl_2$ has the second highest maximum charge SP_{inst} of 0.541 kW $kg_{dry\ ads}^{-1}$. The reason that this value is smaller for FAM-Z02 is due to the low heating rate of 1 K min^{-1} and the maximum charging temperature of 80 °C, which is not the optimum condition for FAM-Z02 [20]. Moreover, the maximum charge SP_{inst} occurs at different temperatures for the sorbent candidates (i.e.

58 °C for FAM-Z02, 48-49 °C for vermiculite+$CaCl_2$ and silicagel+$CaCl_2$, and 80 °C for Na_2S-H_2O).

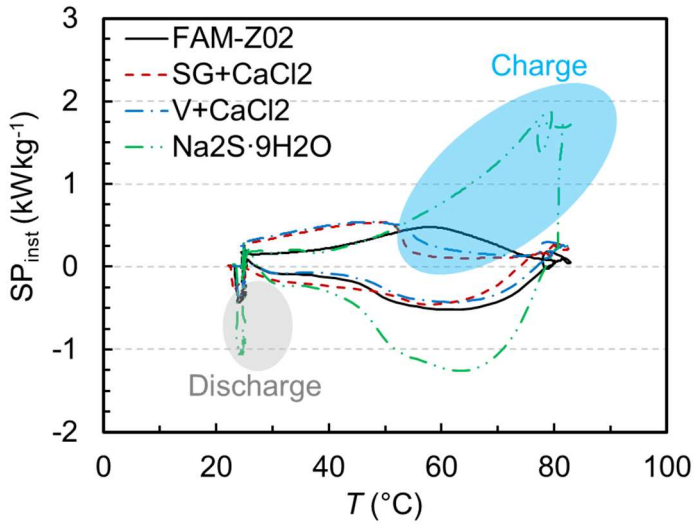

Figure 17. Instantaneous specific power versus temperature for FAM-Z02, silica gel+$CaCl_2$, vermiculite+$CaCl_2$, and Na_2S-H_2O.

Table 7. Maximum instantaneous specific power of charging and discharging of the sorbent candidates.

Sorbent material	**$SP_{ch,inst,max}$** (kW $kg_{dry\ ads}^{-1}$)	**$SP_{dch,inst,max}$** (kW $kg_{dry\ ads}^{-1}$)
FAM-Z02	0.479	0.431
SG+$CaCl_2$	0.535	0.297
V+$CaCl_2$	0.541	0.383
Na_2S-H_2O	1.876	1.061

3.3.5. Sorption capacity and ESD of sorbent candidates

The sorption capacity is a function of the maximum water uptake (shown in Figure 18) and sorption heat. The maximum water uptakes based on the dry mass of the sorbents are 1.07 kg $kg_{dry\ ads}^{-1}$ for Na_2S-H_2O and 0.58 kg $kg_{dry\ ads}^{-1}$ for vermiculite+$CaCl_2$. The lowest water uptake is 0.31 kg $kg_{dry\ ads}^{-1}$ for FAM-Z02.

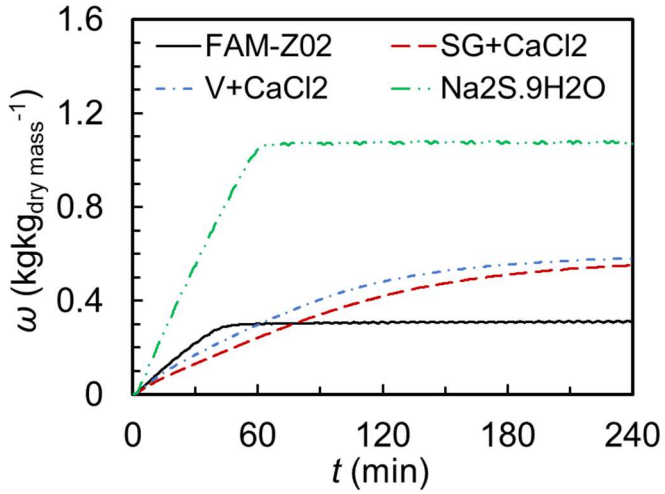

Figure 18. Water uptake of sorbent candidates based on the dry mass through the time.

The ESD of the sorbent candidates per sorbent mass is shown in Figure 19. ESD_{mat} based on the initial mass of the sorbent (i.e. 10 mg for all sorbents regardless of the initial hydration level) is shown in Figure 19a and Figure 19b, which is directly extracted from the software (Proteus) of STA device. However, ESD is commonly reported based on the dry mass of the sorbent, as shown in Figure 19c and Figure 19d. The difference between the ESD based on the initial mass and based on the dry mass was significant for Na_2S-H_2O since it was highly hydrated (Nona hydrate Na_2S) in its initial state. Considering Figure 19c, the highest ESD of 3.44 $MJkg_{dry\ ads}^{-1}$ was obtained for Na_2S-H_2O, although ESD based on the initial mass was the highest for vermiculite+$CaCl_2$ (1.38 $MJkg_{init\ mass}^{-1}$).

Considering the volumetric ESD as shown in Figure 19d, the highest ESD of 4.91 GJm^{-3} is for Na_2S-H_2O and ESD of silica gel+$CaCl_2$ and vermiculite+$CaCl_2$ are 1.56 and 0.76 GJm^{-3}, respectively. The low density of vermiculite+$CaCl_2$ leads to a lower volumetric ESD (half of ESD of silica gel+$CaCl_2$), despite its ESD per sorbent mass is close to that of the silica gel+$CaCl_2$ (see Figure 19c). The lowest ESD of 0.63 GJm^{-3} is for the SAPO family (FAM-Z02), due to its lower sorption capacity compared to the salt-composites and salt-hydrates materials.

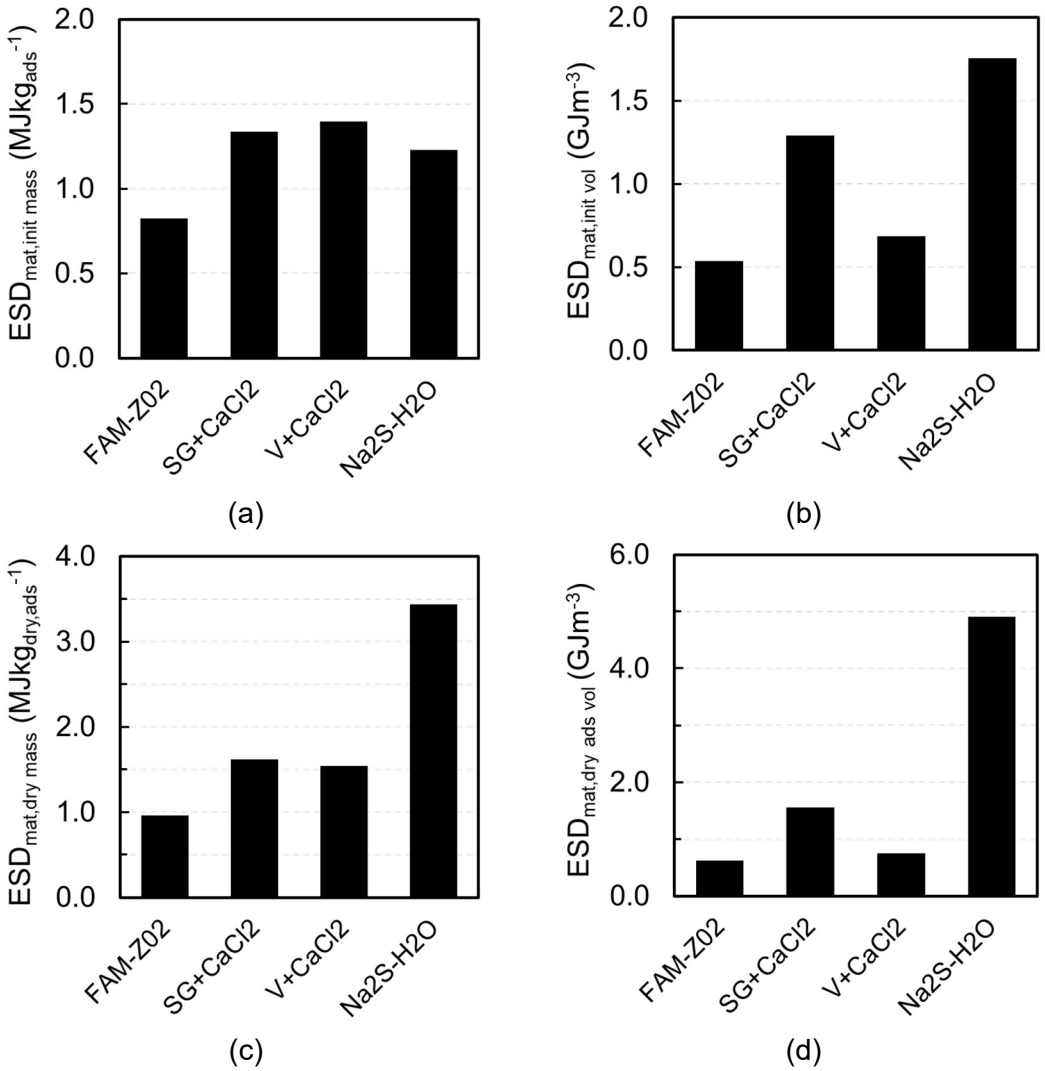

Figure 19. (a) ESD based on initial mass of sorbent material ($ESD_{mat,init\ mass}$), (b) ESD based on initial volume of the sorbent material ($ESD_{mat,init\ vol}$), (c) ESD based on dry mass of the sorbent material ($ESD_{mat,dry\ mass}$), and (d) ESD based on volume of the dry sorbent material ($ESD_{mat,dry\ mass\ vol}$) for desorption temperature of 80 °C, sorption temperature of 25 °C, and sorption vapour pressure of 12 mbar.
Densities of 650 kg m^{-3} [20] for FAM-Z02, 965 kg m^{-3} [116] for silica gel+$CaCl_2$, 491 kg m^{-3} [116] for vermiculite+$CaCl_2$, and 1430 kg m^{-3} [117] for Na_2S-H_2O are considered.

3.3.6. Sorbent configuration and sorption rate

Aside from the material compositions, the material configuration is of great importance. To study the effect of sorbent configuration on the sorption rate, three configurations of FAM-Z02 were investigated: (i) fine powder, (ii) one layer of 2 mm diameter particles, and (iii) two layers of 2 mm diameter particles, as shown in Figure 20. As shown in Figure 21a, the water uptake of fine powder FAM-Z02 was significantly higher

than that of the layers of FAM-Z02 particles, due to the lower thermal contact resistance in the fine powder configuration. Figure 21b shows the initial linear uptake rate (k_{init}) of the three configurations. k_{init} is 2.6 times faster for the powder FAM-Z02 compared to the one-layer arrangement of FAM-Z02 particles. Better heat transfer contact area was provided by the fine powder sorbents, however, in the large-scale storage systems, the mass transfer of the water vapor would be decreased due to the dense packing of fine powder. In Chapter 5 and Chapter 6, the effects of different sorbent configurations on the storage performance in the full-scale experimental testbed are presented in detail.

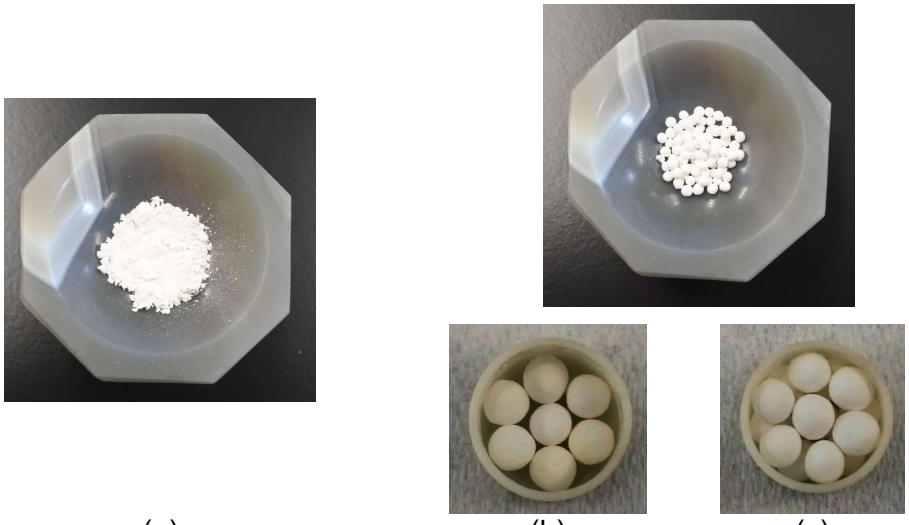

(a) (b) (c)

Figure 20. FAM-Z02 samples with different configurations: (a) fine powder, (b) one layer of 2 mm particles, and (c) two layers of 2 mm particles.

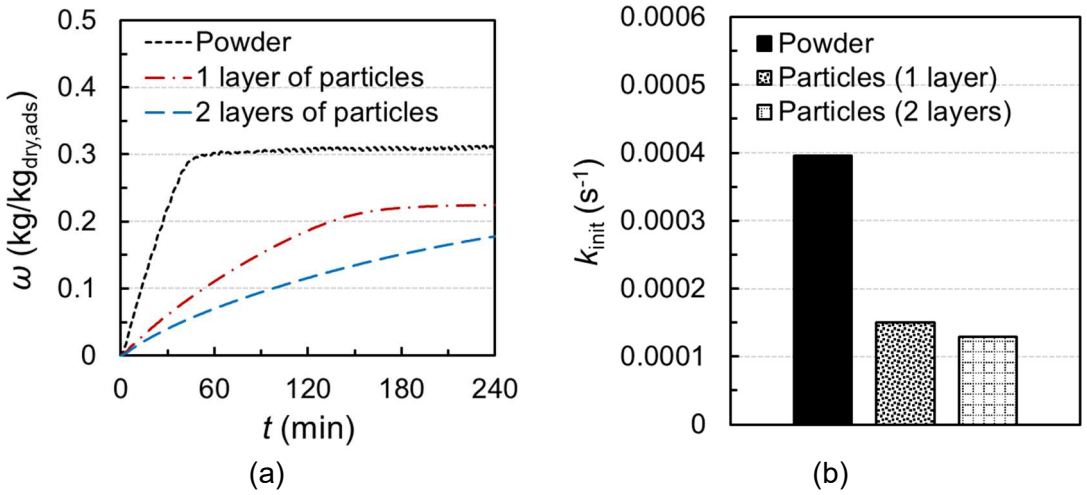

Figure 21. (a) water uptake versus time and (b) initial sorption rate of powder, 1 layer, and 2 layers of 2 mm diameter FAM-Z02 particles.

3.4. Summary of results of the screening process

Four sorbent materials were selected for further investigation for the storage application in residential application: (i) FAM-Z02 (SAPO), (ii) silica gel+$CaCl_2$ (composite sorbent), (iii) vermiculite+$CaCl_2$ (composite sorbent), and (iv) Na_2S-H_2O (salt hydrate). Among these sorbent candidates, FAM-Z02 was selected for more characterization and storage performance assessment in full-scale (Chapter 4, Chapter 5, Chapter 6) since it showed the fastest discharging rate (7×10^{-4} s^{-1}).

Although Na_2S-H_2O provided the highest SP and ESD, there was evidence of outgassing of H_2S, which made it unsafe for the residential environment. Among the rest of sorbent candidates, highest discharge SP (0.431 kW kg^{-1}) was for FAM-Z02 and highest charge SP (0.541 kW kg^{-1}) was for vermiculite+$CaCl_2$. Silica gel+$CaCl_2$ showed ESD of 1.6 MJ kg^{-1}. Due to the low volumetric ESD of vermiculite+$CaCl_2$, the best candidate that provides high volumetric ESD is silica gel+$CaCl_2$, which will be presented in a full-scale S-TES experimental study in Chapter 7. Moreover, $CaCl_2$ confined in silica gel is one of the salt hydrates that can recover their original structure in case of possible structure destruction due to melting, therefore the heating rate is not a limiting factor for this sorbent [24].

Chapter 4.

Effective thermal conductivity of S-TES sorber beds

Low thermal conductivity of adsorbent materials, 0.1-0.8 $W\,m^{-1}K^{-1}$ [37], along with the high thermal contact resistance (TCR) between the sorbent particles and sorber bed metal surfaces suppress the overall performance of S-TES systems through slow charging and discharging periods. A monolayer configuration of sorption bed ensures less heat transfer resistance and higher water uptake rate, although multi-layers are more desirable for storage applications, due to the higher HEX-to-sorbent mass ratio and lower COP of the monolayer configuration [37]. These two competing trends indicate a need for further investigation to establish optimum configurations (optimum number of layers of adsorbents and packed bed arrangements). To this end, measurement and modeling of the heat transfer performance of a multilayer packed bed sorber, including effective thermal conductivity (ETC) of sorber beds as well as its TCR, are presented in this chapter.[2]

4.1. Theoretical model for effective thermal conductivity of loose grain sorber beds

There are three types of models for ETC of packed beds: i) analytical or numerical solutions to the Laplace's equation, ii) thermal resistance network concept, and iii) unit cell approach [118]. The first type of ETC models is either based on limiting assumptions, such as the assumption of no thermal influence between individual particles in a Maxwell analytical solution or based on the numerical models with high computational cost and time [118].

Using a thermal resistance network, Griesinger et al. [119] studied the ETC of zeolite powder at atmospheric pressure, introducing three main parallel heat transfer paths: pure solid, pure fluid, and mixed solid-fluid paths. They defined tuning parameters by fitting the theoretical curve to the measured values [119]. Similarly, Dawoud et al. [120]

[2] The results of this chapter were published in Refs. [2], [4], [5], and presented in: (i) IVth International Symposium on Innovative Materials for Processes in Energy Systems (IMPRES 2016) [1], and (ii) International Sorption Heat Pump Conference (ISHPC 2017) [3].

developed a model to calculate the ETC of wetted zeolite 4A, assuming an isotropic distribution of adsorbed water inside the zeolite crystal. They introduced a tortuosity factor for conductive heat transfer and their model took into account the Knudsen conductivity of the vapor phase through the curve fittings to their experimental data [120]. Nevertheless, thermal conductivity models of small amount of sorbent sample, i.e. a sorbent particle or powder, may not be a proper representative of a large-scale packed bed sorber, since they do not take into account all the thermal resistances inside the packed bed, including the thermal resistance between the sorbent particles as well as TCR.

The third type of ETC models is based on calculating the thermal conductivity of a unit cell (as a representative of the repeating units in a packed bed), using thermal resistance network or basic models such as Maxwell. Luikov et al. [121] defined a thermal resistance circuit for an elementary cell, arranged with a solid skeleton and the surrounding gas. The boundary unit cell and uptake were not considered in their study [121]. In addition to their model, Sarwar and Majumdar [122] took into account the effects of the water content on thermal conductivity of the adsorption desiccant packed beds. Interstitial gas pressure and the contact pressure were not considered as variables in this model [122].

Although the importance of TCR has been raised in the literature [123]–[125], little has been shown regarding the modeling of TCR inside the sorber bed. To consider TCR in the ETC calculation, the measured TCR from the available experimental data was fed into some models in the literature [126], [127]. Rezk et al. [127] presented a lumped analytical model for thermal conductivity of a silica gel packed bed and they applied a correlation fitted to the measured TCR, in ref. [128], to their model. To this end, it is beneficial to develop a comprehensive ETC model, which includes TCR calculation, as a function of temperature, gas pressure, bed arrangement, contact pressure, and surface specifications.

4.1.1. Model description and assumptions

A unit cell approach is adopted by considering a unit-cell as the representative of a uniformly-arranged simple cubic (SC) packed bed, as schematically shown in Figure 22a. Bahrami et al. [129] developed compact analytical models to predict the constriction/spreading and interstitial gas resistances in packed beds of high conductive

particles, i.e. particle thermal resistance was much less than the gas resistance. In the present model, their analytical solutions are followed, as a platform for dry sorber bed, while particle thermal resistance is also considered, and afterwards, extended for the thermal conductivity of wet sorber beds, considering the sorbent particle water uptake and air relative humidity. Thermal conductivities of wet sorbent particles have been modeled through the effective-medium approximation, using Bruggeman's method for multi-component systems. The following highlights the main assumptions of the present model:

- It is assumed that the steady-state condition was reached for both temperature and uptake. Therefore, the uptake of the sorbent particles corresponds to the equilibrium uptake at the steady-state temperature and relative humidity (or pressure ratio, P/P_0, for the closed sorption system) in the bed.
- The distribution of the adsorbed water in the sorbent particle is homogeneous.
- The packed bed arrangement, regardless of the porosity of the bed, is homogeneous with uniform-sized particles.
- Natural convection in the small voids between the sorbents can be neglected [130], moreover, in the model and experimental data, the heat flow is downward to eliminate the natural convection [131], [132].
- Radiation is negligible in the packed beds at low temperatures [133].
- Heat conduction in the unit cell is one-dimensional.

Thus, heat transfer occurs via conduction through solid sorbent and conduction through the interstitial gas. As shown in Figure 22, these conductive heat transfer mechanisms take place in multi-scales: i) macroscale, including macro-contact ($\dot{Q}_{\mathrm{C,macro}}$) and macro-gap ($\dot{Q}_{\mathrm{G,macro}}$) paths; and ii) microscale, including micro-contact ($\dot{Q}_{\mathrm{c,micro}}$) and micro-gap ($\dot{Q}_{\mathrm{g,micro}}$) paths.

A wet sorbent particle is an inhomogeneous medium of three components: (i) solid particle (sorbent skeleton), (ii) adsorbed water on the surface of sorbent pores, and (iii) interstitial gas, which is the air in the open sorption system and water vapor in the closed sorption system. Among various models of effective-medium approximation, Bruggeman's method for the multi-component medium is selected, since it is readily applicable to arbitrary volume fractions [134]. Therefore, the thermal conductivity of a wet sorbent

particle, $k_{p,\mathrm{wet}}$, can be calculated by Eq. (8), where β_i is the volume fraction of each component (solid particle, adsorbed water, and gas), ε is the porosity of the sorbent particle, and ρ_s is the pore-less density of the sorbent material.

$$\sum_{i=1}^{3} \beta_{\mathrm{i}} \frac{k_i - k_{\mathrm{p,wet}}}{k_i + 2k_{\mathrm{p,wet}}} = 0, \qquad \text{where} \qquad \sum_{i=1}^{3} \beta_i = 1$$
$$\beta_{\mathrm{s}} = 1 - \varepsilon \tag{8}$$
$$\beta_{\mathrm{w}} = \omega \frac{\rho_{\mathrm{s}}}{\rho_{\mathrm{w}}}(1 - \varepsilon)$$
$$\beta_{\mathrm{g}} = \varepsilon - \omega \frac{\rho_{\mathrm{s}}}{\rho_{\mathrm{w}}}(1 - \varepsilon)$$

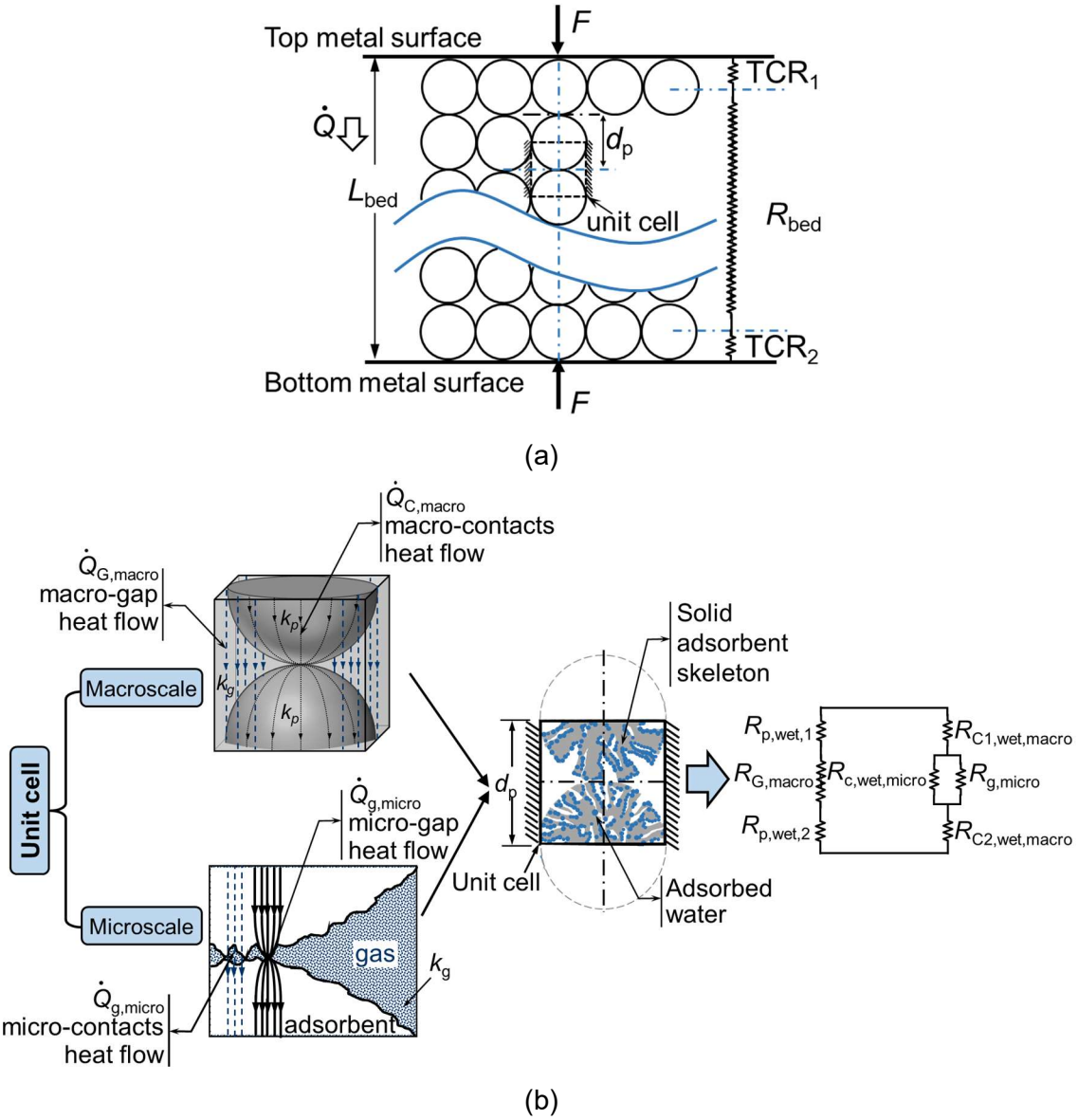

Figure 22. (a) Packed bed sorber of adsorbents with a diameter of d_{p}, for simple cubic (SC) arrangement [129], and (b) heat conduction in the packed bed, shown in macro-scale and micro-scale, and a unit cell of a wet SC-arranged sorber bed with the equivalent electrical circuit.

One-dimensional heat conduction in the unit cell leads to the isothermal top and bottom surfaces, while the lateral walls are adiabatic due to symmetry (see Figure 22a) [129]. As shown in Figure 22b, the thermal resistance of the unit cell consists of (1) bulk thermal resistance of particles, R_{p}, (2) macro-contact constriction/spreading resistance, $R_{\mathrm{C,macro}}$, (3) micro-contact constriction/spreading resistance, $R_{\mathrm{c,micro}}$, (4) resistance of the interstitial gas in the micro-gap, $R_{\mathrm{g,micro}}$, and (5) resistance of interstitial gas in the macro-

gap, $R_{\mathrm{G,macro}}$. The equations used in this model are presented in Appendix A, and more details are found in ref. [129]. Using the proposed unit cell thermal resistance network, shown in Figure 22b, the total thermal resistance of the unit cell is as follows,

$$R_{\mathrm{cell}} = \left[\frac{1}{\left(1/R_{\mathrm{c,micro}} + 1/R_{\mathrm{g,micro}}\right)^{-1} + R_{\mathrm{C,macro}}} + \frac{1}{R_{\mathrm{p}} + R_{\mathrm{G,macro}}}\right]^{-1} \tag{9}$$

The unit cell ETC can be found by $k_{\mathrm{eff,cell}} = L_{\mathrm{cell}}/(R_{\mathrm{cell}}A_{\mathrm{cell}})$, which is also the ETC of the packed bed ($k_{\mathrm{eff,bed}}$), considering a homogenous medium. Thermal resistances of the unit cells along the bed's length (i.e. in the heat transfer direction) are in series, while they are parallel to each other in the direction perpendicular to the heat transfer path. Thus, the thermal resistance of the sorber medium is $R_{\mathrm{bed}} = \left[L_{\mathrm{bed}}/\left(k_{\mathrm{eff,bed}}\, A_{\mathrm{cell}}\right)\right]/m$, where L_{bed} is the bed length in the heat transfer direction and m is the number of unit cells in each layer of the sorber bed.

The TCRs in the unit cells adjacent to the two metal surfaces of HEX medium are also in series with the medium resistance (R_{bed}). Thus, the total bed resistance is $R_{\mathrm{tot}} = R_{\mathrm{bed}} + \mathrm{TCR}$. To this end, the total thermal conductivity of a dry packed bed can be found from:

$$k_{\mathrm{tot}} = \frac{L_{\mathrm{bed}}}{A\,(R_{\mathrm{bed}} + \mathrm{TCR})} \tag{10}$$

where $A = A_{\mathrm{cell}} \times m$ is the total area of the metal surface. Similarly, all the thermal resistances in the sorbent particle and the gas are calculated for the face center cubic (FCC) arrangement, using related equations in ref. [129] and the parameters in Table 8, for FCC arrangement.

Table 8. Specifications of SC and FCC arrangements of a packed bed

Packing arrangement	Solid fraction, ψ_{bed}	Bed length, L_{bed}	Cell area, A_{cell}	Cell length, L_{cell}	Boundary cell length, $L_{\mathrm{b\,cell}}$
SC	0.524	$n \times d_{\mathrm{p}}$	d_{p}^2	d_{p}	$d_{\mathrm{p}}/2$
FCC	0.740	$\left((n-1)\sqrt{2}/2+1\right) \times d_{\mathrm{p}}$	$d_{\mathrm{p}}^2/2$	$\sqrt{2}d_{\mathrm{p}}/2$	$d_{\mathrm{p}}/2$

Therefore, by assuming a linear relationship using the ETC values of SC and FCC arrangements, ETC of the randomly packed bed can be estimated based on its solid fraction, as follows,

$$\frac{\psi_{\mathrm{bed}}-\psi_{\mathrm{SC}}}{\psi_{\mathrm{FCC}}-\psi_{\mathrm{SC}}}=\frac{k_{\mathrm{bed}}-k_{\mathrm{SC}}}{k_{\mathrm{FCC}}-k_{\mathrm{SC}}} \tag{11}$$

where ψ_{SC}, ψ_{FCC} and ψ_{bed} are the solid fractions of the SC, FCC and any randomly packed bed arrangements, respectively. Solid fraction of a randomly packed bed sorber can be found from the literature or can be chosen such that k_{bed} approaches the experimental data collected for thermal conductivity of that randomly packed bed.

The above-mentioned ETC model is coded into MATLAB in four sections: i) water uptake calculation from the equilibrium isotherms, reported by Goldsworthy [135], ii) adsorbent particle thermal resistance model, iii) packed bed cell resistance and iv) packed bed boundary cell resistance models. The ETC model is then compared with the measured values.

4.1.2. Model parameters

The input parameters of this model are either measured or extracted from the available values in the literature. Some thermophysical properties of the sorbent material (FAM-Z02), which were reported in the literature are listed in Appendix B. Thermal accommodation ($\alpha_{T,\mathrm{p}}$) and Young's modulus (E_{p}), as shown in equations in Appendix A, are required for the ETC calculations. In this model, a clean surface is assumed for the sorbent particle, therefore, the correlation for thermal accommodation of clean surfaces, developed by Song and Yovanovich [136], is applied (see Eq. (75) in Appendix A).

A thermomechanical analyzer (TMA Q400EM from TA Instruments), shown in Figure 23a, with a precision of ± 0.1% is used to measure Young's modulus of the sorbent particle. As shown in Figure 23a, a 2-mm diameter FAM-Z02 particle was compressed

with linear ramp force up to 1 N in a dry nitrogen environment at room temperature, between the quartz glass sample stage and macro-expansion probe with a 6.07 mm diameter contact area. The value of 0.5736 GPa^{-1} is obtained for $\left(1-\nu_{\mathrm{p}}^{2}\right)/E_{\mathrm{p}}$ (see Eq. (69) in Appendix A), where ν_{p} is particles Poisson's ratio. Assuming a value of 0.3 for Poisson ratio, E_{p} of FAM-Z02 is 1.59 GPa.

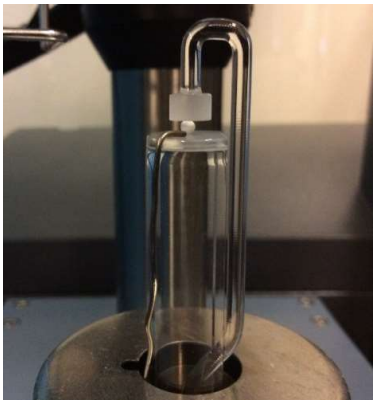

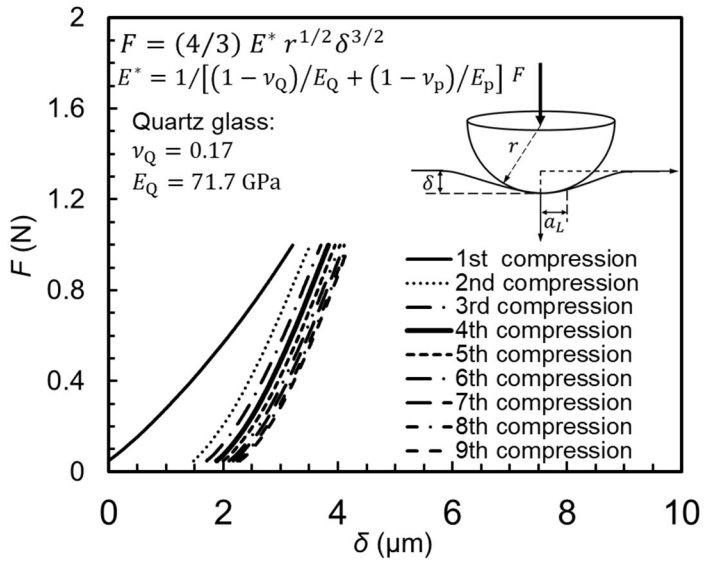

(a) (b)

Figure 23. (a) Thermomechanical analyzer (TMA Q400EM from TA Instruments) with an AQSOA FAM-Z02 particle, placed between quartz glass sample stage and macro-expansion probe and (b) the force applied on the sorbent particle versus half-displacement of the sorbent particle.

The solid fraction (ψ) of SC and FCC arrangements are 0.524 and 0.740, respectively, and ψ of a randomly packed bed falls between that of these two limits, lower bound (SC) and upper bound (FCC) [137], [138]. The solid fraction of a randomly packed bed depends on the method of shaking, pouring and tapping, and usually, vary between 0.57 and 0.65 [139]. However, a decrease in sphericity of the particles increases the solid fraction of randomly packed bed, e.g., solid fractions of 0.707 and 0.731 were reported for the exaggerated limits of oblate ellipsoids and spherocylinders [140].

4.2. Experimental study on the effective thermal conductivity and TCR of a FAM-Z02 packed bed sorber

Thermal conductivity measurement methods, used for various adsorbent materials in the literature, are listed in Table 9. Bjurström et al. [141] measured thermal conductivity

of wet silica gel particles by transient hot strips (THS) method and ETC of a dry packed bed of silica gel through a steady-state measurement, using a custom-built annular testbed. Tanashev and Aristov [142] measured the thermal conductivity of a composite of KSK silica gel and CaCl2 by the transient hot wire (THW) method at 290-330 K and atmospheric pressure. They showed that the thermal conductivity of the composite increased from 0.112 to 0.216 W $m^{-1} K^{-1}$ when water uptake was raised from 0.01 to 0.58 kg kg_{ads}^{-1}. Tanashev et al. [143] later showed that their reported thermal conductivity of the composites of silica gel and salts, under atmospheric pressure, could be used in the closed adsorption systems as well, since their results showed that thermal conductivity was a stronger function of uptake rather than vapor pressure and temperature.

Due to the adsorption heat released by adsorbents, the measured temperature difference in the unsteady thermal conductivity measurement is smaller than that of the test with no adsorption heat, which results in higher thermal conductivity [144]. To eliminate the above-mentioned error in the thermal conductivity measurement of adsorbent materials, steady-state measurements have been found more practical [144]. Sharafian et al. [125] conducted a steady-state measurement with a custom-built guarded-hot plate device to measure the thermal conductivity of consolidated silica gel-PVP samples with a volume of 25.4×25.4×6.6 mm^3.

Table 9. Thermal conductivity measurement techniques used for adsorbent materials in the literature.

Ref.	Measurement method	Standard	Adsorbent	Adsorbent configuration	Uptake ($kgkg^{-1}$)	Temperature (K)	Thermal conductivity ($Wm^{-1}K^{-1}$)	TCR/R_{eff}
[141]	Transient hot strip / Transient Plane Source (TPS)	ISO22007-2	Silica gel	Packed bed (adsorbent packed in a cell (40 × 60 ×10 mm)	0	295	0.147	-
					0.329	295	0.265	-
[145]			Silica gel + $CaCl_2$ + 20 wt% graphite flakes	composite	0.18	308	0.41	-
[142]	Transient Hot wire (THW)	ASTM C1113	Silica gel KSK+ 20 wt% $CaCl_2$	composite	0.01	293	0.112±0.007	-
					0.58	293	0.216±0.012	-
[146]			Silica gel + 36.6 wt% $CaCl_2$ + binder $Al(OH)_3$	composite	0.053	363	0.12	-
					0.286	363	0.227	-
[20]			FAM-Z02	-	-	303	0.117	-
					-	363	0.128	-
[112]	Laser flash	ASTM E1461-13	FAM-Z01	Coated (0.3 mm)	-	293	0.376	-
[147]	Guarded-hot plate	BS-874	Monolithic carbon (sample LM127)	monolithic with coarse powders	-	293	0.45	-
					-	393	0.4	-
[125]		ASTM E1530	Silica gel + PVP with a metallic substrate	composite	-	310	0.282	0.26
					-	321	0.240	0.05

Heat and mass transfer properties of a sorber bed are strongly dependent on the size of the sorber bed [37]. Water uptake rate and thermal conductivity measurements of a small amount of sorbent material, less than 0.1 kg, can only show an ideal design and, instead, a large-scale measurement is essential to realistically study the heat and mass transfer in a packed bed sorber. Table 10 shows the difference between the thermal conductivity of solid grain and packed bed of adsorbent materials, reported in the ref. [37]. Hence, in this work, a steady-state heat flow meter with a test chamber volume of 305×305×100 mm^3 was selected to measure the thermal conductivity of a large-scale packed bed.

Table 10. Comparison between the thermal conductivity of a solid grain adsorbent and a packed bed sorber reported in ref. [37].

Sorbent material	Adsorbent configuration	Thermal conductivity ($Wm^{-1}K^{-1}$)
Zeolite	Solid grain	0.18-0.4
	Granular bed (H_2O)	0.03-0.15
Silica gel	Solid grain	0.37-0.8
	Granular bed	0.05-0.2
	Granular bed (H_2O)	0.04-0.26
Activated carbon	Solid grain	0.54
	Granular bed	0.3-0.5
	Granular bed (methanol)	0.14-0.17

There are few studies on the measurement of TCR in the sorber beds [125], [128]. Based on the test procedure for flat surfaces developed by Antonetti and Yovanovich [148], Wang et al. [128] measured the TCR between the heat exchanger surface and the zeolite granule adsorbent with diameters of 0.297, 0.149 and 0.074 mm by heat flux ratio-measuring instrument, under vacuum conditions, which was later used in an empirical lumped analytical model for thermal conductivity of a silica gel packed bed, developed by Rezk et al. [127]. Sharafian et al. [125] experimentally showed that the ratio of TCR to the total thermal resistance can be as high as 26% at 37 °C and atmospheric pressure for a consolidated block of silica gel-PVP on a metallic substrate.

Although coated and loose grain FAM-Z02 were utilized in adsorption systems and showed promising performance [45], [71], [72], [149]–[151], little information is available concerning thermal properties of FAM-Z02, which are listed in Table 11. Okamoto et al. [112] used a transient hot wire (THW) device to measure the thermal conductivity of FAM-Z02. They reported thermal conductivity of 0.117 and 0.128 $Wm^{-1}K^{-1}$ at 303 and 363 K, respectively. ETC of coated FAM-Z02 with clay as the binder was studied by Frazzica et al. [152]. They showed that ETC of the coated FAM-Z02, under vacuum pressure, dropped by increasing the coating thickness [152]. Moreover, effects of the number of layers of sorber bed on the kinetics of FAM-Z02 loose grain bed were studied by Girnik and Aristov [149], using large temperature jump method, but the effects of the number of layers of sorbent in sorber bed on the thermal conductivity have not been investigated in the literature.

Table 11. Properties of SAPO-34 CHA and FAM-Z02 (commercial SAPO-34 CHA)

Ref.	Sorbent	Sorbent configuration	Specific heat capacity ($Jkg^{-1}K^{-1}$)	Bulk density (kgm^{-3})	Thermal conductivity ($Wm^{-1}K^{-1}$)	Thermal diffusivity (m^2s^{-1})
[112]	FAM-Z02	Powder	822 (303K) 942 (363K)	600-700	0.117 (303K) 0.128 (343K)	2.19E-7 2.09E-7
[152]	FAM-Z02 + 18.5 wt.% Bentonite clay + 1.5 wt.% micro carbon fiber	0.4-mm coated 0.6-mm coated	900	-	0.4413 0.2823	-
[153]	SAPO-34 CHA +Al	Composite	900	1510	9 ± 1	6.62E-6

4.2.1. Testbed for thermal conductivity measurement of FAM-Z02 packed bed adsorbers

A heat flow meter apparatus (HFM 436/3/1E Lambda, NETZSCH Instruments) is used for steady-state thermal conductivity measurements of packed beds of the sorbent. The HFM can measure samples with thermal conductivities of 0.002 to 2.0 W m^{-1} K^{-1}, with an accuracy of ±1-3%. The HFM, shown in Figure 24a, can apply a variable external load on the sample (see Figure 24b), to control the contact pressure and ensure uniform contact between the upper and lower plates and the sample, throughout the plate surface. Heat-flow transducers (flux gauges) are installed in the center of the test chamber and far from the frame. Measurements were carried out at mean temperatures from 10 to 80 °C and 20 °C temperature difference between the hot (upper) and cold (lower) plates.

Packed beds of 2 mm diameter FAM-Z02 spherical particles were prepared with 1, 2, 4 and 6 layers. Similar to a real finned sorber bed, the sorbent particles were randomly packed and as shown in Figure 24c and Figure 24d, sorbent layers were sandwiched between two aluminum sheets (305×305×0.4 mm^3). Narrow adhesive-back EPDM foam strips (Neoprene/EPDM/SBR foam with closed cell), which restricted water and air from being exchanged between the packed bed and the environment [154], were attached around the perimeter of the lower aluminum sheet, forming a frame to hold the sorbent particles (see Figure 24c and Figure 24e). Measurements were carried out after the sorbents reached the equilibrium at the room condition (24 °C and 35% RH). Afterwards, the custom-built sample holder was covered with the upper aluminum sheet and was placed in the test chamber, where it was pressed between the hot and cold plates under the preset contact pressure. Since there is no air exchange between the packed bed and the test chamber environment, if all the water that is in the air inside the packed

bed was adsorbed, the adsorbent water content would change only by 1.5×10^{-5} $kgkg_{ads}^{-1}$. At 80 °C, the air could hold an additional 0.28 kg m_{air}^{-3} of water vapor. If this all came from the adsorbent, the water content would decrease by 5.3×10^{-4} kg kg_{ads}^{-1}. Thus, the adsorbent water uptake shows negligible change. As shown in Figure 24d and Figure 24e, two auxiliary K-type thermocouples were attached to the aluminum sheets, adjacent to the adsorbent medium, to eliminate the effects of the thermal resistance of the aluminum sheets as well as the TCR between the hot/cold plates and aluminum sheets.

The HFM was configured to heat the samples from the top to avoid the natural convection [131], [132]. Moreover, natural convection in the packed beds with small voids is negligible [130]. The measured thermal resistance was the total thermal resistance between the isothermal surfaces at temperatures of T_1 and T_2 (see Figure 24a). The associated thermal resistance network of the 4-layer packed bed sorber is illustrated in Figure 24b and the total thermal resistance of n-layer packed bed is as follows:

$$\begin{aligned} R_{\mathrm{tot}} &= L_{\mathrm{bed}}/(k_{\mathrm{tot}}\,A) = 2\,R_{\mathrm{as-p}} + n\,R_{\mathrm{p}} + (n-1)R_{\mathrm{p-p}} \\ &= 2\,R_{\mathrm{as-p}} + R_{\mathrm{bed}} \\ &= \mathrm{TCR} + R_{\mathrm{bed}} \end{aligned} \tag{12}$$

where $R_{\mathrm{as-p}}$ is the thermal contact resistance between the aluminum sheet and particles and $R_{\mathrm{p-p}}$ is the thermal contact resistances between the adsorbent particles. TCR accounts for the total thermal contact resistance of upper and lower aluminum sheets and sorbent particle ($2\,R_{\mathrm{as-p}}$). The maximum measurement uncertainties of thermal conductivity and thermal resistance are 7-8% and 7% respectively (see Appendix C).

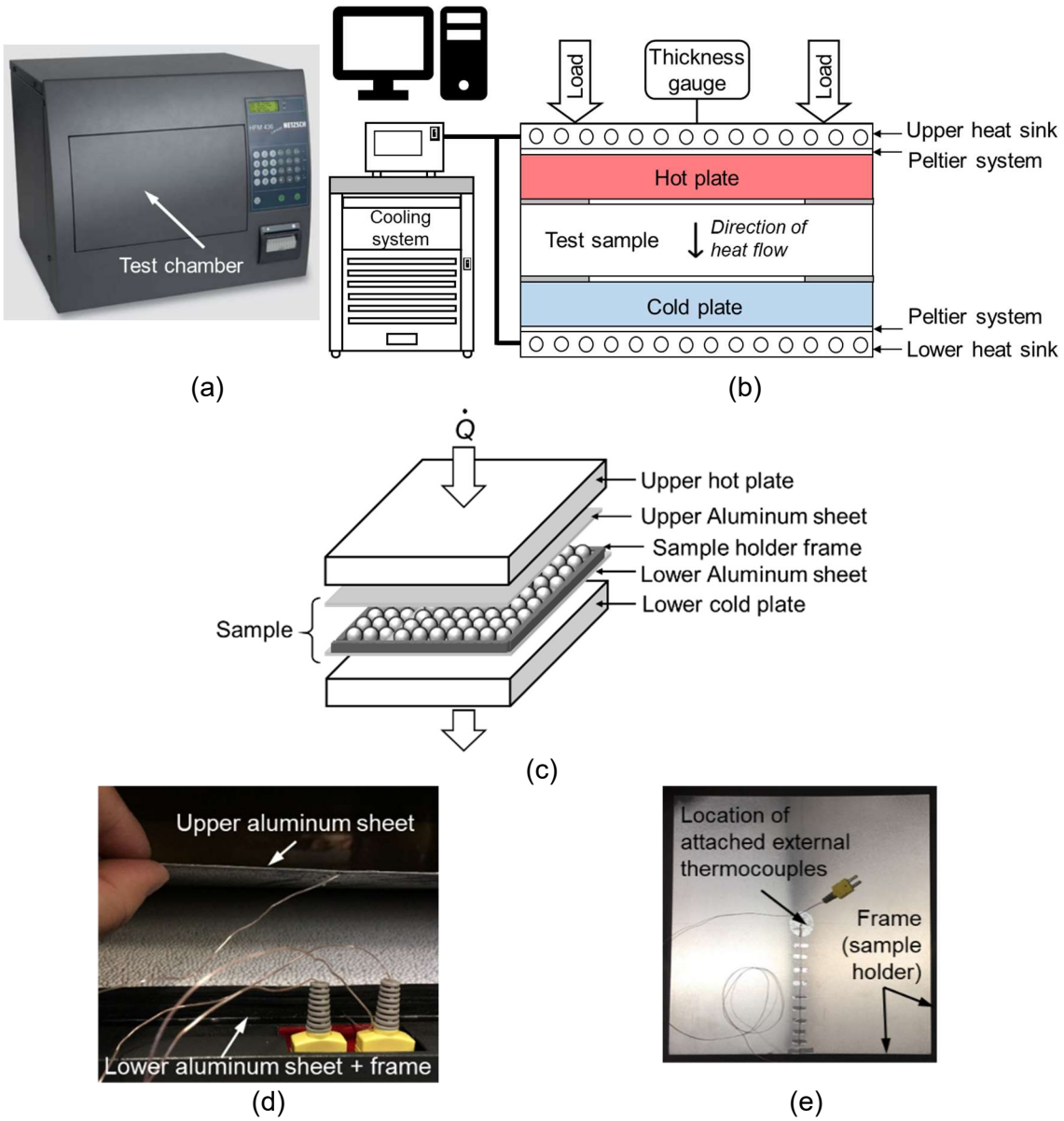

Figure 24. (a) View of instrument and (b) schematic of the NETZSCH HFM 436/3/1 Lambda, (c) schematic of the sorbent particles inside the HFM test chamber, (d) arrangement of sorbents between two aluminum sheets, and (e) attached K-type thermocouples to the inner surface of the lower aluminum sheet, and the frame made of EPDM adhesive-back foam strips used as the sample holder.

Design and optimization of a packed bed sorber require the knowledge of the ETC of the sorbent packed bed medium, which is $k_{\mathrm{eff,bed}} = L_{\mathrm{bed}}/(A\,R_{\mathrm{bed}})$. The bulk thermal resistance of the packed bed medium, R_{bed}, includes the bulk thermal resistance of the sorbent particle, R_{p}, and the contact resistance between the particles, $R_{\mathrm{p-p}}$. Thus, the measured ETC of the packed bed, $k_{\mathrm{eff,bed}}$, is independent of the properties of the HEX surface and can be used for 2-mm FAM-Z02 randomly packed beds in different HEX

designs, but under the same operating conditions. To this end, TCR should be deconvoluted from the measured total resistance, R_{tot}.

By measuring the total thermal resistances for (at least) two different numbers of sorbent layers (i.e. different bed thicknesses), it is possible to deconvolute the TCR from the total resistance. In this method, at each mean temperature, an identical TCR is assumed for different bed thicknesses, due to the similarities in microstructure and bed arrangement. Therefore, the TCR and ETC of packed bed medium are calculated from Eq. (13) for two-thickness method, or for multiple-thickness method [155], and the slope of the line fitted to the R_{tot} versus the bed thickness is $1/\left(k_{\mathrm{eff,bed}}\, A\right)$ and its intercept is TCR.

$$
\begin{aligned}
R_{tot,1} &= TCR + \frac{L_1}{k_{eff,bed}\, A} \\
R_{\mathrm{tot},2} &= \mathrm{TCR} + \frac{L_2}{k_{\mathrm{eff,bed}}\, A} \\
k_{eff,bed} &= \frac{(L_2 - L_1)}{A\left(R_{tot,2} - R_{tot,1}\right)}
\end{aligned}
\tag{13}
$$

4.3. Results and discussion

4.3.1. TCR and its relative importance

$R_{\mathrm{tot}}\, A$ versus the bed thickness (or the number of the sorbent layers) for 2-mm FAM-Z02 packed bed sorber at three temperatures of 25, 60 and 80 °C is plotted in Figure 25a. $R_{\mathrm{tot}}\, A$ decreases with the temperature of the bed, since the sorbent thermal conductivity and the total thermal conductivity of bed increase with a rise in the mean temperature. As illustrated in Figure 25a, $R_{\mathrm{tot}}\, A$ increases with an increase in the number of layers (bed thickness). To provide an accurate value for the bulk thermal conductivity of a packed bed sorber, the effects of the TCR should be deconvoluted from the total thermal resistance of the packed bed, hence, $k_{\mathrm{eff,bed}}$ and TCR are extracted from the slope and intercept of the linear fit to Figure 25a. The relative importance of TCR to the total thermal resistance is shown in Figure 25b, for temperatures varying between 10 to 80 °C and the number of layers of 1, 2, 4, and 6. The contact pressure on the hot and cold plates, P_{contact}, is 0.7 kPa.

TCR forms 67% of k_{tot} for a monolayer of FAM-Z02 at 25 °C and atmospheric pressure, which clearly shows the significant importance of TCR in the packed bed sorbers. As expected, TCR becomes more important for the lower number of layers of sorbent and at lower temperatures. Since monolayer of adsorbent is recommended to achieve higher uptake rate and higher specific cooling power, TCR is a serious issue which should be taken into consideration. TCR decreases by 54%, when temperature increases from 25 to 80 °C. Since porosity in a packed bed of spheres is larger near its boundaries [118], [156], and the filling gas (air) has a higher share of contact area with the aluminum sheets, the increase in the air thermal conductivity has more effect on the thermal contact conductance $(1/\mathrm{TCR})$, compared to its effect on ETC. The other sources of this increase in TCR are unclear, but it could be due to the changes in packed bed configuration and contact points at higher temperatures.

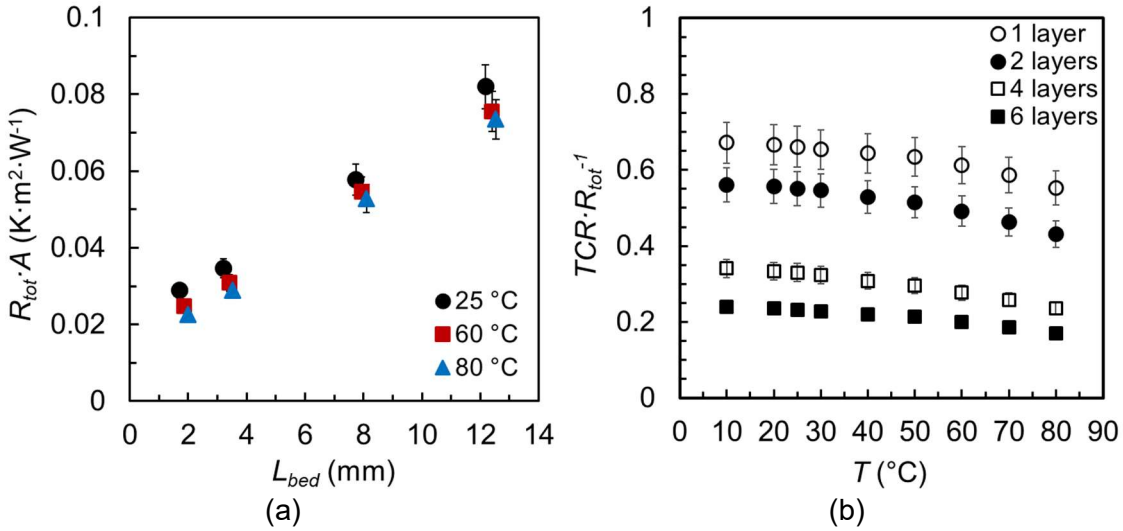

Figure 25. (a) $R_{\mathrm{tot}}\,A$ versus bed thickness of 2-mm FAM-Z02 packed beds for 1, 2, 4, and 6 layers, with water uptake of 0.30 ± 0.02 kg kg_{ads}^{-1}, at temperatures of 25, 60 and 80 °C under contact pressures of 0.7 kPa, and (b) measured values for relative importance of TCR to the total thermal resistance at temperatures of 10 to 80 °C.

4.3.2. Model validation

The comparison between the experimental values and the present model for ETC is shown in Figure 26a, for a 2-mm FAM-Z02 randomly packed bed. The black dashed line represents the results of the present model, where the air thermal conductivity is approximated as the thermal conductivity of dry air, and the blue solid line shows the results from the model, where the effect of RH changes on the air thermal conductivity is also considered by applying the mole-fraction-weighted mixing rule for thermal

conductivity of humid air, as shown in Appendix B. As shown in Figure 26a, the present model can predict $k_{\mathrm{eff,bed}}$ accurately and the agreement between the experimental data and the results from the present model has been improved by considering the effect of the RH changes, from 25% (at 10 °C) to 80% (at 80 °C), on the air thermal conductivity for constant water uptake of 0.30±0.02 kg kg_{ads}^{-1}. For temperatures above 60 °C and RH values above 50%, an increase in RH decreases the thermal conductivity of humid air (see the relationship for k_{ha} in Appendix B). This decrease in the air thermal conductivity marginally decreases the ETC compared to the case where the changes in RH are not considered. The maximum relative difference between the results from the model without consideration of RH changes and the experimental data is 3% at 80 °C, while the maximum relative difference between the results from the model with consideration of RH changes and the experimental data is 2% at 80 °C. ETC of the packed bed adsorber varies between 0.188 and 0.204 $Wm^{-1}K^{-1}$. Total thermal conductivities of the packed beds of 4-layer and 6-layer of 2-mm FAM-Z02 are shown in Figure 26b. The theoretical model can properly predict the total thermal conductivity, which includes the thermal contact conductance as well. The maximum difference between the experimental data and the results from the theoretical model is 8% and lies within the uncertainty of the measurements.

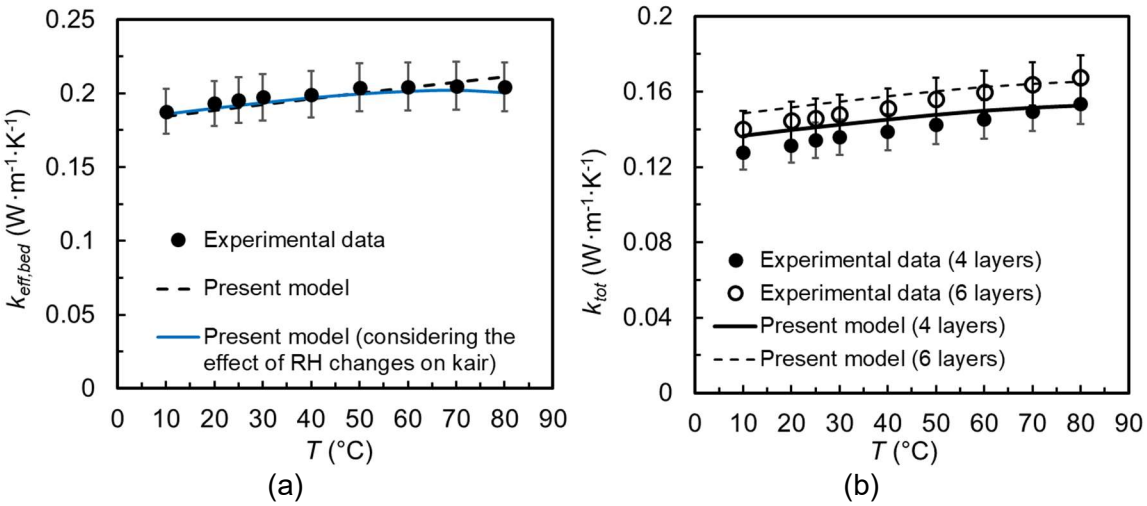

Figure 26. (a) Effective thermal conductivity and (b) total thermal conductivity of 4- and 6-layer packed bed versus temperature for 2-mm FAM-Z02 randomly packed bed with the water uptake of 0.30 ± 0.02 kg kg_{ads}^{-1}, at the atmospheric condition and under contact pressure of 0.7 kPa.

4.3.3. Parametric study

A parametric study is carried out under both adsorption (T=25°C, ω=0.32, and RH=55%) and desorption conditions (T=90°C, ω=0.06, and RH=6%), to study the effect of the input parameters of the model on ETC. The parameters examined are roughness (σ), bed solid fraction (ψ_{bed}), Young's modulus (E_{p}), sorbent porosity (ε), contact pressure (P_{contact}), sorbent particle diameter (d_{p}), thermal accommodation coefficient (α_T), and sorbent thermal conductivity (k_{s}), as shown in Figure 27. Effects of temperature, gas pressure, and equilibrium water uptake on ETC are described in the next sections in more details since these parameters are related to each other through adsorption isotherms. As shown in Figure 27, the key influential parameters on ETC are k_{s} and d_{p} for the considered ranges. It is observed that the increase of ETC with d_{p} is higher for closed systems, since macro-gap resistance (R_{G}) is highly dependent on d_{p} and the value of R_{G} is much higher for the closed system compared to the open system, as illustrated in Figure 32. In contrast, the positive effect of increasing k_{s} on ETC is more dominant in the open systems.

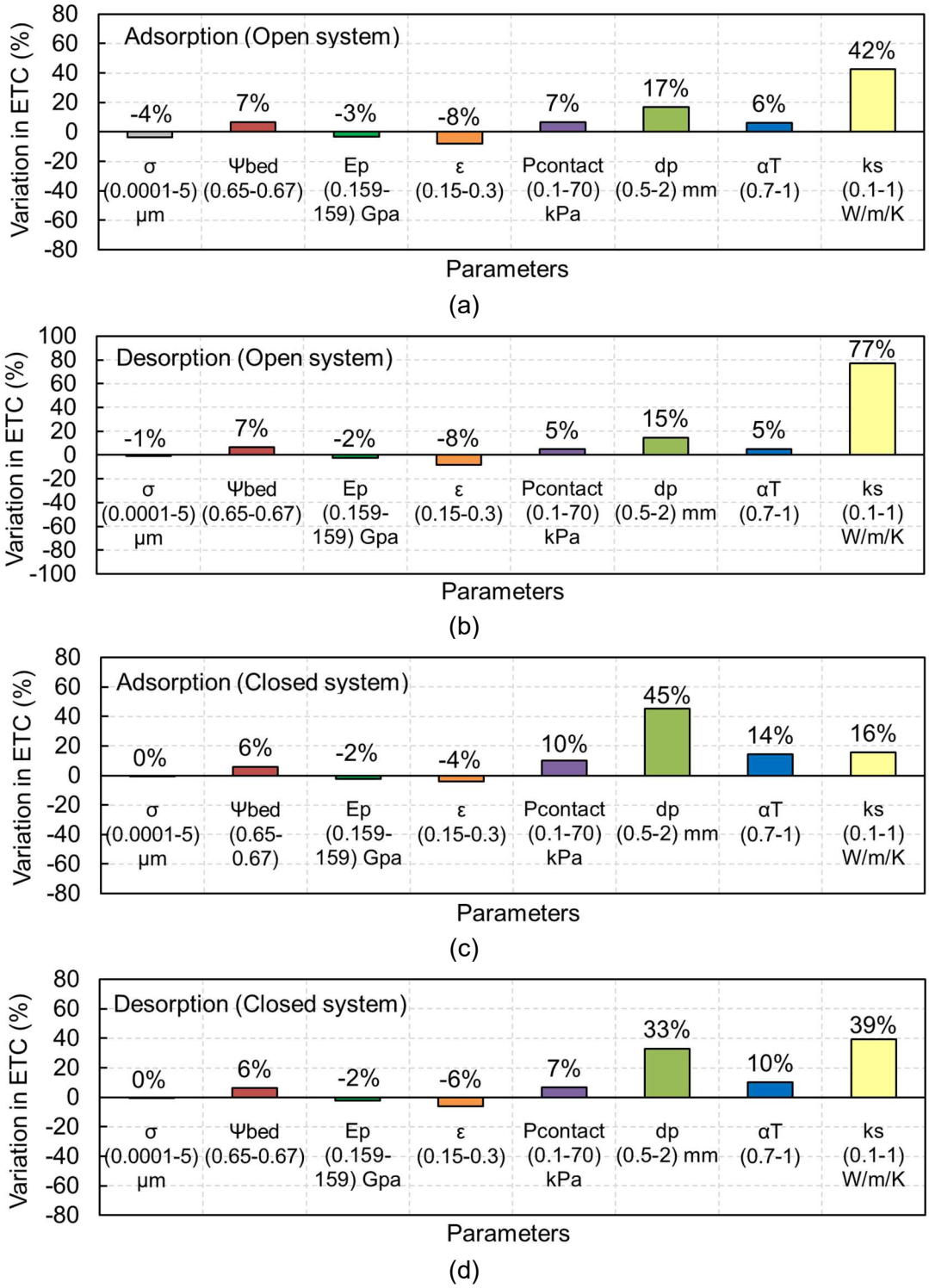

Figure 27. Parametric study of sorption system under (a) sorption (T=25°C, ω=0.32, and RH=55%) and (b) desorption (T=90°C, ω=0.06, and RH=6%) for the following ranges: $\sigma = (0.001, 5)$ μm, $\psi_{\mathrm{bed}} = (0.65, 0.67)$, $E_{\mathrm{p}} = (0.159, 159)$ GPa, $\varepsilon_{\mathrm{p}} = (0.15, 0.3)$, $P_{\mathrm{c}} = (0.1, 70)$ kPa, $d_{\mathrm{p}} = (0.5, 2)$ mm, $\alpha_T = (0.7, 1)$, and $k_{\mathrm{s}} = (0.1, 1)$ $\mathrm{Wm^{-1}K^{-1}}$.

4.3.4. ETC chart for closed-system packed bed sorbers

The dependencies of the ETC on the water uptake, vapor pressure, and mean temperature of SC-arranged and randomly packed beds ($\psi_{\mathrm{bed}} = 0.6$) are shown in Figure 28 for 0.5 mm FAM-Z02, and Figure 29 for 2 mm FAM-Z02. To consider the real effects of water uptake, pressure and temperature on the ETC in closed sorption systems, the water uptake is calculated at each temperature and pressure ratio from the equilibrium uptake isotherms of FAM-Z02, presented by Goldsworthy [135]. Afterwards, using the present model, the ETC is obtained based on the pressure, temperature and water uptake, forming the isobars and isotherms in Figure 28 and Figure 29. ETCs are reported for the temperatures of 10 to 90 °C, pressures of 873 (saturation pressure at 5 °C) and 19,947 Pa (saturation pressure at 60 °C), and water uptakes of 0.03 to 0.33 kg kg_{ads}^{-1}. As shown in Figure 28 and Figure 29, at a fixed gas pressure, ETC does not significantly change with the changes in temperature and water uptake. At constant pressure, an increase in temperature leads to a decrease in the equilibrium water uptake. Temperature rise increases the ETC, while water uptake drop decreases the ETC. The tradeoff between these two effects results in an almost constant ETC. However, at a fixed temperature, equilibrium water uptake increases with an increase in gas pressure and both increases positively affect the ETC. At 90 °C, by increasing the gas pressure from 872 Pa ($\omega_{\mathrm{eq}} = 0.03$ kg kg_{ads}^{-1}) to 19,947 Pa ($\omega_{\mathrm{eq}} = 0.26$ kg kg_{ads}^{-1}), ETC increases from 0.032 to 0.093 W m^{-1} K^{-1} for 0.5 mm, and from 0.055 to 0.119 W m^{-1} K^{-1} for 2 mm randomly packed beds. It can be concluded that ETC is a stronger function of vapor pressure than the temperature in closed systems, for the studied temperature and pressure ranges. Higher thermal conductivities have been predicted for randomly packed beds compared to the SC-arranged beds, due to the lower bed porosity of randomly packed beds, which makes thermal conductivity of adsorbent particle to take higher part in the ETC; thermal conductivity of the adsorbent, i.e. 0.117 W m^{-1} K^{-1} (at 30 °C) and 0.128 W m^{-1} K^{-1} (at 90 °C) [20], is higher than that of the water vapor, i.e. 0.017 W m^{-1} K^{-1} (at 873 Pa) to 0.021 W m^{-1} K^{-1} (at 19947 Pa) [157].

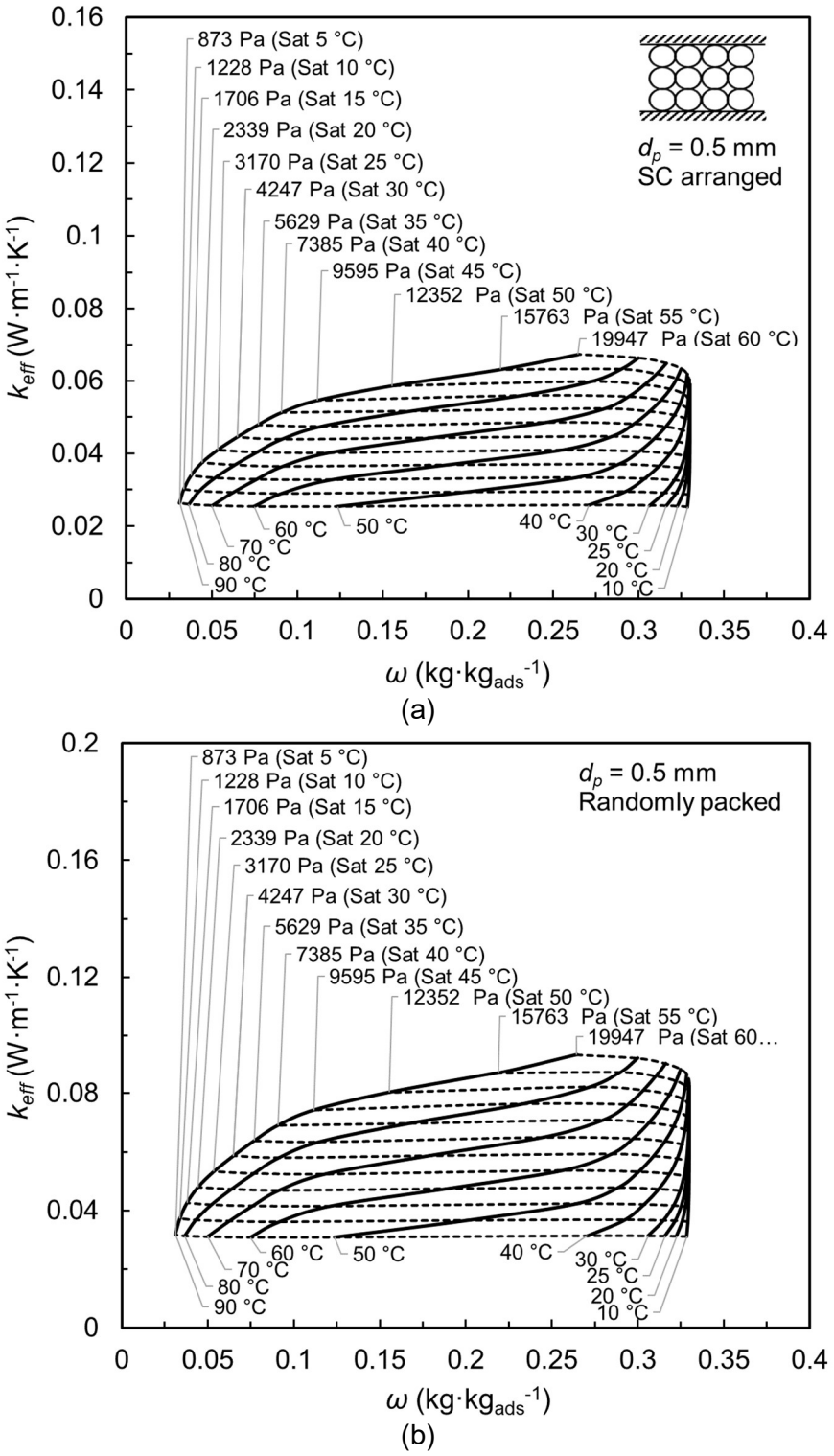

Figure 28. Effective thermal conductivity of closed-system FAM-Z02 packed bed sorber versus water uptake, including the isotherm and isobar lines for (a) SC-arranged bed, and (b) randomly packed bed with 0.5 mm sorbent particles.

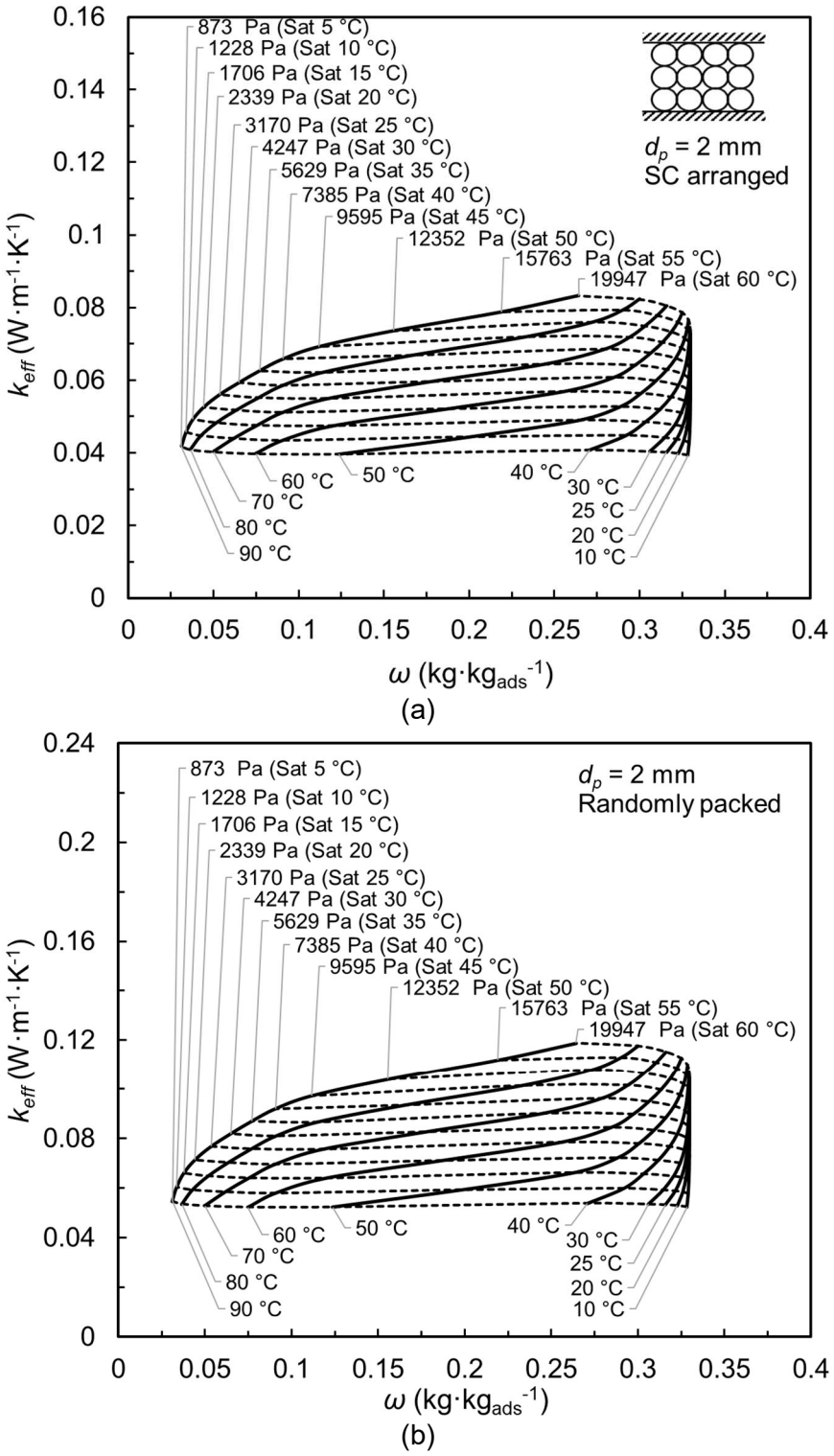

Figure 29. Effective thermal conductivity of closed-system FAM-Z02 packed bed sorber versus water uptake, including the isotherm and isobar lines for (a) SC-arranged bed, and (b) randomly packed bed with 2 mm sorbent particles.

4.3.5. ETC chart for open-system packed bed sorbers

Changes in ETC due to the water uptake, relative humidity and mean temperature in the open-system SC-arranged and randomly packed bed sorbers are shown in Figure 30 for 0.5 mm FAM-Z02 particles, and Figure 31 for 2 mm FAM-Z02. Considering the equilibrium uptake of FAM-Z02, the iso-relative humidity lines and isotherms and their corresponding water uptake and ETC are shown in these figures. ETCs are reported for temperatures of 10 to 90 °C, RH of 5 to 40%, and water uptake of 0.06 to 0.33 kg kg_{ads}^{-1}. ETCs in the open-systems are higher compared to the ETCs of the closed-systems, due to the higher pressure of the filling gas, which leads to lower micro-gap and macro-gap resistances (see Eqs. (55) and (56) in Appendix A) and higher thermal conductivity of air compared to water vapor; at adsorbent temperature of 30 °C and water uptake of 0.32 kg kg_{ads}^{-1} (i.e. water vapor temperature of 15 °C in closed-systems, and RH of 40 % in open-systems), ETC of 2 mm FAM-Z02 open-system randomly packed bed is 0.149 $Wm^{-1}K^{-1}$, while that of a closed-system is 0.065 $Wm^{-1}K^{-1}$, and ETC of 0.5 mm FAM-Z02 randomly packed bed in an open-system is 0.126 $Wm^{-1}K^{-1}$, while that of a closed-system is 0.042 $Wm^{-1}K^{-1}$.

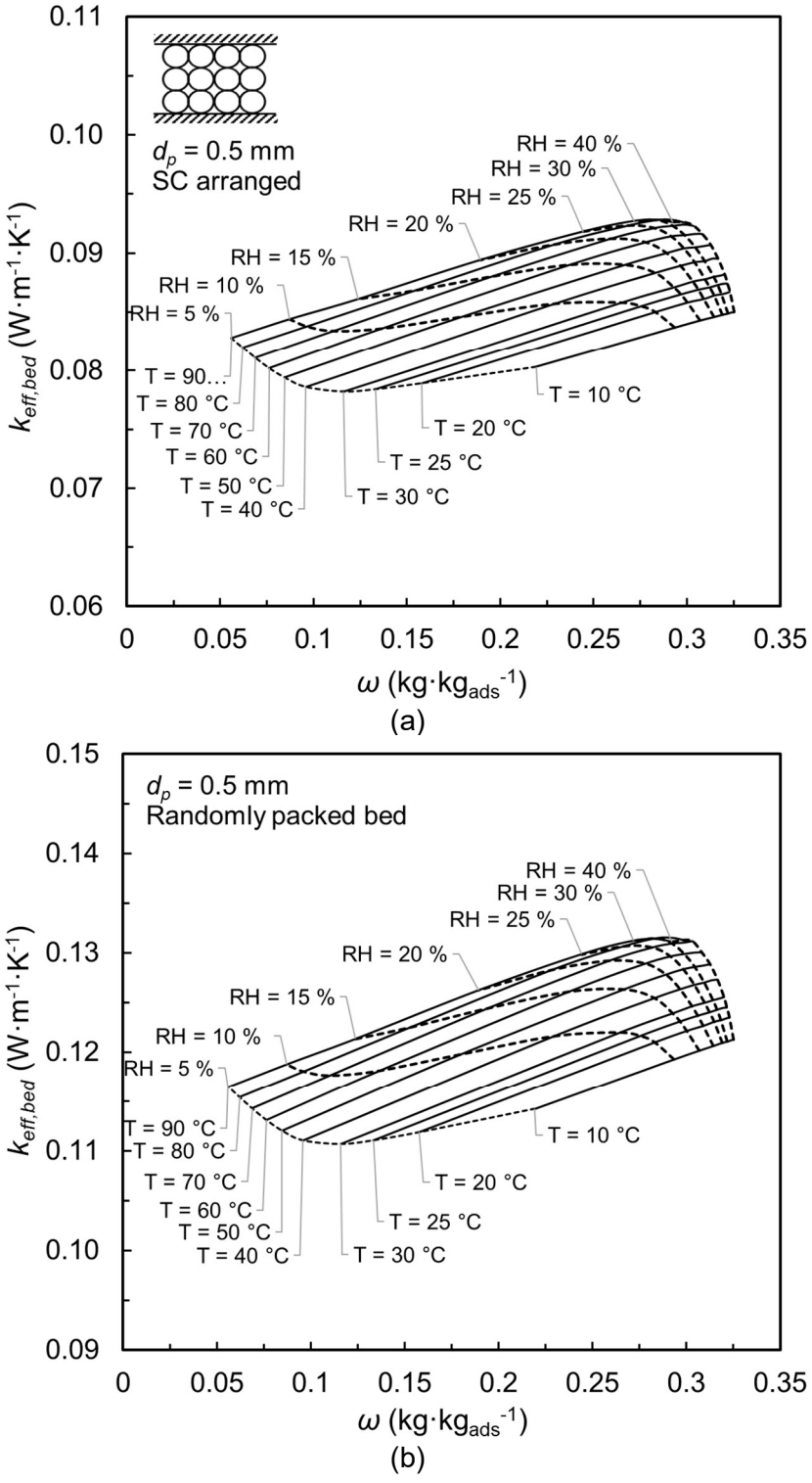

Figure 30. Effective thermal conductivity of open-system FAM-Z02 packed bed sorbers versus water uptake, including the isotherm and isobar lines for (a) SC arranged, and (b) randomly packed bed with 0.5 mm sorbent particles.

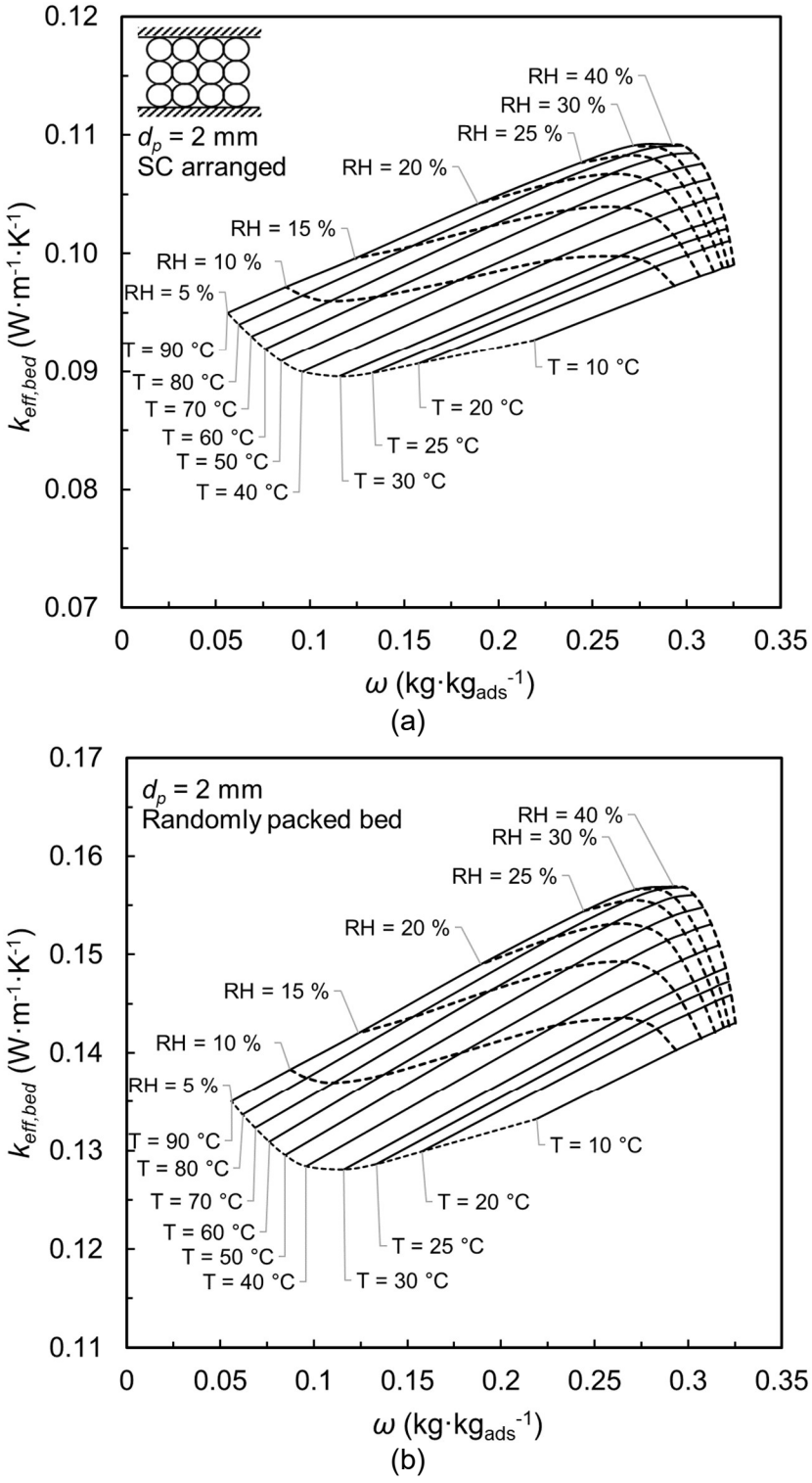

Figure 31. Effective thermal conductivity of open-system FAM-Z02 packed bed sorbers versus water uptake, including the isotherm and isobar lines for (a) SC arranged, and (b) randomly packed bed with 2 mm sorbent particles.

4.3.6. ETC: open-system versus closed-system packed bed sorbers

ETCs of open and closed-system packed bed sorbers of 2 mm FAM-Z02 at equilibrium water uptake of 0.32 kg kg_{ads}^{-1}, are shown in Figure 32a. According to the water uptake isotherms [135], the relative humidity changes from 25% to 80% for temperatures of 10 to 80 °C. As shown in Figure 32a, ETC of open-system is 3.3 times as high as ETC of the closed-system (0.099 compared to 0.030 W m^{-1} K^{-1}) at 10 °C, and 1.2 times as high as that of the closed system (0.107 compared to 0.090 W m^{-1} K^{-1}) at 80 °C. Although the water uptake is kept the same for both open and closed-systems, the gas pressure in closed-system is much lower and varies from 331 Pa (at 10 °C) to 37,612 Pa (at 80 °C). The ratio of macro-gap resistances of the open-system to that of the closed-system, in Figure 32b, shows that the low gas pressure in the closed system leads to relatively high macro-gap resistances, especially at lower temperatures (i.e. lower gas pressures). The $R_{\mathrm{G,open}}/R_{\mathrm{G,closed}}$ is 0.23 at 10 °C (331 Pa) and 0.79 at 80 °C (37,612 Pa).

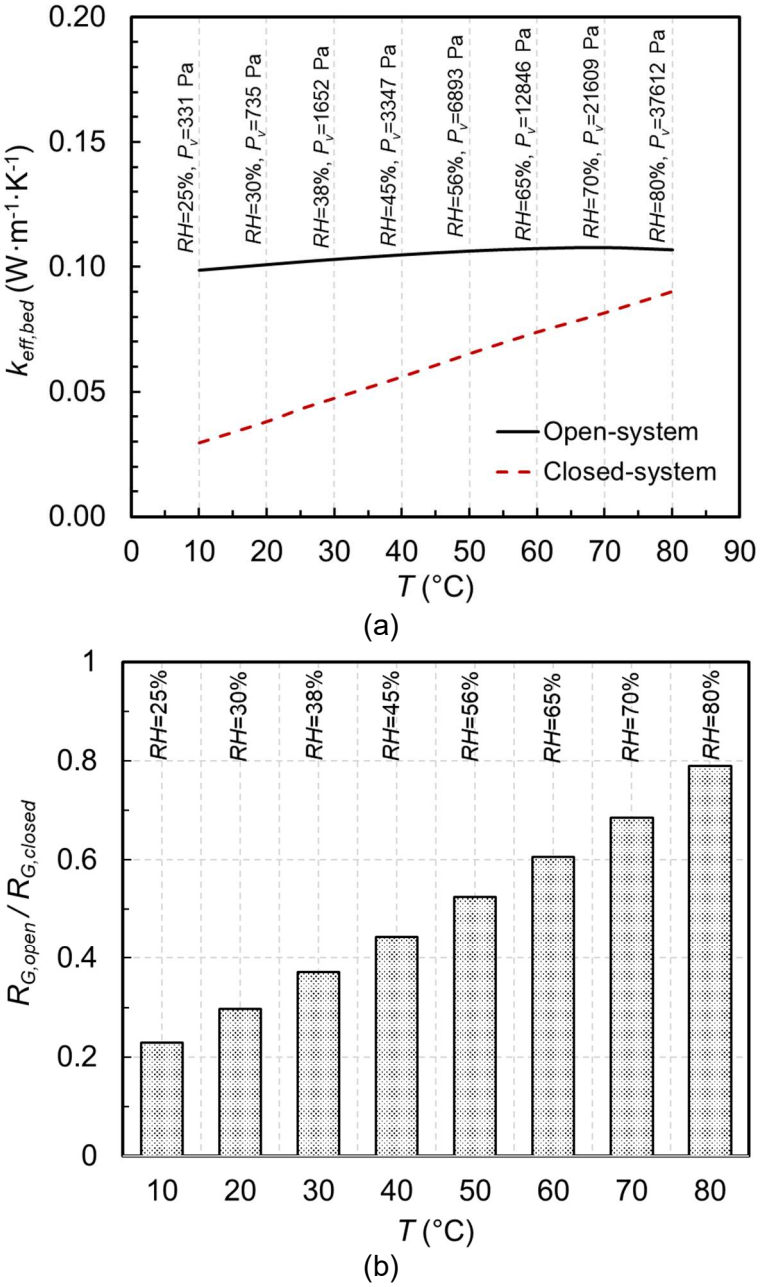

Figure 32. (a) Effective thermal conductivity of SG-arranged packed bed sorber of 2 mm FAM-Z02 versus temperature, for open and closed-systems, at equilibrium water uptake of 0.32 kg kg_{ads}^{-1} and (b) the ratio of the macro-gap resistances of open-system to that of the closed-system.

4.3.7. Effect of contact pressure on the ETC and TCR

ETC and TCR*A* versus the contact pressure are shown in Figure 33a, at 30 °C and water uptake of 0.32 kg kg_{ads}^{-1} for various particle diameters. Increasing the contact pressure leads to better interparticle contacts in the packed bed and, therefore, an

increase in ETC (see Figure 33a). In contrast to ETC, TCR *A* decreases with an increase in the contact pressure, as shown in Figure 33b. For d_p of 0.25 mm ($d_p/L_{bed} = 0.02$), the decrease in TCR *A* due to the increase in contact pressure from 0.7 to 1,000 kPa is 37%, from 0.006 to 0.004 Km^2W^{-1}, while this decrease for d_p of 2 mm ($d_p/L_{bed} = 0.17$) is 31%, from 0.026 to 0.018 Km^2W^{-1}.

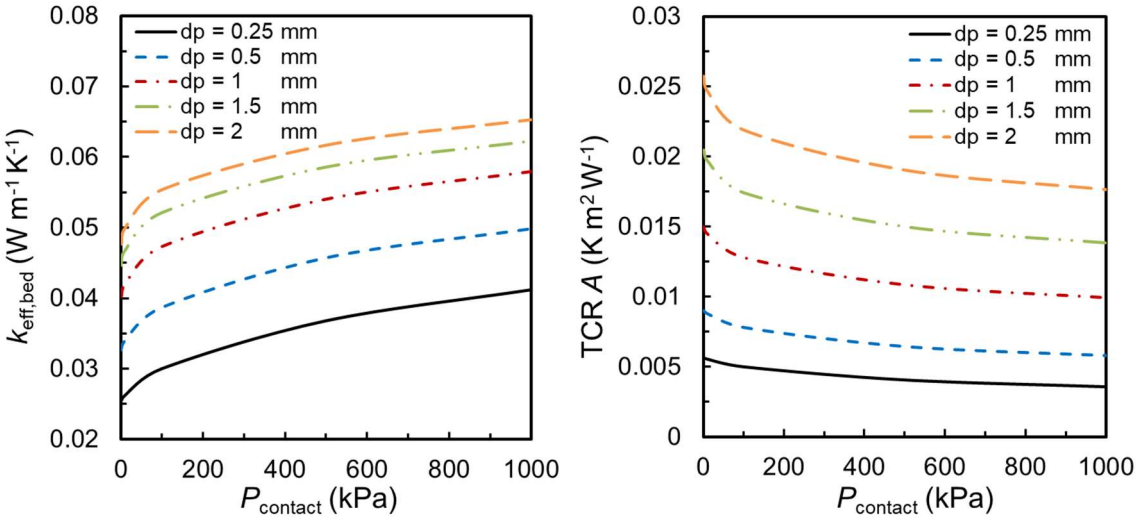

Figure 33. (a) ETC and (b) TCR *A* of a closed-system SC-arranged packed bed sorber vs contact pressure for various particle diameters, at 30 °C and 1706 Pa (ω_{eq}=0.32 kg kg_{ads}^{-1}). L_{bed} is fixed at 12 mm.

4.3.8. Effect of particle size on the ETC and total thermal conductivity

As shown in Figure 33b, TCR increases with an increase in d_p due to the less contact points with the metal surface of heat exchanger. For d_p of 0.5 mm ($d_p/L_{bed} = 0.04$) and under contact pressure of 100 kPa, TCR A is 0.008 K m^2 W^{-1} and TCR/R_{tot} is 0.023, and for d_p of 2 mm ($d_p/L_{bed} = 0.17$), TCR A is 0.022 K m^2 W^{-1} and TCR/R_{tot} is 0.086. However, as shown in Figure 33a, ETC of a packed bed of 0.5 mm FAM-Z02 is 0.039 W m^{-1} K^{-1} and ETC of a packed bed of 2 mm FAM-Z02 is 0.055 W m^{-1} K^{-1}, at 30 °C and under gas pressure of 1706 Pa and contact pressure of 100 kPa.

Total thermal conductivities of an open-system FAM-Z02 SC-arranged packed bed versus the relative particle size, d_p/L_{bed}, for bed thicknesses of 0.6 (A/m_{ads} = 4.90 m^2 kg^{-1}) to 48 mm (A/m_{ads} = 0.06 m^2 kg^{-1}) are shown in Figure 34. For a constant bed thickness, k_{tot} of the packed beds with smaller d_p/L_{bed} (i.e. more number of particle layers) is close

to the ETC of the packed bed, and both ETC and k_{tot} increase with particle size. For higher $d_{\mathrm{p}}/L_{\mathrm{bed}}$ (i.e. less number of particle layers), the thermal contact conductance plays a more important role in the k_{tot} and decreases with an increase in the particle size, since the number of contact points decreases with particle size. Hence, optimum particle size is observed for each bed thickness, which provides the highest k_{tot}. As raised by N'Tsoukpoe et al. [37], predicting the optimum heat flow and mass flow path length for a certain bed volume is immensely beneficial for the design and optimization of a packed bed sorber. The presented model, which takes into account the TCR as well as the ETC for large-scale packed bed sorbers, provides a reliable tool to predict the optimum heat flow path size (i.e. the optimum particle size) for a certain packed bed storage volume, in open and closed ATES systems.

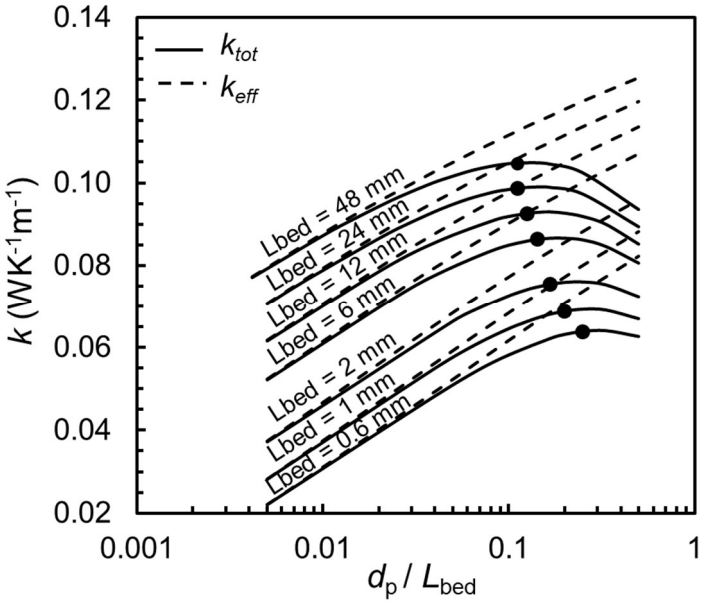

Figure 34. Total thermal conductivity of an open-system FAM-Z02 SC-arranged packed bed sorber vs $d_{\mathrm{p}}/L_{\mathrm{bed}}$, at 30 °C and ω_{eq} = 0.32 kg kg_{ads}^{-1}.

4.3.9. Effect of gas pressure on the ETC

As shown in Figure 35, ETC of a dry and wet closed-system SC-arranged FAM-Z02 packed bed increases with an increase in the gas pressure. Increasing the gas pressure leads to a decrease in the mean free path of the interstitial gas (see Eq. (74) in Appendix A) and, therefore, an increase in the ETC. Moreover, for wet packed beds, the equilibrium uptake is higher at higher gas pressures, which also leads to an increase in ETC. In a wet FAM-Z02 packed bed, by decreasing the gas pressure from 4247 (P_{sat} at

30 °C) to 1706 (P_{sat} at 15 °C) Pa, ETC decreases by 23%, from 0.043 to 0.033 W m^{-1} K^{-1}, for particle size of 0.5 mm, and by 16%, from 0.057 to 0.048 W m^{-1} K^{-1}, for particle size of 0.5 mm. For particle diameter of 0.5 mm, ETC of an open-system packed bed under RH of 40% is 0.079 W m^{-1} K^{-1}, while that of a closed system is 0.031 W m^{-1} K^{-1} at the vapour pressure of 1706 Pa, and 0.040 W m^{-1} K^{-1} at the vapour pressure of 4247 Pa.

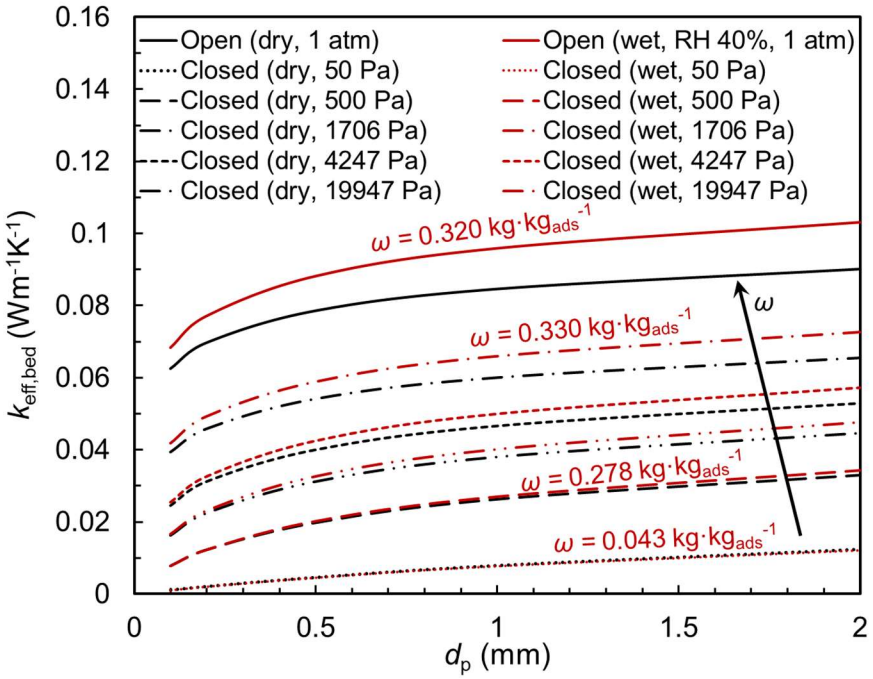

Figure 35. ETC of dry and wet open and closed-systems SC-arranged packed bed sorber vs particle diameter for various gas pressures at sorbent temperature of 30 °C.

4.4. Summary of results

The relative importance of TCR to the total thermal resistance (TCR/R_{tot}) of the monolayer FAM-Z02 packed bed, was 67% at 25 °C. ETC of the randomly packed FAM-Z02 packed bed was 0.1878-0.2043 W m^{-1} K^{-1} for temperatures between 10 to 80 °C. ETC of uniformly-sized packed bed sorber of FAM-Z02 was modeled as a function of water uptake, the number of adsorbent layers, particle size, bed porosity, temperature, contact pressure, and interstitial gas pressure for SC, FCC; which was extended to randomly packed beds. The model was validated with the experimental results, collected by heat flow meter measurements, with a maximum relative difference of 2% for ETC and 8% for total thermal conductivity. The ETC of a randomly packed bed of 2 mm FAM-Z02 was between 0.188 (at 10 °C) and 0.204 W m^{-1} K^{-1} (at 80 °C). The comparison between the

ETC of open-system and closed-system packed bed sorbers showed that ETC of 2 mm FAM-Z02 SC-arranged open-system was 2.2 times higher than the ETC of the closed-system at 30 °C and 0.32 kg kg_{ads}^{-1} (0.1031 compared to 0.0474 W m^{-1} K^{-1}). For realistic analysis of the heat transfer inside the packed bed sorbers, the ETC charts were presented for open and closed-systems, based on the equilibrium water uptake isotherms. It was shown that the model could predict an optimum particle size that corresponded to the highest total thermal conductivity for a certain bed thickness, which should be considered, along with the optimum mass flow path size, for the design and optimization of packed bed sorbers.

Chapter 5.

Sorption dynamics of an S-TES system for heat and cold storage

Alongside the study of heat transfer in the sorber bed, presented in Chapter 4, investigation of the sorption dynamic characteristics, namely, the sorption rate coefficient (k_{ads}), sorption characteristic time (τ_{ads}), and sorption power, are of primary importance. In this chapter, the dynamic characteristics of a full-scale sorber bed are presented.[3]

5.1. Background

Aside from the low thermal conductivity of sorbent materials (elaborated in Chapter 4), low mass diffusivity of sorption working pairs, 10^{-14}-10^{-8} m^2 s^{-1} [158], results in overall low storage performance. In most available studies on the S-TES, the storage performance capacity is evaluated based on ESD and thermal efficiency (η_{th}), which reflect the maximum uptake capacity of the system, compactness, and heat loss. Nevertheless, charge/discharge thermal power of an S-TES system also plays a key role in thermal management systems, particularly for peak load shifting and shaving temperature fluctuations. In an S-TES system, the desorption/sorption dynamics should be fast enough to meet the target charge/discharge period. High ESD and high thermal power are desirable features of S-TES systems, which depend on the sorption kinetics as well as uptake equilibria [31], [83]. An S-TES system with high equilibrium uptake capacity but slow kinetics cannot provide the required thermal power, while a fast S-TES system with small sorption capacity leads to a low ESD since more sorbent may be needed to deliver the target thermal energy. Mass transfer in closed sorption systems is even more crucial than that of the atmospheric (open) sorption systems [37].

Introductions to adsorption isotherm equations and adsorption kinetic measurement methods are presented in Appendix D. As listed in Table 12, most of the available kinetics studies on the FAM-Z02 are conducted in small-scale, using large temperature jump (LTJ) or gravimetric LTJ (GLTJ) methods (see Appendix D). A few

[3] The results of this chapter were presented in Innovative Materials for Processes in Energy Systems (IMPRES 2016) [197].

studies are available in the literature focusing on the sorption dynamic assessment of the full-scale closed sorption systems [42], [158]. Dawoud [42] presented a comparison between the sorption kinetics of a small amount of coated FAM-Z02, using an LTJ method, and a full-scale one-bed coated FAM-Z02 adsorption cooling system. However, for the full-scale kinetic measurement, the net water uptake was estimated based on the cooling load of the evaporator and not a mass measurement [42]. Sharafian et al. [158] performed an in-situ mass measurement of two different finned-tube heat exchangers filled with FAM-Z02 pellets.

In this chapter, a real-time in-situ temperature and mass measurements of a full-size sorber bed (~25 kg: 0.7 kg adsorbent, 2.87 kg heat exchanger and ~ 21.4 kg vacuum chamber and the adsorbed water) with 0.3 mm coated FAM-Z02 sorber bed is presented.

Table 12. Small-scale and full-scale studies on the adsorption kinetic and of FAM-Z02/water in the literature

	Ref.	Method of study	Operating condition ($T_{des}/T_{ads}/T_{cond}/T_{evap}$) °C	Adsorbent configuration	Dry sorbent mass g	Characteristic time (τ) s	Max uptake $\Delta\omega=\omega_\infty-\omega_0$ $kgkg_{ads}^{-1}$	Remarks
Small-scale uptake measurement	Girnik et al. (2016) [149]	LTJ	1) 90/30/30/10 2) 90/35/35/7 3) 90/28/28/15	2, 4, 8 layers of loose grain (0.2-0.9 mm)	0.314 ±0.004		1) 0.22 2) 0.19 3) 0.23	Study the effect of number of layers of adsorbent particles on a flat metal plate
	Glaznev et al. (2010) [23]	LTJ	60/35/10/10	Loose grain (0.8-0.9 mm)	-	>> 600	> 0.12	Study of the effect of residual gas on water uptake for ACS
	Santamaria et al. (2014) [93]	G-LTJ	90/30/30/10	Loose grain (0.15-1.18 mm)	80 (FAM-Z02) + 150 (HEX and net)	τ_{ads}: 114 ± 5 τ_{des}: 76 ± 3	0.21-0.22	Study of the effect of HEX geometry, grain size, and HTF flowrate on kinetics, using a piece of a full-scale finned flat-tube HEX
	Dawoud (2007) [92]	LTJ	90/35/35/5	Mono-layer of loose grain (0.7-2.6 mm)	0.150	$\tau_{0.5,ads}$ = 235, $\tau_{0.5,des}$=186 (for 1.4-1.6 mm)	0.164 (ads), 0.192 (des)	Desorption was 34% faster than sorption. Inter-crystalline diffusion is dominant in sorption kinetics and surface resistance to the heat and mass transfer is dominant in desorption.
	Dawoud (2013) [42]	LTJ	90/35/35/5	Coated	0.200	$\tau_{0.5,ads}$ =108 (for 0.3 mm thickness)	$\Delta\omega_\infty$ = 0.17	0.5 mm is the maximum limit for coating thickness.
	Sapienza et al. (2014) [159]	G-LTJ	90/35/30/10	Mono-layer and multi-layer of loose grain (0.350-2.5 mm)	4.49-33.13	For 1.00–1.18 mm grains: 1) monolayer: τ_{ads} = 189 2) two layers: τ_{des} = 282	1) monolayer: 0.24[a] 2) two layers: 0.21[a]	Introducing the G-LTJ method, a modification for LTJ method.
Large-scale uptake measurement	Dawoud (2013) [42]	Estimated from the cooling load	90/35/35/ 5	Coated (0.15-0.5 mm)	1500-2530	-	For τ_{ads} = 600 s: $0.573 \times \Delta\omega_{max,LTJ}$ For τ_{ads} = 300 s: $0.527 \times \Delta\omega_{max,LTJ}$ * $\Delta\omega_{max,LTJ}$ = 0.17	Comparison of adsorption kinetics in small scale (best case design) with that of the large scale.
	Sharafian et al. (2016) [158]	Full-scale	90/ 30/ 20/ 20	Loose grain (2 mm)	1500	-	0.28	Study of the effects of different adsorber bed designs.

[a] calculated based on $\mathrm{SCP}_{max} = (\Delta\omega_{max}\,\Delta h_{fg})/\tau$ [159].

5.2. Experimental study

A custom-built S-TES testbed was designed and used to study the desorption (charging) and sorption (discharging) dynamics, schematically shown in Figure 36a. A real-time mass measurement was performed by placing the sorber bed of the S-TES on a scale (Setra Supper II) with an accuracy of ±1 g. An engine oil cooler, manufactured by

Hayden Automotive (model #1268), was chosen as the sorber bed, which was coated with FAM-Z02 (0.2 mm coating layer fabricated by Mitsubishi Plastics Inc.) and placed in a custom-built vacuum chamber. Details of the sorber bed are listed in Table 13. Two temperature control systems (Julabo, model #Presto LH50) with 30 °C cooling fluid (TCS_{cf}) and 90 °C heating fluid (TCS_{hf}) were connected to the sorber bed for cooling down and heating up the adsorber bed during adsorption and desorption processes, respectively. Silicone oil (Julabo Inc., Thermal P60) was used as the HTF circulating in the two temperature control systems.

A vacuum chamber including a custom-built HEX with inclined circumferential micro-groove enhanced tubes [160] was connected to the sorber bed, using a vacuum rated flexible hose. This HEX served as both evaporator and condenser, depending on the temperature of the sorber bed, which was imposed by the temperature control systems. The inlet temperature of the evaporator/condenser unit, hereafter called ECU, was maintained constant by another temperature control system (TCS_{EC}) at 20 °C, for both condensation and evaporation. A control valve was located between the sorber bed and the ECU, which was aimed to isolate the sorber bed from the ECU in the heat storage period. The ECU heat transfer coefficient was large enough (U=1540 W $m^2 K^{-1}$ at 20 °C) to ensure that the water vapor generation was not a limiting factor in the system. For cyclic ad-/desorption (with no storage period), the valve was kept open. To reduce the experimental error of mass measurement, a relay switch was controlled automatically, using an in-house LabVIEW program, to switch the connection of the sorber bed to TCS_{cf} and TCS_{hf}; by this switching, the sorber bed was led to an adsorption or desorption process, automatically.

T-type thermocouples (Omega, model #5SRTC-TT-T-36-36) with an accuracy of 0.75% of reading in degree Celsius and two pressure transducers (Omega, model #PX309-005AI) with 0–34.5 kPa absolute pressure range and ±0.4 kPa accuracy were used to measure temperature and pressure of the sorber bed and ECU. Two positive displacement flow meters (FLOMEC, model #OM015S001-222) with an accuracy of 0.5% of reading in $Lmin^{-1}$, were used to measure the flow rates of sorber bed heating/cooling fluid (silicone oil) and ECU chilled/coolant water. To dry the adsorbent in the preparation step, the sorber bed was heated up to 100 °C and outgassed, being connected to a vacuum pump for 8-12 hours.

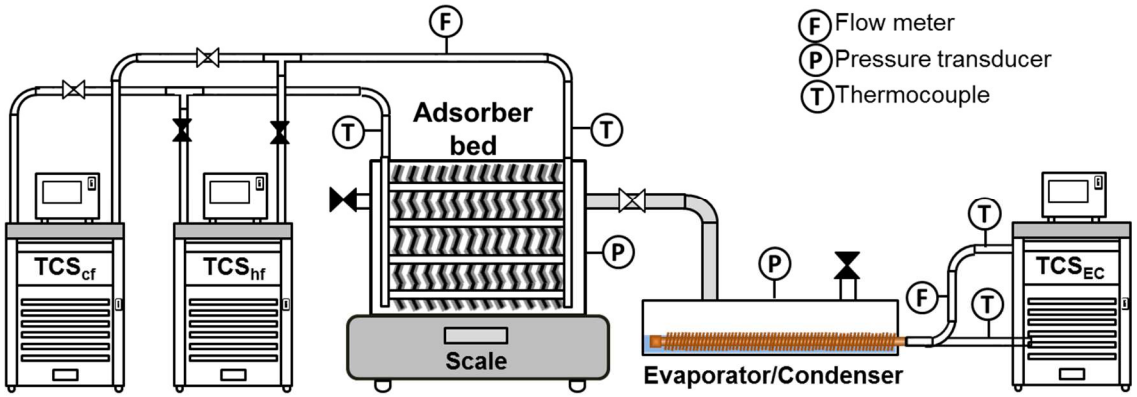

(a)

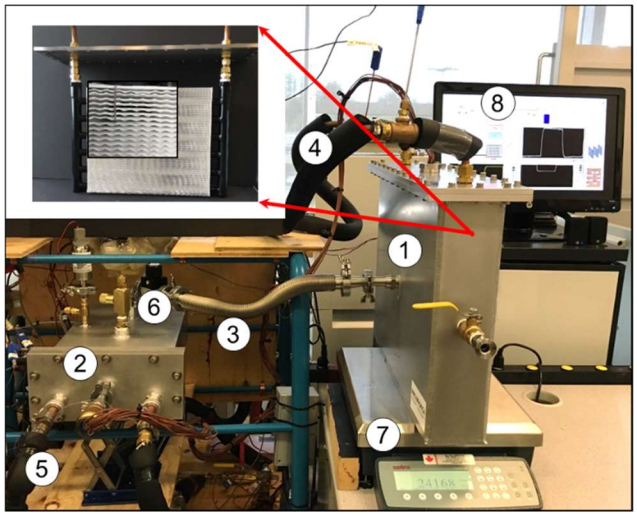

(b)

Figure 36. (a) schematic of the in-situ mass measurement testbed of an S-TES and (b) custom-built testbed, including: 1) sorber bed, 2) evaporator/condenser, 3) flexible hose, 4) HTF ports, 5) chilled/coolant water ports, 6) isolating control valve, 7) scale, and 8) LabVIEW program and data acquisition (DAQ) unit. Temperatures of the sorber bed and evaporator/condenser were maintained constant with three temperature control systems (TCS_{hf}, TCS_{cf} and TCS_{ECU}).

Table 13. Specifications of adsorbent, adsorber bed and operating conditions.

Parameter		Values
Working pairs		FAM-Z02/water
Sorbent coating thickness, mm	mm	0.319
Mass of dry sorbent (m_{s})	kg	0.766 (689 g FAM-Z02 and 77 g binders)
Sorbent density (ρ_{s})	kgm^{-3}	600-700 [20]
Specific heat capacity of sorbent material ($c_{p,s}$)	$Jkg^{-1}K^{-1}$	822 (30 °C) [20] 942 (90 °C)
Metal mass of sorber bed ($m_{\mathrm{HEX,bed}}$)	kg	2.53
Sorber bed dimensions (L×W×H)	cm	33.02×3.81×30.48
Number of fins per inch (FPI)		10
Fin dimensions	cm	43.18 × 30.48 (17” × 12”)
Fin spacing	mm	2.54 (coating thickness is included)
Sorber bed heat transfer area (A_{ht})	m^2	2.80
Effective specific heat capacity of sorber bed heat exchanger with copper tubes and aluminum fins ($c_{\mathrm{bed,HEX}}$)	$Jkg^{-1}K^{-1}$	470
Mass of evaporator (m_{evap})	kg	2.595
Specific heat capacity of evaporator (c_{evap})	$Jkg^{-1}K^{-1}$	385
Mass of water in the evaporator chamber ($m_{\mathrm{w,evap}}$)	kg	1
Heating fluid mass flowrate ($\dot{m}_{\mathrm{hf}}$)	kgs^{-1}	0.058
Cooling fluid mass flowrate ($\dot{m}_{\mathrm{cf}}$)	kgs^{-1}	0.062
Chilled/coolant water flowrate ($\dot{m}_{\mathrm{chilled}}$)	kgs^{-1}	0.035
Specific heat capacity of HTF	$Jkg^{-1}K^{-1}$	1725 (30 °C) 1905 (90 °C)
Inlet temperature of the sorber bed cooling fluid	°C	30
Inlet temperature of the sorber bed heating fluid	°C	90
Inlet temperature of the evaporator/condenser chilled/coolant water	°C	20

5.3. Performance evaluation

Among the performance indicators, introduced in Chapter 1, ESD and specific power (SP) are assessed in this chapter for the coated FAM-Z02 adsorber.

5.3.1. Cold storage

The material-based ESD of a cold storage closed-system is calculated using Eq. (14), where m_{s} is the sorbent mass, m_{bed} is the mass of sorber bed including the sorber bed HEX and the sorbent, and m_{sys} is the mass of the whole sorption storage system. ESD is also reported per volume of the whole system or the sorbent volume. To make a proper comparison between the storage systems published in the literature, the differences in the ESD definition should be taken into consideration. The discharged

energy, $Q_{\mathrm{dch,cold}}$ is defined as the evaporator cooling energy during the discharging process given by Eq. (15).

$$\mathrm{ESD_{cold}\ (MJkg^{-1})} = \frac{Q_{\mathrm{dch,cold}}}{m_{\mathrm{s/bed/sys}}} \tag{14}$$

$$Q_{\mathrm{dch,cold}}\ (\mathrm{J}) = \int_0^{t_{\mathrm{dch}}} \dot{m}_{\mathrm{chilled}}\ c_{p,\mathrm{chilled}}\left(T_{\mathrm{chilled,i}} - T_{\mathrm{chilled,o}}\right) dt \tag{15}$$

where $\dot{m}_{\mathrm{chilled}}$ is the mass flow rate of the chilled water and $T_{\mathrm{chilled,i}}$ and $T_{\mathrm{chilled,o}}$ are the inlet and outlet temperatures of the chilled water, respectively. Specific discharge power, which indicates the acceleration of the discharging process per mass of the sorbent material, is calculated as follows for the cold storage systems,

$$\mathrm{SP_{dch,cold}\ (Wkg^{-1})} = \frac{Q_{\mathrm{dch,cold}}}{m\ t_{\mathrm{dch}}} \tag{16}$$

Considering an ideal evaporator with the effectiveness of one, the ideal cooling energy is calculated as follows,

$$Q_{\mathrm{evap,ideal}}\ (\mathrm{J}) = \Delta\omega_{\mathrm{dch}}\ m\ h_{\mathrm{fg,evap}} \tag{17}$$

where $\Delta\omega_{\mathrm{dch}} = \omega_{\infty,\mathrm{dch}} - \omega_{0,\mathrm{dch}}$ is the maximum net water uptake in the sorption process, according to the operating conditions. Similarly, the following are the definitions for ideal specific discharge power ($\mathrm{SP_{dch,ideal}}$) and ideal material-based ESD ($\mathrm{ESD_{mat,ideal}}$).

$$\mathrm{SP_{dch,cold,ideal}\ (Wkg^{-1})} = \Delta\omega_{\mathrm{dch}}\ h_{\mathrm{fg}(T_{\mathrm{evap}})}\ t_{\mathrm{dch}}^{-1} \tag{18}$$

$$\mathrm{ESD_{cold,ideal}\ (MJkg^{-1})} = \Delta\omega_{\mathrm{dch}}\ h_{\mathrm{fg}(T_{\mathrm{evap}})} \tag{19}$$

For the charging process, the total input energy and specific charge power are calculated as follow,

$$Q_{\mathrm{ch}}\ (\mathrm{J}) = \int_0^{t_{\mathrm{ch}}} \dot{m}_{\mathrm{hf}}\ c_{p,\mathrm{hf}}\left(T_{\mathrm{hf,i}} - T_{\mathrm{hf,o}}\right) dt \tag{20}$$

$$\mathrm{SP_{ch}\ (Wkg^{-1})} = \frac{Q_{\mathrm{ch}}}{m\ t_{\mathrm{ch}}} \tag{21}$$

5.3.2. Heat storage

The discharged energy during the sorption heat storage ($Q_{\mathrm{dch,heat}}$) is the heat delivered to the cooling fluid of the sorber bed and is calculated from Eq. (22). Accordingly, the energy storage density ($\mathrm{ESD}_{\mathrm{heat}}$) and specific discharge power ($\mathrm{SP}_{\mathrm{dch,heat}}$) are obtained from Eqs. (23) and (24).

$$Q_{\mathrm{dch,heat}}\ (\mathrm{J}) = \int_0^{t_{\mathrm{dch}}} \dot{m}_{\mathrm{cf}}\ c_{p,\mathrm{cf}} \left(T_{\mathrm{cf,o}} - T_{\mathrm{cf,i}}\right) dt \tag{22}$$

$$\mathrm{ESD}_{\mathrm{haet}}\ (\mathrm{MJkg^{-1}}) = \frac{Q_{\mathrm{dch,heat}}}{m} \tag{23}$$

$$\mathrm{SP}_{\mathrm{dch,heat}}\ (\mathrm{Wkg^{-1}}) = \frac{Q_{\mathrm{dch,heat}}}{m\ t_{\mathrm{dch}}} \tag{24}$$

5.4. Results and discussion

5.4.1. Sorption and desorption dynamic

Temperature variation of the sorber bed HTF and the chilled/coolant water of ECU for the cyclic operation of 60 min are shown in Figure 37a. Decreasing the HTF inlet temperature from 90 °C (T_{des}) to 30 °C (T_{ads}) initiates the sorption process. In the test-bed shown in Figure 36b, mass change of the sorber bed is due to: (i) the water uptake by sorbent material, and (ii) rest of the mass changes or fluctuations, namely, density changes of the HTF due to the temperature changes, and in part, buoyancy effects, thermal expansion, contraction and vibration of the flexible hose. The HTF, silicon oil (Julabo, Thermal P60), has a relatively significant density variation from 909 to 854 kg m^{-3} when its temperature changes from 30 to 90 °C [158]. To deconvolute the mass change due to the water uptake from the above-mentioned mass changes, a blank (baseline) experiment was carried out for each operating condition. The baseline experiments used the same temperature program as the main experiment while the sorber bed was dried and the isolating valve between the sorber bed and the ECU (component 6 in Figure 36b) was shut. Thus, the mass change obtained from the baseline mass measurement did not include the effect of water uptake. The baseline measurement (shown in red dashed line in Figure 37b) was then subtracted from the total mass change (shown in the solid black line in Figure 37b), and the result exclusively represented the water uptake changes.

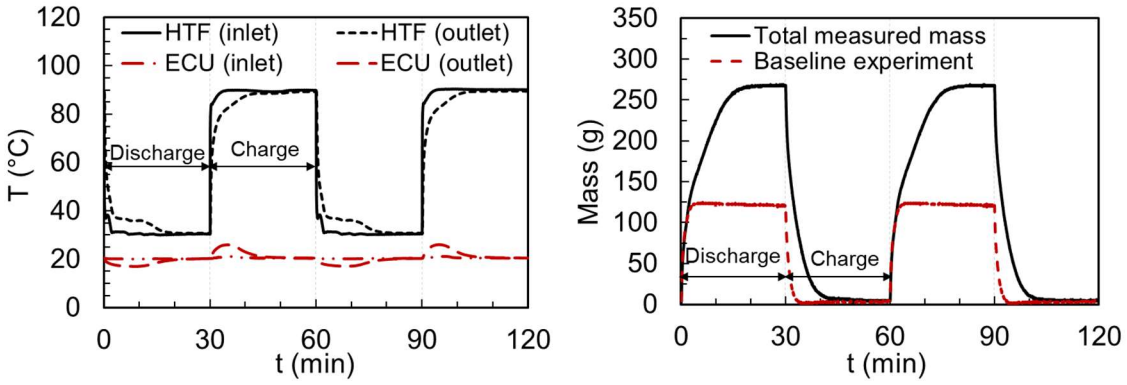

(a) (b)

Figure 37. (a) Inlet and outlet temperatures of the heating/cooling fluid and coolant/chilled water for cycle time of 60 min and (b) mass changes of the sorber bed due to the variations in silicone oil density and buoyancy effects during the sorption (30 °C) and desorption (90 °C).

After the baseline correction, as shown in Figure 38, the experimental dimensionless water uptake (ω_t/ω_∞) curve demonstrates a near-exponential trend for a full-scale 0.3-mm coated FAM-Z02 sorber bed, which is similar to the trend observed for FAM-Z02 in small-scale measurements by LTJ [149] and G-LTJ [93]. By defining the sorption rate constant (k_{ads}) and the sorption characteristic time (τ_{ads}), the evolution of water uptake follows Eq. (25).

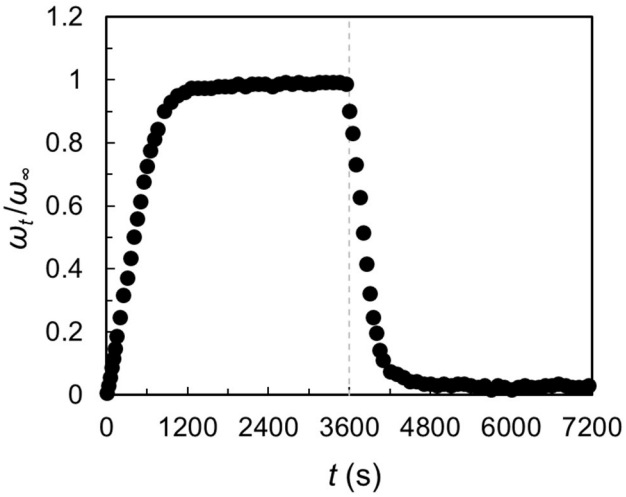

Figure 38. Dimensionless water uptake of a 0.3 mm FAM-Z02 coated sorber bed. $T_{\mathrm{des}} = 90$ °C , $T_{\mathrm{ads}} = 30$ °C , $T_{\mathrm{ECU}} = 20$ °C, and $\omega_\infty = 0.20 \pm 0.01\ \mathrm{kgkg}_{\mathrm{ads}}^{-1}$.

$$\frac{\omega_t}{\omega_\infty} = \frac{\omega(t) - \omega(t=0)}{\omega(t\to\infty) - \omega(t=0)} = 1 - \exp(-k_{\mathrm{ads}}\, t) = 1 - \exp(-\,t/\tau_{\mathrm{ads}}) \qquad (25)$$

In Eq. (25), τ_{ads} indicates how fast the sorption process occurs, under a certain operating condition. Considering one characteristic time for the whole uptake evolution, the sorption characteristic time, τ_{ads}, is 474 s. Similarly, for the desorption process, an exponential trend of $\exp\left(-\left(t-t_{0,\mathrm{des}}\right)/\tau_{\mathrm{des}}\right)$ with τ_{des} of 320 s was observed. The desorption process was 1.48 times faster than that of the sorption due to the higher driving force (pressure difference between sorber bed and ECU) and higher temperature during the desorption process. It is in agreement with the reported desorption/adsorption rate constant ratio of 1.5 for 0.3-0.35 mm FAM-Z02 by G-LTJ measurement [93] and desorption/adsorption rate constant ratio of 1-1.26 for FAM-Z02 grains smaller than 0.8 mm by LTJ measurement [149], under boundary condition of 90-30-30-10 °C.

Girnik and Aristov [149] suggested a two-exponent approximation of sorption dynamic for small granules (0.2-0.5 mm diameter) of FAM-Z02 with two different characteristic times. Therefore, they could capture the fast uptake at the beginning of adsorption, together with the slower uptake close to the sorption equilibrium water uptake. In the present study, other than the two above-mentioned regions, another slow region in the beginning of adsorption/desorption was observed as the characteristic of the full-scale systems: “system-limited region”. This phenomenon occurred due to the thermal mass of the system and the heat and mass transfer resistances, including low vapor supply because of small diameter hosing between the evaporator and sorber bed, low thermal diffusivity in the sorber bed, and thermal contact resistance (TCR). To maximize the performance of an S-TES, the system-limited region should be diminished by mitigating the heat and mass transfer resistances. To perform a more exhaustive analysis of the sorption dynamic, third characteristic time was introduced in this study. Hence, following the two-exponent approximation in ref. [149], a three-exponent approximation is proposed as Eq. (26).

$$\omega_t/\omega_\infty = a\,[1-\exp(-t/\tau_1)] + b\,[1-\exp(-t/\tau_2)] + c\,[1-\exp(-t/\tau_3)] \qquad (26)$$

where the summation of the weighting factors (a, b and c) is unity. Figure 39a shows the sorption kinetics and Figure 39b shows the desorption kinetics. As shown in Figure 39a, the characteristic times of the system-limited region (τ_1), rapid sorption (τ_2), and the slow ending (τ_3) are found to be 625, 270 and 1110 s, respectively. The slow system-limited period takes about 350 s from the 1850 s (about 19%) of the sorption process while it takes about 150 s from the 1210 s (about 12%) of desorption. The sorption/desorption rate

constants, characteristic time as well as coefficients a, b and c are listed in Table 14. Desorption/sorption rate constant ratio is 1.5 in the system-limited and slow ending regions and 1.4 in the rapid sorption(desorption) region.

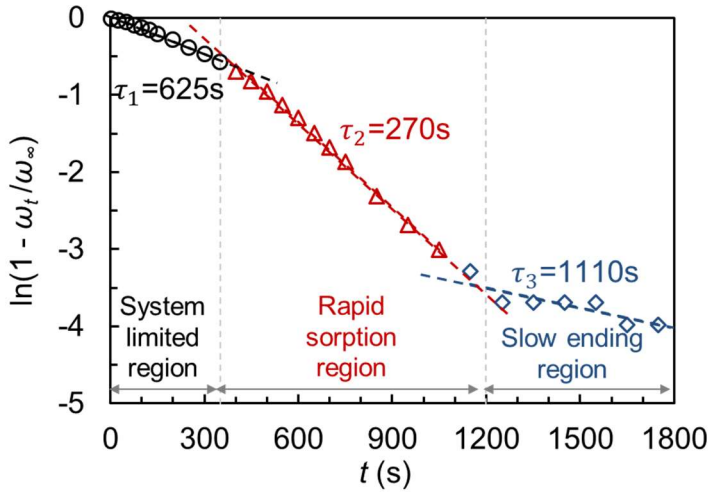

(a)

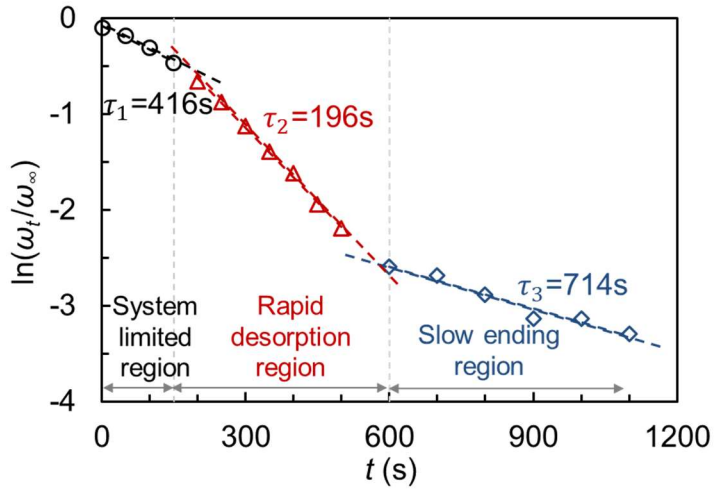

(b)

Figure 39. (a) Sorption kinetics and (b) desorption kinetics in three regions: i) slow beginning (τ_1), ii) fast sorption (τ_2) and iii) slow ending (τ_3) for a full-scale 0.3 mm coated FAM-Z02 sorber bed. $T_{\mathrm{des}} = 90$ ℃, $T_{\mathrm{ads}} = 30$ ℃, and $T_{\mathrm{ECU}} = 20$ ℃.

Table 14. Sorption/desorption rate constant, characteristic time, coefficients a, b, and c, and coefficient of determination for the kinetics of 0.3 mm coated FAM-Z02 sorber bed, introduced in Eq. (26).

	k_1	τ_1	a	k_2	τ_2	b	k_3	τ_3	c	R^2
Sorption (88 to 31 °C)	0.0016	625	0.5	0.0037	270	0.45	0.0009	1110	0.05	0.97
Desorption (31 to 89 °C)	0.0024	416	0.45	0.0051	196	0.54	0.0014	714	0.01	0.97

The sorption/desorption rate constant ($k_{\mathrm{ads/des}}$) is related to the effective diffusivity by Eq. (27) for the coated sorbent layers [161], where D_{e} and l_{coated} are the effective

diffusivity and sorbent coating thickness, respectively. Using Eq. (27), the average effective sorption diffusivities for the three regions shown in Figure 39a are $D_{e,1} = 4.8 \times 10^{-11}$ m^2 s^{-1}, $D_{e,2} = 1.1 \times 10^{-10}$ m^2 s^{-1} and $D_{e,3} = 2.7 \times 10^{-11}$ m^2 s^{-1}. The average effective diffusivity of the coated FAM-Z02 sorber bed is 6.3×10^{-11} m^2 s^{-1} for T_{ads} and T_{evap} of 30 and 20 °C. Although, the obtained D_e is a function of the sorption system as well as the sorbent material, this value is in line with D_e of 1.70–19.7 ×10^{-11} m^2 s^{-1}, reported by Freni et al. [151] for 0.1 mm coated SAPO-34 for temperatures of 50-80 °C.

$$k_{ads/des}\ (s^{-1}) = 3\ \ D_e/l^2_{coated} \quad (27)$$

Table 15 lists the required time to reach 70, 80 and 90% of the equilibrium water uptake, as well as the specific charge/discharge power, and ESD corresponded to these times for cold storage application. Specific discharge power ($SP_{dch,cold}$) has a maximum of 485 W kg^{-1} at $t_{80\%}$, when 80% of the maximum uptake is achieved. As shown in Table 15, the specific charge power (SP_{ch}) is higher for the shorter charging times since its maximum value happens in the very beginning of the charging period. The maximum instant specific charging power is 6.605 kW kg^{-1} at 11 s of charging period and the maximum averaged specific power, based on the minimum charge time, is 4092 W kg^{-1} and occurs at 24 s of charging time. ESD always increases through the time to 0.494 MJ kg^{-1}, when the equilibrium uptake is reached.

Table 15. Required time for the cold storage S-TES to reach 70% (at $t_{70\%}$), 80% (at $t_{80\%}$) and 90% (at $t_{90\%}$) equilibrium water uptake and charge/discharge SP_{cold} and ESD_{cold} at these times.

	$t_{70\%}$	$t_{80\%}$	$t_{90\%}$	$t_{100\%}$	$SP_{70\%}$	$SP_{80\%}$	$SP_{90\%}$	$SP_{100\%}$	$ESD_{70\%}$	$ESD_{80\%}$	$ESD_{90\%}$	$ESD_{100\%}$
	s				Wkg^{-1}				MJkg^{-1} (based on m_s)			
Discharging (90 to 30 °C)	619	725	883	1850	478	485	473	267	0.296	0.352	0.418	0.494
Charging (30 to 90 °C)	356	424	522	1210	1689	1546	1363	663				

5.4.2. Temperature distribution inside the sorber bed

Figure 40a shows the locations of the attached thermocouples ($TC_{b,1}$, $TC_{b,2}$, $TC_{b,3}$, and $TC_{b,4}$) on the surface of the sorbent coating layer. The tips of thermocouples are carefully attached to the coated sorbent by a small piece of aluminum tape at the locations

shown in Figure 40a, which avoided blocking the sorbate penetration into the coated sorbent layer.

Figure 40b shows the temperature and uptake variation of the coated sorbent of the S-TES for long desorption and sorption periods; thermal and uptake equilibrium conditions are reached. The temperatures at the sorbent layers at these four different locations were close to one another under equilibrium condition (i.e. less than 1 °C temperature difference), and the maximum temperature difference between the thermocouples was in the switching time between the sorption and desorption process and was 5 °C. Hence, the averaged of these values through the time was used as the sorber bed temperature for the dynamic study of the coated sorber bed.

The similarity between the sorbent temperatures at different locations of the sorber bed demonstrates the uniformity of heat transfer inside the coated sorber bed. However the sorbent temperature under equilibrium condition was 2 °C higher than the inlet HTF temperature during the sorption process and 3 °C lower than the inlet HTF temperature during desorption process, as depicted in Figure 40a. This indicates that the heat transfer resistance inside the full-scale sorption system that originates the water uptake difference between the full-scale sorption systems and TGA measurements, presented in section 5.4.3. In spite of the immense thermal mass of the full-scale system, thermal equilibrium was reached faster than the water uptake equilibrium. The maximum temperature difference between the surface of the coated sorbent layer at $TC_{b,3}$ (see Figure 40b) and the outlet temperatures of HTF was 16 °C for the sorption and 20 °C for the desorption, which happened at the beginning of sorption and desorption processes.

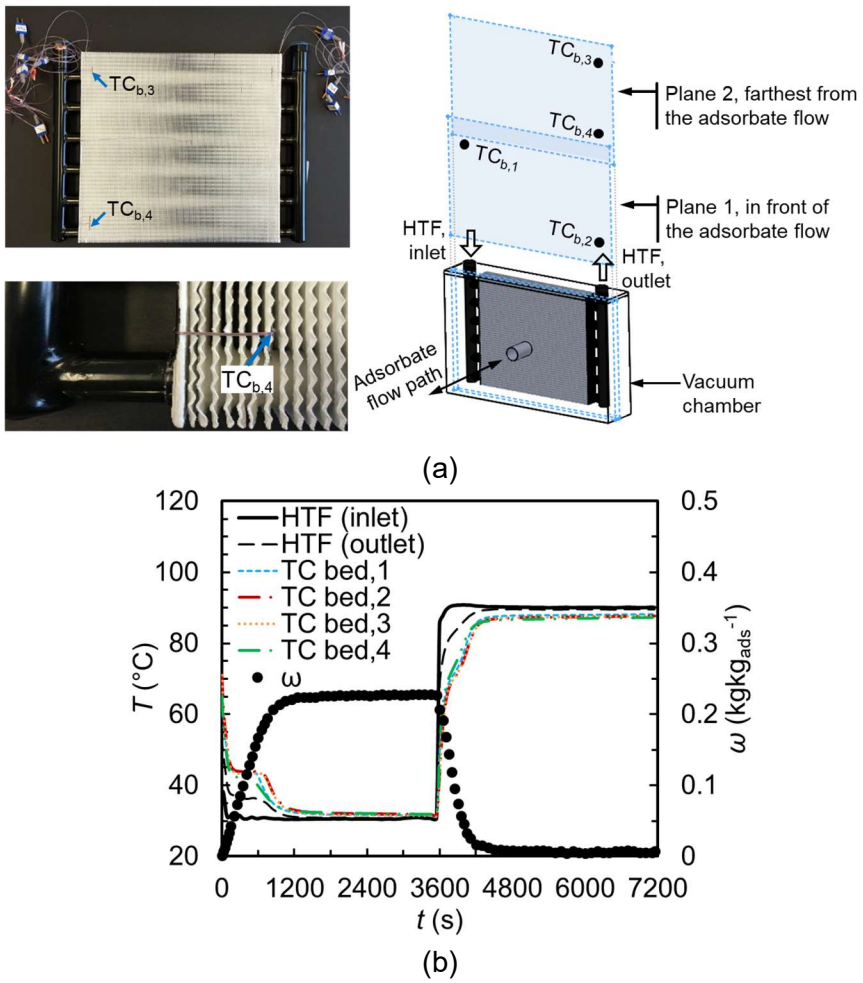

Figure 40. (a) Coated HEX with attached thermocouples on the surface of the coated sorbent, including: $TC_{b,1}$ and $TC_{b,2}$ in the front of the sorbate flow, and $TC_{b,3}$ and $TC_{b,4}$ at the plane farthest from the sorbate flow; (b) uptake and temperature variation inside the coated sorber bed vs time.

5.4.3. Effects of the sorption configuration on the sorption TES performance

Sharafian et al. [158] conducted similar mass measurement with a sorber bed HEX identical to that of the present study, packed with 1.5 kg of 2 mm FAM-Z02 pellets. Figure 41 shows the comparison between the storage performance of the present study and ref. [158], and the following can be noted:

- As shown in Figure 41a, the rate constant of sorption in the thin-layer coated sorber bed is significantly higher than that of the loose grain (i.e. k_{ads} of 2.11×10^{-3} s^{-1} for the coated bed compared to k_{ads} of 5.03×10^{-4} s^{-1} for the loose grain bed).

- However, the maximum reachable uptake for the loose grain bed is higher than the maximum uptake of the coated sorber bed (i.e. 0.28 kg kg_{ads}^{-1} compared to 0.20±0.01 kg kg_{ads}^{-1}). The equilibrium water uptake of 0.22 kg kg_{ads}^{-1} was measured by a thermogravimetric sorption analyzer (IGA-002, Hiden Isochema), in our lab, for the coated FAM-Z02 at $T_{\mathrm{des}} = 90\ ℃,\ T_{\mathrm{ads}} = 30\ ℃,\ T_{\mathrm{ECU}} = 20\ ℃$ [162]. The difference between the maximum achieved water uptake in the present full-scale study and the thermogravimetric measurement is due to the heat transfer resistance inside the full-scale sorber bed, which causes a temperature difference between the actual sorbent temperature and the desired operating condition, as explained in Section 5.4.2, and also the uncertainty of the measurement, presented in Appendix C.

- As shown in Figure 41b, $\mathrm{SP}_{\mathrm{dch,cold,ideal}}$, Eq. (18), of the coated bed reaches a maximum of 560 Wkg^{-1} at 10 min, and after 43 min, $\mathrm{SP}_{\mathrm{dch,cold,ideal}}$ of the coated sorber bed slightly drops below that of the loose grain bed. At 43 min, the net water uptakes of the loose grain and coated beds are equal (0.20 kg kg_{ads}^{-1}).

- $\mathrm{ESD}_{\mathrm{cold,ideal}}$, Eq. (19), shows the same trend as the net uptake (see Figure 41c). Hence, one can conclude that the coated bed is preferable for short-duration energy delivery applications, where fast discharge is the main target. The loose grain bed is suitable for longer discharge time, because of its higher sorption capacity. Therefore, to provide certain required energy, more amount of coated sorbent is required compared to the loose grain sorbent.

- However, for the system-level optimization of an S-TES, assessment of the sorber bed ESD ($\mathrm{ESD}_{\mathrm{bed}}$) is more practical. The active volume of the coated sorber bed is 3835 cm^3 with 0.766 kg of FAM-Z02 and the active volume of the loose grain bed is 2876 cm^3 with 1.5 kg of the sorbent. As shown in Figure 41d, the $\mathrm{ESD}_{\mathrm{bed,cold,ideal}}$ of the loose grain bed is significantly higher than that of the coated bed for all discharge times. For discharge time of 60 min, $\mathrm{ESD}_{\mathrm{bed,cold,ideal}}$ of the loose grain bed is 3.45 times higher than $\mathrm{ESD}_{\mathrm{bed,cold,ideal}}$ of the coated bed (0.345 GJm^{-3} compared to 0.1 GJm^{-3}).

- For a fair comparison between the coated bed and loose grain bed, the possibility of improving $\mathrm{ESD}_{\mathrm{bed,cold,ideal}}$ of the coated bed by increasing the thickness of the

coating layer should be studied. Regardless of the fin spacing, increasing the coating layer to 2 mm (similar to the diameter of the loose grain particles), reduces the sorption rate constant to 4.747×10^{-5} s^{-1}, using Eq. (27), which is 10.6 times lower than the sorption rate constant of the loose grain bed (5.038×10^{-4} s^{-1}). To keep the sorption rate constant of the coated bed at least equal to the rate constant of the loose grain bed, the coating layer should be 0.6 mm, which is suitable considering the fin spacing of 2.54 mm. For the 0.6 mm coating layer, the maximum $\mathrm{ESD}_{\mathrm{bed,cold,ideal}}$ is predicted to be 0.2 GJ m^{-3}, which is still lower than the $\mathrm{ESD}_{\mathrm{bed,cold,ideal}}$ of the loose grain bed (0.345 GJ m^{-3}). Therefore, for volumetric optimization, the coated bed may be less desirable compared with the loose grain bed because of the higher system-based volumetric ESD along with less complexity and lower cost of the loose grain packed beds.

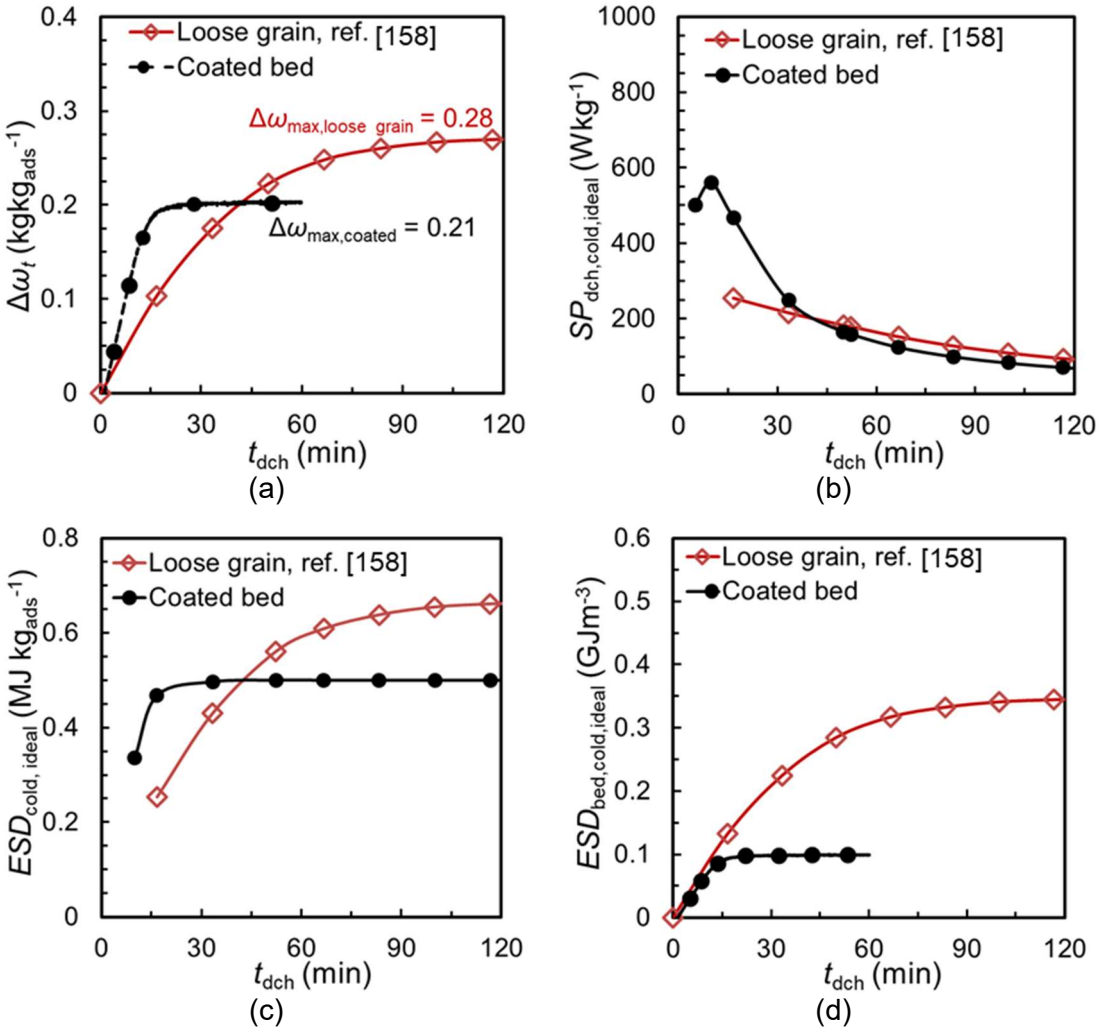

Figure 41. (a) Net water uptake, (b) specific discharge power (Eq. (18)), (c) material-based ESD (Eq. (19)), and (d) sorber bed-based ESD, obtained from $\mathrm{ESD_{bed,cold,ideal}} = (\Delta\omega\ h_{\mathrm{fg}}\ m_{\mathrm{s}})/V_{\mathrm{bed\ HEX}}$, of 0.3-mm coated FAM-Z02 sorption TES compared to a 2-mm diameter FAM-Z02 loose grain (ref. [158]) for cold storage applications. The charging is done long enough to ensure that the S-TES is fully charged. Active volume of coated sorber bed is 3835 cm^3 ($A_{\mathrm{ht}} = 2.8\ \mathrm{cm}^2$) and loose grain sorber bed is 2876 cm^3 ($A_{\mathrm{ht}} = 2.1\ \mathrm{cm}^2$); $T_{\mathrm{des}} = 90\ ℃$, $T_{\mathrm{ads}} = 30\ ℃$, $T_{\mathrm{ECU}} = 20\ ℃$, $(\omega_\infty)_{\mathrm{coated}} = 0.20 \pm 0.01$ kg kg$_{ads}^{-1}$.

5.4.4. Effects of the heat exchanger to sorbent mass ratio on the storage performance of heat storage

The discharged energy to the HTF (Eq. (22)) can be also obtained from the energy balance of the sorber bed, as follows,

$$Q_{\mathrm{dch,heat}} = \int_0^{\mathrm{dch}} m_{\mathrm{s}} \left\{ \Delta h_{\mathrm{sorp}} \frac{d\omega}{dt} - d\left[\left\{ \left(c_{p,s} + \omega\, c_{p,\mathrm{lw}} \right) + c_{\mathrm{bed,HEX}}\, r \right\} T_{\mathrm{s}} \right] / dt - c_{p,\mathrm{vw}} \left(T_{\mathrm{s}} - T_{\mathrm{evap}} \right) \frac{d\omega}{dt} \right\} dt \quad (28)$$

where the first term in the right-hand side is the sorption energy, the second term includes the sensible heat of the sorbent material, adsorbed water, sorber HEX, and the last term is the sensible energy of the refrigerant water vapor from the evaporator to the sorber bed. The ratio of the HEX mass to the sorbent mass (r) has an important effect on the performance of an S-TES. Lower r leads to higher thermal energy efficiency, but can also lower heat transfer rate in the sorber bed [163]. For seasonal heat storage, where the storage medium has been cooled to the ambient temperature, a portion of the sorption energy is required to heat up the sorber HEX, sorber mass, and adsorbed water. Figure 42 shows the discharged energy and $\mathrm{ESD}_{\mathrm{bed,heat}}$ for r of 1 to 6, for cyclic and seasonal storage systems, calculated from Eq. (28), and measured data (Eq. (22)) of the present study at r of 3.3, and the following can be noted:

- The measured values in the present study (at r = 3.3) under cyclic operation are 0.646 MJ for $Q_{\mathrm{dch,heat}}$ and 0.196 MJ kg^{-1} for $\mathrm{ESD}_{\mathrm{bed,heat}}$, which is in good agreement with the calculated values from Eq. (28).

- By optimizing the sorber bed to r of 1 from 3.3, $\mathrm{ESD}_{\mathrm{bed,heat}}$ is predicted to become twice, for the cyclic operation. This indicates that there is room for improving the $\mathrm{ESD}_{\mathrm{bed,heat}}$ by decreasing the mass ratio of HEX to the sorbent.

- For seasonal application, the discharged energy decreases from 0.413 to 0.383 MJ over a range of r from 1 to 6, since a greater portion of the sorption heat is required to heat the system from the ambient to the sorption temperature.

- For cyclic operation, greater thermal mass (higher r) increases the sensible heat of the desorption process, and consequently, the total discharged energy in the sorption process. The discharged energy has increased from 0.580 to 0.679 MJ when r is increased from 1 to 6.

- Considering the $\mathrm{ESD}_{\mathrm{heat}}$ as a function of the total mass of sorbent and HEX ($\mathrm{ESD}_{\mathrm{bed,heat}}$), both seasonal and cyclic operations show a descending trend with r. $\mathrm{ESD}_{\mathrm{bed,heat}}$ for cyclic operation is 3 times higher for r of 1 (0.379 MJ kg^{-1}) compared

to 0.127 MJ kg^{-1} for r of 6 and for seasonal application 3.8 times higher for r of 1 (0.270 MJ kg^{-1}) than r of 6 (0.071 MJ kg^{-1}).

- For r of 1, the predicted seasonal $\mathrm{ESD_{bed,heat}}$ is 71% of the cyclic $\mathrm{ESD_{bed,heat}}$, while for r of 6, the predicted seasonal $\mathrm{ESD_{bed,heat}}$ is 56% of the cyclic $\mathrm{ESD_{bed}}$.

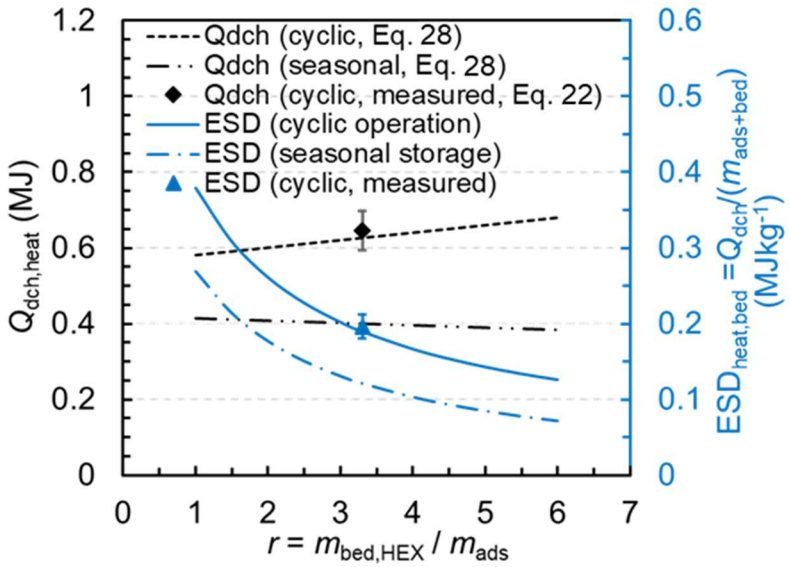

Figure 42. Discharged energy and sorber bed energy storage density ($\mathrm{ESD_{bed,heat}}$) based on the total mass of the sorbent material and the heat exchanger versus the mass ratio of the metal mass of the sorber heat exchanger and the sorbent mass, for a FAM-Z02 coated sorption storage. Cycle time of 30 min is considered for the cyclic operation, while 15 min for the charging process and 15 min for the discharging process are considered for the seasonal operation. $T_{\mathrm{des}} = 90$ ℃, $T_{\mathrm{ads}} = 30$ ℃, and $T_{\mathrm{ECU}} = 20$ ℃.

5.4.5. Effects of cycle time on the sorption TES performance

Figure 43 shows the effect of the cycle time on the net water uptake and specific discharge power for the coated S-TES under cyclic operation. Increasing cycle time leads to an increase in the net water uptake up to the cycle time of 60 min (see Figure 43a). For higher cycle times, $\Delta\omega$ remains constant at 0.20±0.01 kg kg$_{\mathrm{ads}}^{-1}$, i.e. the maximum achievable water uptake under the operating conditions listed in Table 13.

From the energy balance for the evaporator, the discharged energy of the cold storage (Eq. (15)) can be calculated from Eq. (29). The first term in the right-hand side includes the sensible heat of water inside the evaporator and the evaporator HEX and the second term represents the vaporization enthalpy. Figure 43b shows the specific

discharge power of cold ($\mathrm{SP}_{\mathrm{dch,cold}}$) and heat ($\mathrm{SP}_{\mathrm{dch,heat}}$) storage. $\mathrm{SP}_{\mathrm{dch,cold}}$ reaches its maximum (468 W kg^{-1}) for the cycle time of 30 min, but thereafter it drops rapidly because of no changes in the net water uptake for cycle times of more than 30 min. $\mathrm{SP}_{\mathrm{dch,heat}}$ is 1251 W kg^{-1} for 10 min cycle time and drops to 249 W kg^{-1} for cycle time of 120 min. For cycle times of 10 to 120 min, $\mathrm{SP}_{\mathrm{dch,heat}}$ does not show an optimum since, as explained in Section 5.4.1, the maximum $\mathrm{SP}_{\mathrm{dch,heat}}$ occurs at the beginning of the discharge process (24 s).

$$Q_{\mathrm{dch,cold}} = \int_0^{t_{\mathrm{dch}}} m_{\mathrm{s}} \left\{ d\left[\left(c_{\mathrm{evap}} \frac{m_{\mathrm{evap}}}{m_{\mathrm{s}}} + c_{p,\mathrm{lw}} \frac{m_{\mathrm{w,evap}}}{m_{\mathrm{s}}} \right) T_{\mathrm{evap}} \right] / dt + h_{\mathrm{fg}} \frac{d\omega}{dt} \right\} dt \qquad (29)$$

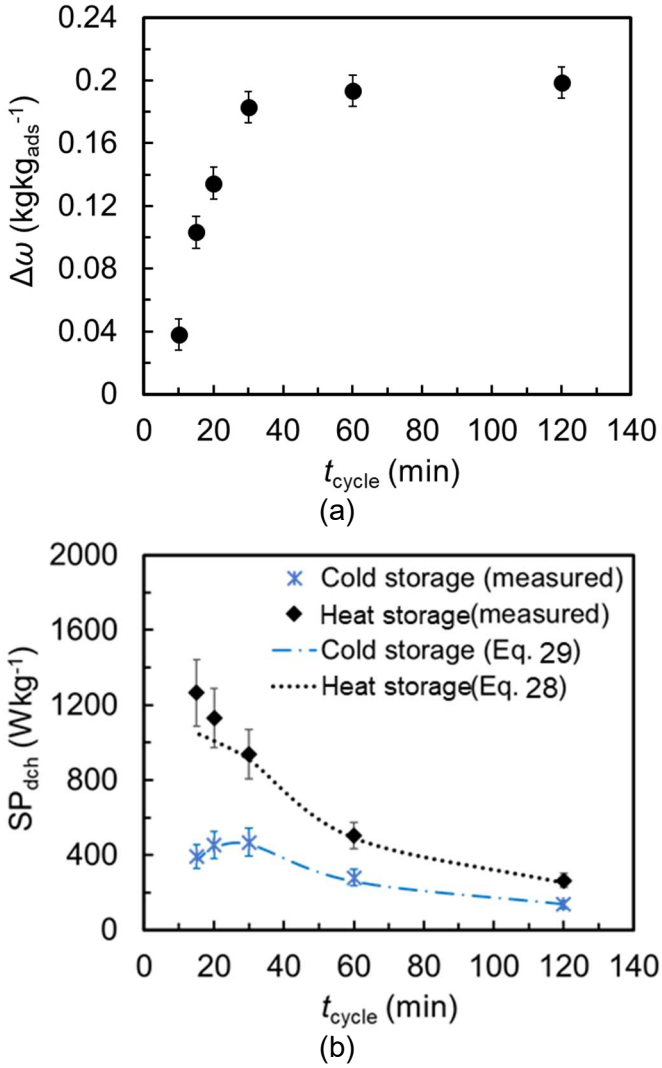

Figure 43. Effects of cycle time on the (a) net water uptake and (b) specific discharge power of a 0.3-mm coated FAM-Z02 heat and cold sorption TES. $T_{\mathrm{des}} = 90$ ℃ , $T_{\mathrm{ads}} = 30$ ℃ and $T_{\mathrm{ECU}} = 20$ ℃.

For cyclic operation, the sensible heat from the desorption process, second term in the right-hand side of Eq. (28), is also added to the sorption energy. Figure 44a shows the share of the sorption energy, Eq. (30), and sensible heat from the total discharged energy. As shown in Figure 44a, for shorter cycle times, since the sorber bed is not completely desorbed, the majority of the discharged energy is accounted for the sensible heat and thermal loss, i.e. 64% for 5 min cycle time. The total thermal mass of the sorber bed includes thermal masses of the sorbent material (23%), HTF (32%), HEX copper tubes (28%), and aluminum fins (17%). Sorption energy share increases by cycle time, reaching a maximum of 70% for the cycle time of 30 min. As shown in Figure 44b, for the

completely charged sorber bed, the share of sorption heat to the total discharged energy reaches an almost constant value of 74% after 15 min of the discharging process.

$$Q_{\mathrm{ads}} = \Delta\omega \, m_{\mathrm{s}} \, \Delta h_{\mathrm{sorp}} \tag{30}$$

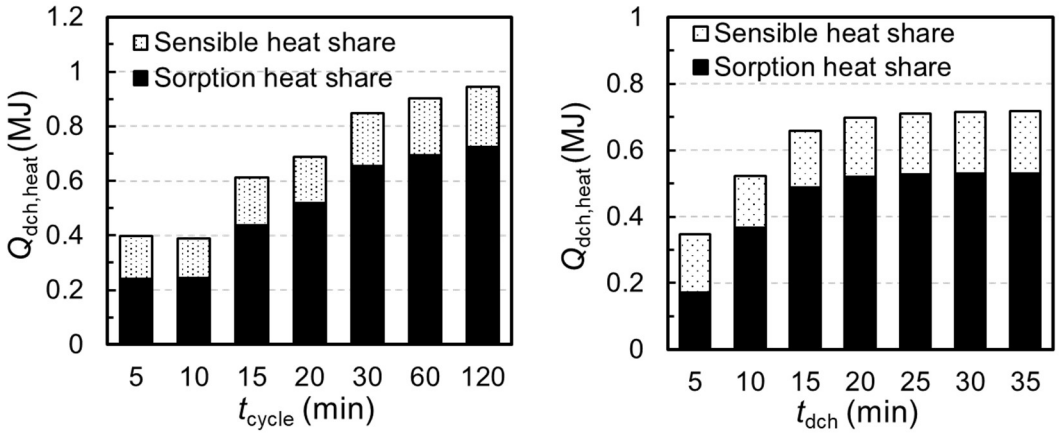

Figure 44. Sorption energy and sensible heat shares from the total discharged energy for (a) various cycle times (5 to 60 min) and (b) various discharging times for the cycle time of 120 min. T_{des} = 90 ℃, T_{ads} = 30 ℃, T_{ECU} = 20 ℃.

5.4.6. Charging process in the S-TES

Energy balance during the charging process of the FAM-Z02 coated bed for the cycle time of 60 min is shown in Figure 45. The sorber bed is fully desorbed at 20 min of charging process and thereafter the desorption heat, Eq. (31), does not change. After a full water uptake of the sorbent materials, the heating energy which is given to the storage medium is used to heat up the sorbent material, sorber HEX, HTF inside the HEX, and thermal loss, which will be lost in the long-term storage applications and partially recovered in the short-term storage. The charging energy, Eq. (20), can be also obtained from Eq. (32), which is derived from the energy balance during the desorption process.

$$Q_{\mathrm{des}} = \Delta\omega_{\mathrm{ch}} \, m_{\mathrm{s}} \, \Delta h_{\mathrm{sorp}} \tag{31}$$

$$Q_{\mathrm{ch}} = \int_0^{t_{\mathrm{ch}}} m_{\mathrm{s}} \left\{ \frac{d\left[\left\{\left(c_{p,\mathrm{s}} + \omega \, c_{p,\mathrm{lw}}\right) + c_{\mathrm{HEX}} \, r\right\} T_{\mathrm{s}}\right]}{dt} - \Delta h_{\mathrm{sorp}} \frac{d\omega}{dt} \right\} dt \tag{32}$$

As shown in Figure 45, the charging energy calculated from the energy balance, Eq. (32), is in good agreement with the measured charging energy and is lower than the measured value due to the heat loss, especially at the beginning of the charging process, where heat loss is significant. The ratio of the desorption heat to the total charging energy varies between 51 to 82% for discharge times of 2.5 to 30 min, with a maximum of 82% at 10 min, when 93% of the weight loss ($\Delta\omega_{\mathrm{ch}} = 0.19\ \mathrm{kg\ kg_{ads}^{-1}}$) is achieved.

Considering seasonal storage application, by increasing the charging time from 15 min to 30 min, the charging energy increases from 0.600 MJ to 0.640 MJ, and the thermal efficiency (η_{th}) decreases by 6%. Finding the optimal charging time to minimize the thermal loss is of great importance to increase overall thermal efficiency, particularly in seasonal applications, and requires tracking or prediction of the water uptake changes.

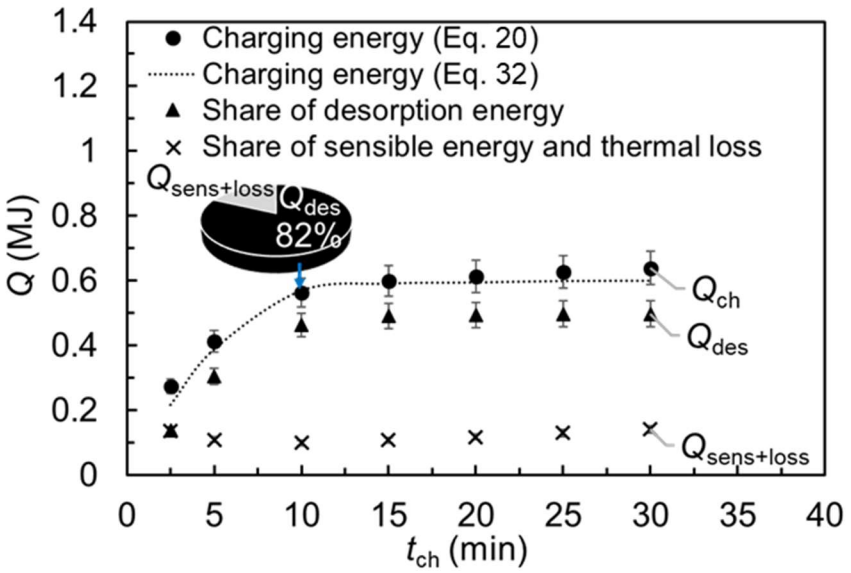

Figure 45. Energy balance of the FAM-Z02 coated S-TES during charging process under cyclic operation with a cycle time of 30 min ($\Delta\omega_{\mathrm{ch}} = 0.20 \pm 0.01\ \mathrm{kg\ kg_{ads}^{-1}}$), at desorption, adsorption, condensation and evaporation temperatures of 90, 30, 20, and 20 °C. ● Charging energy Q_{ch}, Eq. (20), ▲desorption energy Q_{des}, Eq. (31), × sensible heat and thermal loss ($Q_{\mathrm{sens+loss}} = Q_{\mathrm{ch}} - Q_{\mathrm{des}}$), and ··· charging energy calculated from Eq. (32).

5.4.7. Effects of evaporator/condenser temperature on the cold storage performance

Effects of inlet coolant/chilled water temperature of the ECU on the kinetics of sorption as well as the specific discharge power are shown in Figure 46, for the cold

storage application. By decreasing the chilled water temperature from 20 to 15 °C, the amount of water uptake reduces from 0.14 to 0.11 kg kg^{-1} for a cycle time of 20 min, because of the lower vapor pressure during the sorption process (see Figure 46a). Consequently, as shown in Figure 46b, the instant specific discharge power decreases from 0.563 kW kg^{-1} for T_{evap} of 20 °C to 0.406 kW kg^{-1} for T_{evap} of 15 °C for 10 min of discharge. Low water uptake results in a lower amount of water desorption, as shown in Figure 46, although the lower temperature of coolant fluid decreases the condenser pressure, which increases the driving force for the desorption and consequently increases the rate of desorption at the beginning of charging process (see Figure 46a).

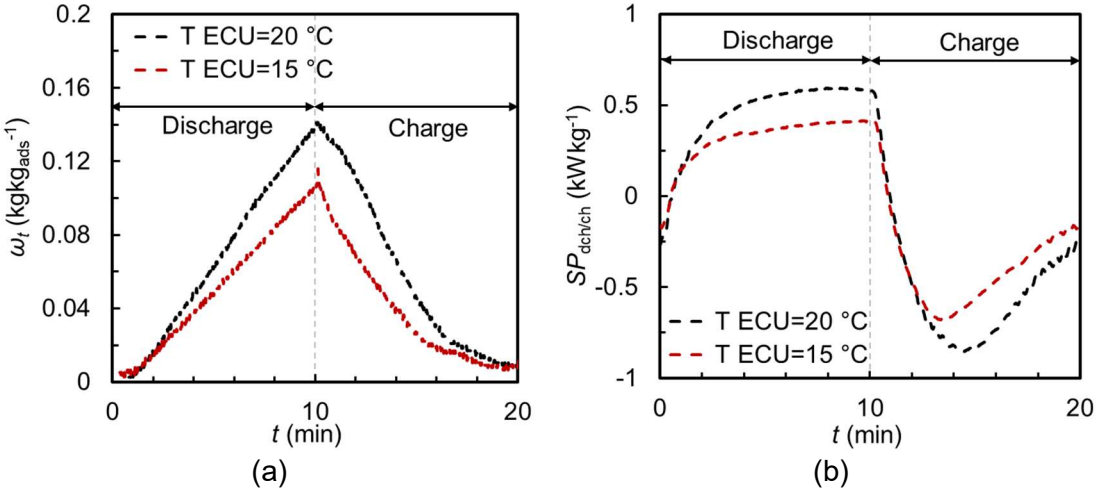

Figure 46. (a) Water uptake and (b) instant specific discharge/charge power of a 0.3-mm coated FAM-Z02 S-TES for coolant/chilled water inlet temperatures of 15 and 20 °C. $T_{\mathrm{des}} = 90$ ℃ and $T_{\mathrm{ads}} = 30$ ℃.

5.5. Summary of results

In this chapter, the sorption dynamics of a 0.3-mm coated FAM-Z02 sorber bed was investigated for the heat and cold S-TES system for both cyclic operation and seasonal storage. The measurement was conducted on a full-scale system, where the weight of the sorbent, FAM-Z02, plus the sorber bed was about 25 kg. The main findings of this study are summarized as follows:

- The uptake evolution of the full-scale FAM-Z02 coated bed showed an exponential trend. Three uptake regions with different characteristic times were observed: (i) the system-limited region with τ of 625 s, (ii) the rapid sorption region with τ of 270 s, and (iii) the slow ending region with τ of 1110

s. It was determined that the thermal mass, as well as heat and mass transfer resistances of the full-scale S-TES, were the main reasons for the slow system-limited region. To improve the performance of the S-TES, this region should be minimized.

- Desorption rate constant was 1.48 times higher than the sorption rate constant, due to the higher driving force (pressure difference between sorber bed and ECU) and higher temperature during the desorption process.

- The average effective diffusivity of the 0.3-mm coated FAM-Z02 S-TES was measured at 6.3×10^{-11} m^2 s^{-1} for desorption, adsorption, and evaporation/condensation temperatures of 90, 30, and 20 °C.

- The coated sorber bed showed higher sorption rate ($k_{\mathrm{ads}} = 2.11\times10^{-3}$ s^{-1}) compared to the loose grain bed ($k_{\mathrm{ads}} = 5.04\times10^{-4}$ s^{-1}) with the identical sorber bed heat exchanger. This makes the coated bed more suitable for short-duration energy delivery, where the fast discharge is the main goal. However, the ideal maximum achievable $\mathrm{ESD}_{\mathrm{cold}}$ of the loose grain bed was higher than that of the coated bed (0.661 MJ kg_{ads}^{-1} compared to 0.500 MJ kg_{ads}^{-1}). Moreover, the volumetric sorber bed $\mathrm{ESD}_{\mathrm{bed,cold}}$, based on the active volume of the sorber bed, was significantly higher for the 2-mm diameter loose grain bed (0.345 GJ m^{-3}) compared to the 0.3 mm coated bed (0.100 GJ m^{-3}).

- By increasing the mass ratio of the sorber bed HEX to sorbent material, r, the discharged energy was predicted to increase for the heat storage under cyclic operation, since an increase in the sorber bed thermal mass led to an increase in the share of sensible heat in the total discharged energy. However, the sorber bed $\mathrm{ESD}_{\mathrm{bed,heat}}$ significantly decreased with r for both cyclic operation and seasonal storage. For seasonal storage, $\mathrm{ESD}_{\mathrm{bed,heat}}$ was predicted as 0.270 MJ kg_{bed}^{-1} for r of 1 and 0.071 MJ kg_{bed}^{-1} for r of 6. Moreover, the possibility of improvement of the sorber bed under study by decreasing r was highlighted; by decreasing r from 3.3 to 1, the $\mathrm{ESD}_{\mathrm{bed,heat}}$ was predicted to be twice.

- The predicted $\mathrm{ESD}_{\mathrm{bed,heat}}$ for seasonal storage was 62% of the measured value from the current study for the cyclic operation for r of 3.3 (i.e. 0.196 MJ kg_{bed}^{-1} compared to 0.121 MJ kg_{bed}^{-1}).

- For the completely charged coated sorber bed, the share of sensible heat and thermal loss to the total discharged energy in the tested S-TES was 51% after 5 min of discharging time and reached an almost constant value of 26% after 15 min discharge. The total thermal mass of the sorber bed included thermal masses of sorbent material (23%), HTF (32%), copper tubes (28%), and aluminum fins (17%).

- It was demonstrated that finding an optimal charging time was essential to minimize thermal loss and increase thermal efficiency, particularly in seasonal storage. By increasing the charging time from 15 min to 30 min, the charging energy would increase from 0.600 MJ to 0.640 MJ, while the thermal efficiency would decrease by 6%.

- For cold storage, the material-based $\mathrm{ESD}_{\mathrm{cold}}$ of 0.493 MJ kg_{ads}^{-1} (0.320 GJ m^{-3}) and averaged specific discharge power of 267 W kg_{ads}^{-1} were achieved. For heat storage, the material-based ESD_{heat} of 0.934 MJ kg_{ads}^{-1} (0.607 GJ m^{-3}) and averaged specific discharge power of 504 W kg_{ads}^{-1} were achieved. For the charging process, the averaged specific charge power was 663 W kg_{ads}^{-1}.

Chapter 6.

Sorption thermal energy storage: experimental study and modeling

Alongside the detailed heat and mass transfer analysis of the sorber bed, presented in Chapter 4 and Chapter 5, the system modeling including all components, i.e. sorber bed, evaporator, and condenser, is essential for performance prediction, design, application feasibility study, and optimization. In this chapter, a lumped thermodynamic resistance-capacitance model is developed and validated against the experimental data collected for a lab-scale S-TES system.[4]

6.1. Background

To design, evaluate and optimize an S-TES system, developing a reliable easy-to-use model is crucial. Three types of models were defined by Yong et al. [164]: (i) thermodynamic steady-state models, (ii) dynamic lumped-parameter models, and (iii) heat and mass transfer models. Thermodynamic steady-state models are simple but not practical for the sorption systems due to the transient nature of sorption. However, such models present the upper performance limits, which can be valuable in the early-stage design and material selection.

The complexity and nonlinearity of the coupled heat and mass transfer make developing an analytical solution highly unlikely without simplifying assumptions, which leads to some limitations for model application. Numerical heat and transfer models provide more details of the heat transfer and adsorption dynamic, although they are more complex and may not be possible for modeling the whole sorption system, including all the components.

Proper model selection is of great importance and should be done considering complexity, accuracy, realistic assumptions, and computational time and cost. An alternative approach in modeling the operation of S-TES, namely transient temperatures,

[4] The results of this chapter were presented in International Sorption Heat Pump Conference (ISHPC 2017) [8].

uptake, and performance, is developing lumped-parameter models which require accurate thermophysical and thermochemical properties of sorption materials as well as heat and mass transfer coefficients in heat/mass exchangers.

6.1.1. The ideal closed S-TES cycle

The S-TES systems usually consist of two HEXs: sorber/desorber HEX and evaporator/condenser HEX, as schematically shown in Figure 47a. However, a separate HEX for the condenser is considered in some designs [56]. The ideal thermodynamic cycle of the S-TES is shown in a temperature-pressure diagram in Figure 47b, consisting of 4 processes, which are preheating (1-2), desorption-condensation (2-3), precooling (3-4), and sorption-evaporation (4-1). A brief overview of the cycle for the main processes is given below.

Isosteric preheating process (1-2):

Before the charging process when the sorbent is cold and saturated with the sorbate at $\omega_{\max}$, heat is transferred from the driving heat source to the sorber bed, while the valve between the sorber bed and the condenser is closed. Thus, the pressure inside the sorber bed increases, while ideally, the uptake inside the sorbent remains constant (i.e. at $\omega_{\max}$). The constant-uptake preheating (1-2) is valid if the volume of vapor inside the sorber bed is negligibly small (i.e. low dead volume) [165].

Desorption-condensation process (2-3):

When the sorber bed pressure reaches the condenser pressure, i.e. saturation pressure at heat sink temperature of T_{cond}, the valve between the sorber bed and condenser is open. Thereafter, the desorption-condensation process (2-3) starts and the sorbate is desorbed from the sorbent and then condensed in the condenser, ideally at the constant pressure (P_{cond}) [165]. The constant-pressure desorption-condensation is valid when the condenser HEX provides an infinite overall heat transfer coefficient, and hence, the desorbed vapor shall be condensed immediately [165]. Moreover, for an ideal cycle, the temperature gradient between the sorber bed and the driving heat source should be negligible to reach the maximum desorption temperature [165]. This clearly indicates the importance of designing superior HEX for sorber beds and reducing thermal resistance in the heat transfer path, including TCR at the interface between the sorbent coating/particle

and HEX surface. The desorption process proceeds until the sorbent water uptake reaches the cycle minimum uptake ($\omega_{\min}$) at state point 3 (see Figure 47).

Isosteric precooling process (3-4):

By rejecting the sorber bed heat to the district heating network or another heat sink, sorber bed is cooled down and consequently vapor pressure inside the sorber bed decreases. During the precooling process, the sorbent is ideally at constant uptake ($\omega_{\min}$).

Sorption-evaporation process (4-1):

When the sorber bed pressure reaches the evaporator pressure, i.e. saturation pressure at T_{evap}, the valve between the sorber bed and evaporator is open. The vapor sorption by sorber bed continues until the sorbent is saturated at $\omega_{\max}$. The heat of sorption is transferred to the heating network as the useful heat [165]. In an ideal cycle, the evaporation-sorption process takes place under constant pressure assuming that the evaporator HEX has an infinite heat transfer capacity.

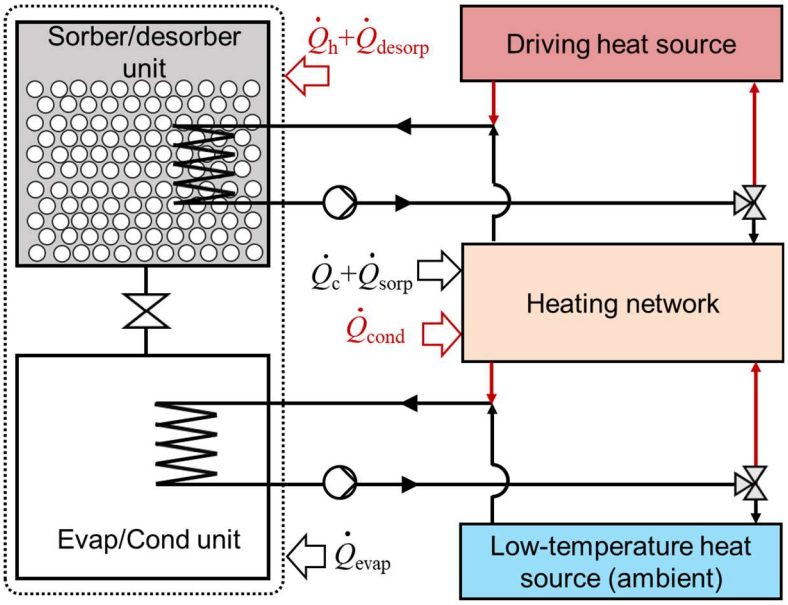

(a)

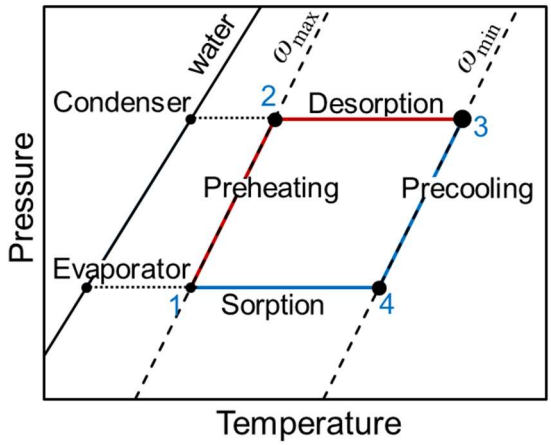

(b)

Figure 47. (a) A two-HEX S-TES concept [165], and (b) the ideal closed sorption thermodynamic cycle.

6.2. Lumped-parameter model for closed S-TES

In this study, a fully transient lumped-parameter model has been developed to study the performance of a closed S-TES system, shown in Figure 47. The main assumptions of the present model are [166]:

(i) Thermal equilibrium condition between the sorbate and sorbent,

(ii) Uniform sorbent particle size in a loose grain sorber bed, and/or uniform coating thicknesses in a coated sorber bed,

(iii) Negligible heat loss to the ambient for the cyclic operation,

(iv) Uniform water uptake in the sorbent, and

(v) Negligible vapor pressure losses in the sorbate flow, both from the evaporator to the sorber bed and from the sorber bed to the condenser; during the sorption process, the pressure inside the sorber equals that of the inside the evaporator, and during the desorption process, the pressure inside the sorber equals that inside the condenser.

6.2.1. Charging process modeling

During the preheating process, as explained in Section 1.4, the sorber bed is heated by the heat source at desorption temperature, while it is disconnected from the condenser. Hence, the energy balance of the sorber bed is given by the following equation:

$$d\left[\left\{m_{\mathrm{s}}\left(c_{p,\mathrm{s}}+\omega_{\max}\,c_{p,\mathrm{lw}}\right)+c_{\mathrm{HEX}}\,m_{\mathrm{HEX}}\right\}T_{\mathrm{s}}\right]/\,dt=\dot{m}_{\mathrm{hf}}c_{p,\mathrm{hf}}\left(T_{\mathrm{hf,in}}-T_{\mathrm{hf,out}}\right) \tag{33}$$

In Eq. (33), the left-hand side presents the change rate of the internal energy of the sorber bed due to the total thermal inertia, including sorbents, adsorbed sorbate, and sorber bed HEX. The maximum water uptake, which is achieved at the end of the sorption process, is shown as $\omega_{\max}$ and assumed to remain unchanged during the preheating process. The right-hand side in Eq. (33), represents the extracted amount of heat from the heating fluid. Considering short time intervals, for the small temperature difference across the heating fluid, the log mean temperature difference (LMTD) method can be applied. Therefore, the outlet heating fluid temperature is as follows:

$$T_{\mathrm{hf,out}}=T_{\mathrm{s}}+\left(T_{\mathrm{hf,in}}-T_{\mathrm{s}}\right)\exp\left(\frac{-U_{\mathrm{bed}}\,A_{\mathrm{bed}}}{\dot{m}_{\mathrm{hf}}\,c_{p,\mathrm{hf}}}\right) \tag{34}$$

where U_{bed} and A_{bed} are the sorber bed overall heat transfer coefficient and heat transfer surface area, respectively. When the sorber bed pressure exceeds the condenser pressure, the connecting valve between the sorber bed and condenser is opened, which leads to an increase in the sorber bed temperature and pressure, leading to water desorption. During desorption, the mass balance in the sorber bed is governed by Eq. (35).

$$d\left[\left\{m_{\mathrm{s}}\left(c_{p,\mathrm{s}}+\omega\, c_{p,\mathrm{lw}}\right)+c_{\mathrm{HEX}}\, m_{\mathrm{HEX}}\right\}T_{\mathrm{s}}\right]/\,dt = \Delta h_{\mathrm{ads}}\, m_{\mathrm{s}}\frac{d\omega}{dt}+\dot{m}_{\mathrm{hf}}c_{p,\mathrm{hf}}\left(T_{\mathrm{hf,in}}-T_{\mathrm{hf,out}}\right) \quad (35)$$

The first term in the right-hand side of Eq. (35) expresses the gained desorption heat through releasing of the sorbate by means of the sorption enthalpy, Δh_{ads}, and the sorbate uptake, ω. The energy balance in the condenser is shown in Eq. (36), which is coupled with the temperature and the uptake changes in the sorber bed.

$$\begin{aligned} d\left[\left(c_{\mathrm{cond}}\, m_{\mathrm{cond}}+c_{p,\mathrm{lw}}\, m_{\mathrm{lw}}\right)T_{\mathrm{cond}}\right]/\,dt \\ = -L_{\mathrm{w}}\, m_{\mathrm{s}}\frac{d\omega}{dt}+c_{p,\mathrm{vw}}\, m_{\mathrm{s}}\,\frac{d\omega}{dt}\,(T_{\mathrm{s}}-T_{\mathrm{cond}}) \\ +\dot{m}_{\mathrm{coolant}}\, c_{p,\mathrm{coolant}}\left(T_{\mathrm{coolant,in}}-T_{\mathrm{coolant,out}}\right) \end{aligned} \quad (36)$$

The left-hand side term in Eq. (36) shows the internal energy change of the condenser due to the thermal mass of the condenser HEX and the liquified sorbate. On the right-hand side, the first term represents the released latent heat of condensation of the desorbed sorbate, while the second term gives the released sensible heat of the desorbed sorbate. The last term in Eq. (36) represents the total amount of heat transferred to the coolant fluid with the outlet temperature, as follows:

$$T_{\mathrm{coolant,out}} = T_{\mathrm{cond}} + \left(T_{\mathrm{coolant,in}}-T_{\mathrm{cond}}\right)\exp\left(\frac{-U_{\mathrm{cond}}\, A_{\mathrm{cond}}}{\dot{m}_{\mathrm{coolant}}\, c_{p,\mathrm{coolant}}}\right) \quad (37)$$

6.2.2. Storage period modeling

Under cyclic operation, i.e. without storage period, the heat loss from the storage medium is assumed negligible. However, for the short-term storage, the component temperatures are functions of the storage time, their surrounding temperature (T_{a}), and their thermal mass, as shown in Eq. (38).

$$\left(T_{i,t}-T_{\mathrm{a}}\right)/\left(T_{i,0}-T_{\mathrm{a}}\right) = \exp(-\,t/(R_i C_i)) \quad (38)$$

where i indicate the component of the S-TES (i.e. sorber bed, evaporator, and condenser) and $T_{i,0}$ is the initial component temperature. The ambient convection resistance and the lumped thermal capacitance are $R_i = 1/(h_{i-\mathrm{a}}\, A_i)$ and $C_i = m_i c_i$, respectively. For long-term storage period, the component temperatures reach the ambient temperature, T_{a}.

6.2.3. Discharging process modeling

For cyclic operation or short-term storage, precooling of the sorber bed is required prior to the adsorption process. The energy balance of the sorber bed during the precooling process and the outlet cooling fluid temperatures are given by the following equations, where $\omega_{\min}$ is the minimum water uptake at the end of desorption:

$$d\left[\left\{m_{\mathrm{s}}\left(c_{p,\mathrm{s}}+\omega_{\min}\,c_{p,\mathrm{lw}}\right)+c_{\mathrm{HEX}}\,m_{\mathrm{HEX}}\right\}T_{\mathrm{s}}\right]/\,dt=\dot{m}_{\mathrm{cf}}c_{p,\mathrm{cf}}\left(T_{\mathrm{cf,in}}-T_{\mathrm{cf,out}}\right) \tag{39}$$

$$T_{\mathrm{cf,out}}=T_{\mathrm{s}}+\left(T_{\mathrm{cf,in}}-T_{\mathrm{s}}\right)\exp\left(\frac{-U_{\mathrm{bed}}\,A_{\mathrm{bed}}}{\dot{m}_{\mathrm{cf}}\,c_{p,\mathrm{cf}}}\right) \tag{40}$$

The valve between sorber bed and evaporator is opened, as soon as the sorber bed pressure falls below the evaporator pressure. The mass balance in the sorber bed is given by Eq. (41).

$$\begin{aligned}d\left[\left\{m_{\mathrm{s}}\left(c_{p,\mathrm{s}}+\omega\,c_{p,\mathrm{lw}}\right)+c_{\mathrm{HEX}}\,m_{\mathrm{HEX}}\right\}T_{\mathrm{s}}\right]/\,dt&\\ =\Delta h_{\mathrm{sorp}}\,m_{\mathrm{s}}\frac{d\omega}{dt}-m_{\mathrm{s}}\,c_{p,\mathrm{vw}}\left(T_{\mathrm{s}}-T_{\mathrm{evap}}\right)\frac{d\omega}{dt}&\\ +\dot{m}_{\mathrm{cf}}c_{p,\mathrm{cf}}\left(T_{\mathrm{cf,in}}-T_{\mathrm{cf,out}}\right)&\end{aligned} \tag{41}$$

The second term on the right-hand side of Eq. (41) is the sensible heat transferred from the evaporator to the bed through the adsorbed sorbate vapor. The energy balance and the outlet chilled water temperature are given by Eqs. (42) and (43).

$$\begin{aligned}d\left[\left(c_{\mathrm{evap}}\,m_{\mathrm{evap}}+c_{p,\mathrm{aw}}\,m_{\mathrm{w}}\right)T_{\mathrm{evap}}\right]/\,dt&\\ =-L_{\mathrm{w}}\,m_{\mathrm{s}}\frac{d\omega}{dt}+c_{p,\mathrm{w}}\,m_{\mathrm{s}}\,\frac{d\omega}{dt}\left(T_{\mathrm{cond}}-T_{\mathrm{evap}}\right)&\\ +\dot{m}_{\mathrm{chilled}}\,c_{p,\mathrm{chilled}}\left(T_{\mathrm{chilled,in}}-T_{\mathrm{chilled,out}}\right)&\end{aligned} \tag{42}$$

$$T_{\mathrm{chilled,out}}=T_{\mathrm{evap}}+\left(T_{\mathrm{chilled,in}}-T_{\mathrm{evap}}\right)\exp\left(\frac{-U_{\mathrm{evap}}\,A_{\mathrm{evap}}}{\dot{m}_{\mathrm{chilled}}\,c_{p,\mathrm{chilled}}}\right) \tag{43}$$

6.2.4. Sorption uptake modeling

The non-equilibrium uptake change is calculated based on the classical linear driving force (LDF) solution proposed by Glueckauf [167], shown in Eq. (44).

$$\frac{d\omega}{dt}=k_{\mathrm{LDF}}\left(\omega_{\mathrm{eq}}-\omega\right) \tag{44}$$

The sorption rate constant, k_{LDF}, is obtained by equation Eq. (45) for the sorbent particles [168] and by Eq. (46) for the coated adsorbent layers [161], where D_{s0}, E_{a}, r_{p} and l_{coated} are the pre-exponent diffusivity constant, sorbent activation energy, sorbent particle diameter and sorbent coating thickness, respectively. The coefficients of k_{LDF}, D_{s0}, and E_{a} are extracted from the experimental data on the uptake changes and listed in Table 16.

$$k_{\mathrm{LDF}} = \left(15\ D_{\mathrm{s0}} \exp(-E_a/RT)\right)/r_p^2 \tag{45}$$

$$k_{\mathrm{LDF}} = \left(3\ D_{\mathrm{s0}} \exp(-E_a/RT)\right)/l_{\mathrm{coated}}^2 \tag{46}$$

Table 16. Parameters of linear driving force model including sorption rate constant (k_{LDF}), pre-exponent diffusivity constant (D_{so}), and sorbent activation energy (E_{a}).

Parameter		Loose grain bed	Coated bed
k_{LDF}	(s^{-1})	5.1208×10^{-4}	2.1277×10^{-3}
D_{s0}	(m^2s^{-1})	5.55×10^{-6}	1.04×10^{-5}
E_{a}	($Jmol^{-1}$)	30240	30240

6.2.5. Thermal resistance-capacitance (RC) network of a closed S-TES

The heat flow in energy Eqs. (33)-(43) of the above-mentioned lumped-parameter model can be illustrated as the proposed resistance-capacitance (RC) thermal networks analogue to electric circuits in Figure 48. Sorption heat is represented as the current source while the constant inlet temperatures of HTF, coolant and chilled water are shown as a voltage source. All the resistance, capacitance, and heat source equations are listed in Table 17.

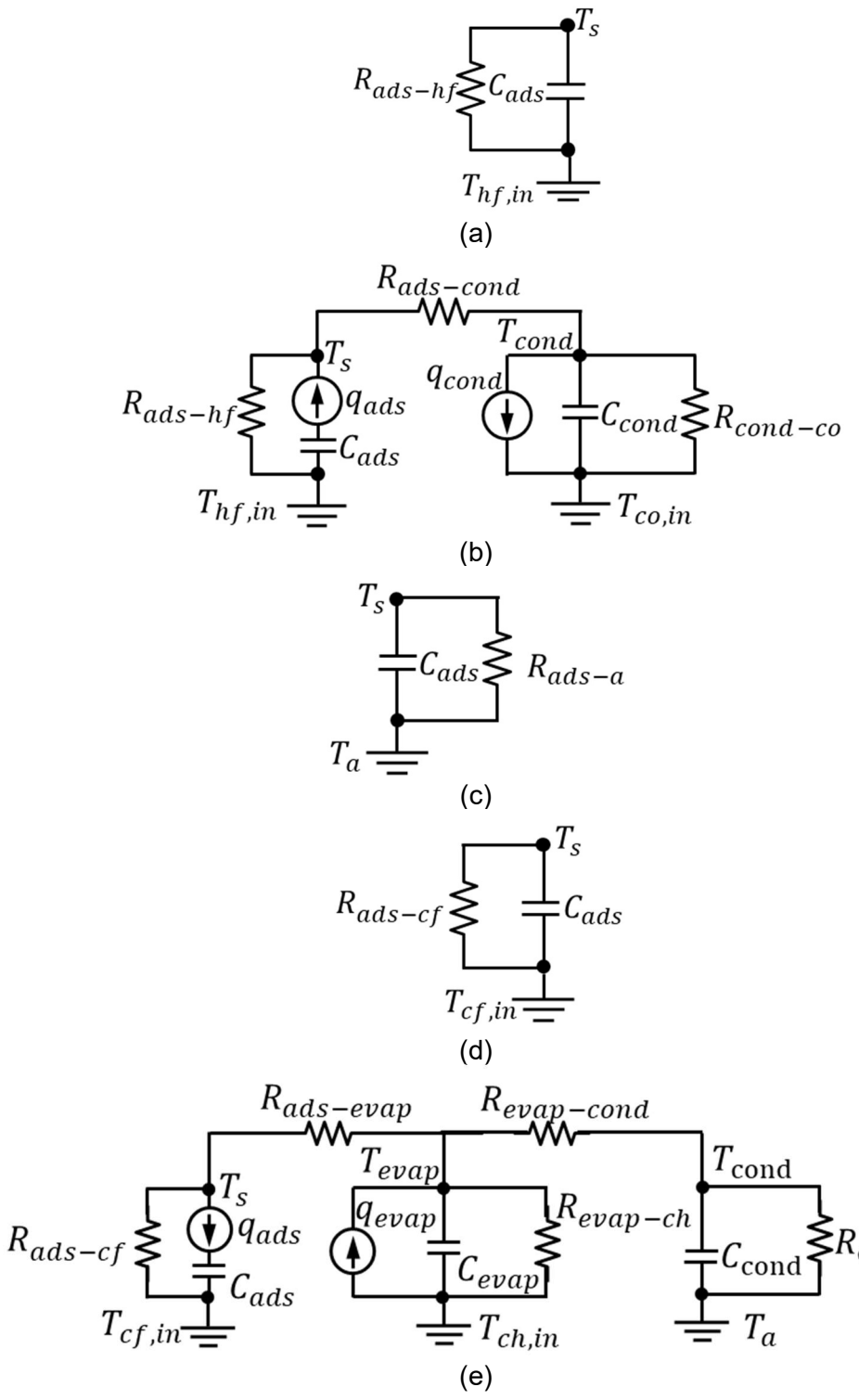

Figure 48. Simplified resistance-capacitance (RC) circuit model for the (a) preheating, (b) desorption (charging), (c) storage, (d) precooling, and (e) adsorption (discharging) processes in an S-TES system, considering negligible heat loss to the ambient.

Table 17. Resistance, capacitance, and heat source equations for charging, discharging, and storage periods, corresponding to the RC networks shown in Figure 48.

Parameter		Formula	
		Charging	
		Preheating	**Desorption**
$R_{\text{ads-hf}}$	Resistance between sorber bed and heating fluid	$\frac{1}{\dot{m}_{\text{hf}} c_{p,\text{hf}} \left[1 - \exp\left(\frac{-U_{\text{bed}} A_{\text{bed}}}{\dot{m}_{\text{hf}} c_{p,\text{hf}}}\right)\right]}$	
$R_{\text{cond-co}}$	Resistance between condenser and coolant fluid	-	$\frac{1}{\dot{m}_{\text{co}} c_{p,\text{co}} \left[1 - \exp\left(\frac{-U_{\text{cond}} A_{\text{cond}}}{\dot{m}_{\text{hf}} c_{p,\text{hf}}}\right)\right]}$
$R_{\text{ads-cond}}$	Resistance between condenser and sorber bed	-	$1/\left(c_{p,\text{vw}} m_{\text{s}} \frac{d\omega}{dt}\right)$
C_{ads}	Thermal capacitance of sorber bed	$\{m_{\text{s}} (c_{p,s} + \omega_{\max} c_{p,\text{lw}}) + c_{\text{HEX}} m_{\text{HEX}}\}$	$\{m_{\text{s}}(c_{p,s} + \omega c_{p,\text{lw}}) + c_{\text{HEX}} m_{\text{HEX}}\}$
C_{cond}	Thermal capacitance of condenser	-	$(c_{\text{cond}} m_{\text{cond}} + c_{p,\text{lw}} m_{\text{lw}})$
q_{ads}	Heat source in sorber bed	-	$\Delta h_{\text{sorp}} m_{\text{s}} \frac{d\omega}{dt}$
q_{cond}	Heat source in condenser	-	$L_{\text{w}} m_{\text{s}} \frac{d\omega}{dt}$
		Discharging	
		Precooling	**Adsorption**
$R_{\text{ads-cf}}$	Resistance between sorber bed and heating fluid	$\frac{1}{\dot{m}_{\text{cf}} c_{p,\text{cf}} \left[1 - \exp\left(\frac{-U_{\text{bed}} A_{\text{bed}}}{\dot{m}_{\text{cf}} c_{p,\text{cf}}}\right)\right]}$	
$R_{\text{evap-ch}}$	Resistance between condenser and coolant fluid	-	$\frac{1}{\dot{m}_{\text{ch}} c_{p,\text{ch}} \left[1 - \exp\left(\frac{-U_{\text{evap}} A_{\text{evap}}}{\dot{m}_{\text{ch}} c_{p,\text{ch}}}\right)\right]}$
$R_{\text{evap-cond}}$	Resistance between condenser and evaporator	-	$1/\left(c_{p,\text{w}} m_{\text{s}} \frac{d\omega}{dt}\right)$
$R_{\text{ads-evap}}$	Resistance between condenser and sorber bed	-	$1/\left(c_{p,\text{vw}} m_{\text{s}} \frac{d\omega}{dt}\right)$
C_{ads}	Thermal capacitance of sorber bed	$\{m_{\text{s}} (c_{p,s} + \omega_{\min} c_{p,\text{lw}}) + c_{\text{HEX}} m_{\text{HEX}}\}$	$\{m_{\text{s}} (c_{p,s} + \omega c_{p,\text{lw}}) + c_{\text{HEX}} m_{\text{HEX}}\}$
C_{evap}	Thermal capacitance of condenser	-	$(c_{\text{evap}} m_{\text{evap}} + c_{p,\text{aw}} m_{\text{w}})$
q_{ads}	Heat source in sorber bed	-	$\Delta h_{\text{sorp}} m_{\text{s}} \frac{d\omega}{dt}$
q_{evap}	Heat source in condenser	-	$L_{\text{w}} m_{\text{s}} \frac{d\omega}{dt}$
		Storage	
$R_{\text{ads-amb}}$	Resistance of sorber bed	$1/(h_s A_{\text{s}})$	
C_{ads}	Thermal capacitance of sorber bed	$\{m_{\text{s}} (c_{p,s} + \omega_{\min} c_{p,\text{lw}}) + c_{\text{HEX}} m_{\text{HEX}}\}$	

6.2.6. Model parameters

Sorption equilibrium properties

Experimental data of water sorption onto the microporous sorbent material is widely described by Polanyi potential theory, using the sorption potential $A(\mathrm{J\,mol^{-1}})$, as defined in Eq. (47) [169]. Among the isotherms based on the micro-pore filling theory of Polanyi, Dubinin–Astakhov, Eq. (48), is widely used for describing sorption equilibrium uptake for TES applications since it allows to directly obtain the differential heat of sorption for storage applications and only has three unknown parameters [169]. These parameters, the maximum sorbed volume, ω_0 (kg kg^{-1}), characteristic energy, E (J mol^{-1}), and empirical constant, n, can be determined by the thermogravimetric measurements [169]. It also has been proved to correlate the uptake behavior of FAM-Z02 properly [104], [170]. The parameters used in the equilibrium uptake Eq. (48) are listed in Table 18, using the TGA data reported by Goldsworthy [135] for the sorbent particles, and McCague et al. [162] for the coated FAM-Z02.

$$A = RT \ln\left(\frac{P_s}{P}\right) \tag{47}$$

$$\omega_{eq} = \omega_0 \exp\left(-\left(\frac{A}{E}\right)^n\right) \tag{48}$$

Table 18. The constants used in the water uptake equilibrium Eq. (48) for loose grain and coated FAM-Z02. $A = RT \ln(P_s/P)$, ω_0 (kg kg^{-1}), E (J mol^{-1}), and n are the Polanyi sorption potential, maximum sorbed volume, characteristic energy, and empirical constant, respectively.

	Loose grain FAM-Z02				Coated FAM-Z02			
	ω_0 (kgkg^{-1})	n		E (Jmol^{-1})	ω_0 (kgkg^{-1})	n		E (Jmol^{-1})
Ads	0.31	3	$A < 2550\ (\mathrm{Jmol^{-1}})$	8910	0.29	3	$A < 3550\ (\mathrm{Jmol^{-1}})$	8197
			$A \geq 2550\ (\mathrm{Jmol^{-1}})$	7128			$A \geq 3550\ (\mathrm{Jmol^{-1}})$	7840
Des	0.28	3	$A < 2450\ (\mathrm{Jmol^{-1}})$	7425	0.28	3	$A < 4200\ (\mathrm{Jmol^{-1}})$	8315
			$A \geq 2450\ (\mathrm{Jmol^{-1}})$	6534			$A \geq 4200\ (\mathrm{Jmol^{-1}})$	7128

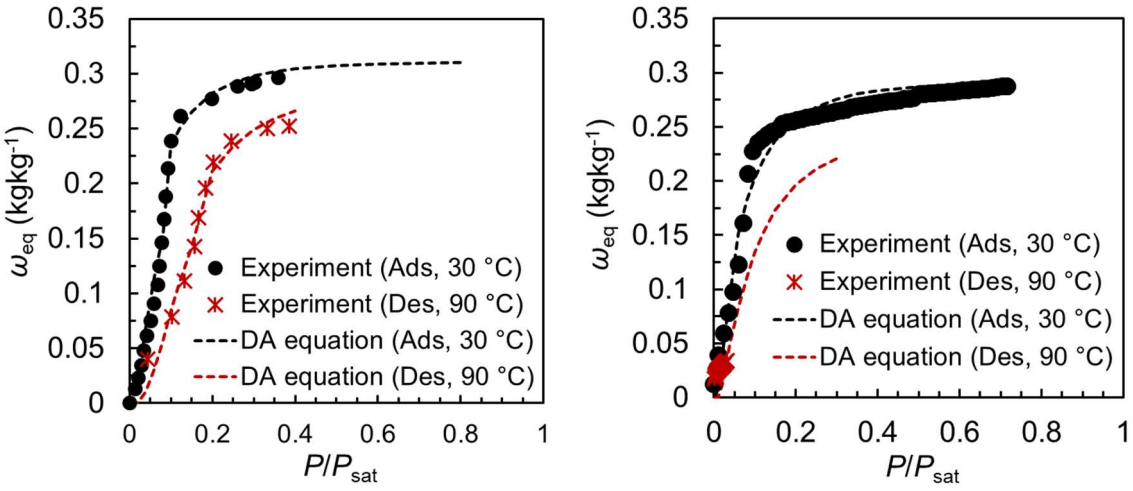

(a) (b)

Figure 49. Measured sorption equilibrium isotherm and fitted line to DA equation (Eq. (48)) for FAM-Z02 in the form of (a) 2 mm particles [135], and (b) 0.3 mm coating layer, collected in our lab [162].

Heat exchangers design parameters

Since heat transfer plays an important role in the sorption dynamic, it is beneficial to calculate the heat transfer coefficient between the sorber bed HEX and the sorbent material. The heat generated in the sorber bed is removed by the HTF in the sorber bed HEX, therefore, the overall heat transfer coefficient (U_{bed}) is a function of (i) HTF temperature, (ii) HTF flow rate, (iii) sorbent thermal conductivity, and (iv) HEX geometry, design, and material. The overall thermal conductance, $(UA)_{\mathrm{bed}}$, is evaluated using Eq. (49).

$$(UA)_{\mathrm{bed}} = \frac{\dot{Q}_{\mathrm{ads/des}}}{\overline{\Delta T}_{\mathrm{ads/des}}} \tag{49}$$

$\overline{\Delta T}_{\mathrm{ads/des}}$ is the averaged temperature difference between sorption/desorption processes and defined by $\mathrm{LMTD}_{\mathrm{ads/des}}$ (Eq. (50)).

$$\mathrm{LMTD}_{\mathrm{ads/des}} = \frac{T_{\mathrm{htf,in}} - T_{\mathrm{htf,out}}}{\ln\left(\frac{T_{\mathrm{ads/des}} - T_{\mathrm{htf,in}}}{T_{\mathrm{ads/des}} - T_{\mathrm{htf,out}}}\right)} \tag{50}$$

The arithmetic mean temperature difference (AMTD) is another approximate for $\overline{\Delta T}_{\mathrm{ads/des}}$ [118], [171], which is the difference between the average temperatures of HTF and the sorber bed, as defined in Eq. (51).

$$\mathrm{AMTD}_{\mathrm{ads/des}} = T_{\mathrm{ads/des}} - \left(\frac{T_{\mathrm{htf,in}} + T_{\mathrm{htf,out}}}{2}\right) \quad (51)$$

Overall thermal conductance of sorber bed $(UA)_{\mathrm{bed}}$, evaporator $(UA)_{\mathrm{evap}}$, and condenser $(UA)_{\mathrm{cond}}$ are listed in Table 19.

Table 19. Model parameters of sorber bed, evaporator, and condenser HEXs.

Parameter		Packed bed	Coated bed
$(UA)_{\mathrm{evap}}$	(W K^{-1})	150 ($T_{\mathrm{evap}} = 10$ ℃) 250 ($T_{\mathrm{evap}} = 15$ ℃)	
A_{evap}	(m^2)	0.49	
$(UA)_{\mathrm{cond}}$	(W K^{-1})	167 ($T_{\mathrm{cond}} = 30$ ℃) 96 ($T_{\mathrm{cond}} = 40$ ℃)	
A_{cond}	(m^2)	2	
$(UA)_{\mathrm{ave,ads,HEX}}$	(W K^{-1})	-	98
$(UA)_{\mathrm{max,ads,HEX}}$	(W K^{-1})	-	815 (beginning of sorption)
$A_{\mathrm{ads,HEX}}$	(m^2)	2.1 (1500 g of sorbent) 0.74 (500 g of sorbent)	2.8
$(mc)_{\mathrm{ads,HEX}}$	(J K^{-1})	3351	

6.3. Experimental study

A front view of a modular vacuum sorption system, built in our lab [71], is shown in Figure 50. An off-the-shelf engine oil cooler, manufactured by Hayden Automotive (model #1268), was chosen as the sorber bed, shown in Figure 50b. Two sorbent configurations were studied: (i) packed bed with 0.5 kg of 2 mm FAM-Z02 particles (Figure 50c), and (ii) coated sorber bed with 0.3 mm coating layer of FAM-Z02 (Figure 50d), fabricated by Mitsubishi Plastics. Two TCS were used (details are described in Section 5.2) at 30 °C for cooling down the sorber bed and at 90 °C for heating up the bed during the charging process. As shown in Figure 50e, a custom-built capillary-assisted low-pressure evaporator with inclined circumferential micro-groove enhanced tubes [172] was used as the sorbate vapor generator. Details of the sorber HEX and evaporator are listed in Table 27 and Table 28 in Appendix E. A custom-built shell-and-tube HEX (Figure 50f) was used as the condenser. The expansion valve was a needle valve with high precision flow adjustment. A control valve was located between the sorber bed and evaporator, which was aimed to isolate the sorber bed from the evaporator in the heat storage period. A relay

switch was controlled automatically, using a LabVIEW program, to switch the connection of sorber bed to TCS. Working pair specifications and operating conditions are listed in Table 20.

T-type thermocouples (Omega, model #5SRTC-TT-T-36-36) with an accuracy of 0.75% of reading in degree Celsius and pressure transducers (Omega, model #PX309-005AI) with 0–34.5 kPa absolute pressure range and ±0.4 kPa accuracy were used to measure temperature and pressure. Two positive displacement flow meters (FLOMEC, Model#OM015S001-222) with an accuracy of 0.5% of reading in $Lmin^{-1}$, were used to measure the flow rates of sorber bed heating/cooling fluid (silicone oil) and chilled/coolant (water). In order to dry the sorbent in the preparation step, the sorber bed was heated up to 100 °C and outgassed, being connected to a vacuum pump for 8-12 hours.

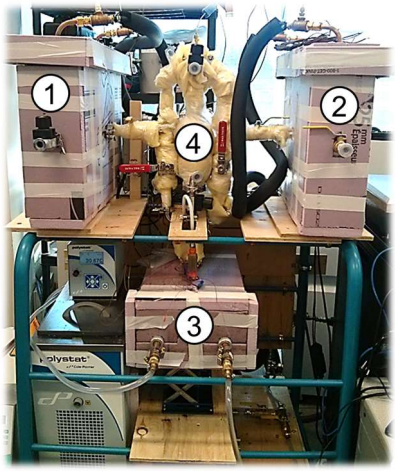

(a)

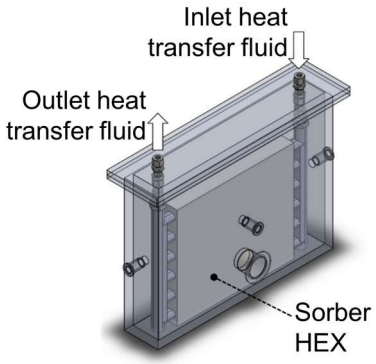

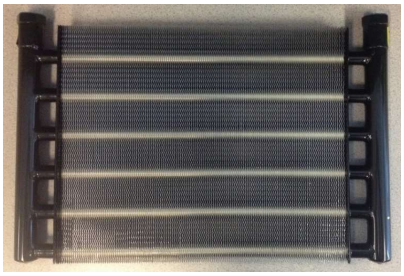

(b)

(c)

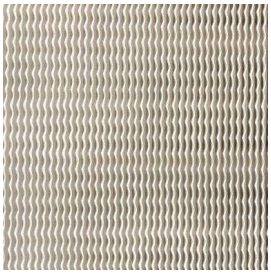

(d)

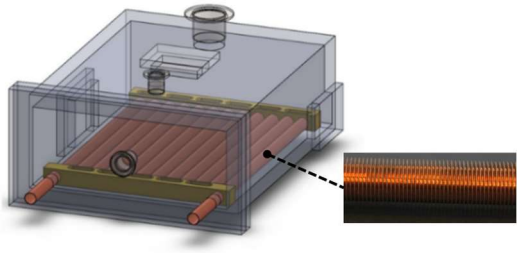

(e)

(f)

Figure 50. Custom-built experimental test bed: (a) front-view of the sorption closed system including (1) and (2) sorber beds, (3) evaporator, and (4) condenser, (b) off-the-shelf fin-tube sorber HEX with copper tube (black painted) and aluminum fins, (c) packed bed with 2 mm FAM-Z02 particles, (d) coated HEX with 0.3 mm layer of FAM-Z02, (e) custom-built capillary-assisted low-pressure evaporator, and (d) off-the-shelf condenser.

Table 20. Working pair specifications and operating conditions.

Parameter	Packed bed	Coated bed
Working pair	AQSOA FAM-Z02 / water	
Adsorbent particles diameter (mm)	2	-
Adsorbent coating thickness (mm)	-	0.3
Adsorbent mass (kg)	0.5	0.766
Heating fluid mass flow rate (kg s^{-1})	0.058	
Cooling fluid mass flow rate (kg s^{-1})	0.062	
Coolant water mass flow rate (kg s^{-1})	0.052	
Chilled water mass flow rate (kg s^{-1})	0.037	
Heating fluid temperature (°C)	90	
Cooling fluid temperature (°C)	30	
Condensation temperature (°C)	30	
Evaporation temperature (°C)	15	

6.4. Results and discussion

6.4.1. Effect of the sorption-to-desorption time ratio on the storage performance

Figure 51 shows the estimated sorption uptake and ESD of the S-TES versus the sorption-to-desorption time ratio (r_t). Considering total time ($t_{\mathrm{ch}} + t_{\mathrm{dch}}$) of 1800 s, the maximum sorption uptake of 0.15 kg kg_{ads}^{-1}, heat storage ESD of 0.505 GJm^{-3}, and cold storage ESD of 0.239 GJm^{-3} were achieved. The optimum r_t is between 1.5 and 2. Due to the higher desorption rate compared to the sorption rate (as explained in Section 5.4.1), increasing the sorption-to-desorption time ratio to 1.5-2 improves the storage performance. One can conclude that finding the optimal r_t for a certain total time is of great importance. The theoretical model successfully can predict the trend and value of the experimental data.

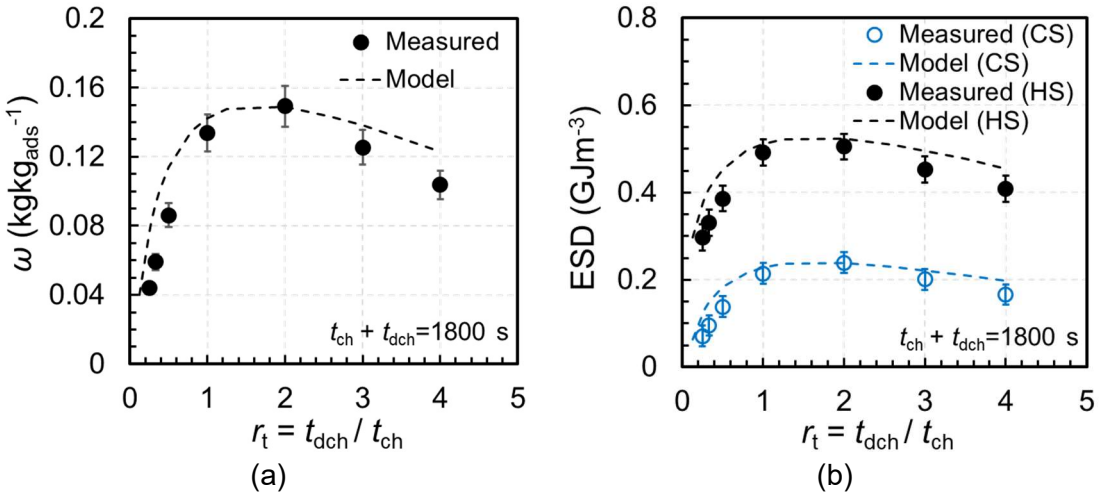

Figure 51. (a) Sorption uptake and (b) material-based ESD of the cold storage (CS) and heat storage (HS) vs sorption-to-desorption time ratio (r_t) for the 0.3 mm FAM-Z02 coated bed. The total time ($t_{\mathrm{ch}} + t_{\mathrm{dch}}$) of 1800 s is considered and operating temperatures are $T_{\mathrm{hf,in}} = 90$ °C , $T_{\mathrm{cf,in}} = 30$ °C , $T_{\mathrm{coolant,in}} = 30$ °C , $T_{\mathrm{chilled,in}} = 15$ °C .

Considering the optimum r_t of 1.625, Figure 52 shows the sorption uptake, ESD, and SP for the total time ($t_{\mathrm{ch}} + t_{\mathrm{dch}}$) of 525-4200 s. Both sorption uptake and ESD increase by total time until the maximum uptake of 0.184 kg kg_{ads}^{-1}, ESD_{heat} of 0.604 GJ m^{-3}, and ESD_{cold} of 0.295 GJ m^{-3} are reached. As shown in Figure 52c, a maximum SP_{cold} of 335 W kg_{ads}^{-1} is observed for the total time of 1050 s, while the highest SP_{heat} is 1207 W kg_{ads}^{-1}.

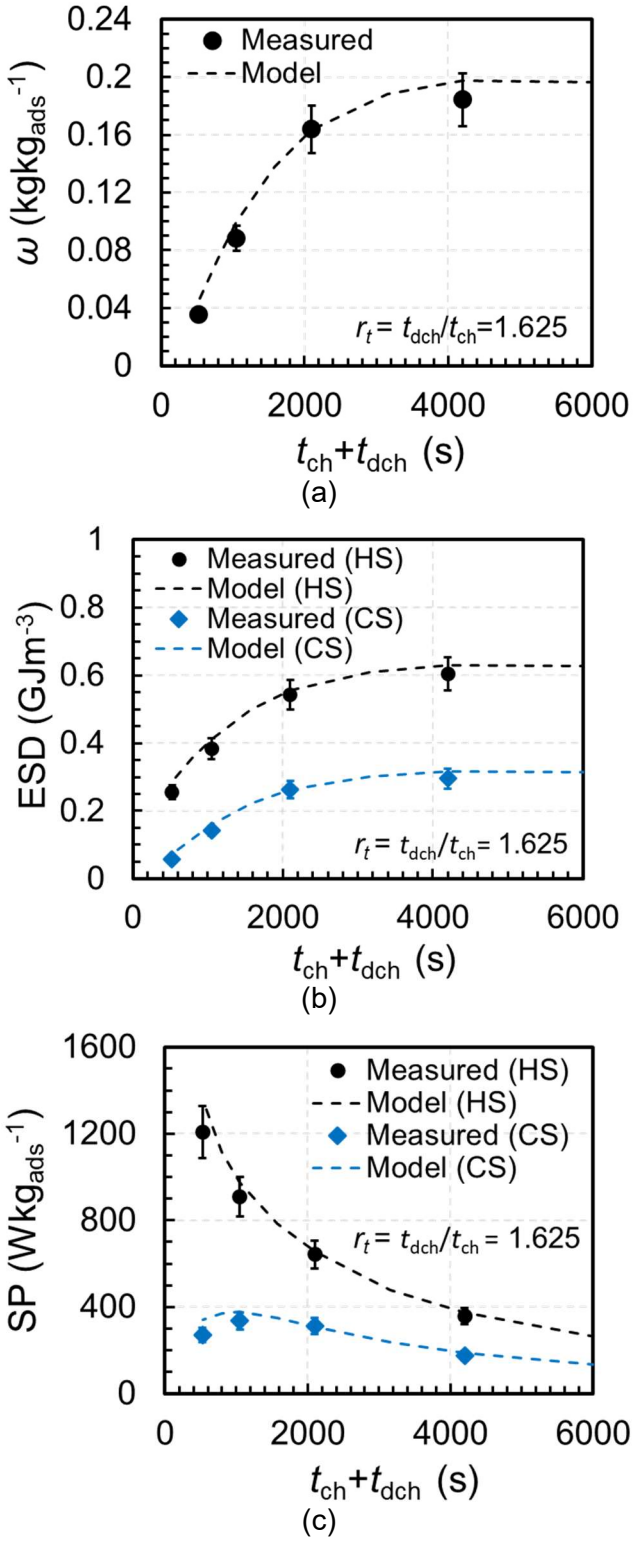

Figure 52. (a) Sorption uptake, (b) material-based ESD, and (c) SP of heat storage (HS) and cold storage (CS) versus total time ($t_{\mathrm{ch}} + t_{\mathrm{dch}}$) for the 0.3 mm FAM-Z02 coated bed. r_t is 1.625.
Operating temperatures are $T_{\mathrm{hf,in}} = 90$ ℃, $T_{\mathrm{cf,in}} = T_{\mathrm{coolant,in}} = 30$ ℃, and $T_{\mathrm{chilled,in}} = 15$ ℃.

6.4.2. Temperature changes: Model validation

Apart from the overall performance indicators such as ESD and average SP, the model should be able to predict the transient performance of S-TES, particularly for temperature regulation and peak load shaving applications. As shown in Figure 53, there is a satisfactory agreement between the measured temperatures and the model results, both for the loose grain (Figure 53a) and coated (Figure 53b) heat exchangers; the maximum temperature relative difference is 4% for loose grain bed and 3% for coated bed.

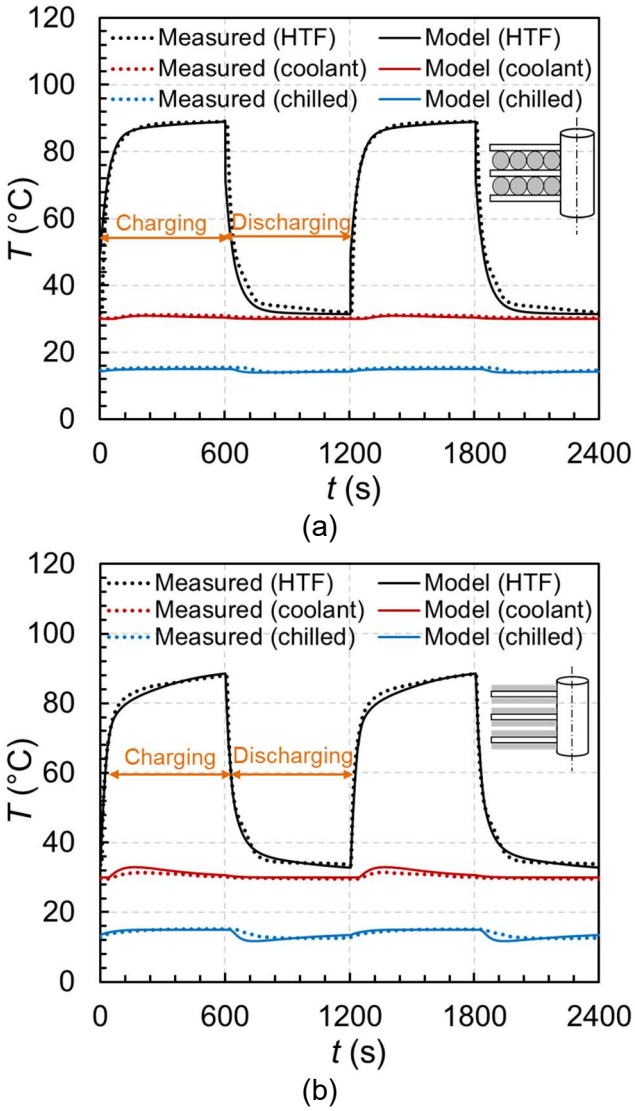

Figure 53. Temperature variation in the sorber bed, evaporator and condenser versus time, for (a) loose grain and (b) coated sorber bed — comparison between the theoretical model and experimental results. $T_{\mathrm{hf,in}} = 90\ ℃$, $T_{\mathrm{cf,in}} = T_{\mathrm{coola\ \ ,in}} = 30\ ℃$, $T_{\mathrm{chilled,in}} = 15\ ℃$, $r_t = t_{\mathrm{dch}}/t_{\mathrm{ch}} = 1$, and $t_{\mathrm{ch}} + t_{\mathrm{dch}} = 1200\ s$. The experimental data for loose grain and coated bed is presented in Appendix F.

6.4.3. System-based ESD: Loose grain vs coated bed

Figure 54 compares the system-based ESD of the coated and loose grain S-TES for heat and cold storage under cyclic operation. In both cold and heat storage at different cycle times, $\mathrm{ESD_{sys}}$ is higher for loose grain sorber bed. $\mathrm{ESD_{sys,heat}}$ is significantly higher than the $\mathrm{ESD_{sys,cold}}$ because: (i) heat of sorption, which is the useful energy in the heat storage, is more than the evaporation cooling, which is the useful energy in the cold storage, and (ii) sensible heat that is delivered to the bed in the charging process, is used

at the beginning of the sorption process as a part of the heat delivery. At cycle time of 1800 s, i.e. 600 s of charging and 600 s of discharging, $\mathrm{ESD_{sys,cold}}$ of loose grain sorber is 1.66 times higher than $\mathrm{ESD_{sys,cold}}$ of coated sorber, 0.106 GJ m^{-3} compared to 0.064 GJ m^{-3}. $\mathrm{ESD_{sys,heat}}$ of loose grain sorber is 2.63 times higher than $\mathrm{ESD_{sys,heat}}$ of coated sorber, 0.386 GJm^{-3} compared to 0.147 GJ m^{-3}.

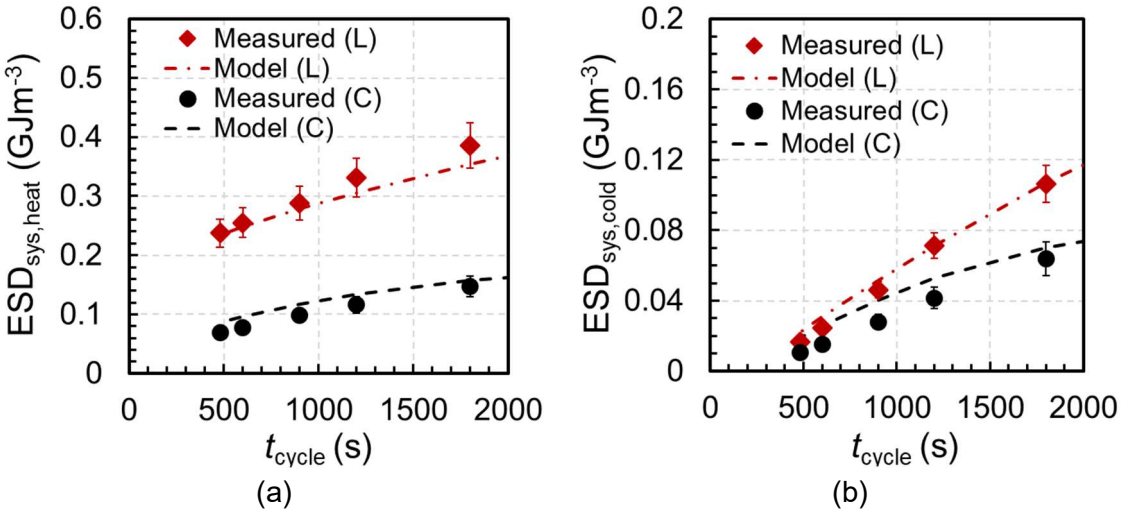

Figure 54. System-based ESD of (a) heat and (b) cold S-TES systems for loose grain (L) and coated (C) bed versus cycle time under cyclic operation. Operating conditions are as follows: $T_{\mathrm{hf,in}} = 90\ ^{\circ}\mathrm{C}$, $T_{\mathrm{cf,in}} = T_{\mathrm{coolant,in}} = 30\ ^{\circ}\mathrm{C}$, and $T_{\mathrm{chilled,in}} = 15\ ^{\circ}\mathrm{C}$. The ESD is per active volume of the sorber beds; active volume of the coated sorber bed is 3835 cm^3 ($A_{\mathrm{ht}} = 2.8\ \mathrm{cm}^2$) and active volume of loose grain sorber bed is 1013 cm^3 ($A_{\mathrm{ht}} = 0.74\ \mathrm{cm}^2$).

6.4.4. Effect of heating fluid temperature on the storage performance

Material-based ESD versus heating fluid temperature is shown in Figure 55a for loose grain and in Figure 55b for coated FAM-Z02. By increasing the heating fluid temperature from 70 to 90 °C, $\mathrm{ESD_{heat}}$ changes from 0.250 to 0.436 GJ m^{-3}, a 74% increase, for the loose grain bed, and from 0.245 to 0.378 GJ m^{-3}, a 54% increase, for the coated bed. Similarly, by increasing the heating fluid temperature from 70 to 90 °C, $\mathrm{ESD_{cold}}$ increases from 0.022 to 0.094 GJ m^{-3} for the loose grain bed and from 0.069 to 0.135 GJ m^{-3} for the coated bed.

Average SP versus heating fluid temperature is shown in Figure 55c for loose grain and in Figure 55d for coated FAM-Z02. By increasing the heating fluid temperature from 70 to 90 °C, $\mathrm{SP_{heat}}$ increases from 640 to 1119 W $\mathrm{kg_{ads}^{-1}}$ for the loose grain bed and from 627 to 970 W $\mathrm{kg_{ads}^{-1}}$ for the coated bed.

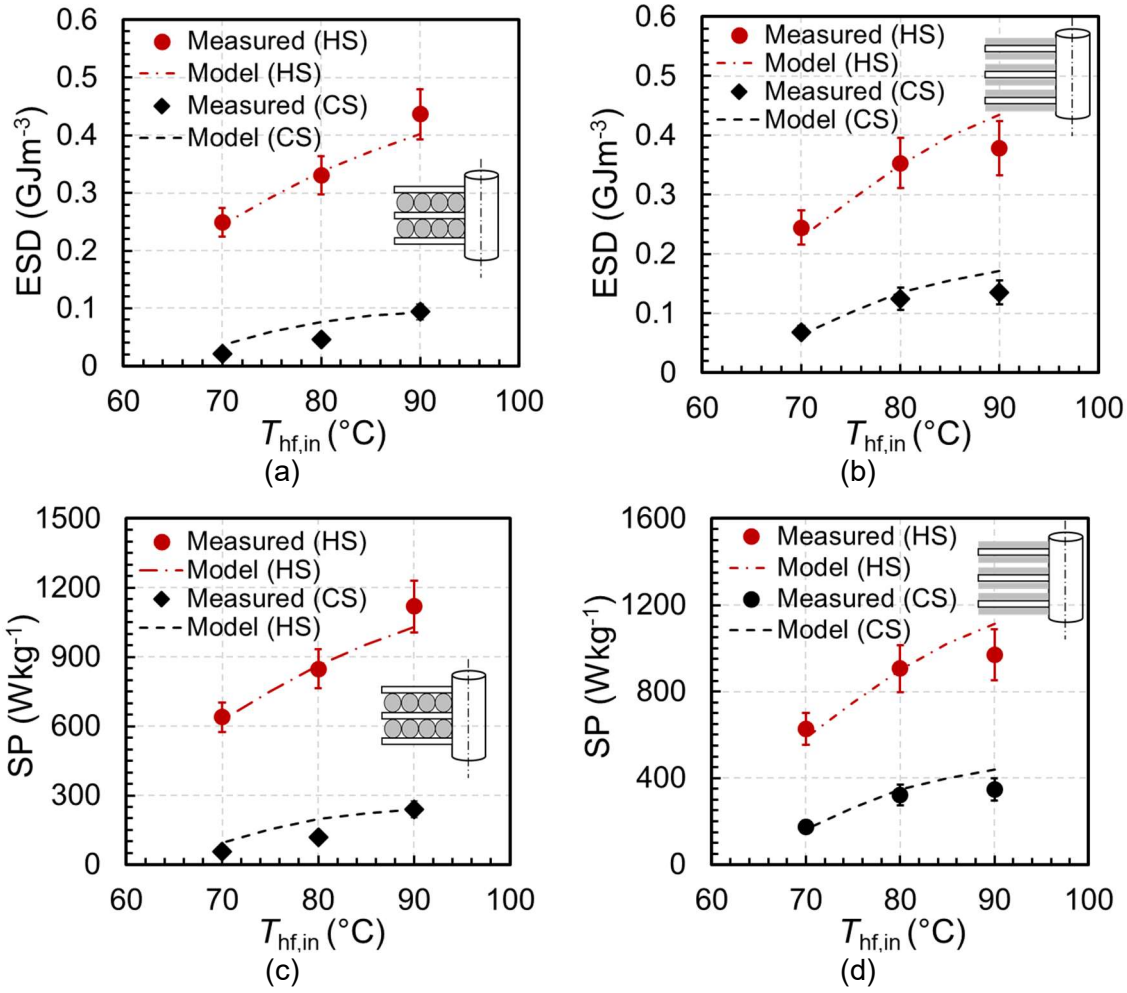

Figure 55. Material-based ESD of cold and heat storage versus heating fluid temperature for (a) 2 mm loose grain packed bed and (b) 0.2 mm coated FAM-Z02 sorber bed and average SP for (c) 2 mm loose grain packed bed and (d) 0.2 mm coated FAM-Z02 sorber bed. $T_{\mathrm{cf,in}} = T_{\mathrm{coolant,in}} = 30$ ℃, $T_{\mathrm{chilled,in}} = 15$ ℃, $r_t = 1$, and $t_{\mathrm{cycle}} = t_{\mathrm{ch}} + t_{\mathrm{dch}} = 1200$ s.

6.4.5. Effect of cooling fluid temperature on the storage performance

Figure 56 shows the effects of the cooling fluid temperature on the ESD and SP for 2 mm loose grain FAM-Z02 sorber bed. An increase in the cooling fluid temperature leads to a decrease in ESD and SP. By increasing the cooling fluid temperature from 30 to 45 °C, the ESD and SP are estimated to decrease by 24%.

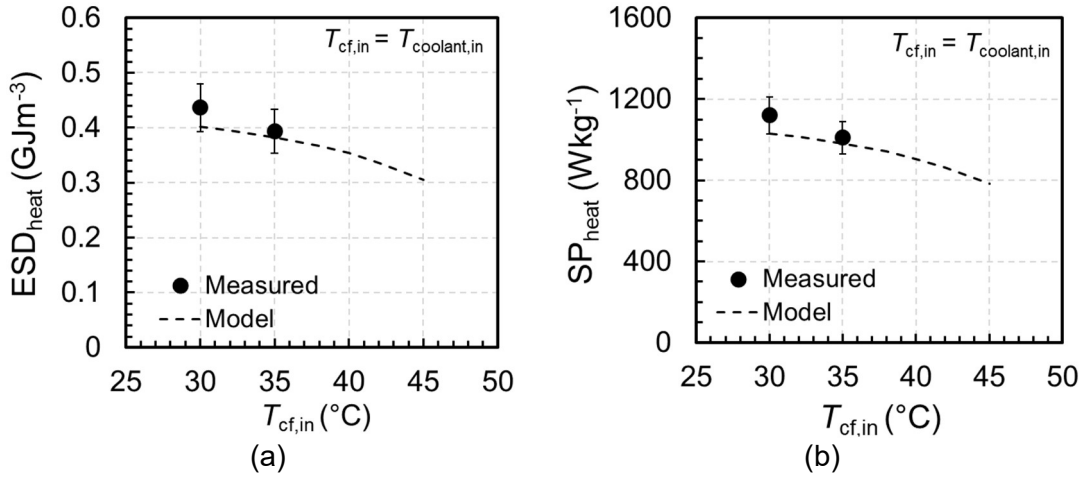

Figure 56. (a) ESD and (b) SP of heat storage 2 mm loose grain FAM-Z02 sorber bed vs cooling fluid inlet temperature. $T_{\mathrm{hf,in}} = 90$ ℃, $T_{\mathrm{chilled,in}} = 15$ ℃, $r_t = 1$, and $t_{\mathrm{cycle}} = t_{\mathrm{ch}} + t_{\mathrm{dch}} = 1200$ s.

6.4.6. Effect of chilled water temperature on the storage performance

Effect of the chilled water temperature on the storage performance is shown in Figure 57. An increase in the chilled water temperature leads to a higher sorption pressure, which improves storage performance. As shown in Figure 57a, sorption uptake increases from 0.045 kg kg_{ads}^{-1} for $T_{\mathrm{chilled,in}}$ of 5 °C to 0.069 kg kg_{ads}^{-1} for $T_{\mathrm{chilled,in}}$ of 30 °C. Improvement in ESD and SP due to an increase in the chilled water temperature is higher for the cold storage compared to the heat storage. As shown in Figure 57b and Figure 57c, by increasing the chilled water temperature from 5 to 30 °C, 47% improvement is observed in ESD_{cold} (from 0.074 to 0.109 GJ m^{-3}) and SP_{cold} (from 191 to 280 W kg_{ads}^{-1}), while 10% improvement is estimated in ESD_{heat} (from 0.383 to 0.421 GJm^{-3}) and SP_{heat} (from 982 to 1080 W kg_{ads}^{-1}). As shown in Figure 57d, changes in COP_{heat} due to the increase in the chilled water temperature is negligible (0.5% improvement), while COP_{cold} increases by 34% when $T_{\mathrm{chilled,in}}$ increases from 5 to 30 °C.

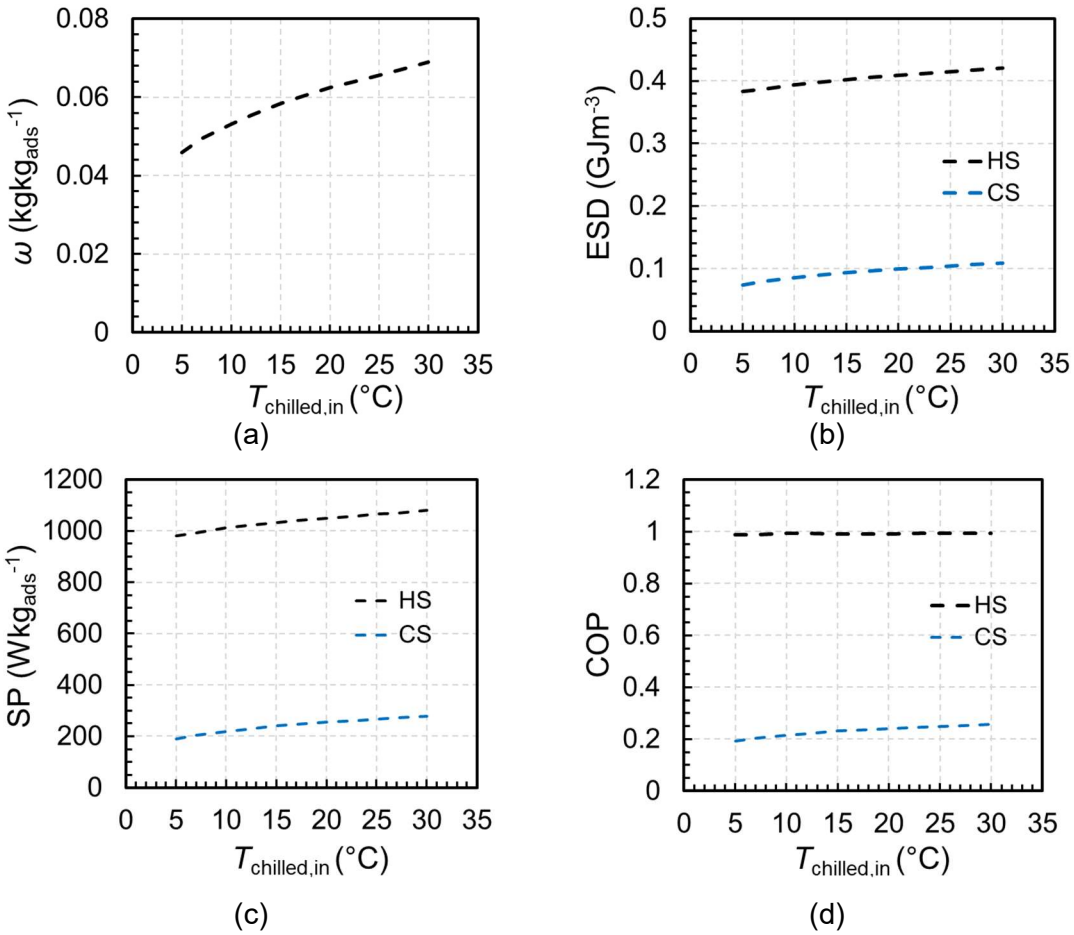

Figure 57. (a) Sorption uptake, (b) ESD, (c) SP, and (d) COP of heat storage and cold storage versus chilled water temperature. $T_{\mathrm{hf,in}} = 90$ ℃ , $T_{\mathrm{cf,in}} = T_{\mathrm{coolant,in}} = 30$ ℃, $r_t = t_{\mathrm{dch}}/t_{\mathrm{ch}} = 1$, and $t_{\mathrm{cycle}} = t_{\mathrm{ch}} + t_{\mathrm{dch}} = 1200$ s.

6.5. Summary of results

An accurate transient lumped-parameter RC model was developed for a closed S-TES, which considered the equilibrium and kinetics properties of the sorption working pair candidates as well as heat and mass transfer coefficients in the sorber bed HEX. The present model was successfully validated with the experimental data, which was collected from a custom-built S-TES in our lab, under various operating conditions. The model could be used for the material selection, application feasibility studies, design optimization, performance evaluation, and parametric study.

For cyclic operation, ESD of heat storage was significantly higher than the ESD of cold storage, because (i) heat of sorption, which was released in the heat storage, was more than the evaporation cooling, which was delivered during cold storage, and (ii)

sensible heat that was delivered to the bed in the charging process, was used at the beginning of the sorption process as a part of heat delivery. System-based ESDs, for both cold and heat storage, were higher for loose grain sorber bed compared to the coated one. At cycle time of 1800 s, the $\mathrm{ESD}_{\mathrm{sys,cold}}$ of the loose grain bed was 1.66 times higher than that of the coated sorber (0.106 GJ m^{-3} compared to 0.064 GJ m^{-3}) and $\mathrm{ESD}_{\mathrm{sys,heat}}$ of the loose grain bed was 2.63 times higher than $\mathrm{ESD}_{\mathrm{sys,heat}}$ of coated bed (0.386 GJ m^{-3} compared to 0.147 GJ m^{-3}).

Chapter 7.

Thermo-chemical energy storage systems

As discussed in Chapter 3, composite sorbent of silica gel+$CaCl_2$ shows high theoretical ESD potential for heating and cooling in residential applications. Hence, the performance of a lab-scale S-TES with silica gel+$CaCl_2$ is investigated and the effects of storage time and adding high-conductive additives on ESD and specific power are presented in this chapter.[5]

7.1. Experimental study on the performance of a salt composite S-TES

Our custom-made S-TES prototype is shown in Figure 58, which consists of (i) two fin-tube sorber beds, (ii) a shell-and-tube condenser, and (iii) a custom-built capillary-assisted low-pressure evaporator. The detailed description of the setup is provided in Chapter 5 and Chapter 6, and some upgrades have been made to the S-TES system including installation of four-way valves for faster desorption to adsorption temperature switches, especially for cyclic operations, and larger diameter pipes and gate valves between the evaporator and sorber beds. Moreover, the HTF of the sorber bed is water, unlike Chapter 5 and Chapter 6, where silicon oil is used. The operating temperatures of desorption, condensation, adsorption, and evaporation are 90, 30, 30, and 15 °C, respectively, and the flow rate of HTF and chilled water are 7.6 and 6.1 L min^{-1}.

One of the sorber beds is filled with 1.302 kg silica gel-$CaCl_2$ (SG-CC: 55 wt% B150 silica gel, 30 wt% $CaCl_2$, and 15 wt% PVA) with the HEX-to-sorbent mass ratio of 1.94, while the second one is filled with 1.513 kg silica gel-$CaCl_2$-graphite flake (SG-CC-G: 42 wt% B150 silica gel, 23 wt% $CaCl_2$, 20 wt% graphite flakes, and 15 wt% PVA) with the HEX-to-sorbent mass ratio of 1.67. Therefore, the $CaCl_2$ to silica gel mass ratio is kept 0.55 for both samples. Table 21 lists specifications of the sorbent composites with and without

[5] The results of this chapter were presented in: (i) Heat Powered Cycles (HPC 2018) conference [9], and (ii) 5th Experts meeting of the Joint IEA Technology Collaboration Programs on Solar Heating and Cooling (SHC) Task 58 and Energy Conservation through Energy Storage (ECES) Annex 33 on Compact Thermal Energy Storage R&D, May 1-3 2019.

graphite flakes. By adding graphite flakes, the thermal conductivity of the new composite improved by 2.36 times from 0.098 to 0.231 W m^{-1} K^{-1}.

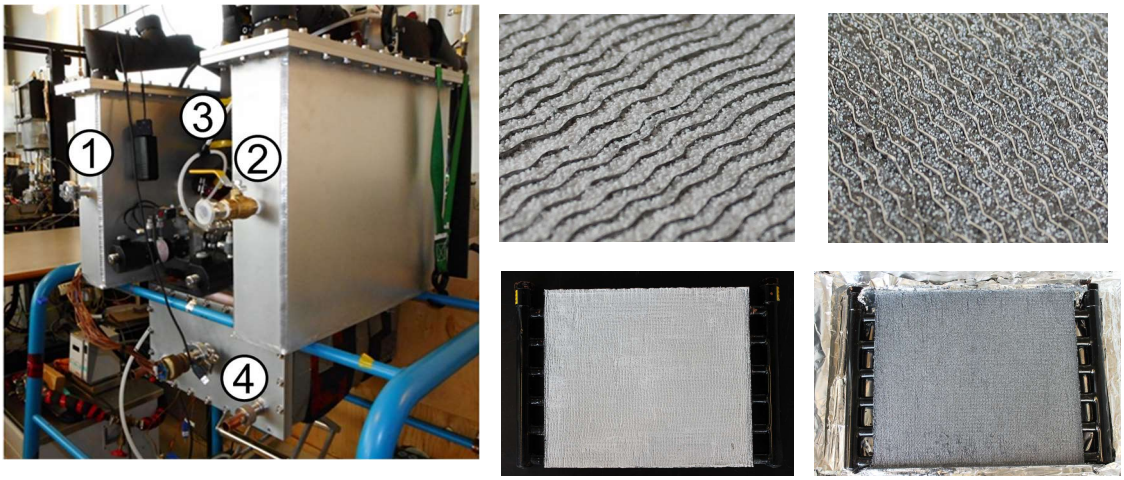

(a) (b) (c)

Figure 58. (a) S-TES prototype, including: two sorber beds (1,2), condenser (3), and evaporator (4), (b) sorber bed (1) packed with silica gel+$CaCl_2$ with the HEX-to-sorbent mass ratio of 1.94, and (c) sorber bed (2) packed with silica gel + $CaCl_2$ + graphite flakes (20%) with the HEX-to-sorbent mass ratio of 1.67.

Table 21. Specification of the sorbent composites: (i) silica gel + $CaCl_2$, and (ii) silica gel + $CaCl_2$ + graphite flakes (20%).

	Silica gel + $CaCl_2$ (SG-CC)	**Silica gel + $CaCl_2$ + graphite flakes (20%) (SG-CC-G)**
Composition	55% B150 silica gel 30% $CaCl_2$ 15% PVA	42% B150 silica gel 23% $CaCl_2$ 15% PVA 20% graphite flakes
m_{ads} (kg)	1.302	1.513
k_{ads} ($Wm^{-1}K^{-1}$)	0.098 +/- 0.002	0.231 +/- 0.006
$c_{p,ads}$ ($MJm^{-3}K^{-1}$)	0.42 +/- 0.06	0.45 +/- 0.03

7.1.1. Experimental procedure

Each bed is examined separately. Prior to the experiments, the entire sorption system is evacuated at 90 °C for 8-10 hours to remove the residual gas. To study the effect of storage duration on the performance, the S-TES is discharged in a cyclic mode (no storage time), and afterwards, for various storage durations. In cyclic operation

(considered as a baseline test), periodically a quick degassing (few seconds) is performed between the half-cycles, to prevent possible accumulation of non-condensable gases in the condenser. As shown in Figure 59, after 5 to 6 cyclic operations, short-term storage times are considered before the discharge process. Sorption and desorption periods of 35 min are considered. For seasonal application, the system is turned off and reaches the ambient temperature, which takes around 1 day for this testbed. In the discharging process, after the evaporator reaches a constant temperature of 15 °C, the valve between the evaporator and the sorber bed is opened and water vapor goes to the sorber bed.

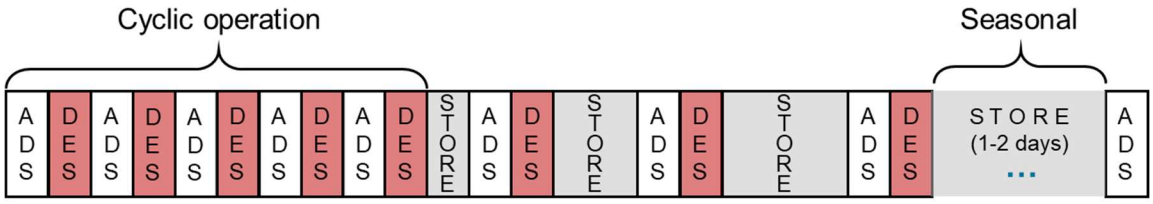

Figure 59. Experimental procedure for studying the effect of storage time on the performance of S-TES. It includes 5-6 cyclic operation, a few short-term storage periods, and seasonal storage condition, which is achieved after 1-2 days.

7.2. Results and discussion

7.2.1. Temperature changes in the sorber bed and evaporator

Inlet and outlet temperatures of the sorber bed HTF and inlet and outlet temperatures of the evaporator chilled water are shown in Figure 60a and Figure 60b for the composite of SG-CC-G. As depicted in Figure 60, after five cyclic charging-discharging, storage times of 35, 70 and 105 min are considered. The maximum temperature rise/drop of the HTF in the switching time is 56-58 °C. After the charging process and during the storage period, the temperature of HTF reduces exponentially and it reaches the ambient temperature for seasonal application.

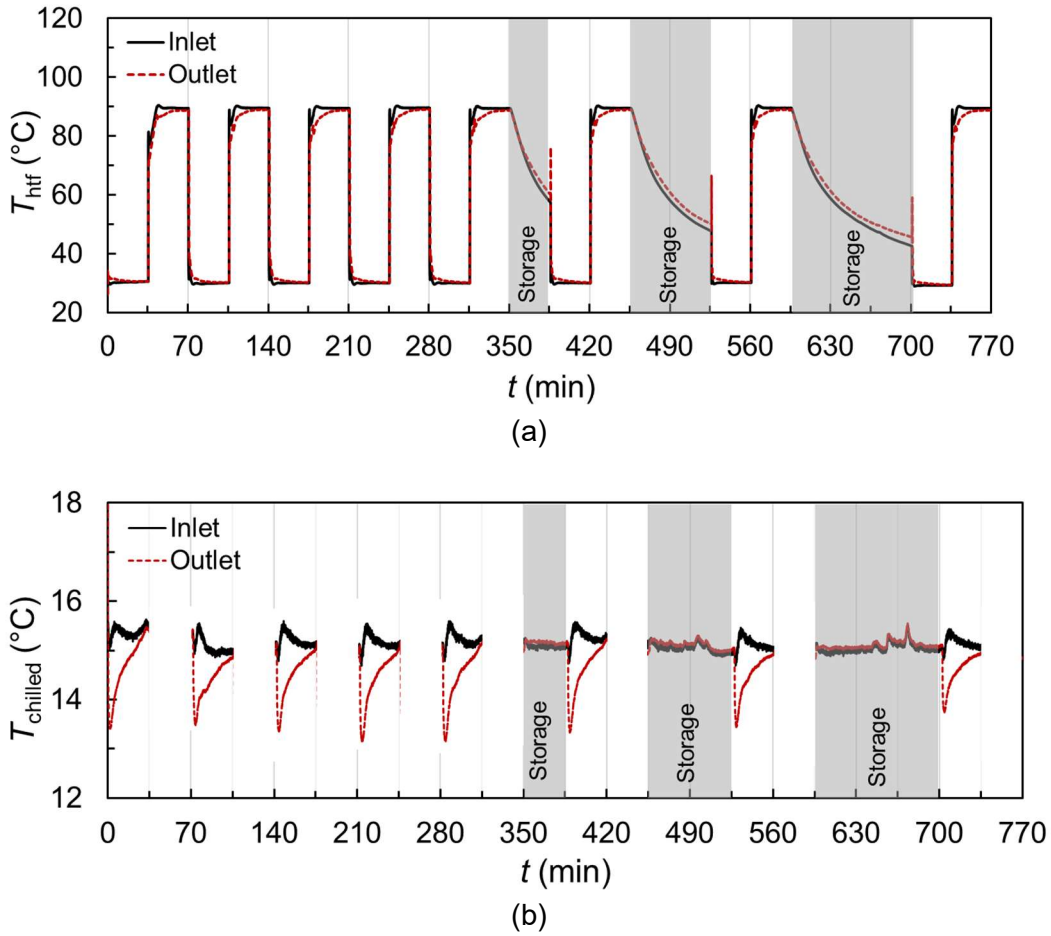

Figure 60. (a) The temperature of heat transfer fluid of the sorber bed with Silica gel + $CaCl_2$ + graphite flake and (b) temperature of evaporator chilled water vs time.

7.2.2. Effect of storage period on the ESD of the S-TES

Figure 61 shows the effect of storage duration on the heat and cold storage ESD. Cold ESD slightly decreases from the cyclic mode to a few minutes of storage and seasonal application. S-TES systems are known for having no cold energy loss [28], and this drop in the cold ESD is due to the uncertainty of the experiment, as shown in the error bars in Figure 61, and possible pressure build-up inside the condenser, as a result of existence of non-condensable gases by the corrosion reactions in the salt composite sorber bed. The residual gases add to the mass transfer resistance inside the sorber bed and, other than using corrosion-resistant materials and corrosion-protection layer, as stated in ref. [173], occasional degassing is necessary for long-term use of a closed sorption system, due to the residual gases and leakage.

For heat storage, a significant decrease is observed from the cyclic operation mode (1.03 MJ kg^{-1}) to seasonal application (0.43 MJ kg^{-1}), due to sensible heat loss in the sorber bed and, in part, due to the possible non-condensable gases in the condenser. The S-TES heat storage systems are more suitable for short-term storage rather than seasonal applications, where a part of the input sensible heat can be discharged as well. ESD of 1.1 MJ kg^{-1} is achieved for SG-CC S-TES under cyclic operation.

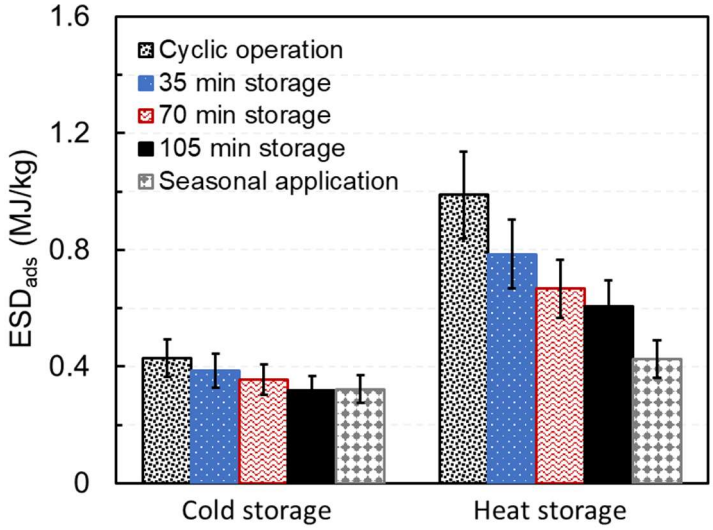

Figure 61. Effects of storage duration on the ESD of SG-CC-G S-TES for cold and heat storage. Storage periods of 35, 70, and 105 min, as well as cyclic and seasonal operations, are considered.
Operating conditions are: T_{des}=90 °C, T_{ads}=T_{cond}=30 °C, T_{evap}=15 °C, and charge time of 35 min.

7.2.3. Effect of high-conductive additives on the discharge power

Figure 62 shows the specific discharge power of the SG-CC and SG-CC-G sorber beds for heat storage. The discharge power based on the active mass of the sorbent (i.e. silica gel and $CaCl_2$) is higher for the composite with graphite (732 W kg^{-1}) compared to the composite without graphite (573 W kg^{-1}), because of the higher thermal diffusivity of graphite flake, which expedites the discharging process and makes it more suitable for fast-heat delivery applications

However, the average specific discharge power based on the total mass of the sorbent (i.e. including the graphite mass for the SG-CC-G bed) is slightly lower for the SG-CC-G bed (476 W kg^{-1}) compared to the SG-CC bed (487 W kg^{-1}). Hence, adding graphite does not improve the average specific power based on the total mass in this study. The

discharge power for the first 10 min is still higher for the bed with graphite flake (1.30 kW kg^{-1}) compared to the bed without graphite flake (1.25 kW kg^{-1}). One can conclude that adding graphite makes the composite suitable for fast-heat delivery applications, regardless of the total ESD and system compactness.

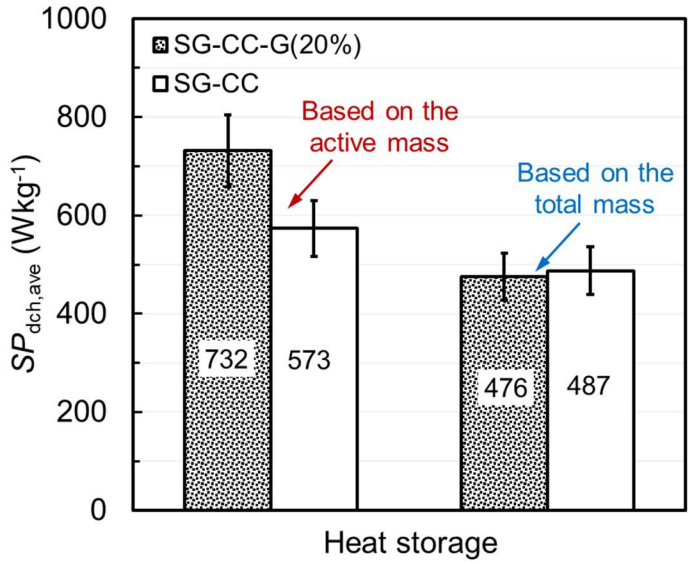

Figure 62. Effect of high-conductive additives on ESD and discharge power and (b) effects of storage duration and residual gas on ESD.
Operating conditions are: T_{des}=90 °C, T_{ads}=T_{cond}=30 °C, T_{evap}=15 °C, and t_{dch}= 35 min.

7.2.4. ESD vs COP of the S-TES

Figure 63 shows the heat storage COP vs ESD of the SG-CC-G bed for various storage periods and desorption temperatures of 70, 80, and 90 °C. For 90 °C desorption temperature, COP decreases by 62% from 0.70 to 0.25, and ESD drops by 55% from 0.95 to 0.43 MJ kg^{-1}, when cyclic operation changes to seasonal application. By increasing the desorption temperature, a trade-off is observed between COP and ESD. As shown in Figure 63, when desorption temperature increases from 70 to 90 °C, ESD increases from 0.63 to 0.95 MJ kg^{-1}, while COP decreases from 0.92 to 0.7.

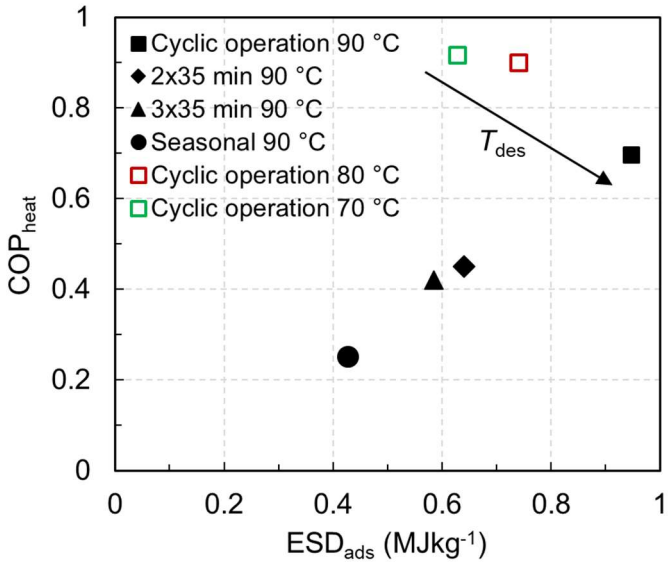

Figure 63. Heat storage COP vs ESD for the SG-CC-G S-TES under desorption temperatures of 70, 80, and 90 °C and various storage periods.

7.2.5. Comparison between the STES with silica gel + $CaCl_2$ and STES with FAM-Z02

Table 22. lists the specifications of the S-TES with 0.3 mm coated FAM-Z02, discussed in Chapter 5 and Chapter 6, and S-TES with SG-CC under cyclic operation and temperatures of 90-30-30-15 °C. By changing the coated FAM-Z02 to packed SG-CC, the $ESD_{ads,heat}$ has been increased to 1.061 GJ m^{-3} from 0.629 GJ m^{-3}.

Table 22. Specifications of the heat storage S-TES with FAM-Z02, discussed in Chapter 6, vs S-TES with silica gel+$CaCl_2$

	FAM-Z02 (coated)	**Silica gel + $CaCl_2$**
m_{ads} (kg)	0.76	1.302
HEX-to-sorbent mass ratio	3.3	1.94
$ESD_{ads,heat}$ (MJ kg^{-1})	0.967	1.1
$ESD_{ads,heat}$ (GJ m^{-3})	0.629	1.061
$SP_{dch,heat,ave}$ (W kg^{-1})	372 (at $\dot{m}_{\mathrm{HTF}} = 3.6\ \mathrm{L\ min^{-1}}$)	485 (at $\dot{m}_{\mathrm{HTF}} = 7.6\ \mathrm{L\ min^{-1}}$)
ΔT_{lift} (°C)	46	54

7.3. Summary of results

An experimental study was conducted to investigate the effects of storage time, and high-conductivity additives on the overall performance of a salt composite S-TES. For

heat storage, the S-TES was preferable for short-term storage, due to a 56% decrease in ESD, from 0.95 MJ kg^{-1} (no storage-time) to 0.43 MJ kg^{-1} (seasonal applications) for SG-CC-G. There was no significant difference between the heat storage averaged specific discharge power of the SG-CC (487 W kg^{-1}) and SG-CC-G (467 W kg^{-1}). However, the averaged specific discharge power of SG-CC-G, for the first 10 min of the discharge process, was higher (1.30 kW kg^{-1} compared to 1.25 kW kg^{-1}). Compared to the ESD of 0.629 GJ m^{-3} for the coated FAM-Z02 S-TES (in Chapter 5 and Chapter 6), ESD of 1.061 GJ m^{-3} was achieved for the SG-CC S-TES.

Chapter 8.

Conclusions and outlook

8.1. Conclusions

This PhD project was set out to assess the performance of low-grade heat-driven S-TES systems. The focus of this study was on the thermal and sorption characterization of the sorber bed, mathematical S-TES system modeling, and experimental testing of an S-TES prototype.

In Chapter 1, an introduction to TES technology and particularly S-TES technology was briefly presented and the state of the art in S-TES was reviewed. The key storage performance indicators were introduced and quantified for various thermochemical energy materials. In Chapter 2, a comprehensive literature review on the sorption and thermochemical storage systems was presented. The main concerns in market penetration of the S-TES systems were realized as (i) fulfilling the application-based ESD target, while (ii) speeding up the response rate of the S-TES to the energy demand, and (iii) reducing the charging time. Since the previous studies have mostly focused on the investigation of small-amount of sorbent materials in terms of ESD, a major literature gap was found for the performance assessment of the full-scale S-TES systems, in terms of ESD, as well as sorption kinetics, and charge/discharge power.

In Chapter 3 properties of suitable sorbent candidates for storage were presented and screening of sorbent material candidates was performed for four sorbent candidates: (i) FAM-Z02 (SAPO), (ii) silica gel+$CaCl_2$ (composite sorbent), (iii) vermiculite+$CaCl_2$ (composite sorbent), and (iv) Na_2S-H_2O (salt hydrate). Although Na_2S-H_2O provided the highest SP and ESD, there was evidence of outgassing of H_2S, which made it unsafe for the residential environment. Among the rest of sorbent candidates, AQSOA FAM-Z02 showed highest discharging rate (7×10^{-4} s^{-1}) and highest discharge SP (0.431 kW kg^{-1}). Hence, FAM-Z02 was selected for further investigations on its thermal conductivity (Chapter 4), sorption kinetics (Chapter 5), and storage system performances (Chapter 6). Due to the low density of vermiculite+$CaCl_2$, the best candidate in terms of volumetric ESD was silica gel+$CaCl_2$, which provided ESD of 1.563 GJ m^{-3} (1.6 MJ kg^{-1}). System performance of silica gel+$CaCl_2$ S-TES was studied in Chapter 7.

In Chapter 4, the experimental and theoretical study on the effective thermal conductivity (ETC) and thermal contact resistance (TCR) of a FAM-Z02 packed sorber bed were conducted and reported. The measured ratio of the TCR to the overall thermal resistance of a loose grain monolayer of 2-mm FAM-Z02, sandwiched between two aluminum fins, was 67% at 25 °C and atmospheric pressure. The proposed ETC model demonstrated that under atmospheric condition, increasing thermal conductivity of a 2-mm sorption packed bed by five times, from 0.2 to 1 W m^{-1} K^{-1}, would increase the ETC by 26%, from 0.216 to 0.272 W m^{-1} K^{-1}, while by further improving the sorbent thermal conductivity from 1 to 5 W m^{-1} K^{-1}, ETC would increase by a lower rate (13% rise), from 0.272 to 0.306 W m^{-1} K^{-1}.

Moreover, for monolayer randomly packed bed, it was predicted that by decreasing the particle resistance to one fifth, namely by increasing the particle thermal conductivity by 5 times from 0.2 to 1 W m^{-1} K^{-1}, the overall bed thermal conductivity would increase by 38 % from 0.108 to 0.149 at 25 °C. However, by decreasing the TCR to one fifth, the overall bed thermal conductivity would improve by 58%, from 0.108 to 0.171 W m^{-1} K^{-1}. Thus, for monolayer sorption packed bed, treating the surface and applying thermal grease between the fins and sorbents were found to be more beneficial and effective than increasing the sorbent thermal conductivity, e.g. by using high conductive additives, which also would reduce the sorption capacity of the packed bed due to lower active material. On the other hand, for highly-packed S-TES with multi-layers of sorbent materials, increasing thermal conductivity of sorbent particles showed higher heat transfer improvement, compared to reducing the TCR.

It was also demonstrated that grain size had a significant effect on the heat transfer in a packed bed sorber and for a certain volume of storage, optimal particle size should be selected to provide better charge/discharge power for a targeted application. For instance, at 25 °C and uptake of 0.3 kg kg_{ads}^{-1}, for a 1-mm fin spacing, the optimal grain size was 0.25 mm, which provided a maximum overall thermal conductivity of 0.068 W m^{-1} K^{-1} and for 12-mm fin spacing, the optimal grain size was 2 mm, corresponding to an overall thermal conductivity of 0.092 $Wm^{-1}K^{-1}$. Using the proposed model, the ETC charts were provided for 0.5 and 2 mm FAM-Z02 for SC and randomly packed bed for both open and closed packed bed sorbers. ETC of a 2 mm FAM-Z02 open-system, with water uptake of 0.32 kg kg_{ads}^{-1}, was predicted to be 3.3 times as high as the ETC of a closed-system

(0.099 compared to 0.030 W $m^{-1} K^{-1}$) at 10 °C, and 1.2 times as high as that of the closed system (0.107 compared to 0.090 W $m^{-1} K^{-1}$) at 80 °C.

In Chapter 5, an experimental study of in-situ mass measurement of a full-scale coated FAM-Z02 sorber bed was reported. The measured water uptake evolution revealed an exponential trend with three sorption regions with different characteristic times: (i) the system-limited region with a characteristic time, τ, of 625 s, (ii) the rapid sorption region with τ of 270 s, and (iii) the slow ending region with τ of 1110 s. It was determined that the thermal mass, as well as heat and mass transfer resistances of the full-scale S-TES, were the main reasons for the slow system-limited region. The desorption rate was observed to be 1.48 times higher compared to the sorption rate, which is close to the values reported in the literature for FAM-Z02, i.e. reported as 1.5, under operating temperatures of 90–30–10 °C. The average effective diffusivity of a 0.3-mm coated FAM-Z02 S-TES was measured as 6.3×10^{-11} $m^2 s^{-1}$ under operating temperatures of 90–30–20-20 °C.

Moreover, the storage performance comparison of packed bed vs coated bed was presented in Chapter 5. The coated sorber bed showed higher sorption rate of $k_{\mathrm{ads}} = 2.11\times10^{-3}$ s^{-1} compared to the loose grain bed of $k_{\mathrm{ads}} = 5.04\times10^{-4}$ s^{-1}, with the identical sorber bed heat exchanger. The coated bed was more suitable for short-duration energy delivery target. However, the ideal maximum achievable $\mathrm{ESD}_{\mathrm{cold}}$ of the loose grain bed was higher than that of the coated bed (0.661 MJ kg_{ads}^{-1} compared to 0.500 MJ kg_{ads}^{-1}). Moreover, the volumetric sorber bed $\mathrm{ESD}_{\mathrm{bed,cold}}$, based on the active volume of the sorber bed, was significantly higher for the 2-mm diameter loose grain bed (0.345 GJ m^{-3}) compared to the 0.3 mm coated bed (0.100 GJ m^{-3}).

In Chapter 5, the importance of the effect of the mass ratio of sorber bed HEX to the sorbent material, r, on the storage performance was highlighted. The sorber bed $\mathrm{ESD}_{\mathrm{bed,heat}}$ significantly decreased with r, for both cyclic operation and seasonal storage. For seasonal storage, $\mathrm{ESD}_{\mathrm{bed,heat}}$ was predicted as 0.270 MJ kg_{bed}^{-1} for r of 1 and 0.071 MJ kg_{bed}^{-1} for r of 6. The possibility of improvement of the sorber bed prototype, under study, by decreasing r was shown; by decreasing r from 3.3 to 1, the $\mathrm{ESD}_{\mathrm{bed,heat}}$ was predicted to be twice.

The predicted $\mathrm{ESD}_{\mathrm{bed,heat}}$ of the studied S-TES prototype for seasonal storage was 62% of the measured value for the cyclic operation, i.e. 0.196 MJ kg_{bed}^{-1} compared to

0.121 MJ kg_{bed}^{-1}. For the completely charged coated sorber bed, the share of sensible heat and thermal loss to the total discharged energy was 51% after 5 min of discharging time and reached an almost constant value of 26% after 15 min discharge. The total thermal mass of the sorber bed included thermal masses of the sorbent material (23%), HTF (32%), copper tubes (28%), and aluminum fins (17%). Furthermore, it was demonstrated that finding an optimal charging time to minimize the thermal loss was essential to increase thermal efficiency, particularly for seasonal storage.

Developing a reliable mathematical model for S-TES systems was found an essential task to optimize the design parameters and predict storage performance. In Chapter 6, a fully-dynamic model was presented and validated, which contains the equilibrium and kinetics properties of the sorption working pair candidates. The geometry complexity of the sorber bed, evaporator and condenser were simplified through a lumped-parameter resistance-capacitance model. Since the sorption properties reported from the small-scale had not been found as proper representatives of the performance of full-scale S-TES systems, the measured dynamic characterizations of the full-scale prototype (extracted from the experimental results, in Chapter 5) were fed into the S-TES model.

Moreover, in Chapter 6, comprehensive experimental studies were presented for both loose grain and coated custom-built sorp-TES systems, at various charge/discharge time and temperatures. System-based ESDs, for both cold and heat storage, are higher for loose grain sorber bed compared to the coated one. At cycle time of 1800 s, $\mathrm{ESD}_{\mathrm{sys,cold}}$ of the loose grain bed was 1.66 times higher than $\mathrm{ESD}_{\mathrm{sys,cold}}$ of coated adsorber (0.106 GJ m^{-3} compared to 0.064 GJ m^{-3}) and $\mathrm{ESD}_{\mathrm{sys,heat}}$ of the loose grain bed was 2.63 times higher than $\mathrm{ESD}_{\mathrm{sys,heat}}$ of coated bed (0.386 GJ m^{-3} compared to 0.147 GJ m^{-3}) under temperatures of 90-30-30-15 °C. The proposed model was successfully validated under various operating conditions with the experimental data collected in our custom-built testbed. The model could be used for material selection, application feasibility studies, performance evaluation, and parametric study.

In Chapter 7 effects of storage time and high-conductivity additives on the overall performance of a salt composite S-TES with silica gel+$CaCl_2$ were reported. Compared to the ESD_{heat} of 0.63 GJ m^{-3} for the coated FAM-Z02 S-TES (in Chapter 5 and Chapter 6), ESD_{heat} of 1.1 GJ m^{-3} was achieved for the silica gel+$CaCl_2$ S-TES under temperatures of 90-30-30-15 °C. Adding 20% graphite flakes to silica gel+$CaCl_2$ increased the initial

specific power (SP) from 1.25 kW kg^{-1} to 1.30 kW kg^{-1}, for the first 10 min. However, the averaged SP of the composite without graphite was higher, i.e. 487 Wkg^{-1} for silica gel+$CaCl_2$ 467 W kg^{-1} for the same composite with 20% graphite flakes, due to its more active sorbent material. ESD_{heat} of the composite with graphite decreased from 0.95 MJ kg^{-1} for cyclic operation (no storage-time) to 0.43 MJ kg^{-1} for seasonal applications.

The main novelties and findings presented in this study could be summarized as follows:

- ETC and TCR of packed bed sorbers were modeled, as a function of the number of sorbent layers, temperature, gas pressure, particle size, packed bed arrangement, contact pressure, and surface characteristics. The innovative features of the proposed model were: (i) considering all the key geometrical and operational variables, (ii) obtaining the water uptake from the sorbent isotherm and considering the effect of water uptake on the thermal conductivity, (iii) proposing an asymptotic solution to cover randomly packed beds, as well as the SC and FCC arrangements, and (iv) predicting the TCR in the sorber beds.

- Thermal conductivity of packed beds of FAM-Z02 particle, which is one of the best candidates for fast S-TES and ACS with low desorption temperature of below 90 °C, was measured by a heat flow meter (HFM) for the first time. Randomly packed beds of 1, 2, 4, and 6 layers of 2 mm FAM-Z02 particles were arranged and their ETC and TCR were obtained by deconvoluting TCR from the total thermal resistance.

- The relative importance of TCR to the total thermal resistance was investigated for different temperatures and sorbent layers. It was shown that for a monolayer sorbent between two metal sheets at 25 °C and under atmospheric pressure, reducing the TCR by surface treating and using thermal interface materials, e.g. thermal grease, was more effective and easier to implement, than reducing the particle thermal resistance, by increasing particle thermal conductivity.

- The key importance of sorbent grain size on the heat transfer in packed bed sorber was highlighted and optimal grain sizes were predicted as functions of the bed thickness, application, and other operating conditions.

- The ETC charts, based on the equilibrium water uptake was presented for both open and closed S-TES of FAM-Z02 packed bed, which is beneficial for ETC prediction and design of S-TES system under real operating conditions.

- In-situ mass and temperature measurement of a lab-scale coated FAM-Z02 S-TES were conducted and the uptake evolution showed an exponential trend. Three characteristic times were found for the uptake, which corresponded to three zones: (i) the system-limited region, (ii) the rapid sorption region, and (iii) the slow ending region. It was determined that the thermal mass, as well as heat and mass transfer resistances of the S-TES, were the main reasons for the slow system-limited region. To improve the performance of the S-TES, this region should be minimized.

- A transient resistance-capacitance lumped-parameter model was developed to assess the performance of a closed S-TES system. The main features of this model were: (i) low computing time, (ii) being applicable to different working pairs and operating conditions, and (iii) being fed by the sorbent kinetics characteristics, overall heat transfer coefficients of sorber bed, evaporator, and condenser, extracted from the experimental data. The model was proved to be accurate in comparison with the experimental data and offered a reliable platform for the design and optimization of an S-TES system.

- Since a major literature gap was found for the performance assessment of the full-scale S-TES systems, comprehensive experimental studies were carried on the custom-built lab-scale S-TES in our lab to study storage performance under various conditions, namely, i) coated vs loose grain sorbent configurations, ii) various heat storage durations, iii) adding high conductive additives in the sorbent material, iv) different operating temperatures, and v) different discharge-to-charge time ratios.

- ESD of 1.1 GJ m^{-3} was achieved for the silica gel+$CaCl_2$ custom-built S-TES system.

8.2. Future research

The developed models and outcome of this thesis can be applied to design, optimize, and control efficient S-TES systems for the target applications. The followings are the recommendations on future researches.

8.2.1. Tailored sorbent materials

Sorbent storage materials are the key element in the S-TES since they impose the ideal sorption capacity of S-TES. In other words, an optimized sorber bed cannot guarantee the target ESD when the material sorption capacity is not high enough, considering the application operating condition.

For an efficient S-TES system, development of storage materials with high sorption capacity and binding energy, high thermal diffusivity, and fast kinetics is essential. Although adding high additive materials increases thermal conductivity and kinetics, ESD decreases due to adding non-sorbent materials, as highlighted in Chapter 7.

8.2.2. Optimization of system design

Although promising ESDs have been reported for sorbent materials, system inefficiencies associated with the storage system decreases the storage performance in the system-level. Sorber bed is the core of the S-TES system, where coupled heat and mass transfer occur. However, the common sorber beds suffer from low thermal conductivity and low permeability [174]. Optimized sorber beds require higher heat transfer surfaces to increase the heat transfer in the bed and provides higher kinetics and higher charge/discharge power. Having said that, increasing the surface area increases the HEX-to-sorbent mass ratio, which results in (i) lower ESD, (ii) lower SP, and (iii) lower COP for seasonal storage since more sensible heat is required to heat up the sorber bed with more extended surfaces. This trade-off should be considered for optimization of sorber bed for the storage application.

Moreover, the sorbent configuration, i.e. coated, consolidated, and packed bed, strongly affect the storage performance indicator, and finding an optimal coating thickness

in coated beds [152] and optimal particle diameter in packed beds (Chapter 4) is essential to optimize the performance of sorber bed.

Although compactness of evaporator/condenser unit (ECU) is of great importance in the closed system since the vapor generator is a part of the storage volume, optimization of ECU in S-TES systems has been overlooked, and mostly oversized ECU HEXs were used to provide constant sorbate vapor and avoid restriction of sorption process.

8.2.3. Efficient operating and control strategies

Advanced cycles

Advanced sorption cycles have been used to improve the power and specifically the thermal efficiency of the adsorption cooling systems, which can be used for S-TES systems with at least two sorber beds, and continuous operation. Some of the advanced cycles in the literature are: (i) heat recovery cycles (double-effect cycle) with heat recovery between two the sorber beds [175], (ii) mass recovery cycles with transferring of vapor adsorbate from the desorber bed to the sorber bed [176], (iii) internal heat recovery between the condenser and the evaporator [177], (iii) cascading cycle [178], and (iv) thermal wave [179].

Control strategy

In order to meet the heating/cooling demand, a mechanism to control the heating/cooling output power and the temperature is required which is dictated by the application. To fully exploit the TES in the buildings integrated with TES (BITES), an effective control strategy is imperative. The transient lumped parameter model, presented in Chapter 6, can be used to predict the thermal behavior of the TES system. Thereafter, this prediction can be combined with optimization algorithms in order to determine the optimal control inputs [180].

Moreover, the developed model in Chapter 6 can be used for simulating the possible operating scenarios that may be difficult to investigate experimentally, to find the optimal condition. For instance, finding the optimum charging time is of great importance, as shown in Chapter 5, or in case of seasonal storage, the sensible heat can be stored in buffer storage to increase the thermal efficiency of S-TES.

System integration and application

Although thermochemical materials have shown promising storage performances on the material level, the system integration and system performance test require further investigations. System integration of TES consists (i) analysis of demands according to the application boundary conditions, (ii) simulation of different scenarios, and (iii) prototype development and application test [181], which requires an easy-to-use accurate transient system model. Integration of TCES in building [35], and dishwasher [182] were demonstrated. Moreover, simulation-based feasibility studies of the integration of TCES into an industrial batch process with cogeneration energy supply [53], and in a closed greenhouse [183], were performed. For wide-spread adoption of S-TES systems, more application-based researches and demonstrations should be carried out.

References

[1] M. Rouhani, W. Huttema, and M. Bahrami, “Heat flow meter measurement of the thermal conductivity and contact resistance of FAM AQSOA-Z02 pellets between aluminium plates,” in *IVth International Symposium on Innovative Materials for Processes in Energy Systems (IMPRES2016)*, 2016.

[2] M. Rouhani, W. Huttema, and M. Bahrami, “Effective thermal conductivity of packed bed adsorbers: Part 1 - Experimental study,” *Int. J. Heat Mass Transf.*, vol. 123, pp. 1204–1211, 2018.

[3] M. Rouhani, W. Huttema, and M. Bahrami, “Effective thermal conductivity of adsorption packed beds,” in *International Sorption Heat Pump Conference 2017*, 2017.

[4] M. Rouhani and M. Bahrami, “Effective thermal conductivity of packed bed adsorbers : Part 2 ─ Theoretical model,” *Int. J. Heat Mass Transf.*, vol. 123, pp. 1212–1220, 2018.

[5] M. Rouhani, W. Huttema, and M. Bahrami, “Thermal conductivity of AQSOA FAM-Z02 packed bed adsorbers in open and closed adsorption thermal energy storage systems,” *Int. J. Refrig.*, vol. In press, 2018.

[6] M. Rouhani, W. Huttema, A. Sharafian, C. McCague, and M. Bahrami, “Dynamic study of a full-scale AQSOA FAM-Z02 sorption cold storage system, In preparation,” 2019.

[7] M. Rouhani, W. Huttema, and M. Bahrami, “Theoretical and experimental study of cold storage sorption thermal energy storage systems, In preparation,” 2019.

[8] M. Rouhani, A. Sharafian, P. Cheppudira, W. Huttema, and M. Bahrami, “Thermal management of a greenhouse with adsorption energy storage,” in *International Sorption Heat Pump Conference 2017*, 2017.

[9] M. Rouhani, W. Huttema, C. Mccague, M. Khajehpour, and M. Bahrami, “Effects of storage period on the performance of salt composite sorption thermal energy storage,” in *Heat Powered Cycles 2018 Conference Proceedings*, 2018, pp. 243–248.

[10] International Energy Agency, “key world energy statistics,” 2016.

[11] D. Ürge-Vorsatz, L. F. Cabeza, S. Serrano, C. Barreneche, and K. Petrichenko, “Heating and cooling energy trends and drivers in buildings,” *Renew. Sustain. Energy Rev.*, vol. 41, pp. 85–98, 2015.

[12] Natural Resources Canada, “Renewable energy facts.” [Online]. Available: https://www.nrcan.gc.ca/renewable-energy-facts/20069. [Accessed: 22-Aug-2019].

[13] International Renewable Energy Agency (IRENA), *Global Energy Transformation: A Roadmap to 2050*. 2018.

[14] L. F. Cabeza, *Advances in Thermal Energy Storage Systems : Methods and Applications*. Woodhead Publishing, 2014.

[15] H. Mehling and L. F. Cabeza, *Heat and cold storage with PCM — An up to date introduction into basics and applications*. Springer, 2008.

[16] J. Lizana, R. Chacartegui, A. Barrios-Padura, and J. M. Valverde, “Advances in thermal energy storage materials and their applications towards zero energy buildings: A critical review,” *Appl. Energy*, vol. 203, pp. 219–239, 2017.

[17] Y. I. Aristov, “Current progress in adsorption technologies for low-energy buildings,” *Futur. Cities Environ.*, vol. 1, no. 1, p. 10, 2015.

[18] K. E. N’Tsoukpoe, H. Liu, N. Le Pierrès, and L. Luo, “A review on long-term sorption solar energy storage,” *Renew. Sustain. Energy Rev.*, vol. 13, no. 9, pp. 2385–2396, Dec. 2009.

[19] D. Aydin, S. P. Casey, X. Chen, and S. Riffat, “Novel ‘open-sorption pipe’ reactor for solar thermal energy storage,” *Energy Convers. Manag.*, vol. 121, pp. 321–334, 2016.

[20] H. Kakiuchi, M. Iwade, S. Shimooka, and K. Ooshima, “Novel zeolite adsorbents and their application for AHP and Desiccant system,” in *Proceeding of IEA-Annex-17 Meeting*, 2004.

[21] P. Tatsidjodoung, N. Le Pierrès, and L. Luo, “A review of potential materials for thermal energy storage in building applications,” *Renew. Sustain. Energy Rev.*, vol. 18, pp. 327–349, Feb. 2013.

[22] J. Xu, R. Z. Wang, and Y. Li, “A review of available technologies for seasonal thermal energy storage,” *Sol. Energy*, vol. 103, pp. 610–638, May 2014.

[23] I. Glaznev, D. Ovoshchnikov, and Y. I. Aristov, “Effect of residual gas on water adsorption dynamics under typical conditions of an adsorption chiller,” *Heat Transf. Eng.*, vol. 31, no. 11, pp. 924–930, 2010.

[24] K. E. N’Tsoukpoe, T. Schmidt, H. U. Rammelberg, B. A. Watts, and W. K. L. Ruck, “A systematic multi-step screening of numerous salt hydrates for low temperature thermochemical energy storage,” *Appl. Energy*, vol. 124, pp. 1–16, 2014.

[25] İ. D. M.A. Rosen, *Thermal Energy Storage: Systems and Applications*. 2010.

[26] IEA-ETSAP and International Renewable Energy Agency (IRENA), “Thermal energy storage, technology brief,” 2013.

[27] A. I. Fernandez, M. Martnez, M. Segarra, I. Martorell, and L. F. Cabeza, “Selection of materials with potential in sensible thermal energy storage,” *Sol. Energy Mater. Sol. Cells*, vol. 94, no. 10, pp. 1723–1729, 2010.

[28] X.-R. Zhang and I. Dincer, *Energy Solutions to Combat Global Warming*. 2017.

[29] N. Yu, R. Z. Wang, and L. W. Wang, “Sorption thermal storage for solar energy,” *Prog. Energy Combust. Sci.*, vol. 39, no. 5, pp. 489–514, 2013.

[30] A. Solé, I. Martorell, and L. F. Cabeza, “State of the art on gas–solid thermochemical energy storage systems and reactors for building applications,” *Renew. Sustain. Energy Rev.*, vol. 47, pp. 386–398, 2015.

[31] D. E. Worch, *Adsorption Technology in Water Treatment*. 2012.

[32] C. Bales and S. Nordlander, “TCA Evaluation - Lab Measurements, Modelling and Systems Simulations,” *Evaluation*, no. December, 2005.

[33] T. X. Li, R. Z. Wang, and T. Yan, “Solid–gas thermochemical sorption thermal battery for solar cooling and heating energy storage and heat transformer,” *Energy*, vol. 84, pp. 745–758, 2015.

[34] N. Yu, R. Z. Wang, Z. S. Lu, and L. W. Wang, “Three-Phase Sorption Process for Thermal Energy Storage : Theoretical Analysis and Implementation Solutions with Porous Matrix,” in *International Soprtion Heat Pump Conference*, 2014, pp. 1–11.

[35] A. Hauer, “Thermal Energy Storage with Zeolite for Heating and Cooling Applications,” in *International Sorption Heat Pump Conference 2002*, 2002, pp. 385–390.

[36] L. Scapino, H. A. Zondag, J. Van Bael, J. Diriken, and C. C. M. Rindt, “Sorption heat storage for long-term low-temperature applications: A review on the advancements at material and prototype scale,” *Appl. Energy*, vol. 190, pp. 920–948, 2017.

[37] K. E. N’Tsoukpoe, G. Restuccia, T. Schmidt, and X. Py, “The size of sorbents in low pressure sorption or thermochemical energy storage processes,” *Energy*, vol. 77, pp. 983–998, 2014.

[38] A. M. Papadopoulos, S. Oxizidis, and N. Kyriakis, “Perspectives of solar cooling in view of the developments in the air-conditioning sector,” *Renew. Sustain. Energy Rev.*, vol. 7, no. 5, pp. 419–438, 2003.

[39] L. F. Cabeza, A. Sole, and C. Barreneche, “Review on sorption materials and technologies for heat pumps and thermal energy storage,” *Renew. Energy*, vol. 110, 2016.

[40] C. Bales, “Report B3 of Subtask B: Laboratory Prototypes of Thermo-Chemical and

Sorption Storage Units, A Report of IEA Solar Heating and Cooling programme - Task 32: Advanced storage concepts for solar and low energy buildings," 2007.

[41] R. Wang, L. Wang, and J. Wu, *Adsorption Refrigeration Technology, Theory and Application*. Wiley, 2014.

[42] B. Dawoud, "Water vapor adsorption kinetics on small and full scale zeolite coated adsorbers; A comparison," *Appl. Therm. Eng.*, vol. 50, no. 2, pp. 1645–1651, 2013.

[43] J. Jänchen and H. Stach, "Adsorption properties of porous materials for solar thermal energy storage and heat pump applications," *Energy Procedia*, vol. 30, pp. 289–293, 2012.

[44] C. Barreneche, a. I. Fernández, L. F. Cabeza, and R. Cuypers, "Thermophysical Characterization of Sorption TCM," *Energy Procedia*, vol. 48, pp. 273–279, 2014.

[45] A. Frazzica and A. Freni, "Adsorbent working pairs for solar thermal energy storage in buildings," *Renew. Energy*, vol. 110, pp. 87–94, 2017.

[46] Y. Z. Lu, R. Z. Wang, M. Zhang, and S. Jiangzhou, "Adsorption cold storage system with zeolite-water working pair used for locomotive air conditioning," *Energy Convers. Manag.*, vol. 44, no. 10, pp. 1733–1743, 2003.

[47] G. Li, Y. Hwang, and R. Radermacher, "Investigation of Adsorption Cold Storage for Residential Application," pp. 1–10, 2014.

[48] D. Jähnig and W. Wagner, "Modestore Deliverable D3: Evaluation report of WP2 – Monitoring and evaluation of the 1st generation system installed in Austria," 2004.

[49] D. Jähnig and W. Wagner, "Modestore Deliverable D6: System Prototype Storage Module (Austria)," 2004.

[50] G. Gartler, D. Jähnig, G. Purkarthofer, and W. Wagner, "Development of a High Energy Density Sorption Storage System - Basic Principles of an Adsorption Heat Storage System," *Eurosun*, 2003.

[51] H. Ö. Paksoy, *Thermal Energy Storage for Sustainable Energy Consumption — Fundamentals, Case Studies and Design*. Springer, 2005.

[52] C. Bales, "Laboratory Tests of Chemical Reactions and Prototype Sorption Storage Units," 2008.

[53] H. Schreiber, S. Graf, F. Lanzerath, and A. Bardow, "Adsorption thermal energy storage for cogeneration in industrial batch processes: Experiment, dynamic modeling and system analysis," *Appl. Therm. Eng.*, vol. 89, pp. 485–493, 2015.

[54] G. Li, Y. Hwang, and R. Radermacher, "Experimental investigation on energy and exergy performance of adsorption cold storage for space cooling application," *Int.*

J. Refrig., vol. 44, pp. 23–35, 2014.

[55] G. Li, S. Qian, H. Lee, Y. Hwang, and R. Radermacher, “Experimental investigation of energy and exergy performance of short term adsorption heat storage for residential application,” *Energy*, vol. 65, pp. 675–691, 2014.

[56] S. Narayanan *et al.*, “Thermal battery for portable climate control,” *Appl. Energy*, vol. 149, pp. 104–116, 2015.

[57] S. Narayanan *et al.*, “A thermophysical battery for storage-based climate control,” *Appl. Energy*, vol. 189, pp. 31–43, 2017.

[58] V. Palomba, S. Vasta, and A. Freni, “Experimental testing of AQSOA FAM Z02/water adsorption system for heat and cold storage,” *Appl. Therm. Eng.*, vol. 124, pp. 967–974, 2017.

[59] A. Hauer and F. Fischer, “Open Adsorption System for an Energy Efficient Dishwasher,” *Chemie Ing. Tech.*, vol. 83, no. 1–2, pp. 61–66, Jan. 2011.

[60] A. H. Germany, “International Energy Agency Implementing Agreement on Energy Conservation through Energy Storage Annex 17,” *Change*.

[61] A. D. Grekova, L. G. Gordeeva, and Y. I. Aristov, “Composite ‘LiCl/vermiculite’ as advanced water sorbent for thermal energy storage,” *Appl. Therm. Eng.*, vol. 124, pp. 1401–1408, 2017.

[62] N. Yu, R. Z. Wang, Z. S. Lu, and L. W. Wang, “Development and characterization of silica gel-LiCl composite sorbents for thermal energy storage,” *Chem. Eng. Sci.*, vol. 111, pp. 73–84, 2014.

[63] V. Brancato *et al.*, “Water adsorption equilibrium and dynamics of LICL/MWCNT/PVA composite for adsorptive heat storage,” *Sol. Energy Mater. Sol. Cells*, vol. 193, no. November 2018, pp. 133–140, 2019.

[64] L. C. Sögütoglu, P. A. J. Donkers, H. R. Fischer, H. P. Huinink, and O. C. G. Adan, “In-depth investigation of thermochemical performance in a heat battery: Cyclic analysis of K2CO3, MgCl2and Na2S,” *Appl. Energy*, vol. 215, no. January, pp. 159–173, 2018.

[65] B. Michel, N. Mazet, S. Mauran, D. Stitou, and J. Xu, “Thermochemical process for seasonal storage of solar energy: Characterization and modeling of a high density reactive bed,” *Enegy*, vol. 47, pp. 553–563, 2012.

[66] P. A. J. Donkers, L. C. Sögütoglu, H. P. Huinink, H. R. Fischer, and O. C. G. Adan, “A review of salt hydrates for seasonal heat storage in domestic applications,” *Appl. Energy*, vol. 199, pp. 45–68, 2017.

[67] D. Zhu, H. Wu, and S. Wang, “Experimental study on composite silica gel supported

CaCl2 sorbent for low grade heat storage," *Int. J. Therm. Sci.*, vol. 45, no. 8, pp. 804–813, 2006.

[68] R. de Boer, W. G. Haije, J. B. J. Veldhuis, and S. F. Smeding, "Solid-Sorption Cooling With Integrated Thermal Storage: The SWEAT Prototype," *Int. Conf. Heat Powerd Cycles, Larnaca, Cyprus*, no. August, 2004.

[69] C. Bales and O. Ayadi, "Modelling of a Commercial Absorption Heat Pump with Integral Storage," *Effstock 2009 - 11th Int. Conf. Energy Storage*, p. Stockholm, 2009.

[70] C. Bales, "Chemical and sorption storage - Selection of concepts, A Report of IEA Solar Heating and Cooling programme - Task 32," 2005.

[71] A. Sharafian, S. M. Nemati Mehr, P. C. Thimmaiah, W. Huttema, and M. Bahrami, "Effects of adsorbent mass and number of adsorber beds on the performance of a waste heat-driven adsorption cooling system for vehicle air conditioning applications," *Energy*, vol. 112, pp. 481–493, 2016.

[72] A. Sapienza *et al.*, "An innovative adsorptive chiller prototype based on 3 hybrid coated / granular adsorbers," *Appl. Energy*, vol. 179, pp. 929–938, 2016.

[73] A. Fopah-Lele *et al.*, "Lab-scale experiment of a closed thermochemical heat storage system including honeycomb heat exchanger," *Energy*, vol. 114, pp. 225–238, 2016.

[74] S. Graf, F. Lanzerath, A. Sapienza, A. Frazzica, A. Freni, and A. Bardow, "Prediction of SCP and COP for adsorption heat pumps and chillers by combining the large-temperature-jump method and dynamic modeling," *Appl. Therm. Eng.*, vol. 98, no. 2016, pp. 900–909, 2016.

[75] F. Lanzerath, U. Bau, J. Seiler, and A. Bardow, "Optimal design of adsorption chillers based on a validated dynamic object-oriented model," *Sci. Technol. Built Environ.*, vol. 21, no. September, pp. 248–257, 2015.

[76] S. Mauran, H. Lahmidi, and V. Goetz, "Solar heating and cooling by a thermochemical process. First experiments of a prototype storing 60 kW h by a solid/gas reaction," *Sol. Energy*, vol. 82, no. 7, pp. 623–636, 2008.

[77] Y. J. Zhao, R. Z. Wang, T. X. Li, and Y. Nomura, "Investigation of a 10 kWh sorption heat storage device for effective utilization of low-grade thermal energy," *Energy*, vol. 113, pp. 739–747, 2016.

[78] A. Freni, A. Sapienza, I. S. Glaznev, Y. I. Aristov, and G. Restuccia, "Experimental testing of a lab-scale adsorption chiller using a novel selective water sorbent 'silica modified by calcium nitrate,'" *Int. J. Refrig.*, vol. 35, no. 3, pp. 518–524, 2012.

[79] D. Jähnig, R. Hausner, W. Wagner, and C. Isaksson, "Thermo-chemical storage for

solar space heating in a single-family house," *AEE – INTEC (Austria), Ecostock Conf. New Jersey; 31 May - 02 June*, pp. 1–7, 2006.

[80] G. Li, S. Qian, H. Lee, Y. Hwang, and R. Radermacher, "Experimental investigation of energy and exergy performance of short term adsorption heat storage for residential application," *Energy*, vol. 65, pp. 675–691, Feb. 2014.

[81] H. Schreiber, F. Lanzerath, C. Reinert, C. Grüntgens, and A. Bardow, "Heat lost or stored : Experimental analysis of adsorption thermal energy storage," *Appl. Therm. Eng.*, vol. 106, pp. 981–991, 2016.

[82] B. Dawoud, E.-H. Amer, and D.-M. Gross, "Experimental investigation of an adsorptive thermal energy storage," *Int. J. ENERGY Res. Int. J. Energy Res*, vol. 31, pp. 135–147, 2007.

[83] D. D. Do, *Adsorption Analysis: Equilibria and Kinetics*, vol. 2, no. Imperial College Press. Imperial College Press, 1998.

[84] M. Suzuki, *Adsorption Engineering*. Elsevier, 1990.

[85] Y. I. Aristov, "Challenging offers of material science for adsorption heat transformation: A review," *Appl. Therm. Eng.*, vol. 50, no. 2, pp. 1610–1618, 2013.

[86] T. J. Barton *et al.*, "Tailored Porous Materials," *Chem. Mater.*, vol. 11, no. 10, pp. 2633–2656, 1999.

[87] Y. Aristov, "Concept of adsorbent optimal for adsorptive cooling/heating," *Appl. Therm. Eng.*, vol. 72, no. 2, pp. 166–175, 2014.

[88] a. Hauer, "Evaluation of adsorbent materials for heat pump and thermal energy storage applications in open systems," *Adsorption*, vol. 13, no. 3–4, pp. 399–405, 2007.

[89] V. Brancato and A. Frazzica, "Characterisation and comparative analysis of zeotype water adsorbents for heat transformation applications," *Sol. Energy Mater. Sol. Cells*, vol. 180, no. February, pp. 91–102, 2018.

[90] S. T. Wilson, B. M. Lok, C. A. Messina, T. R. Cannan, and E. M. Flanigen, "Aluminophosphate Molecular Sieves: A New Class of Microporous Crystalline Inorganic Solids," *J. Am. Chem. Soc.*, vol. 104, pp. 1146–1147, 1982.

[91] A. Ristić, N. Z. Logar, S. K. Henninger, and V. Kaučič, "The performance of small-pore microporous aluminophosphates in low-temperature solar energy storage: The structure-property relationship," *Adv. Funct. Mater.*, vol. 22, no. 9, pp. 1952–1957, 2012.

[92] B. Dawoud, "On the effect of grain size on the kinetics of water vapor adsorption and desorption into/from loose pellets of FAM-Z02 under a typical operating

condition of adsorption heat pumps," *J. Chem. Eng. Japan*, vol. 40, no. 13, pp. 1298–1306, 2007.

[93] S. Santamaria, A. Sapienza, A. Frazzica, A. Freni, I. S. Girnik, and Y. I. Aristov, "Water adsorption dynamics on representative pieces of real adsorbers for adsorptive chillers," *Appl. Energy*, vol. 134, pp. 11–19, 2014.

[94] S. K. Henninger, F. Jeremias, H. Kummer, P. Schossig, and H. M. Henning, "Novel sorption materials for solar heating and cooling," *Energy Procedia*, vol. 30, pp. 279–288, 2012.

[95] S. K. Henninger, F. Jeremias, J. Ehrenmann, and C. Janiak, "The potential of PCPs/MOFs for the use in adsorption heat pump processes," in *International Soprtion Heat Pump Conference*, 2011, pp. 415–424.

[96] L. G. Gordeeva, M. V. Solovyeva, and Y. I. Aristov, "NH2-MIL-125 as a promising material for adsorptive heat transformation and storage," *Energy*, vol. 100, pp. 18–24, 2016.

[97] M. Sohail *et al.*, "Synthesis of Highly Crystalline NH2-MIL-125 (Ti) with S-Shaped Water Isotherms for Adsorption Heat Transformation," *Cryst. Growth Des.*, vol. 17, pp. 1208–1213, 2017.

[98] G. Gediz Ilis, "Influence of new adsorbents with isotherm Type V on performance of an adsorption heat pump," *Energy*, vol. 119, pp. 86–93, 2017.

[99] N. Douss and F. Meunier, "Effect of operating temperatures on the coefficient of performance of active carbon-methanol systems," *Heat Recover. Syst. CHP*, vol. 8, no. 5, pp. 383–392, 1988.

[100] E. A. Levitskij, Y. I. Aristov, M. M. Tokarev, and V. N. Parmon, "'Chemical Heat Accumulators': A new approach to accumulating low potential heat," *Sol. Energy Mater. Sol. Cells*, vol. 44, no. 3, pp. 219–235, 1996.

[101] L. Scapino, H. A. Zondag, J. Van Bael, J. Diriken, and C. C. M. Rindt, "Sorption heat storage for long-term low-temperature applications: A review on the advancements at material and prototype scale," *Appl. Energy*, vol. 190, pp. 920–948, 2017.

[102] H. T. Chua, K. C. Ng, A. Chakraborty, N. M. Oo, and M. a Othman, "Adsorption Characteristics of Silica Gel + Water Systems," pp. 1177–1181, 2002.

[103] A. Haji Abedin, "Energy and Exergy Analyses of an Open Thermochemical Energy Storage System: Methodology and Illustrative Application," *Open Renew. Energy J.*, vol. 5, no. 1, pp. 41–48, 2012.

[104] S. Kayal, S. Baichuan, and B. B. Saha, "Adsorption characteristics of AQSOA zeolites and water for adsorption chillers," *Int. J. Heat Mass Transf.*, vol. 92, pp.

1120–1127, 2016.

[105] T. Wu, J. Lucero, Z. Zong, S. K. Elsaidi, P. K. Thallapally, and M. A. Carreon, “Microporous Crystalline Membranes for Kr/Xe Separation: Comparison Between AlPO-18, SAPO-34, and ZIF-8,” *ACS Appl. Nano Mater.*, vol. 1, no. 1, pp. 463–470, 2018.

[106] R. H. Mohammed, O. Mesalhy, M. L. Elsayed, M. Su, and L. C. Chow, “Revisiting the adsorption equilibrium equations of silica-gel/water for adsorption cooling applications,” *Int. J. Refrig.*, vol. 86, pp. 40–47, 2018.

[107] H. O. Helaly, M. M. Awad, I. I. El-Sharkawy, and A. M. Hamed, “Theoretical and experimental investigation of the performance of adsorption heat storage system,” *Appl. Therm. Eng.*, vol. 147, no. October 2018, pp. 10–28, 2019.

[108] M. V. Trindade, “Modelling and optimization of an adsorption cooling system for automotive applications,” UNIVERSIDAD POLITÉCNICA DE VALENCIA, 2015.

[109] L. Calabrese *et al.*, “Development and characterization of silane-zeolite adsorbent coatings for adsorption heat pump applications,” vol. 116, pp. 364–371, 2017.

[110] M. V. Solovyeva, Y. I. Aristov, and L. G. Gordeeva, “NH2-MIL-125 as promising adsorbent for adsorptive cooling: Water adsorption dynamics,” *Appl. Therm. Eng.*, vol. 116, pp. 541–548, 2017.

[111] L. Gordeeva and Y. Aristov, “Dynamic study of methanol adsorption on activated carbon ACM-35.4 for enhancing the specific cooling power of adsorptive chillers,” *Appl. Energy*, vol. 117, pp. 127–133, 2014.

[112] K. Okamoto, M. Teduka, T. Nakano, S. Kubokawa, and H. Kakiuchi, “The development of AQSOA water vapor adsorbent and AQSOA coated heat exchanger,” in *the international sorption heat pump conference 2011*, 2010.

[113] Y. Aristov, “Novel Materials for Heat Pump and Storage: Screening and Nanotailoring of Sorption Properties,” *J. Chem. Eng. Japan*, vol. 40, no. 13, pp. 1242–1251, 2007.

[114] A. F. Lele, “A Thermochemical Heat Storage System for Households: Thermal Transfers Coupled to Chemical Reaction Investigations,” Universitat Luneburg, 2015.

[115] C. Mccague, K. Fayazmanesh, C. Berlanga, and M. Bahrami, “EVALUATION OF CaCl 2 – SILICA GEL SORBENT FOR WATER SORPTION COOLING SYSTEMS,” *Heat Pipe Sci. Technol. An Int. J.*, vol. 6, no. 3–4, pp. 229–239, 2015.

[116] S. P. Casey, J. Elvins, S. Riffat, and A. Robinson, “Salt impregnated desiccant matrices for ‘open’ thermochemical energy storage - Selection, synthesis and characterisation of candidate materials,” *Energy Build.*, vol. 84, pp. 412–425, 2014.

[117] L. Scapino, H. A. Zondag, J. Van Bael, J. Diriken, and C. C. M. Rindt, “Energy density and storage capacity cost comparison of conceptual solid and liquid sorption seasonal heat storage systems for low-temperature space heating,” *Renew. Sustain. Energy Rev.*, vol. 76, no. March, pp. 1314–1331, 2017.

[118] *VDI Heat Atlas*, Second ed. Springer, 2010.

[119] A. Griesinger, K. Spindler, and E. Hahne, “Measurements and theoretical modelling of the effective thermal conductivity of zeolites,” *Int. J. Heat Mass Transf.*, vol. 42, no. 23, pp. 4363–4374, 1999.

[120] B. Dawoud, M. I. Sohel, A. Freni, S. Vasta, and G. Restuccia, “On the effective thermal conductivity of wetted zeolite under the working conditions of an adsorption chiller,” *Appl. Therm. Eng.*, vol. 31, no. 14–15, pp. 2241–2246, 2011.

[121] A. V. Luikov, A. G. Shashkov, L. L. Vasiliev, and Y. E. Fraiman, “Thermal conductivity of porous systems,” *Int. J. Heat Mass Transf.*, vol. 11, pp. 117–140, 1968.

[122] M. K. Sarwar and P. Majumdar, “Thermal conductivity of wet composite porous media,” *Heat Recover. Syst. CHP*, vol. 15, no. 4, pp. 369–381, 1995.

[123] A. Rezk, R. K. Al-Dadah, S. Mahmoud, and A. Elsayed, “Effects of contact resistance and metal additives in finned-tube adsorbent beds on the performance of silica gel/water adsorption chiller,” *Appl. Therm. Eng.*, vol. 53, no. 2, pp. 278–284, 2013.

[124] X. H. Li, X. H. Hou, X. Zhang, and Z. X. Yuan, “A review on development of adsorption cooling - Novel beds and advanced cycles,” *Energy Convers. Manag.*, vol. 94, pp. 221–232, 2015.

[125] A. Sharafian, K. Fayazmanesh, C. McCague, and M. Bahrami, “Thermal conductivity and contact resistance of mesoporous silica gel adsorbents bound with polyvinylpyrrolidone in contact with a metallic substrate for adsorption cooling system applications,” *Int. J. Heat Mass Transf.*, vol. 79, pp. 64–71, 2014.

[126] D. B. Riffel *et al.*, “Transient modeling of an adsorber using finned-tube heat exchanger,” *Int. J. Heat Mass Transf.*, vol. 53, no. 7–8, pp. 1473–1482, 2010.

[127] A. R. M. Rezk and R. K. Al-Dadah, “Physical and operating conditions effects on silica gel/water adsorption chiller performance,” *Appl. Energy*, vol. 89, no. 1, pp. 142–149, 2012.

[128] D. Zhu and S. Wang, “Experimental investigation of contact resistance in adsorber of solar adsorption refrigeration,” *Sol. Energy*, vol. 73, no. 3, pp. 177–185, 2002.

[129] M. Bahrami, M. M. Yovanovich, and J. R. Culham, “Effective thermal conductivity of rough spherical packed beds,” *Int. J. Heat Mass Transf.*, vol. 49, no. 19–20, pp.

3691–3701, 2006.

[130] E. Tsotsas and H. Martin, “Thermal conductivity of packed beds: A review,” *Chem. Eng. Process.*, vol. 22, no. 1, pp. 19–37, 1987.

[131] F. P. Incropera, D. P. Dewitt, T. L. Bergman, and A. S. Lavine, *Fundamentals of Heat and Mass Transfer*. 2007.

[132] H. Czichos, T. Saito, and L. Smith, *Springer Handbook of Metrology and Testing*, 2nd ed. Springer, 2011.

[133] Yovanovich, “Thermal Spreading and Contact Resistances,” in *A. Bejan, D. Kraus, Heat Transfer Handbook*, New York: John Wiley and Sons Inc., 2003.

[134] D. Stroud, “The effective medium approximations: Some recent developments,” *Superlattices Microstruct.*, vol. 23, no. 3, pp. 567–573, 1998.

[135] M. J. Goldsworthy, “Measurements of water vapour sorption isotherms for RD silica gel, AQSOA-Z01, AQSOA-Z02, AQSOA-Z05 and CECA zeolite 3A,” *Microporous Mesoporous Mater.*, vol. 196, pp. 59–67, 2014.

[136] S. Song and M. M. Yovanovich, “Correlation of thermal accomodation coefficient for engineering surfaces,” *Proceedings of the Twenty-fourth National Heat Transfer Conference and Exhibition*. pp. 107–116, 1987.

[137] C. L. Tien and K. Vafai, “Statistical Upper and Lower Bounds of Effective Thermal Conductivity of Fibrous Insulation,” in *2nd AIAA/ASME thermophysics and heat transfer conference*, 1978.

[138] P. Karayacoubian, M. Bahrami, and J. R. Culham, “Asymptotic solutions of effective thermal conductivity,” in *2005 ASME International Mechanical Engineering Congress and Exposition*, 2005.

[139] A. J. Slavin, V. Arcas, C. A. Greenhalgh, E. R. Irvine, and D. B. Marshall, “Theoretical model for the thermal conductivity of a packed bed of solid spheroids in the presence of a static gas, with no adjustable parameters except at low pressure and temperature,” *Int. J. Heat Mass Transf.*, vol. 45, no. 20, pp. 4151–4161, 2002.

[140] R. Mari, L. Portal, A. Baule, H. A. Makse, and L. Bo, “Mean-field theory of random close packings of axisymmetric particles,” *Nat. Commun.*, vol. 4, no. 1, pp. 1–11, 2013.

[141] H. Bjurström, E. Karawacki, and B. Carlsson, “Thermal conductivity of a microporous particulate medium: moist silica gel,” *Int. J. Heat Mass Transf.*, vol. 27, no. 11, pp. 2025–2036, 1984.

[142] Y. Y. Tanashev and Y. I. Aristov, “Thermal conductivity of a silica gel + calcium

chloride system: The effect of adsorbed water," *J. Eng. Phys. Thermophys.*, vol. 73, no. 5, pp. 876–883, 2000.

[143] Y. Y. Tanashev, A. V. Krainov, and Y. I. Aristov, "Thermal conductivity of composite sorbents 'salt in porous matrix' for heat storage and transformation," *Appl. Therm. Eng.*, vol. 61, no. 2, pp. 401–407, 2013.

[144] L. W. Wang, Z. Tamainot-Telto, S. J. Metcalf, R. E. Critoph, and R. Z. Wang, "Anisotropic thermal conductivity and permeability of compacted expanded natural graphite," *Appl. Therm. Eng.*, vol. 30, no. 13, pp. 1805–1811, 2010.

[145] K. Fayazmanesh, C. McCague, and M. Bahrami, "Consolidated adsorbent containing graphite flakes for heat-driven water sorption cooling systems," *Appl. Therm. Eng.*, vol. 123, pp. 753–760, 2017.

[146] A. Freni, M. M. Tokarev, G. Restuccia, A. G. Okunev, and Y. I. Aristov, "Thermal conductivity of selective water sorbents under the working conditions of a sorption chiller," *Appl. Therm. Eng.*, vol. 22, no. 14, pp. 1631–1642, 2002.

[147] Z. Tamainot-Telto and R. E. Critoph, "Monolithic carbon for sorption refrigeration and heat pump applications," *Appl. Therm. Eng.*, vol. 21, no. 1, pp. 37–52, 2001.

[148] V. W. Antonetti and M. M. Yovanovich, "Enhancement of Thermal Contact Conductance By Metallic Coatings: Theory and Experiment.," *J. Heat Transfer*, vol. 107, no. 3, pp. 513–519, 1985.

[149] I. S. Girnik and Y. I. Aristov, "Dynamic optimization of adsorptive chillers: The 'AQSOA^{TM}-FAM-Z02 – Water' working pair," *Energy*, vol. 106, pp. 13–22, 2016.

[150] G. Gullì *et al.*, "Innovative Adsorption Chiller for Marine Applications: Design and Building," *Energy Procedia*, vol. 82, pp. 432–438, 2015.

[151] A. Freni, L. Bonaccorsi, L. Calabrese, A. Caprì, A. Frazzica, and A. Sapienza, "SAPO-34 coated adsorbent heat exchanger for adsorption chillers," *Appl. Therm. Eng.*, vol. 82, pp. 1–7, 2015.

[152] A. Frazzica, G. Füldner, A. Sapienza, A. Freni, and L. Schnabel, "Experimental and theoretical analysis of the kinetic performance of an adsorbent coating composition for use in adsorption chillers and heat pumps," *Appl. Therm. Eng.*, vol. 73, no. 1, pp. 1022–1031, 2014.

[153] U. Wittstadt, G. Füldner, O. Andersen, R. Herrmann, and F. Schmidt, "A new adsorbent composite material based on metal fiber technology and its application in adsorption heat exchangers," *Energies*, vol. 8, no. 8, pp. 8431–8446, 2015.

[154] "McMaster-CARR, Light Duty Blended EPDM Foam Strip." [Online]. Available: https://www.mcmaster.com/#8694k111/=1ajm4w7. [Accessed: 22-Aug-2019].

[155] P. Teertstra, “Thermal conductivity and contact Resistance measurments for adhesives,” in *Proceedings of IPACK2007*, 2007.

[156] M. Kaviany, *Principles of Heat Transfer in Porous Media*, Second Edi. 1995.

[157] W. Wagner and H.-J. Kretzschmar, *International SteamTables - Properties ofWater and Steam Based on the Industrial Formulation IAPWS-IF97*, Second. Berlin: Springer-Verlag, 2008.

[158] A. Sharafian, S. M. Nemati Mehr, W. Huttema, and M. Bahrami, “Effects of different adsorber bed designs on in-situ water uptake rate measurements of AQSOA FAM-Z02 for vehicle air conditioning applications,” *Appl. Therm. Eng.*, vol. 98, pp. 568–574, 2016.

[159] A. Sapienza, S. Santamaria, A. Frazzica, A. Freni, and Y. I. Aristov, “Dynamic study of adsorbers by a new gravimetric version of the Large Temperature Jump method,” *Appl. Energy*, vol. 113, pp. 1244–1251, 2014.

[160] P. C. Thimmaiah, A. Sharafian, M. Rouhani, W. Huttema, and M. Bahrami, “Evaluation of low-pressure flooded evaporator performance for adsorption chillers,” *Energy*, vol. 122, pp. 144–158, 2017.

[161] A. Patton, B. D. Crittenden, and S. P. Perera, “Use of the Linear Driving Force Approximation to Guide the Design of Monolithic Adsorbents,” *Chem. Eng. Res. Des.*, vol. 82, no. 8, pp. 999–1009, 2004.

[162] C. McCague, M. Bahrami, and A. Ismail, “Thermogravimetric analysis of water and methanol vapor sorption of silicoalumino phosphate zeolite (AQSOA-Z02),” in *IVth International Symposium on Innovative Materials for Processes in Energy Systems (IMPRES2016)*, 2016.

[163] P. Bendix *et al.*, “Optimization of power density and metal-to-adsorbent weight ratio in coated adsorbers for adsorptive heat transformation applications,” *Appl. Therm. Eng.*, vol. 124, pp. 83–90, 2017.

[164] L. Yong and K. Sumathy, “Review of mathematical investigation on the closed adsorption heat pump and cooling systems,” *Renew. Sustain. Energy Rev.*, vol. 6, no. 4, pp. 305–337, 2002.

[165] A. Freni *et al.*, *Characterization of Zeolite-Based Coatings for Adsorption Heat Pumps*. Springer briefs in applied sciences and technology: Springer, Cham, 2015.

[166] G. Zhang, D. C. Wang, J. P. Zhang, Y. P. Han, and W. Sun, “Simulation of operating characteristics of the silica gel-water adsorption chiller powered by solar energy,” *Sol. Energy*, vol. 85, no. 7, pp. 1469–1478, 2011.

[167] B. Y. E. Glueckauf, “Theory of Chromatography. Part 10. Formulae for Diffusion into Spheres and their Application to Chromatography,” *Trans. Faraday Soc.*, vol.

51, pp. 1540–1551, 1955.

[168] E. Glueckauf, “Theory of chromatography,” *Trans. Faraday Soc.*, vol. 51, p. 1540, 1955.

[169] A. Frazzica and L. F. Cabeza, *Recent Advancements in Materials and Systems for Thermal Energy Storage — An Introduction to Experimental Characterization Methods*. Springer, 2019.

[170] H. Wei Benjamin Teo, A. Chakraborty, and W. Fan, “Improved adsorption characteristics data for AQSOA types zeolites and water systems under static and dynamic conditions,” *Microporous Mesoporous Mater.*, vol. 242, pp. 109–117, 2017.

[171] G. Sidebotham, *Heat transfer modeling: an inductive approach*. Springer, 2015.

[172] P. Cheppudira Thimmaiah, A. Sharafian, W. Huttema, C. McCague, and M. Bahrami, “Effects of capillary-assisted tubes with different fin geometries on the performance of a low-operating pressure evaporator for adsorption cooling system applications,” *Appl. Energy*, vol. 171, pp. 256–265, 2016.

[173] A. Sapienza, A. Frazzica, A. Freni, and Y. Aristov, “Dramatic effect of residual gas on dynamics of isobaric adsorption stage of an adsorptive chiller,” *Appl. Therm. Eng.*, vol. 96, pp. 385–390, 2016.

[174] K. Edem, N. Tsoukpoe, G. Restuccia, T. Schmidt, and X. Py, “The size of sorbents in low pressure sorption or thermochemical energy storage processes,” *Energy*, vol. 77, pp. 983–998, 2014.

[175] M. J. Pons and F. Poyelle, “Adsorptive machines with advanced cycles for heat pumping or cooling applications,” *Int. J. Refrig.*, vol. 22, no. 1, pp. 27–37, 1999.

[176] A. Akahira, K. C. a. Alam, Y. Hamamoto, A. Akisawa, and T. Kashiwagi, “Mass recovery adsorption refrigeration cycle—improving cooling capacity,” *Int. J. Refrig.*, vol. 27, no. 3, pp. 225–234, 2004.

[177] K. Thu, B. B. Saha, A. Chakraborty, W. G. Chun, and K. C. Ng, “Study on an advanced adsorption desalination cycle with evaporator-condenser heat recovery circuit,” *Int. J. Heat Mass Transf.*, vol. 54, no. 1–3, pp. 43–51, 2011.

[178] N. Douss and F. Meunier, “Experimental study of cascading adsorption cycles,” *Chem. Eng. Sci.*, vol. 44, no. 2, pp. 225–235, 1989.

[179] S. V. Shelton, W. J. Wepfer, and D. J. Miles, “Ramp Wave Analysis of the Solid/Vapor Heat Pump,” *J. Energy Resour. Technol.*, vol. 112, no. 1, p. 69, 1990.

[180] Z. Yu, G. Huang, F. Haghighat, H. Li, and G. Zhang, “Control strategies for integration of thermal energy storage into buildings: State-of-the-art review,” *Energy*

Build., vol. 106, pp. 203–215, 2015.

[181] T. Osterland *et al.*, “Conception of a heat storage system for household applications,” *Proc. 7th Int. Renew. Energy Storage Conf. Exhib. (IRES 2012)*, no. March 2015, pp. 429–432, 2012.

[182] a Hauer, E. Lävemann, and K. Steinle, “Sorption Storage System for a Dishwasher,” 2008.

[183] M. Rouhani, A. Sharafian, P. Cheppudira, W. Huttema, and M. Bahrami, “Thermal management of a greenhouse with adsorption energy storage,” in *International Sorption Heat Pump Conference ISHPC2017*, 2017.

[184] M. Bahrami, J. R. Culham, M. M. Yananovich, and G. E. Schneider, “Review of Thermal Joint Resistance Models for Nonconforming Rough Surfaces,” *Appl. Mech. Rev.*, vol. 59, no. 1, p. 1, 2006.

[185] P. T. Tsilingiris, “Review and critical comparative evaluation of moist air thermophysical properties at the temperature range between 0 and 100 °C for Engineering Calculations,” *Renew. Sustain. Energy Rev.*, no. January, pp. 1–14, 2017.

[186] J. P. Holman, *Experimental methods for engineers*, vol. 9, no. 2. 1994.

[187] Y. I. Aristov, “Adsorptive transformation of heat: Principles of construction of adsorbents database,” *Appl. Therm. Eng.*, vol. 42, pp. 18–24, 2012.

[188] Y. I. Aristov, “Optimal adsorbent for adsorptive heat transformers: Dynamic considerations,” *Int. J. Refrig.*, vol. 32, no. 4, pp. 675–686, 2009.

[189] Y. I. Aristov, “Adsorptive transformation of heat: Principles of construction of adsorbents database,” *Appl. Therm. Eng.*, vol. 42, pp. 18–24, 2012.

[190] D. M. Ruthven, *Principles of Adsorption and Adsorption Processes*. John Wiley and sons, 1984.

[191] Y. I. Aristov, M. M. Tokarev, A. Freni, I. S. Glaznev, and G. Restuccia, “Kinetics of water adsorption on silica Fuji Davison RD,” *Microporous Mesoporous Mater.*, vol. 96, no. 1–3, pp. 65–71, 2006.

[192] A. Sapienza, A. Frazzica, A. Freni, and Y. Aristov, *Dynamics of Adsorptive Systems for Heat Transformation_ Optimization of Adsorber*. Springer, 2018.

[193] B. Dawoud and Y. Aristov, “Experimental study on the kinetics of water vapor sorption on selective water sorbents, silica gel and alumina under typical operating conditions of sorption heat pumps,” *Int. J. Heat Mass Transf.*, vol. 46, no. 2, pp. 273–281, 2003.

[194] Y. I. Aristov, “Adsorptive transformation and storage of renewable heat: Review of current trends in adsorption dynamics,” *Renew. Energy*, vol. 110, pp. 105–114, 2017.

[195] Y. I. Aristov, B. Dawoud, I. S. Glaznev, and A. Elyas, “A new methodology of studying the dynamics of water sorption/desorption under real operating conditions of adsorption heat pumps: Experiment,” *Int. J. Heat Mass Transf.*, vol. 51, no. 19–20, pp. 4966–4972, 2008.

[196] A. Sharafian and M. Bahrami, “Assessment of adsorber bed designs in waste-heat driven adsorption cooling systems for vehicle air conditioning and refrigeration,” *Renew. Sustain. Energy Rev.*, vol. 30, pp. 440–451, 2014.

[197] M. Rouhani *et al.*, “Performance enhancement of an adsorption cooling system with AQSOA FAM-Z02 and low-finned tube evaporator,” in *Innovative Materials for Processes in Energy Systems 2016*, 2016, pp. 309–310.

Appendix A.

Supplementary information on the equations used in Chapter 4

The equations used for the theoretical model in Chapter 4, to find the micro/micro-contact and micro/macro-gap resistances, are listed in Table 23 (for more details, see refs. [129], [136]).

Table 23. Equations used to find the thermal resistance of the unit cell, R_{cell}, [129], [136]

Equations		Ref.	Eq. number
$R_{\mathrm{cell}} = \left[\dfrac{1}{\left(1/R_{\mathrm{c,micro}} + 1/R_{\mathrm{g,micro}}\right)^{-1} + R_{\mathrm{C,macro}}} + \dfrac{1}{R_{\mathrm{p}} + R_{\mathrm{G,macro}}}\right]^{-1}$	(KW^{-1})	[129]	(52)
$R_{\mathrm{c,micro}} = \left[0.565\, H_{\mathrm{mic}}\left(\sigma_{\mathrm{p}}/m_{\mathrm{p}}\right)\right]/(k_{\mathrm{s}}F)$	(KW^{-1})	[129]	(53)
$R_{\mathrm{C,macro}} = 1/(2k_{\mathrm{s}}a_{\mathrm{macro}})$	(KW^{-1})	[129]	(54)
$R_{\mathrm{g,micro}} = \left(2\sqrt{2}\,\sigma_{\mathrm{p}}\,a_2\right)\Big/\left\{\pi k_{\mathrm{g}} a_L^2 \ln\left(1 + \dfrac{a_2}{a_1 + M/\left[2\sqrt{2}\,\sigma_{\mathrm{p}}\right]}\right)\right\}$	(KW^{-1})	[129]	(55)
$R_{\mathrm{G,macro}} = \dfrac{2}{\pi\, k_{\mathrm{g}}\left[\mathrm{S}\ln\left(\dfrac{S-B}{S-A}\right) + B - A\right]}$	(KW^{-1})	[129]	(56)
$k_{\mathrm{s}} = \dfrac{2k_{\mathrm{p,1}}\,k_{\mathrm{p,2}}}{k_{\mathrm{p,1}} + k_{\mathrm{p,2}}}$	(Wm^{-1}K^{-1})	[129]	(57)
$H_{\mathrm{micro}} = c_1(d_v/\sigma_0)^{c_2}$	(Pa)	[129]	(58)
$\sigma_0 = 1\ \mu\mathrm{m}, \quad d_v = \sqrt{2\pi}\,a_{\mathrm{C,macro}} = 0.95\left(\sigma_{\mathrm{p}}/m_{\mathrm{p}}\right)$	(m)	[184]	(59)
$c_1 = H_{\mathrm{BGM}}\,(4.0 - 5.77\kappa + 4.0\kappa^2 - 0.61\kappa^3), \qquad \kappa = H_{\mathrm{B}}/H_{\mathrm{BGM}}$	(Pa)	[129]	(60)
$c_2 = -0.57 + 0.82\kappa - 0.41\kappa^2 - 0.06\kappa^3$		[129]	(61)
$H_{\mathrm{BGM}} = 3.178\ \mathrm{GPa}, \quad 1.3 \le H_{\mathrm{B}} \le 7.6\ \mathrm{GPa}$	(Pa)	[129]	(62)
$m_{\mathrm{p}} = \sqrt{m_{\mathrm{p1}}^2 + m_{\mathrm{p2}}^2}\,, \qquad m_{\mathrm{p1}} = 0.076\,\sigma_{\mathrm{p1}}^{0.52}$		[129]	(63)
$\sigma_{\mathrm{p}} = \sqrt{\sigma_{\mathrm{p1}}^2 + \sigma_{\mathrm{p2}}^2}$	(m)	[129]	(64)

$$\frac{a_{\mathrm{macro}}}{a_{\mathrm{H}}}=\begin{cases}1.605/\sqrt{\acute{P}_0} & 0.01\le \acute{P}_0\le 0.47\\ 3.51-2.51\acute{P}_0 & 0.47\le \acute{P}_0\le 1\end{cases}$$ [129] (65)

$$\acute{P}_0=P_0/P_{0,\mathrm{H}}=1/(1+1.37\alpha(\rho/a_{\mathrm{H}})^{-0.075}),\quad \alpha=\frac{\sigma\rho}{a_{\mathrm{H}}^2}$$ [129] (66)

$$P_{0,\mathrm{H}}=1.5F/\left(\pi a_{\mathrm{H}}^2\right)$$ (Pa) [129] (67)

$$a_{\mathrm{H}}=\left(0.75F\rho/\acute{E}\right)^{1/3}$$ (m) [129] (68)

$$\acute{E}=\left[\left(1-\nu_{\mathrm{p1}}^2\right)/E_{\mathrm{p1}}+\left(1-\nu_{\mathrm{p2}}^2\right)/E_{\mathrm{p2}}\right]^{-1}$$ (Pa) [129] (69)

$$\rho_{\mathrm{p}}=\left(1/\rho_{\mathrm{p1}}+1/\rho_{\mathrm{p2}}\right)^{-1}$$ (m) [129] (70)

$$a_1=\mathrm{erfc}^{-1}\left(2P_0/\acute{H}\right),\quad a_2=\mathrm{erfc}^{-1}\left(0.003P_0/\acute{H}\right)-a_1$$ [129] (71)

$$\acute{H}=c_1\left(1.62\left(\sigma_{\mathrm{p}}/\sigma_0\right)/m_{\mathrm{p}}\right)^{c_2}$$ (GPa) [129] (72)

$$M=\left(\frac{2-\alpha_{T1}}{\alpha_{T1}}+\frac{2-\alpha_{T2}}{\alpha_{T2}}\right)\left(\frac{2\gamma_{\mathrm{g}}}{1+\gamma_{\mathrm{g}}}\right)\frac{1}{Pr}\Lambda$$ (m) [129] (73)

$\Lambda=\frac{P_0}{P_{\mathrm{g}}}\frac{T_{\mathrm{g}}}{T_0}\Lambda_0$,
Λ_0: mean free path value at reference gas temperature T_0 and pressure P_0 (m) [129] (74)

$\alpha_T=\exp\left[-0.57\left(\frac{T_{\mathrm{s}}-T_0}{T_0}\right)\right]\left(\frac{M^*}{6.8+M^*}\right)+\frac{2.4\mu}{(1+\mu)^2}\left\{1-\right.$
$\left.exp\left[-0.57\left(\frac{T_{\mathrm{s}}-T_0}{T_0}\right)\right]\right\}$,
$\mu=M_{\mathrm{g}}/M_{\mathrm{s}}$ [136] (75)

$$M^*=\begin{cases}M_{\mathrm{g}} & \text{monoatomic gas}\\ 1.4M_{\mathrm{g}} & \text{diatomic/polyatomic gas}\end{cases}$$ (kgmol^{-1}) [136] (76)

$A=2\sqrt{\rho_{\mathrm{p}}^2-a_L^2},\quad B=2\sqrt{\rho_{\mathrm{p}}^2-b_L^2},\quad S=2(\rho-\omega_0)+M,\ \omega_0=a_L^2/(2\rho)$ (m) [129] (77)

Appendix B.

Thermo-physical and chemical specification of working pairs: adsorbent and adsorbate

B.1. Adsorbent

B.1.1. AQSOA FAM-Z02

Table 24 provides the specifications of FAM-Z02, reported in the literature.

Table 24. Specifications of AQSOA FAM-Z02.

Material	**FAM-Z02**
Provider	Mitsubishi Plastic Inc.
Chemical formula	$Al_{0.56}Si_{0.02}P_{0.42}O_2$ [104]
Structure IZA code	SAPO34 CHA [112]
Differential heat of adsorption ($kJkg_w^{-1}$)	3240 (298 K)[20]
Bulk density (kgm^{-3})	0.6-0.7 [20]
Specific heat ($Jkg^{-1}K^{-1}$)	0.822 (303 K) 0.942 (363 K) [20]
Thermal conductivity ($Wm^{-1}K^{-1}$)	0.117 (303 K) 0.128 (363 K) [20]
Particle diameter (mm)	0.1-2 [20]
Pore diameter (Å)	3.8 [112]
BET surface area (m^2g^{-1})	590 [104]
Micro-pore volume (cm^3g^{-1})	0.2769 [104]

B.2. Adsorbate

Thermal conductivity of the humid air is calculated from eq. (78), where k_{a} and k_{v} are thermal conductivities of dry air and water vapor, respectively.

$$k_{\mathrm{ha}} = k_{\mathrm{a}}\left(1 - \mathrm{RH}\frac{P_{\mathrm{sat}}}{P_0}\right) + k_{\mathrm{v}}\ \mathrm{RH}\ \frac{P_{\mathrm{sat}}}{P_0} \qquad [185] \qquad (78)$$

Appendix C.

C.1. Uncertainty analysis for the experimental study in Chapter 4

The operational definition of thermal conductivity, for HFM measurement, is obtained from the following equation (ASTM C 518),

$$k = \frac{f_{\text{calib}}\, V\, L_{\text{bed}}}{\Delta T} \tag{79}$$

where $f_{\text{calib}}\ [\text{W}/(\text{m}^2\text{V})]$ is the calibration factor, and $V\ [\text{V}]$ is the heat flux transducer output. Therefore, According to the uncertainty propagation [186], the systematic error of the thermal conductivity is as follows,

$$\frac{\delta k}{k} = \left[\left(\frac{\delta f_{\text{calib}}}{f_{\text{calib}}}\right)^2 + \left(\frac{\delta V}{V}\right)^2 + \left(\frac{\delta L_{\text{bed}}}{L_{\text{bed}}}\right)^2 + \left(\frac{\delta(\Delta T)}{\Delta T}\right)^2\right]^{1/2} \tag{80}$$

where the last term in the right-hand side of this equation is calculated as follows,

$$\frac{\delta(\Delta T)}{\Delta T} = \left[\left(\frac{\delta T_1}{\Delta T}\right)^2 + \left(\frac{\delta T_2}{\Delta T}\right)^2\right]^{1/2} \tag{81}$$

The accuracies and relative errors of bed thickness, heat flux measurement and calibration factor (supplied by the manufacturer) and external thermocouples are listed in Table 25. The systematic uncertainty of thermal conductivity is 7-8%. The difference between the thermal conductivity uncertainty of the experiment and the reported value by the manufacturer is due to the thermocouple accuracy of the external thermocouples (±1 °C) compared to that of the embedded thermocouples in HFM (±0.01 °C). As mentioned before, external thermocouples are used to eliminate the effect of thermal contact resistance between the hot/cold plate and the sample.

Table 25. Accuracies and relative error of HFM measurements

δL_{bed} (cm)	δT (°C)	δV (μV)	$\left(\frac{\delta f_{\text{calib}}}{f_{\text{calib}}}\right)$	$\left(\frac{\delta L_{\text{bed}}}{L_{\text{bed}}}\right)$	$\left(\frac{\delta V}{V}\right)$	$\frac{\delta(\Delta T)}{\Delta T}$
0.01	1 (external thermocouple)	5	0.01	0.008 - 0.036	2×10^{-4}	0.05

Similarly, the uncertainty of thermal resistance is calculated as follows,

$$\frac{\delta R}{R} = \left[\left(\frac{\delta f_{\text{calib}}}{f_{\text{calib}}}\right)^2 + \left(\frac{\delta V}{V}\right)^2 + \left(\frac{\delta(\Delta T)}{\Delta T}\right)^2\right]^{1/2} \tag{82}$$

Therefore, the maximum systematic uncertainty of thermal resistance is 7%. The random error from the repeatability measurement is negligible.

C.2. Uncertainty analysis for the experimental study in Chapter 5 and Chapter 6

According to the uncertainty propagation [186], the systematic error in the measurement of the evaporative cooling energy can be calculated as:

$$\left(\frac{\delta Q_{\text{evap}}}{Q_{\text{evap}}}\right)_{\text{systematic}} = \sqrt{\left(\frac{\delta \dot{m}_{\text{chilled}}}{\dot{m}_{\text{chilled}}}\right)^2 + \left(\frac{\delta\left(T_{\text{i,chilled}} - T_{\text{o,chilled}}\right)}{T_{\text{i,chilled}} - T_{\text{o,chilled}}}\right)^2} \tag{83}$$

where the last term in the right-hand side of Eq. (83) is calculated as follows,

$$\frac{\delta\left(T_{\text{i,chilled}} - T_{\text{o,chilled}}\right)}{T_{\text{i,chilled}} - T_{\text{o,chilled}}} = \sqrt{\left(\frac{\delta T_{\text{i,chilled}}}{T_{\text{i,chilled}} - T_{\text{o,chilled}}}\right)^2 + \left(\frac{\delta T_{\text{o,chilled}}}{T_{\text{i,chilled}} - T_{\text{o,chilled}}}\right)^2} = 0.042 \tag{84}$$

The maximum systematic uncertainty of evaporative cooling energy is:

$$\left(\frac{\delta Q_{\text{evap}}}{Q_{\text{evap}}}\right)_{\text{systematic}} = \sqrt{0.005^2 + 0.042^2} = 0.042 = 4.2\% \tag{85}$$

The random error of Q_{evap}, based on the maximum standard deviation, was 8%. Therefore, the maximum uncertainty in the calculation of Q_{evap} was 12.2% (8%+4.2%). Therefore, the uncertainty of SP is as follows:

$$\frac{\delta \text{SP}_{\text{cold}}}{\text{SP}_{\text{cold}}} = \sqrt{\left(\frac{\delta Q_{\text{evap}}}{Q_{\text{evap}}}\right)^2 + \left(\frac{\delta m_{\text{ads}}}{m_{\text{ads}}}\right)^2 + \left(\frac{\delta t_{\text{dch}}}{t_{\text{dch}}}\right)^2} = 0.122 = 12.2\% \tag{86}$$

Appendix D.

Introduction to adsorption isotherms and kinetics

D.1. Adsorption isotherms equations

The maximum degree to which the adsorbent can accommodate the adsorbate phase is represented by the adsorption equilibrium relationship between the adsorbed amount of adsorbate, operating pressure, and temperature. Some common adsorption equilibrium relationships and their details are listed in Table 26.

Table 26. Adsorption isotherm models and their specifications [31], [187].

	Model	Equation	Remarks
Theoretical	Henry	$\omega_{\mathrm{eq}}(P,T) = K(T)\,P$	■ Simple and linear relationship. ■ Limiting case of low partial pressures (low concentrations)
	Langmuir	$\omega_{\mathrm{eq}}(P,T) = \omega_0 \frac{b(T)P}{1+b(T)P}$	■ At low partial pressure, reduces to the Henry isotherm and at high partial pressure, reaches the maximum saturation uptake; applicable for a wide range of pressure ■ Based on the monolayer assumption ■ Based on the assumption of surface homogeneity
Semi-empirical	Freundlich	$\omega_{\mathrm{eq}}(P,T) = K(T)P^{1/n(T)}$	■ Simple relationship. ■ Only suitable for medium partial pressures (neither low nor high pressures); not applicable over a wide range of pressure. ■ Including the surface energy heterogeneity parameter, $n(T)$.
	Sips	$\omega_{\mathrm{eq}}(P,T) = \omega_0 \frac{K(T)P^{1/n(T)}}{1+K(T)P^{1/n(T)}}$	■ Not valid for low partial pressure; does not follow the Henry isotherm at low pressures. ■ At high partial pressures, reaches the maximum saturation uptake.
	Tóth	$\omega_{\mathrm{eq}}(P,T) = \omega_0 \frac{KP^m}{(1+KP^m)^{1/m}}$	■ Including both partial pressure limiting cases (very low and high pressures); applicable over a wide range of pressure.
Empirical	Dubinin-Radushkevich	$\omega_{\mathrm{eq}}(P,T) = \omega_0 \exp\left(-\left(\frac{RT\ln(P/P_0)}{\beta E_0}\right)^2\right)$	■ Temperature dependent relationship. ■ Not being thermodynamically consistent at very low pressures (at Henry's law region). ■ For both homogeneous and heterogeneous surfaces.
	Dubinin-Astakhov	$\omega_{\mathrm{eq}}(P,T) = \omega_0 \exp\left(-\left(\frac{RT\ln(P/P_0)}{\beta E_0}\right)^n\right)$	■ More general equation compared to Dubinin-Radushkevich
	Brunauer, Emmett and Teller (BET)	$\omega_{\mathrm{eq}}(P,T) = \omega_0 \frac{C\,\frac{P}{P_0}}{\left(1-\frac{P}{P_0}\right)\left[1+(C-1)\left(\frac{P}{P_0}\right)\right]}$	■ For multilayer adsorption ■ For relative pressures, P/P0, between 0.05 to 0.30.

D.2. Adsorption kinetics

The most common method to study the dynamics of adsorption systems, for the small-scale assessment, is isothermal differential steps (IDS) using a thermo-gravimetric system. The driving force for the water vapor adsorption is small pressure jumps and the heat dissipation rate during the adsorption should be fast enough to guarantee the isothermal condition and small differential change in the uptake [188], [189]. Assuming a linear equilibrium uptake relationship, the analytical solution of the mass diffusion equation is used in this model, which is valid for small uptakes ($\omega_t/\omega_\infty < 0.3$). [190], [191]. Moreover, the operating condition in the IDS method is not similar to that of a closed sorption TES [192].

Volumetric large pressure jump (LPJ) method is a non-isothermal method, in which the adsorption process is initiated by a large pressure rise around the adsorbent material [193]. The sample measurement chamber is maintained at the adsorption temperature by a cold plate located under the sample holder and after reaching an equilibrium condition, the valve between the water vapor reservoir and the measurement chamber is opened and consequently, the pressure is decreased due to the water vapor adsorption [188]. The kinetic models which can be applied to LPJ method are not simple and also operating condition of LPJ does not exactly follow a real adsorption cycle, where adsorption is driven by the adsorbent temperature drop [194].

Aristov et al. [195] developed a large temperature jump (LTJ) method, which can properly replicate the isobaric adsorption/ desorption process in an adsorption cycle. As listed in Table 12, LTJ has been widely used to study kinetics and adsorption capacity of FAM-Z02 for small-scale measurements. In this method, the vapor pressure over the sample is kept constant, while the adsorption process is initiated by the adsorbent temperature change due to the change in the HTF temperature, flowing under the sample holder [195]. It is, nevertheless, not applicable for a large amount of adsorbent and complex heat exchanger (HEX) medium [194].

Sapienza et al. [159] proposed a gravimetric LTJ (G-LTJ) method, which added a real-time mass measurement to the LTJ approach. Their G-LTJ testbed was suitable for a larger amount of adsorbent material in the range of 5- 600 g (adsorbent material + HEX) and various adsorbent configurations (powder, loose grain, and coating) [159]. Although G-LTJ is a reliable approach for adsorption dynamic study, the kinetic of a full-scale

adsorber bed, including the HEX (e.g., 0.636-260 kg, reported in ref. [196]) and adsorbent material (e.g., 0.35-140 kg, reported in ref. [196]), undergoes more challenges in both mass and heat transfer. Bulkiness of the storage system, particularly the sorber heat exchanger, leads to (i) a decrease in thermal efficiency due to higher energy required to heat up the mass of the sorber bed, and (ii) a decrease in ESD due to more volume of the storage system and sensible heat loss by the sorber mass.

Accordingly, real-time mass measurement of the full-scale adsorber bed during the adsorption/desorption process is beneficial for realistic dynamic analysis of the system and optimizing the design and operating parameters.

Few studies are available in the literature focusing on the sorption dynamics of the full-scale closed adsorption systems [42], [158]. Dawoud [42] presented a comparison between the adsorption kinetics of a full-scale one-bed coated FAM-Z02 ACS and the adsorption kinetics measure for a small amount of coated FAM-Z02, using LTJ method. For the full-scale kinetic measurement, the net water uptake was estimated based on the cooling load of the evaporator [42]. Sharafian et al. [158] performed an in-situ mass measurement of two different finned-tube heat exchangers filled with the FAM-Z02 pellets. In this work, a real-time in-situ temperature and mass measurement of a full-size adsorber bed (~25 kg: 0.7 kg adsorbent, 2.87 kg heat exchanger and ~ 21.4 kg vacuum chamber and the adsorbed water) was conducted for a 2 mm-thickness coated FAM-Z02 adsorber bed of a short-delivery adsorption cold storage system.

Appendix E.

Component specifications of the S-TES testbed

E.1. Specifications of sorber bed in the S-TES testbed

Table 27 presents the specifications of the finned tube adsorber bed used in Chapter 5 and Chapter 6.

Table 27. Specifications of the adsorber bed used in the studied S-TES

Parameter	Packed bed	Coated bed
Metal mass of adsorber (kg)	2.87	
Adsorber bed heat transfer area (m^2)	0.74	2.8
Fin spacing (mm)	2.34	
Fin thickness (mm)	0.4	

E.2. Specifications of the evaporator in the sorp-TES testbed

Table 28 presents the specifications of the capillary-assisted evaporator used in Chapter 5 and Chapter 6.

Table 28. Specifications of the evaporator used in the studied sorp-TES

Parameter	
Evaporator tube model	GEWA®-K-2615 (Wieland Thermal Solutions)
Evaporator outer diameter (mm)	12.7 (1/2”)
Evaporator fin type	Continuous and parallel fins
Evaporator number of fins per meter	1024 (26 fins per inch)
Evaporator fin spacing (mm)	1
Evaporator fin height (mm)	1.5
Evaporator inside surface area ($m^2\,m^{-1}$)	0.024
Evaporator outside surface area ($m^2\,m^{-1}$)	0.124
Evaporator tube length (m)	4.3
Evaporator total heat transfer area (m^2)	0.53
Evaporator effectiveness, ε	0.7

Appendix F.

Experimental data for three cycles of sorption-desorption and calculated water uptake, energy storage density, specific power, and COP of the FAM-Z02 S-TES system

F.1. Experimental data of packed bed with 0.5 kg of 2-mm FAM-Z02

Table 29. Experimental data of the S-TES system with a packed bed filled with 0.5 kg of 2-mm FAM-Z02, for three sorption-desorption cycles.

t	t	$T_{ambient}$	T_{Bed_in}	T_{Bed_out}	T_{Evap_in}	T_{evap_out}	T_{cond_in}	$T_{cond,out}$	P_{bed}	P_{evap}	P_{cond}	$\dot{m}_{evap}$	$\dot{Q}_{evap}$	$\dot{Q}_{ads}$	$\dot{Q}_{des}$	$\dot{Q}_{cond}$
s	min	°C	°C	°C	°C	°C	°C	°C	kPa	kPa	kPa	L/min	W	W	W	W
1	0.02	23.35	30.8	32.3	15.4	15.4	30.5	30.5	0.32	1.36	6.57	2.23	-0.7	-152.0	-149.3	-3.9
60	1	23.65	31.0	33.9	15.2	14.0	30.4	30.4	0.32	1.19	6.49	2.24	192.2	-313.7	-293.5	-2.4
120	2	23.3	30.9	34.0	15.1	13.9	30.3	30.4	0.38	1.21	6.49	2.22	184.8	-324.8	-303.8	-6.1
180	3	23.2	30.8	33.7	15.1	13.9	30.3	30.3	0.42	1.22	6.47	2.25	184.2	-302.5	-283.0	-5.3
240	4	23.06	30.7	33.3	15.1	14.0	30.3	30.3	0.46	1.24	6.48	2.23	178.1	-284.2	-265.8	-2.6
300	5	23.41	30.5	33.0	15.2	14.1	30.2	30.3	0.50	1.26	6.47	2.20	167.2	-266.0	-248.8	-10.9
360	6	22.85	30.5	32.8	15.3	14.3	30.2	30.2	0.55	1.28	6.45	2.22	155.0	-242.4	-226.8	-3.4
420	7	23.39	30.5	32.5	15.3	14.4	30.3	30.3	0.59	1.30	6.46	2.25	142.0	-214.1	-200.3	-4.7
480	8	23.01	30.4	32.3	15.3	14.5	30.2	30.3	0.62	1.32	6.45	2.24	124.5	-196.1	-183.5	-6.7
540	9	23.29	30.4	32.0	15.3	14.6	30.2	30.3	0.65	1.34	6.44	2.20	109.3	-178.1	-166.6	-3.2
600	10	23.05	30.5	31.8	15.3	14.7	30.2	30.3	0.67	1.35	6.44	2.21	94.1	-144.5	-135.2	-3.1
660	11	23.25	86.5	77.6	15.4	15.0	30.3	30.3	4.94	1.41	6.43	2.22	52.6	1026.7	960.4	-2.4
720	12	23.09	89.2	84.6	15.4	15.2	30.4	30.8	6.69	1.43	6.79	2.21	37.1	541.9	506.9	-97.6
780	13	23.45	90.4	87.0	15.5	15.3	30.5	31.1	6.78	1.44	6.86	2.21	21.5	398.7	373.0	-138.1
840	14	23.42	90.9	88.1	15.5	15.4	30.6	31.2	6.78	1.45	6.89	2.22	12.2	331.3	309.9	-139.7
900	15	23.37	90.9	88.5	15.5	15.4	30.4	31.2	6.73	1.45	6.86	2.22	7.2	279.8	261.8	-163.0
960	16	23.47	90.9	88.7	15.5	15.5	30.7	31.2	6.67	1.45	6.86	2.24	4.4	251.4	235.2	-104.7
1020	17	23.54	90.7	88.8	15.5	15.5	30.7	31.1	6.62	1.45	6.83	2.22	3.9	226.9	212.2	-87.9
1080	18	23.56	90.7	88.9	15.5	15.5	30.6	31.1	6.57	1.45	6.83	2.22	2.4	211.1	197.5	-116.0
1140	19	23.58	90.6	89.0	15.5	15.5	30.6	31.0	6.51	1.45	6.81	2.20	3.1	196.1	183.4	-67.7
1200	20	23.64	90.6	89.1	15.5	15.5	30.6	31.0	6.49	1.45	6.79	2.20	1.0	174.2	163.0	-88.9
1260	21	24.33	37.9	47.4	15.4	15.4	30.6	30.6	1.54	1.45	6.61	2.19	3.8	-1032.2	-965.6	7.7
1320	22	23.75	31.4	38.7	15.4	15.1	30.5	30.5	0.58	1.36	6.52	2.23	53.7	-781.1	-730.7	1.2
1380	23	23.79	30.8	34.6	15.3	14.3	30.5	30.5	0.43	1.23	6.51	2.21	150.8	-405.6	-379.4	-2.3
1440	24	23.23	31.0	34.0	15.2	14.0	30.4	30.4	0.43	1.22	6.49	2.21	173.4	-319.7	-299.1	-4.7
1500	25	23.3	30.9	33.7	15.1	14.1	30.3	30.4	0.46	1.23	6.48	2.22	166.3	-293.4	-274.4	-4.1
1560	26	23.24	30.8	33.3	15.2	14.2	30.3	30.3	0.51	1.25	6.46	2.21	158.5	-267.7	-250.4	-3.0
1620	27	23.48	30.5	32.9	15.2	14.3	30.2	30.3	0.56	1.28	6.41	2.20	141.5	-246.8	-230.9	-8.4
1680	28	23.51	30.5	32.5	15.3	14.5	30.2	30.3	0.61	1.31	6.34	2.22	124.2	-212.3	-198.6	-4.8
1740	29	23.05	30.5	32.2	15.3	14.6	30.2	30.3	0.65	1.33	6.28	2.22	109.8	-182.3	-170.5	-2.4
1800	30	23.47	30.3	31.9	15.3	14.7	30.2	30.2	0.67	1.35	6.21	2.21	95.3	-161.9	-151.5	-4.2
1860	31	23.11	86.6	77.7	15.4	15.0	30.3	30.3	5.53	1.40	6.09	2.21	50.9	1020.8	954.9	-0.3
1920	32	23.63	89.3	84.7	15.4	15.2	30.4	30.8	6.60	1.42	6.74	2.22	33.5	534.6	500.1	-85.5
1980	33	23.8	90.5	87.1	15.5	15.3	30.5	31.1	6.70	1.43	6.85	2.22	22.2	396.6	371.0	-132.5
2040	34	23.4	90.9	88.1	15.5	15.4	30.5	31.2	6.69	1.44	6.85	2.19	13.0	332.3	310.8	-151.8

t s	t min	$T_{ambient}$ °C	T_{Bed_in} °C	T_{Bed_out} °C	T_{Evap_in} °C	T_{evap_out} °C	T_{cond_in} °C	$T_{cond,out}$ °C	P_{bed} kPa	P_{evap} kPa	P_{cond} kPa	$\dot{m}_{evap}$ L/min	$\dot{Q}_{evap}$ W	$\dot{Q}_{ads}$ W	$\dot{Q}_{des}$ W	$\dot{Q}_{cond}$ W
2100	35	23.65	90.9	88.5	15.5	15.4	30.6	31.2	6.61	1.44	6.85	2.18	7.6	278.1	260.2	-141.6
2160	36	23.81	90.8	88.7	15.5	15.4	30.7	31.1	6.58	1.44	6.83	2.24	6.1	253.2	236.9	-81.3
2220	37	23.69	90.7	88.8	15.5	15.4	30.5	31.1	6.52	1.44	6.81	2.22	2.4	226.8	212.2	-135.7
2280	38	23.7	90.7	88.9	15.5	15.4	30.7	31.0	6.42	1.44	6.79	2.24	2.0	209.1	195.6	-56.3
2340	39	23.92	90.7	89.0	15.4	15.4	30.4	31.0	6.38	1.44	6.77	2.20	-0.1	195.2	182.6	-111.8
2400	40	23.72	90.6	89.1	15.5	15.5	30.7	30.9	6.32	1.44	6.75	2.21	1.5	178.0	166.6	-37.7
2460	41	24.03	37.9	47.4	15.4	15.4	30.4	30.6	1.45	1.44	6.58	2.23	1.0	-1026.1	-959.9	-33.5
2520	42	23.69	31.4	38.7	15.4	15.0	30.4	30.5	0.57	1.35	6.49	2.23	59.5	-785.2	-734.5	-12.6
2580	43	23.53	30.7	34.6	15.2	14.2	30.4	30.4	0.41	1.22	6.46	2.18	157.6	-406.8	-380.6	-3.1
2640	44	23.06	30.9	34.0	15.1	14.0	30.4	30.4	0.42	1.21	6.44	2.25	176.3	-325.1	-304.1	-1.6
2700	45	23.3	30.9	33.7	15.1	14.0	30.4	30.4	0.46	1.22	6.43	2.23	170.0	-297.3	-278.1	-5.4
2760	46	23.21	30.7	33.3	15.2	14.1	30.3	30.3	0.50	1.24	6.42	2.18	163.1	-273.3	-255.7	-7.7
2820	47	23.1	30.6	32.9	15.2	14.3	30.3	30.3	0.55	1.27	6.41	2.23	150.2	-243.5	-227.8	-4.0
2880	48	23.38	30.5	32.6	15.3	14.4	30.3	30.3	0.59	1.30	6.40	2.19	137.0	-219.8	-205.6	-4.0
2940	49	23.6	30.4	32.3	15.3	14.6	30.3	30.3	0.63	1.32	6.41	2.23	120.6	-194.2	-181.6	-2.8
3000	50	23.55	30.4	32.0	15.3	14.6	30.2	30.3	0.65	1.33	6.39	2.25	104.7	-166.7	-155.9	-4.4
3060	51	23.34	86.6	77.7	15.3	15.0	30.3	30.3	4.91	1.40	6.38	2.21	55.9	1022.5	956.5	-1.8
3120	52	23.1	89.3	84.7	15.4	15.2	30.4	30.8	6.63	1.41	6.76	2.22	37.6	530.3	496.1	-93.6
3180	53	23.65	90.6	87.1	15.5	15.3	30.5	31.2	6.72	1.43	6.86	2.25	24.8	397.0	371.4	-135.5
3240	54	24.05	90.8	88.1	15.5	15.4	30.5	31.1	6.69	1.44	6.85	2.22	12.8	318.5	297.9	-143.7
3300	55	23.96	90.9	88.5	15.5	15.4	30.6	31.2	6.65	1.43	6.85	2.22	8.8	280.2	262.1	-125.9
3360	56	23.56	90.8	88.7	15.5	15.4	30.6	31.1	6.57	1.44	6.82	2.20	4.8	240.9	225.4	-119.0
3420	57	23.55	90.7	88.8	15.4	15.4	30.5	31.0	6.49	1.44	6.80	2.23	1.2	226.1	211.5	-106.6
3480	58	23.85	90.6	88.9	15.4	15.4	30.6	31.0	6.46	1.43	6.79	2.21	2.1	197.1	184.4	-87.2
3540	59	23.7	90.6	89.0	15.4	15.4	30.6	31.0	6.40	1.44	6.77	2.22	1.1	189.9	177.7	-81.7
3600	60	23.52	90.6	89.1	15.4	15.4	30.6	30.9	6.34	1.44	6.76	2.23	0.3	173.1	162.0	-69.3

$\omega_{estimated}$ kg/kg	ESD_{cold} GJ/m³	ESD_{heat} GJ/m³	SCP W/kg
0.058	0.092	0.435	118.1

SP_{cold} W/kg	SP_{heat} W/kg	COP_{cold}	COP_{heat}
236.57	1116.1	0.246	1.163

F.2. Experimental data of 0.3-mm coated bed with 0.766 kg FAM-Z02

Table 30. Experimental data of the S-TES system with a 0.3-mm coated bed with 0.766 kg of FAM-Z02, for three sorption-desorption cycles.

t	t	$T_{ambient}$	T_{bed_in}	T_{bed_out}	T_{evap_in}	T_{evap_out}	T_{cond_in}	T_{cond_out}	P_{bed}	P_{evap}	P_{cond}	$\dot{m}_{evap}$	$\dot{Q}_{evap}$	$\dot{Q}_{ads}$	$\dot{Q}_{des}$	$\dot{Q}_{cond}$
s	min	°C	°C	°C	°C	°C	°C	°C	kPa	kPa	kPa	L/min	W	W	W	W
1	0.02	24.22	29.87	29.95	14.90	14.91	29.67	29.66	0.07	1.37	4.29	2.15	-0.8	9.7	-9.1	3.0
60	1	23.83	29.90	33.34	14.84	13.09	29.66	29.58	0.43	1.06	3.73	2.22	270.2	384.1	-359.3	16.8
120	2	23.96	30.01	34.02	14.61	12.76	29.68	29.66	0.53	0.98	3.75	2.14	275.8	447.7	-418.8	4.6
180	3	23.78	29.98	34.06	14.57	12.65	29.68	29.65	0.58	0.94	3.75	2.14	286.2	455.6	-426.2	6.7
240	4	23.78	29.88	33.98	14.64	12.64	29.67	29.65	0.62	0.93	3.75	2.18	304.5	457.0	-427.6	2.7
300	5	23.74	29.82	33.89	14.71	12.67	29.65	29.64	0.65	0.94	3.75	2.18	311.7	454.8	-425.4	1.4
360	6	23.70	29.75	33.81	14.78	12.68	29.63	29.61	0.68	0.93	3.75	2.17	318.5	452.8	-423.5	5.7
420	7	23.81	29.73	33.77	14.81	12.68	29.61	29.61	0.71	0.94	3.75	2.17	323.9	451.4	-422.3	1.1
480	8	23.82	29.79	33.73	14.84	12.71	29.62	29.60	0.75	0.94	3.75	2.20	326.4	440.4	-412.0	2.9
540	9	23.77	29.76	33.73	14.87	12.74	29.62	29.60	0.79	0.94	3.75	2.16	320.6	443.1	-414.5	3.6
600	10	23.75	29.73	33.66	14.86	12.78	29.62	29.61	0.83	0.95	3.75	2.16	313.5	438.9	-410.6	2.5
660	11	23.72	85.76	75.49	14.97	13.96	29.61	29.90	5.22	1.21	4.24	2.21	155.6	-1146.5	1072.5	-61.9
720	12	23.86	88.23	81.56	15.12	14.43	29.83	30.97	6.66	1.27	4.70	2.22	107.4	-744.0	696.0	-247.3
780	13	23.88	89.42	83.58	15.19	14.71	30.12	31.39	6.83	1.31	4.80	2.23	73.6	-651.8	609.7	-276.4
840	14	23.93	89.82	84.78	15.20	14.91	29.96	31.30	6.83	1.34	4.77	2.18	44.7	-561.9	525.6	-289.1
900	15	24.07	89.95	85.43	15.24	15.06	29.90	31.10	6.42	1.34	4.71	2.18	27.6	-504.5	471.9	-259.1
960	16	24.10	89.90	85.93	15.26	15.14	30.18	30.99	6.01	1.36	4.68	2.18	17.8	-443.6	415.0	-176.8
1020	17	24.13	89.87	86.48	15.21	15.17	29.90	30.70	5.67	1.37	4.61	2.19	5.9	-379.2	354.7	-172.4
1080	18	24.24	89.82	87.05	15.22	15.19	29.84	30.58	5.40	1.37	4.58	2.18	4.4	-309.3	289.4	-159.6
1140	19	24.19	89.87	87.52	15.18	15.19	30.06	30.32	5.19	1.36	4.53	2.23	-0.9	-262.6	245.6	-56.1
1200	20	24.40	89.83	87.98	15.19	15.20	29.79	30.20	5.06	1.36	4.50	2.21	-0.6	-206.0	192.7	-90.2
1260	21	24.68	37.30	48.12	15.14	14.93	30.02	29.87	0.79	1.26	4.36	2.23	32.7	1207.3	-1129.4	31.6
1320	22	24.29	30.89	40.12	15.00	13.83	29.80	29.87	0.53	1.05	4.35	2.20	179.9	1030.1	-963.7	-15.0
1380	23	24.14	30.17	35.35	14.81	12.99	29.84	29.83	0.42	0.93	4.35	2.19	277.6	578.5	-541.1	3.1
1440	24	23.94	30.35	34.54	14.69	12.71	29.79	29.79	0.48	0.91	4.35	2.20	303.2	468.4	-438.2	0.5
1500	25	23.99	30.20	34.30	14.69	12.61	29.73	29.72	0.54	0.90	4.35	2.17	314.3	456.6	-427.2	1.8
1560	26	23.70	30.13	34.19	14.73	12.59	29.70	29.69	0.59	0.91	4.35	2.17	325.1	453.0	-423.8	1.1
1620	27	23.89	30.05	34.11	14.78	12.60	29.67	29.66	0.62	0.91	4.35	2.17	330.0	452.9	-423.7	1.5
1680	28	24.51	29.97	34.07	14.79	12.58	29.64	29.63	0.65	0.91	4.34	2.15	331.9	456.7	-427.3	3.0
1740	29	23.84	29.72	33.90	14.81	12.57	29.60	29.60	0.68	0.92	4.33	2.16	337.2	466.5	-436.4	0.9
1800	30	24.23	29.69	33.78	14.86	12.63	29.61	29.60	0.72	0.92	4.32	2.18	339.5	456.3	-426.8	1.7
1860	31	23.69	85.88	75.70	14.96	13.79	29.61	29.77	5.43	1.18	4.46	2.19	178.3	-1135.1	1061.9	-34.8
1920	32	24.00	88.31	81.58	15.07	14.27	30.07	31.16	6.73	1.25	4.76	2.18	121.1	-750.9	702.5	-235.5
1980	33	23.86	89.60	83.61	15.15	14.61	30.00	31.45	6.76	1.30	4.85	2.19	82.4	-668.1	625.0	-313.1
2040	34	23.81	90.06	84.70	15.15	14.81	29.93	31.26	6.47	1.33	4.78	2.18	53.0	-598.2	559.6	-286.6
2100	35	24.02	90.17	85.47	15.20	14.98	29.84	31.06	6.11	1.34	4.72	2.17	33.5	-524.4	490.6	-262.9
2160	36	24.01	90.22	86.20	15.22	15.09	30.16	30.90	5.74	1.36	4.68	2.20	19.4	-447.8	418.9	-160.3
2220	37	23.93	90.10	86.84	15.18	15.12	29.80	30.64	5.42	1.36	4.62	2.17	9.4	-364.0	340.5	-180.7
2280	38	24.00	90.12	87.49	15.13	15.11	29.85	30.45	5.18	1.36	4.57	2.19	4.4	-293.6	274.7	-128.5
2340	39	23.86	90.12	88.00	15.12	15.11	29.97	30.18	5.01	1.37	4.52	2.17	0.9	-236.8	221.5	-46.7
2400	40	24.05	90.08	88.42	15.10	15.11	29.69	30.07	4.93	1.36	4.49	2.18	-1.0	-184.7	172.8	-80.4
2460	41	24.81	37.25	48.42	15.08	14.85	29.97	29.82	0.70	1.24	4.36	2.18	34.2	1246.7	-1166.2	32.5
2520	42	24.53	30.94	40.18	14.97	13.87	29.77	29.85	0.39	1.06	4.36	2.20	168.2	1032.0	-965.4	-17.6
2580	43	24.25	30.08	35.37	14.76	12.97	29.80	29.79	0.40	0.94	4.37	2.18	272.8	590.5	-552.4	2.9
2640	44	24.03	30.33	34.52	14.64	12.68	29.74	29.72	0.48	0.91	4.36	2.19	298.9	467.3	-437.2	3.8
2700	45	23.99	30.26	34.32	14.64	12.56	29.69	29.68	0.55	0.91	4.36	2.19	317.6	453.0	-423.8	1.8
2760	46	23.88	30.13	34.18	14.67	12.53	29.66	29.64	0.59	0.91	4.36	2.14	318.6	452.2	-423.0	5.3
2820	47	23.84	30.08	34.16	14.73	12.55	29.65	29.63	0.63	0.91	4.36	2.15	326.4	456.0	-426.5	4.8

t s	t min	$T_{ambient}$ °C	T_{bed_in} °C	T_{bed_out} °C	T_{evap_in} °C	T_{evap_out} °C	T_{cond_in} °C	T_{cond_out} °C	P_{bed} kPa	P_{evap} kPa	P_{cond} kPa	$\dot{m}_{evap}$ L/min	$\dot{Q}_{evap}$ W	$\dot{Q}_{ads}$ W	$\dot{Q}_{des}$ W	$\dot{Q}_{cond}$ W
2880	48	23.70	29.90	33.99	14.74	12.53	29.60	29.59	0.65	0.91	4.35	2.19	337.4	456.2	-426.7	0.9
2940	49	24.36	29.86	33.99	14.84	12.63	29.65	29.62	0.68	0.91	4.34	2.21	341.0	460.6	-430.9	5.4
3000	50	23.97	29.73	33.84	14.81	12.58	29.60	29.59	0.72	0.92	4.33	2.19	340.5	458.3	-428.7	2.7
3060	51	24.01	85.98	75.90	14.95	13.73	29.58	29.75	5.48	1.17	4.47	2.18	186.3	-1124.6	1052.0	-38.4
3120	52	24.11	88.32	81.60	15.12	14.25	29.91	31.21	6.72	1.25	4.78	2.18	132.6	-749.6	701.3	-280.6
3180	53	24.22	89.50	83.59	15.16	14.59	29.95	31.39	6.73	1.30	4.85	2.18	86.8	-659.9	617.3	-311.0
3240	54	24.13	89.79	84.57	15.18	14.82	29.81	31.16	6.40	1.33	4.78	2.18	55.3	-582.5	545.0	-292.9
3300	55	24.03	89.93	85.34	15.19	14.97	29.94	30.94	6.04	1.35	4.71	2.20	33.4	-512.0	478.9	-216.7
3360	56	24.15	89.91	86.04	15.22	15.09	29.92	30.89	5.68	1.36	4.67	2.19	20.2	-432.6	404.7	-211.2
3420	57	24.08	89.89	86.71	15.19	15.13	30.08	30.60	5.37	1.36	4.62	2.20	9.0	-355.6	332.7	-112.6
3480	58	24.07	89.84	87.33	15.18	15.16	29.94	30.29	5.13	1.36	4.55	2.20	2.6	-280.2	262.1	-75.7
3540	59	24.43	89.97	87.91	15.22	15.20	29.83	30.15	4.99	1.37	4.51	2.15	2.6	-229.7	214.9	-69.3
3600	60	24.85	89.88	88.32	15.18	15.19	29.83	30.18	4.92	1.37	4.50	2.17	-1.8	-174.6	163.3	-76.7

$\omega_{estimated}$ kg/kg	ESD_{cold} GJ/m^3	ESD_{heat} GJ/m^3	SCP W/kg
0.085	0.208	0.582	173.5

SP_{cold} W/kg	SP_{heat} W/kg	COP_{cold}	COP_{heat}
347.030	970.004	0.400	1.12